1998

The synthesis and characterization of new tantalum chalcogenide halide cluster compounds

Mark Douglas Smith
Iowa State University

The synthesis and characterization of new tantalum chalcogenide halide cluster compounds

by

Mark Douglas Smith

A dissertation submitted to the graduate faculty
in partial fulfillment of the requirements for the degree of
DOCTOR OF PHILOSOPHY

Major: Inorganic Chemistry
Major Professor: Gordon J. Miller

Iowa State University
Ames, Iowa
1998

UMI Number: 9841030

UMI
300 North Zeeb Road
Ann Arbor, MI 48103

Graduate College
Iowa State University

This is to certify that the Doctoral dissertation of

Mark Douglas Smith

has met the dissertation requirements of Iowa State University

Signature was redacted for privacy.

Major Professor

Signature was redacted for privacy.

For the Major Program

Signature was redacted for privacy.

For the Graduate College

TABLE OF CONTENTS

CHAPTER ONE

INTRODUCTION AND LITERATURE REVIEW

Introduction

The solid-state ternary chalcogenide halide chemistry of tantalum has been receiving spotty attention in the literature for about 25 years, since the first compound to contain both tantalum-chalcogen and tantalum-halogen bonds simultaneously was reported in 1972. This compound, formulated as "$TaSCl_3 \cdot PhNCCl_2$", was obtained by refluxing a hexane solution of a sulfur-containing adduct of $TaCl_5$.[1] The first reported pure ternary tantalum chalcogenide halide was $TaSCl_3$, obtained in 1975 by reaction of Sb_2S_3 with $TaCl_5$ at 120°C.[2] In the intervening quarter century, however, the number of well-characterized tantalum chalcogenide halides has grown exceedingly slowly. A current literature survey shows a total of only *eleven* such compounds, of which only five have been acceptably structurally characterized. Furthermore, these five compounds are all structurally very similar, and can be classed together as members of a family, abbreviated to $Ta(Q_4)_nX_y$ (Q = Se, Te; X = Br, I). These will be discussed in more detail below. Clearly, exploratory synthetic chemistry of tantalum has lagged far behind that of its lighter relative niobium, whose binary halide and ternary chalcogenide halide chemistry features a multitude of compounds. $NbTe_4I$,[3] $Nb_2Se_2Br_6$,[4] Nb_3Cl_8,[5] NbSeI,[6,7] Nb_6SI_9,[8] display remarkable structural diversity, adopting structures with isolated niobium atoms, Nb-Nb dimers, Nb_3 triangular clusters, Nb_4 tetrahedral clusters, and Nb_6 octahedral clusters, respectively. Additionally, centered Nb_6 trigonal prismatic clusters in the case of the rubidium salt $Rb_3Nb_6SBr_{17}$,[9] and tetranuclear butterfly clusters in the cesium salt $CsNb_4Cl_{11}$ have been characterized.[10]

Owing to the lack of negative results published in the literature, it's uncertain if this lack of representation is due to the reluctance of tantalum to engage in chemistry as rich and diverse as that of niobium, or is simply due to a lack of any vigorous synthetic

study. Indications from the research presented in the following thesis suggest the latter is probably true.

As is well known, congeneric second and third row transition metals are almost identical in size because of the lanthanide contraction, and frequently behave chemically as duplicates of the other. Nevertheless they diverge most bafflingly in some cases. In particular, tantalum has up to now refused to show as marked an affinity for clustering to varying degrees of nuclearity as has niobium. A discrepancy of central interest between the two elements is the existence of trinuclear niobium clusters in the binary halides Nb_3X_8 (X = Cl, Br, I). Nb_3X_8 [5, 11] have been known for thirty years, are readily made and characterized, and are stable up to ca. 900°C. Contrarily, the tantalum analogs remain unknown. In fact, until the present work, only one trinuclear cluster of tantalum had been synthesized, the $[Ta_3Cl_{10}(PEt_3)_3]^-$ anion of Cotton, et al., reported in 1988.[12] This green compound, crystallized as the $[HPEt_3]^+$ salt at room temperature, was accidentally discovered. Even here a discrepancy exists between the chemistries of niobium and tantalum. Similar niobium trinuclear cluster anions containing both six and eight electrons per Nb_3 cluster were prepared, demonstrating the robustness of the Nb species towards redox chemistry.[12] However, such a variable electron count was not observed with tantalum; only the six-electron compound could be isolated. No tetranuclear tantalum clusters are known, again differing from niobium. With the remarkable variety of cluster structures displayed by niobium, it is perhaps surprising that Ta has shown such limited halide cluster chemistry.

The synthesis, characterization, and reactivity of Ta_3QX_7 (Q = S, Se, Te; X = Cl, Br, I), a new family of tantalum chalcogenide halide cluster compounds containing the first examples of tantalum trinuclear clusters obtained by high-temperature solid-state methods and some related compounds is the subject of this thesis. The intent of this thesis is to report several new examples of such tantalum chemistry, thereby expanding the known ternary solid-state cluster chemistry of tantalum both in size and in diversity, and to demonstrate the potential rewards of further tantalum chalcogenide halide exploration.

Literature review of tantalum halides and chalcogenide halides

Relevant properties of tantalum metal

Tantalum metal possesses several properties for which it is justly renowned, but which present challenges to the synthetic chemist hoping to engage the element in a reaction. As the pure element, tantalum metal is virtually inert to all acids, with the exception of a mixture of concentrated sulfuric, nitric, and hydrofluoric acids, where formation of the soluble TaF_7^{2-} anion drives dissolution. It will dissolve only very slowly in fused alkali. At ambient temperatures tantalum is virtually impervious to attack. It owes this corrosion resistance to the formation of an especially tenacious passivating surface oxide layer. The creep of this layer into the interior of the metal is exceedingly slow, even at elevated temperatures.[13] A positive side to this is that even tantalum metal which has been exposed to air for long periods of time can remain relatively pure, protected by its oxide coating. The shallow surface layer can be conveniently removed by washing with the $H_2SO_4/HNO_3/HF$ solution described above.

Table 1-1 gives values for selected thermodynamic properties of tantalum directly impacting the present work, and compares the same quantities for Nb, Zr, Hf, Mo, W, Tc and Re. A general trend in the transition metal series is that ΔH_{fus}, ΔH_{vap}, ΔH_{atom}, T_{melt}, and T_{boil} increase when descending a group, so the third row (5d) metals all have the highest values of these properties in their respective triads. Noteworthy is the large heat of atomization of Ta, which at 782 kJ/mol is the second highest in the periodic table, behind only tungsten metal (849 kJ/mol) in magnitude. The great deal of energy required to convert the bulk metal to a monatomic vapor is a consequence of the great strength of the metallic Ta-Ta bonds. Important here is the fact that ΔH_{vap} and ΔH_{atom} of Ta are higher than the Nb values. This has been interpreted as a rationalization of the greater tendency shown by Ta to engage in metal-metal bonding compared to its lighter group member Nb, and has consequences for metal-rich and cluster compounds where both of these elements are present and competing for chemically different sites. For example, the

Table 1-1. Some properties of the transition elements near tantalum.[13]

Element	MP (°C)	BP (°C)	ΔH_{fus} (kJ/mol)	ΔH_{vap} (kJ/mol)	$\Delta H_{atomization}$ (kJ/mol)
Zr	1857	4200	19.2	567	612
Hf	2222	4450	25	571	611
Nb	2468	4758	26.8	680.2	724
Ta	2980	5534	24.7	758.2	782
Mo	1620	4650	28	590	664
W	3380	5500	35	824	849
Tc	2200	4567	23.8	585	-
Re	3180	5650	34	704	779

mixed compound $Ta_{3.28}Nb_{1.72}S_2$ forms a layered structure in which a five-sheet-thick metal layer consisting of Nb and Ta is sandwiched between layers of sulfur.[14] Instead of random occupation of the crystallographic metal sites, however, partial ordering occurs. Tantalum atoms are observed to congregate preferentially in the metal-rich interior of the M_5S_2 slabs, where metal-metal interactions are maximized. The sites on the exterior of these slabs, near the sulfur layers, are then occupied by mostly niobium.

These physical properties of tantalum metal (high melting and boiling point, large heats of fusion and vaporization, reluctance to react), which reach a maximum in the region of the periodic table including Ta, W, and Re, reflect the metal-metal bond strengths, and have observable ramifications in the behavior of these elements with regard to cluster formation and stability.

This great strength and chemical inertness have led to the use of tantalum metal in diverse industrial and commercial applications. The pure metal is used as a liner in the construction of chemical storage and processing equipment, as surface-exposed parts in nuclear reactors and aircraft and missile components; medically its non-irritability and complete inertness to bodily fluids make it ideal for use as artificial joints and as bone

replacement parts. It has also been used as a filament or filament support, and its insulating oxide film has been extensively exploited by the electronics industry in the manufacture of capacitors. On a smaller scale, tantalum is used as a container for high-temperature chemical reactions, where unwanted involvement of the reaction container in the reaction is a troublesome issue.

Useful physical properties aside, the great chemical resistance of tantalum make the pure metal problematic for synthetic chemistry. Clearly, the metal is quite unreactive to halogens and chalcogens at room temperatures. The task of converting the pure element into a chemical compound requires the action of oxidizing agents at high temperatures, and is greatly aided by chemical vapor transport reactions using temperature gradients. Chemical transport is essential for reactions to occur on a reasonable timescale (several days or weeks), and for the formation of pure products, distinctly separated from unreacted Ta metal and nonvolatile binary compounds forming and remaining on the metal surface.

Binary tantalum and niobium halides

The family of compounds Ta_3QX_7 (Q = S, Se, Te; X = Cl, Br, I) that form the nucleus of this thesis are best considered chalcogen-substituted halides, and a brief review of tantalum halide chemistry is therefore in order. Also, because much of the importance of the aforementioned compounds is highlighted by comparison with niobium, because Ta and Nb halide chemistries are often so similar (but with puzzling dissimilarities), and finally because a large part of this thesis concerns mixed Ta / Nb compounds, the two elements will be discussed together, with a special focus on the cluster compounds Nb_3X_8, forerunners of Ta_3QX_7.

The known tantalum and niobium halides are gathered together in Table 1-2, grouped by formal metal oxidation state. There is a clear trend: Reduction of the metal center is accompanied by an increasing tendency toward metal cluster formation. In the +5 oxidation state, the metal centers are isolated from each other; no metal-metal bonding

Table 1-2. The known halides of niobium and tantalum. Structural features are discussed further in the text.

Oxidation number	Ta	ref	Nb	ref	Structural features
	$TaCl_5$	15	$NbCl_5$	18	
+5	$TaBr_5$	16	$NbBr_5$	19	M_2X_{10} molecules
	TaI_5	17	NbI_5	20	
	$TaCl_4$	21	$NbCl_4$	21	$^1_\infty[MX_2X_{4/2}]$ chains
+4	$TaBr_4$	22	$NbBr_4$	24	with M-M dimers
	TaI_4	23	NbI_4	25	
	-		α-Nb_3Cl_8	5	Close-packed halide layers,
+2.67	-		α-, β-Nb_3Br_8	11	Nb_3 clusters
	-		β-Nb_3I_8	11	
	Ta_6Cl_{15}	26	-		
+2.5	Ta_6Br_{15}	26	-		$[Ta_6X_{12}]^{3+}$ clusters
	Ta_6I_{15}	27	-		
	-		Nb_6Cl_{14}	30	
+2.33	Ta_6Br_{14}	28	-		$[M_6X_{12}]^{2+}$ clusters
	Ta_6I_{14}	29	-		
+1.33	-		Nb_6I_{11}	31	$[Nb_6I_8]^{3+}$ clusters

occurs. Reduction by one electron per metal causes formation of metal dimers: the one electron is now occupied in a metal-metal bond. Further reduction (in the case of Nb only) results in trinuclear cluster formation. Even further reduction leads to hexanuclear clusters. Interestingly, the occurrence of seemingly non-integral oxidation states is peculiar to the second and third rows of group five only; vanadium is found only in the +2, +3, +4 and +5 states.

Pentahalides

All pentahalides of Ta and Nb crystallize as M_2X_{10} molecular solids. In the gas phase, however, the chlorides and bromides are thought to exist as monomeric trigonal bipyramidal molecules.[32] No gas-phase information is known about the pentaiodides. The pentahalides are most easily made by direct halogenation of the metal, and can be purified by sublimation. The M_2X_{10} units, shown in Figure 1-1, are edge-sharing bioctahedra, with the metal atoms displaced from the octahedron centers away from one another due to coulombic repulsion. Metal-metal distances are greater than 3.5 Å for all halides. The M_2X_{10} molecules condense so that the halide matrix is still nearly close-packed. From this point of view, the solids can be described as nearly close-packed networks of halide, with the metal atoms in 1/5 of the octahedral sites.

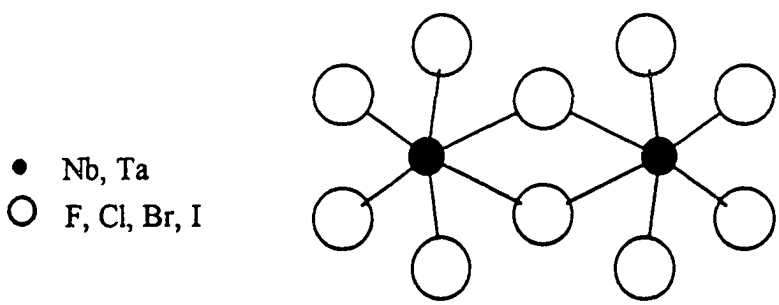

Figure 1-1. M_2X_{10} units found in tantalum and niobium pentahalide solids. The repulsive interaction between +5 metal centers forces them away from one another and distorts the coordination environment.

Tetrahalides

Niobium and tantalum tetrahalides can all be made by reduction of the pentahalides by the corresponding metal itself, or with reducing agents like aluminum.[22] Though there are slight differences in the extended three-dimensional structures adopted by the various

tetrahalides, in general all are characterized by edge-sharing distorted octahedra forming linear $MX_2X_{4/2}$ chains with alternating short-long metal-metal distances. Such a chain is illustrated in Figure 1-2. In $NbCl_4$, the Nb-Nb distances are 3.029 Å and 3.794 Å. The alternating bond length pattern is due to dimerization of the metals within the chains. The unpaired electron one might expect from a simple consideration of the +4 oxidation state of the metal (d^1 configuration) is instead involved in a metal-metal bond. Accordingly, the compounds are diamagnetic. The packing of the $MX_2X_{4/2}$ chains in the extended structure is also consistent with viewing the structures as close-packed networks of halide, with the metal ordered in 1/4 of the octahedral sites; see Figure 1-3.

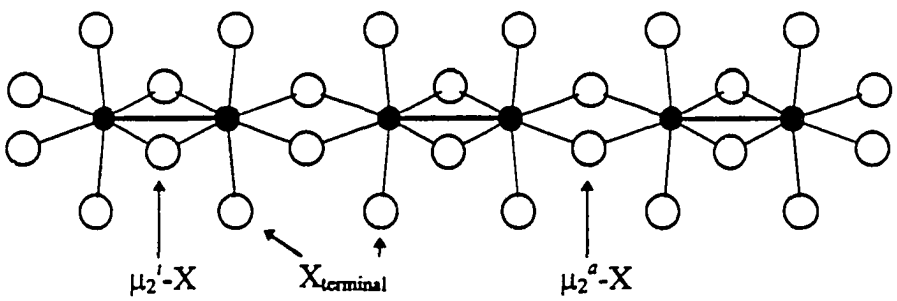

Compound	M-M	M-$X_{terminal}$	M-(μ_2^i-X)	M-(μ_2^a-X)
$NbCl_4$	3.029, 3.794	2.291	2.425	2.523
α-NbI_4	3.309, 4.361	2.675	2.741	2.894

Figure 1-2. The $MX_2X_{4/2}$ chains in tantalum and niobium tetrahalides. Various bond distances, where known, are also given (Å). The superscripts *i* and *a* refer to the *innen* and *aussen* notation of Schäfer and von Schnering.

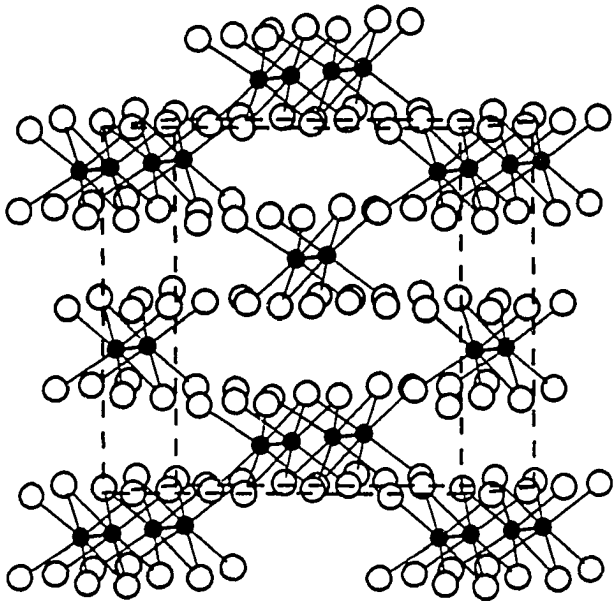

(a) Extended structure of α-NbI_4, showing the interstitial occupation of the close-packed iodide layers by Nb dimers.

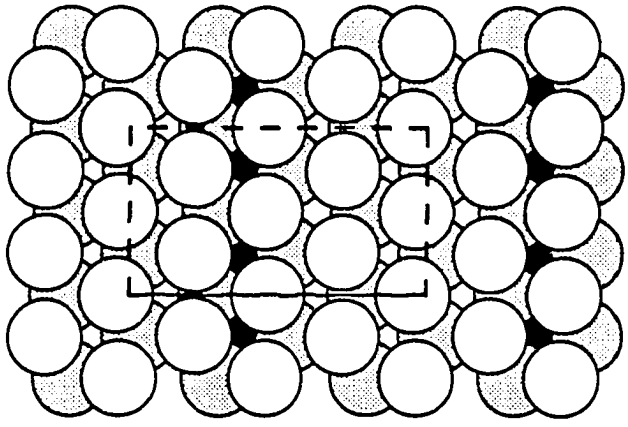

(b) View perpendicular to the close-packed iodide layers, showing the distribution of occupied octahedral sites. Large grey circles represent the lower cp layer, large white circles the upper cp layer, and black circles the metal atoms.

Figure 1-3. Structural views of α-NbI_4. Other niobium and tantalum tetrahalides are similar.

At formal oxidation states below +4, the chemistries of the binary halides of niobium and tantalum begin to deviate from expected simple oxidation-number patterns, and to display unusual structural features and dissimilarities from each other, involving extensive metal clustering and non-integral oxidation states.

Trihalides

The older literature is replete with tantalizing mentions of lower halides, including "$TaCl_2$" [33], "$NbCl_2$" [30], "$TaBr_2$" [34], "$TaX_{2.5}$" [35], "$TaCl_3$" [36], "$TaBr_3$" [37] and "NbI_3"[38]. Their characterization was usually limited to elemental analysis and powder x-ray diffraction. The verity of these compounds is dubious at best; they are most likely misidentified hexanuclear cluster compounds. The phase thought to be "$NbCl_2$" was later proven to be Nb_6Cl_{14} contaminated with niobium metal and niobium oxides.[30] Of all the various enigmatic lower halides, $TaCl_{2.80}$ and $TaBr_{2.83}$ are the most thoroughly studied.[39] They are reported to be mixed-valent compounds containing $Ta_6X_{12}^{n+}$ clusters and hexahalotantalate(V) ions.

Lower oxidation states

Metal-metal interactions dominate the structure and bonding of the more highly reduced Ta and Nb halides, and determine their stability. It is here in the lower oxidation-state chemistries of tantalum and niobium that the most severe dissimilarities between the structural chemistries of the pair emerge. The first and most glaring chasm occurs with the binary halides Nb_3X_8, having a formal oxidation state of +2.67. Nb_3X_8 exist only for niobium; remarkably, no such compounds have been reported for tantalum, whose reduced-oxidation state chemistry is dominated by octahedral clusters. (Ta_3X_8 have been alluded to in the literature, but falsely.[40]) Nb_3X_8 can be prepared by reduction of the pentahalides with Nb, or by stoichiometric combination of the elements at ca. 800°C.

Structurally, Nb_3X_8 are defect-CdI_2 compounds, comprised of close-packed layers of halide containing trinuclear Nb_3 clusters between every other layer. Two modifications

of Nb_3X_8, the hexagonal α form and the rhombohedral β form, are known, and are described in full below.

While β-Nb_3Br_8 and β-Nb_3I_8 are apparently stoichiometric "line phase" compounds (no "β-Nb_3Cl_8" has been reported), the α modifications α-Nb_3Cl_8, α-Nb_3Br_8, and α-Nb_3I_8 are reported to actually be part of a series of nonstoichiometric phases $Nb_{3-x}X_8$, with Nb_3X_8 representing the most reduced (end) member of this series.[11] To date there is no rationalization for why only the α form and not the β form of Nb_3X_8 exhibits non-stoichiometry. For α-$Nb_{3-x}Br_8$, $x \leq 0.36$, and for α-$Nb_{3-x}I_8$, $0.23 \leq x \leq 0.38$. α-Nb_3Cl_8 is the best-characterized of these three. It shows a homogeneity range from from $Nb_{2.56}Cl_8$ to Nb_3Cl_8 ($x \leq 0.44$). The non-stoichiometry of α-Nb_3Cl_8 has been interpreted as the formation of a solid-solution of Nb_3 triangles and Nb_2 dimers within the halide matrix,[42] i.e., formation of a mixed $(Nb_3)_{1-x}(Nb_2)_xCl_8$ crystal. Electronic structure calculations on this system have shown that as the concentration of Nb_2 dimers is increased, the Nb_3 triangles are increasingly oxidized due to electron transfer to lower-lying Nb_2 δ* orbitals until, at some point, disproportionation into $NbCl_4$ and a more reduced halide is favored.[42]

The reason for the continued absence of Ta_3X_8 is not evident, but perhaps has to do with the greater M-M bonding tendencies of the heavier element, predisposing tantalum to clusters of nuclearity greater than three, in particular the highly stable octahedral clusters described next.

Hexanuclear cluster compounds

In the most reduced oxidation states exhibited in extended solids of tantalum and niobium, a series of octahedral cluster compounds based on quasi-infinite three-dimensional linkages of $[M_6X_{12}]^{n+}$ or $[M_6X_8]^{n+}$ clusters forms. The core of these structural units is an M_6 hexanuclear cluster, which either has perfect octahedral symmetry or is distended along a three-fold axis, depending on the symmetry of the solid. The halides coordinate the cluster either by bridging all twelve cluster edges ($[M_6X_{12}]^{n+}$), or by

capping all eight cluster faces ($[M_6X_8]^{a+}$). Intercluster linkage is accomplished by halide bridges through the vacant cluster vertex sites. Representations of the two cluster types are given in Figure 1-4, and a diagram of how $[M_6X_{12}]^{2+}$ units link up in a typical solid is shown in the structure picture of Ta_6I_{14} (Figure 1-5), a common by-product of many of the reactions discussed later in this thesis. For group five binary halides, the $[M_6X_8]^{a+}$ cluster type occurs only in Nb_6I_{11}.

Review of ternary tantalum chalcogenide halide chemistry

Transition metal chalcogenide halides will be defined in this thesis as follows: a ternary compound between a transition metal, a chalcogen (S, Se, Te) and a halogen where distinct bonds between the metal and both the chalcogen and the halogen exist. Such a distinction has been made before,[43] and eliminates complex, mixed salts such as $MoTe_3Cl_{16}$, better formulated as $(TeCl_3^+)_3(MoCl_6^{2-})(Cl^-)$, where the coordination sphere of the molybdenum atom consists of only chlorides; no Mo-Te bonds are present. Also eliminated are compounds consisting of chalcogen polycations and halometallates, like $(Te_4^{2+})(WCl_6^-)$, where again the only bonds to the metal are from the halogen. Even after narrowing the definition in this way, transition metal chalcogenide halides as a class still offer astonishing structural diversity and a host of practically and impractically interesting chemical properties. Classical salt-like compounds are known, and so are novel low-dimensional, strongly metal-metal bonded compounds. Some puzzling absences remain: the heavier members of groups three (La) and five (Nb, Ta) form numerous chalcogenide halides, but still none have been reported for Zr and Hf. Tungsten forms several sulfide halides and selenide halides, but no tungsten telluride halide is known. Likewise with the prolific cluster compound-former molybdenum, though a substituted Chevrel phase is known in this system.

Table 1-3 gathers together ionic radii and Pauling electronegativity values of the chalcogens and halogens. Oxygen and fluorine are included for comparison. An interesting and perhaps surprising fact is that the least electronegative halogen (iodine) is

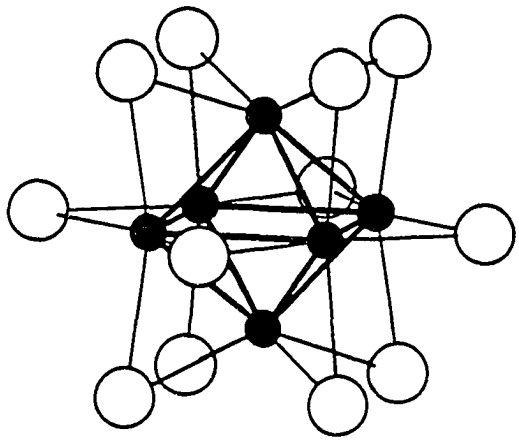

(a) $[M_6X_{12}]^{n+}$

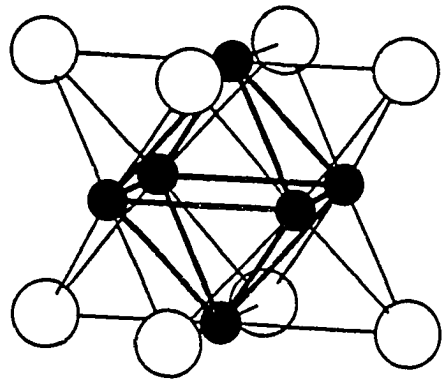

(b) $[Nb_6I_8]^{3+}$

(a) The $[M_6X_{12}]^{n+}$ cluster unit found in the reduced binary tantalum and niobium halides Nb_6Cl_{14}, Ta_6Cl_{15}, Ta_6Br_{14}, Ta_6Br_{15}, Ta_6I_{14} and Ta_6I_{15}, in the mixed halides $Nb_6Cl_{12}I_2$ and $Nb_6Cl_{10.8}Cl_{3.2}$, in ternary halides like $K_4Nb_6Cl_{18}$, and in numerous compounds like $Ta_6Cl_{14}\bullet 7H_2O$ isolated from solution.

(b) The $[Nb_6I_8]^{3+}$ cluster unit found only in Nb_6I_{11} and its derivatives.

Figure 1-4. $[M_6X_{12}]^{n+}$ and $[Nb_6I_8]^{3+}$ hexanuclear cluster units and their coordination environments found in reduced niobium and tantalum halides.
In the three-dimensional solids, these cluster units link up by means of intercluster halide bridges between the vertex sites.

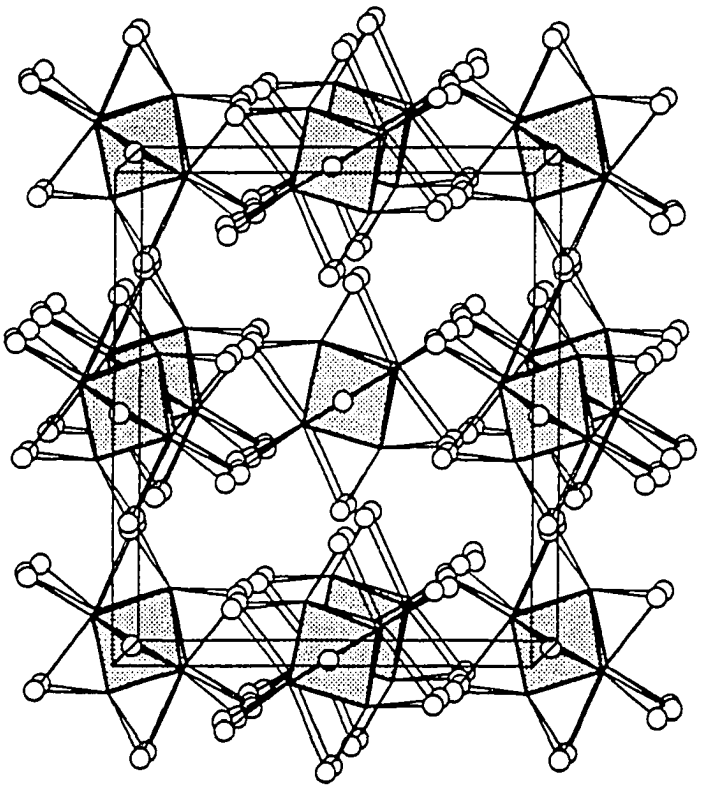

Figure 1-5. Structure diagram of Ta_6I_{14} ($[Ta_6I_{12}]^{2+}(I^-)_2$). Ta_6 clusters are shaded. The $[Ta_6I_{12}]^{2+}$ units are linked together by iodide atoms (open circles) bridging four cluster vertices.

Table 1-3. Pauling electronegativities [44] and ionic radii (Shannon and Prewitt [45]) of the chalcogens and halogens.

Chalcogens			Halogens		
Atom	Electronegativity (Pauling)	Ionic Radius (Q^{2-}) CN=6	Atom	Electronegativity (Pauling)	Ionic Radius (X^-) CN=6
O	3.44	1.40	F	3.98	1.33
S	2.58	1.84	Cl	3.16	1.81
Se	2.55	1.98	Br	2.96	1.96
Te	2.10	2.21	I	2.66	2.20

still more electronegative than the most electronegative chalcogen (sulfur). This is a crucial point in rationalizing site preferences in a structure. The systematic, evenly gradated variation of size and electronegativity parameters characteristic of this group of elements (S, Se, Te and Cl, Br, I) offers to the chalcogenide halide chemist many appealing synthetic options. The wide range of electronegativities (from 2.10 for Te to 3.16 for Cl) allows for interplay and opposition of covalency and ionicity. Systems containing similar elements (Se and Br for example) can be expected to behave quite differently from those containing polar opposites, like a Te / Cl or S / I system. The range of ionic radii, especially halide radii, will be important in M_3QX_7 systems, whose anion matrix is predominantly halide.

Theory has been used successfully to correlate these atomic parameters with observed structure, a forteriori. Structural preferences based on hard-core repulsions are seen - chlorides favor structures that minimize interaction of the hard Cl^- anions, while compounds of the larger, more polarizable bromides or iodides are influenced primarily by the Madelung term.[42]

The stability of the compounds is limited to chalcogens and halogens of the third period and below; oxygen and fluorine are too electronegative to be compatible with these reduced systems. When oxygen is introduced, M^{4+} and M^{5+} oxyhalides are observed instead.

The chalcogens (and to a lesser extent halogens) are known to concatenate. The capacity to form either isolated monochalcogenides (Q^{2-}) or polychalcogenide linkages (Q_n^{2-}) means that there are additional stable alternate compounds that might form. Although this is clearly more likely for chalcogen-rich systems, dumbbell Te_2^{2-} groups have been observed in $Nb_2Te_2I_6$ and $Nb_2Se_2Br_6$.

As noted earlier, the tantalum chalcogenide halide compounds known until this work fall into two main classes, grouped together in Table 1-4:

I. Halide-rich chalcogen chlorides and bromides, synthesized at low temperatures, often from solution, and inadequately structurally characterized.

II. Chalcogen-rich compounds of the type $Ta(Q_4)_xX_y$, containing varying length linear chains of Ta atoms coordinated in a square antiprismatic fashion by Q_2^{2-} groups.

Table 1-4. Summary of all reported tantalum chalcogenide halides.

I. Early chalcogenide halides		II. $Ta(Q_4)_xX_y$ (Q = Se, Te; X = Br, I: x = 1, 2, 4; y = 1, 2)	
Compound	Reference	Compound	Reference
$TaSCl_3$	46, 47	$(TaSe_4)_4Br$	56
TaS_2Cl [a]	48	$Ta_4Se_{16}Br_2$	57
TaS_2Cl_2	49	$(TaSe_4)_2I$	58
$TaSCl_9$ [a]	50	$(TaSe_4)_3I$	59
$TaSBr_3$	46	$TaTe_4I$	3
$TaSeBr_3$	46		

[a] compounds for which no information is available except chemical formulae.

$TaQX_3$, (Q = S, Se; X = Cl, Br) and similar compounds

Until the present work, seven halide-rich chalcogen halide compounds of tantalum were known. $TaSCl_3$, $TaSBr_3$ and $TaSeBr_3$ have all been made by reaction of the tantalum pentahalide with the proper antimony chalcogenide in a solution of CS_2 at room temperature.[46] $TaSCl_3$ has also been prepared in sealed tubes at 80°C using B_2S_3 as the sulfur source.[47] SbX_3 and BCl_3 are the by-products, respectively. Because these compounds were formed under relatively mild conditions, it is not surprising that single crystals were never obtained, but rather polycrystalline material only. As such, structural characterization has been limited to elemental analysis and spectroscopic techniques. $TaSCl_3$ is the most extensively characterized of these. It forms yellow moisture-sensitive powders reported to be soluble in acetonitrile with formation of the adduct $TaSCl_3 \cdot 2CH_3CN$.[47] The pure solid decomposes at 200°C, into an uncharacterized compound with formula "TaS_2Cl".[48] Based on the (terminal) tantalum-sulfur stretching frequency of 463 cm^{-1}, $TaSCl_3$ (and $TaSBr_3$) has been assigned to the $MoOBr_3$ structure type (distorted double chains of edge-sharing $MoO_{2/2}Br_{2/2}Br_2$ octahedra propagated through inequivalent trans-O atom bridges) by Drew and Tomkins.[51] However, Baghlaf and Thompson[47] suggest it to be isostructural with $NbSCl_3$, which is agreed to adopt the $NbOCl_3$ structure (linear double chains of edge-sharing $NbO_{2/2}Cl_{2/2}Cl_2$ octahedra propagated through equivalent *trans*-O atom bridges).[52] This controversy has not been resolved, and clearly further study is required. TaS_2Cl_2, TaS_2Cl, $TaSCl_9$, and $TaSeBr_3$ remain almost totally uncharacterized.

Additionally, Russian scientists have thoroughly explored the phase diagram for three double-binary Ta-Q-X systems formed between $TaCl_5$ and chalcogen chlorides.[53] Ta-Se-Cl, Ta-Te-Cl and Ta-S-Cl systems were examined using mixtures of $TaCl_5$ + $TeCl_4$, $TaCl_5$ + $TeCl_4$, and $TaCl_5$ + S_2Cl_2, respectively, from 0-100 mole % of each component. Differential thermal analysis with visual observation was the method used. In the Se and Te studies, incongruently melting 1:1 compounds were reported, but no other information was provided on such "$TaCl_5 \cdot QCl_4$" (Q = Se, Te). Interestingly, no compounds were

reported in the Ta-S-Cl system, though $TaSCl_3$, TaS_2Cl_2 and "$TaCl_9S$" (formulated as the 1:1 adduct $TaCl_5 \cdot SCl_4$) were reported to be stable in the region studied.[46, 51] Clearly, since the mixtures studied are quite halide-heavy, such a study is doomed to miss metal-rich compounds. Also, compounds stable beyond the pressure-temperature limits of the study will obviously not be represented.

$Ta(Q_4)_xX_y$ (Q = Se, Te; X = Br, I)

Structural understanding of the series of compounds $Ta(Q_4)_xX_y$ (Q = Se, Te; X = Br, I) is much better, due to the fact that single crystals grow readily from these reactions. Five $Ta(Q_4)_xX_y$ compounds are known, and can be prepared easily by direct combination of the elements in evacuated fused silica tubes at an appropriate temperature (generally 460°C to 625°C). All structures consist of one-dimensional $Ta(Q_2)_2$ chains in which Ta^{4+} and/or Ta^{5+} ions are rectangular antiprismatically coordinated by four Q_2^{2-} groups. Columns of halide ions intersperse the chains, providing crosslinks and charge balance. A typical structure is represented in Figure 1-6. These compounds have generated much interest due to the nearly linear chains of metal atoms, which can be evenly spaced as in $(TaSe_4)_2I$, or can exhibit short and long M-M lengths, as in $(TaSe_4)_3I$ and $(TaSe_4)_4Br$.

Niobium: Review of Nb_3QX_7 (Q = S, Se, Te; X = Cl, Br, I)

Recently a new class of niobium cluster compounds was discovered, the chalcogen-substituted halides Nb_3QX_7. These compounds nicely demonstrate how theoretical understanding can drive successful synthetic chemistry. The binary halides Nb_3X_8 had been known for thirty years. The gross aspects of their electronic structures were figured out early, and a comprehensive band structure study on β-Nb_3Br_8 has been reported. Nb_3X_8 are paramagnetic,[11] with one electron delocalized over the cluster. The extent of delocalization differs depending on the halide. α-Nb_3Cl_8 follows Curie-Weiss behavior with an effective moment of 1.86 Bohr magnetons, consistent with the spin-only value for one unpaired electron. However β-Nb_3Br_8 and β-Nb_3I_8 show anomalously low

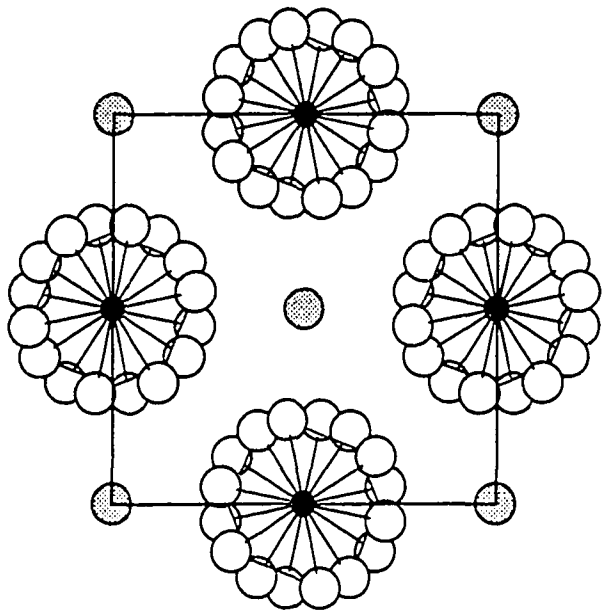

(a) [001] view of $Ta_2(Se_4)_2I$, showing the packing of the $[Ta_2(Se_2)_2]$ chains and the distribution of the iodide anions. Black circles, metal atoms; Open circles, chalcogen atoms; Grey circles, halide atoms.

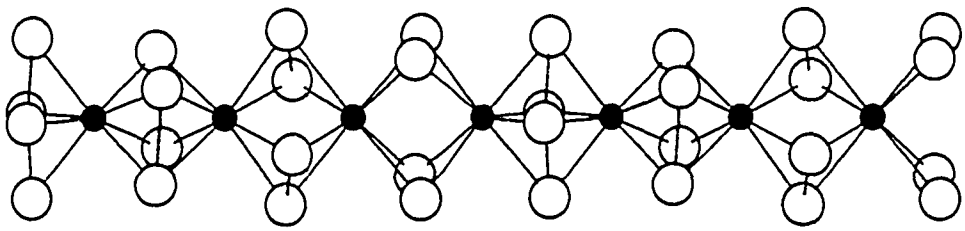

(b) The $M(Q_2)_2$ chains found in $Ta(Q_4)_nX_y$. Black circles, Nb, Ta; Open circles, chalcogen. Halides are not shown. In $Ta_2(Se_4)_2I$, the metal atoms are evenly spaced (d(Ta-Ta) = 3.206 Å), and the compound shows a low electrical resistivity of 1.5×10^{-3} Ω·cm. In other $M(Q_4)_nX_y$ compounds like $Ta_4Se_{16}Br_2$ short and long M-M distances alternate (Ta-Ta: 3.055(1), 3.187(1)), and the compounds have higher electrical resistivities.

Figure 1-6. Structural views of $M(Q_4)_nX_y$.

moments of 1.0 B.M. (Br) and 0.8 B.M. (I), which remain almost constant between 90 K and 350 K, and increase only slightly at higher temperatures. This phenomenon has been ascribed to a superexchange interaction mechanism between the clusters operating through the surrounding halide matrix.[11] The idea that substitution of a divalent element (i.e. a chalcogen) for a halogen might be possible, thereby "oxidizing" the compound by one electron and leading to a closed-shell, diamagnetic compound, was proposed in 1976 by Hulliger.[41] In 1988 Hönle, et al., succeeded in carrying this idea to fruition with the synthesis of Nb_3TeBr_7.[58] Subsequently, nearly all members of the family have been reported. Table 1-6 compiles these, and gives references and some structural information. Their structures and electronic properties will now be discussed.

Table 1-6. Nb_3X_8 and Nb_3QX_7 compounds, and structural information.

Compound	Space group	Stacking variant	Nb-Nb (Å)	Nb-Q (Å)	Nb-X (Å)	Ref.
Nb_3Cl_8	$P\bar{3}m1$	...h...	2.809	2.462	2.424 - 2.624	5
Nb_3TeCl_7	$P\bar{3}m1$	...h...	2.897	2.699	2.414 - 2.674	42
β-Nb_3Br_8	$R\bar{3}m$	...hhcc...	2.882	2.596	2.552 - 2.792	11
Nb_3SBr_7	P3m1	...h...	2.901	2.416	2.544 - 2.805	58, 59
Nb_3SeBr_7	P3m1	...h...	3.010	2.520	2.530 - 2.820	58
Nb_3TeBr_7	P3m1	...hc...	2.958	2.702	2.557 - 2.819	58
β-Nb_3I_8	$R\bar{3}m$	...hhcc...	3.002	2.755	2.756 - 3.020	11
Nb_3SI_7	$P6_3mc$	...hc...	2.995	2.404	2.737 - 2.993	58
Nb_3SeI_7	$P6_3mc$	...hc...	3.017	2.533	2.716 - 3.002	58
Nb_3TeI_7	$P6_3mc$	...hc...	3.040	2.695	2.722 - 3.001	58
Nb_3TeI_7	P3m1	...h...	3.059	2.713	2.737 - 3.026	60

Structural relationship between CdI_2, Nb_3X_8 and M_3QX_7

A facile structural relationship exists between the binary halides Nb_3X_8, the chalcogenide halides M_3QX_7, and the CdI_2 (or $Cd(OH)_2$) structure type. The CdI_2 type can be considered the parent type of Nb_3X_8 and M_3QX_7, with the latter two types derived from CdI_2 by the existence of metal-site vacancies, the presence of metal-metal bonding, and the substitution of a chalcogen for a halide. All three types are layered structures, built up of close-packed anion layers interleaved in every other layer by metal atoms. Since alternate layers are empty, a convenient way to view the extended three-dimensional structures of these three types is to conceive of each {anion layer-metal layer-anion layer} "slab" as a two-dimensional subunit, extending in the x and y directions. In conventional solid-state chemistry nomenclature, these slabs are represented as ${}^{2}_{\infty}$[chemical formula], with the superscript denoting the two-dimensional (layered) nature of the compounds, and the subscript denoting the (quasi) infinite nature of solids. Thus the salient structural features of the three structures discussed here are then conveniently represented as stacking of ${}^{2}_{\infty}[CdI_2]$, ${}^{2}_{\infty}[Nb_3X_8]$, or ${}^{2}_{\infty}[M_3QX_7]$ slabs. The slabs are weakly held together, cohesed by dispersion forces acting through the intervening van der Waals gap. The weak interslab interactions allow the slabs to slide over one another with relative ease, and is responsible for the lubricating feel such layered compounds have during mortar and pestle grinding.

For present purposes, the structural relationship between CdI_2, Nb_3X_8 and M_3XQ_7 can be nicely illustrated simply by reference to the individual ${}^{2}_{\infty}$[metal-anion] slabs that are their building blocks. These slabs are described as follows:

CdI_2

The occupation of the octahedral interstices formed between the two anion layers is complete, with every possible site filled with a metal atom. The coordination of the metal atoms is perfectly octahedral, with local site symmetry $\bar{3}m$. The spacing between the metal atoms is equivalent to the hexagonal a-axis length, and there is no metal-metal

bonding present. A [001] projection of a single $^{2}_{\infty}[CdI_2]$ slab, and a [100] view of two $^{2}_{\infty}[CdI_2]$ slabs of this common structural archetype are shown in Figure 1-7.

Nb_3X_8 (X = Cl, Br, I)

In the binary niobium halides, only three-quarters of all possible "octahedral" interstices sites between the anion layers are occupied by metal atoms, and the remaining site is vacant. Another formulation of Nb_3X_8 is $Nb_3(vacancy)_1X_8$, whose 2:1 anion:(metal + vacancy) ratio highlights its link to CdI_2: i.e., a metal-deficient CdI_2. Three nearest niobium atoms are displaced from the centers of their interstitial sites toward each other, drawn together to form trinuclear clusters. This displacement creates the distorted, eight-coordinate environment found in Nb_3X_8. Six halides and two metal atoms make up the bicapped distorted octahedron coordination sphere of each Nb. Alternately, the slabs are condensed trimers of edge-sharing distorted octahedra with Nb-Nb bonding, as shown in Figure 1-8. The local metal cluster unit is the common M_3X_{13} type, with one μ_3 bridging atom, three μ_2 edge-bridging atoms, and nine atoms that provide bridges between clusters and link the extended slabs together. The cluster has local symmetry C_{3v} (in hexagonal structures). [001] and [100] projections of this structure are shown in Figure 1-8.

M_3QX_7 (M = Nb, Ta; Q = S, Se, Te; X = Cl, Br, I)

The metal site occupation is the same as in Nb_3X_8, with the metal atoms forming triangular clusters. However, introduction of a chalcogen into the halide matrix creates a site-preference problem. M_3QX_7 slabs differ from Nb_3X_8 slabs only in the identity of the atom that occupies the μ_3 bridging position, capping the face of the trinuclear cluster. In M_3QX_7, this site is always occupied by the chalcogen, with important electronic ramifications discussed further below. The [001] projection of one $^{2}_{\infty}[M_3QX_7]$ slab is shown in Figure 1-9.

The reason for the chalcogen's preference for this site has been explained based on site electron density calculations. The electron richness or poorness of a particular

The CdI_2 structure

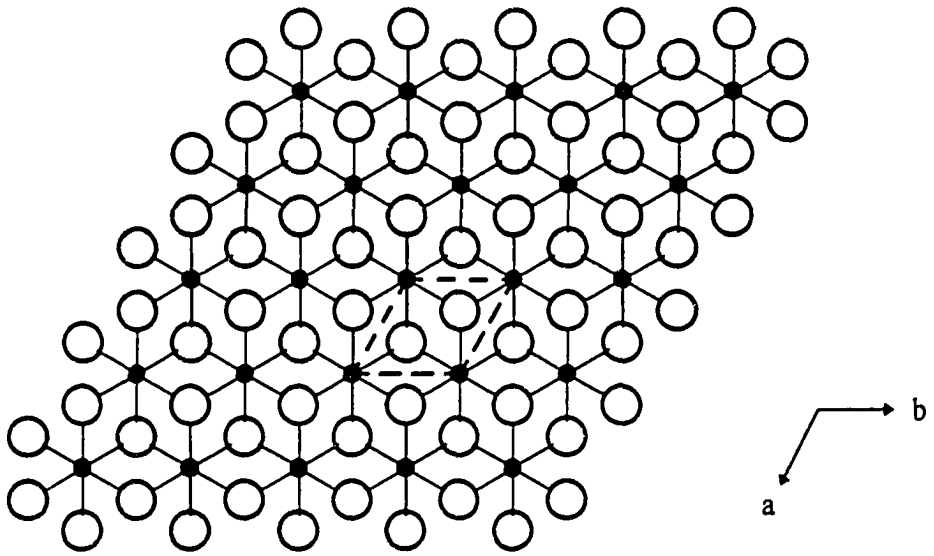

(a) [001] projection of a single ${}^{2}_{\infty}[CdI_2]$ slab. Metal atoms (small black circles) are evenly spaced in the perfectly octahedral coordination sites formed by close-packed anion layers (open circles). Metal-anion bonds are represented; there is no metal-metal bonding.

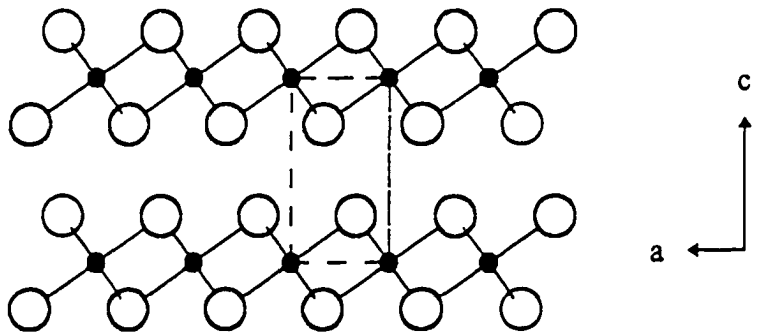

(b) [100] view of the stacking of two ${}^{2}_{\infty}[CdI_2]$ slabs. The unit cell is indicated.

Figure 1-7. The CdI_2 structure, in (a) [001] and (b) [100] projections.

Nb_3X_8 (X = Cl, Br, I)

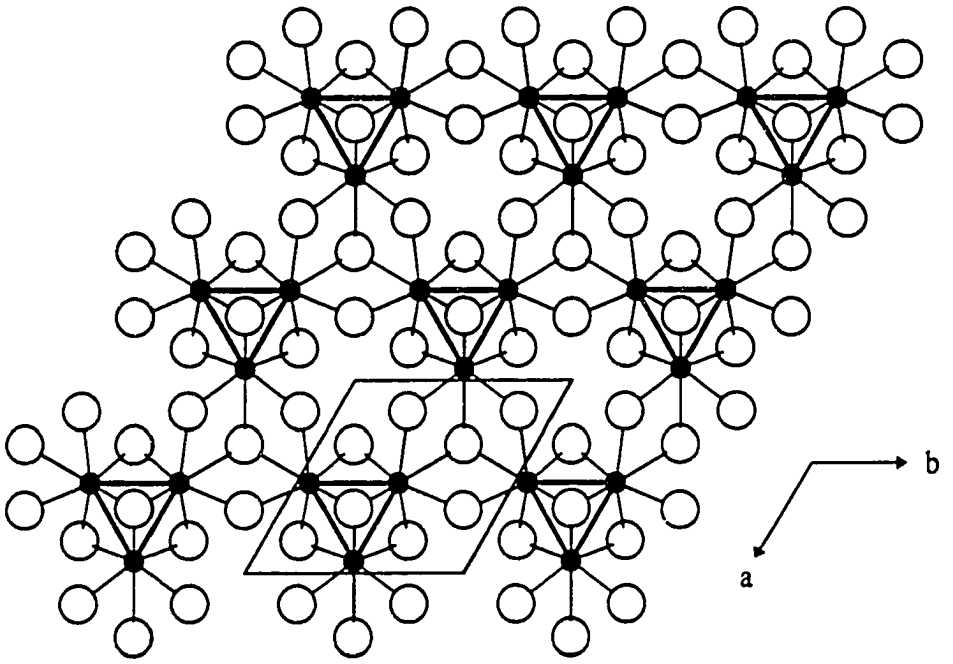

(a) [001] projection of a single $^{2}_{\infty}[Nb_3X_8]$ slab (X = Cl, Br, I). The vacancy position (see text) is located at (0, 0). A hexagonal unit cell is also drawn.

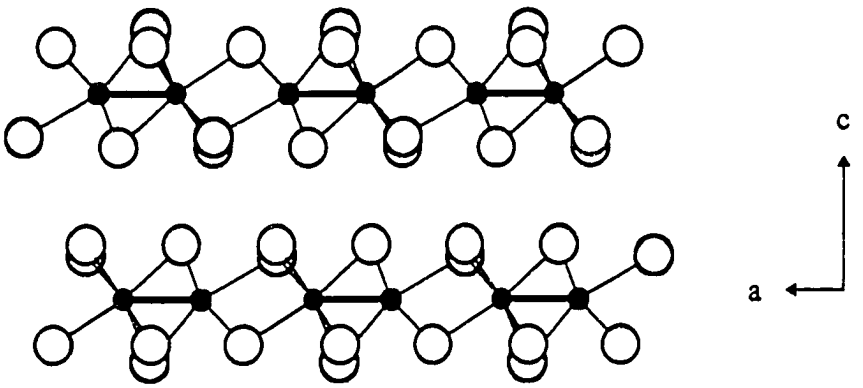

(b) [100] projection of two (antiferroelectric) $^{2}_{\infty}[Nb_3X_8]$ slabs

Figure 1-8. The Nb_3X_8 structure. The triangular Nb_3 clusters are emphasized by heavy bonds between the metal atoms (small black circles). Open circles are halide atoms. (a) Projection down the stacking direction ([001]). (b) Side view ([100]) .

M_3QX_7 (M = Nb, Ta; Q = S, Se, Te; X = Cl, Br, I)

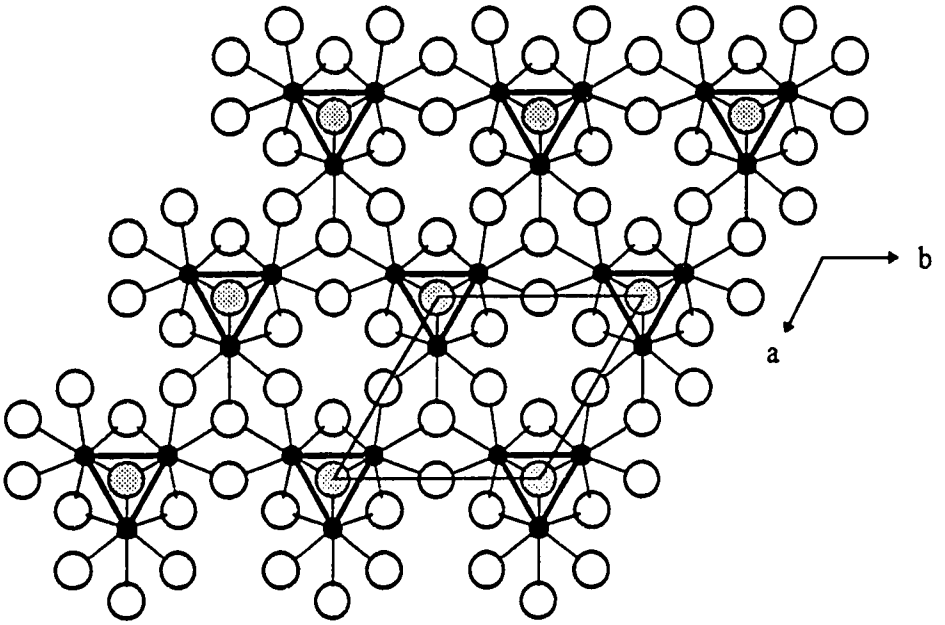

(a) [001] projection of a single ${}^{2}_{\infty}[M_3QX_7]$ slab. A hexagonal unit cell is shown. The vacancy site in this projection is located at (1/3, 2/3).

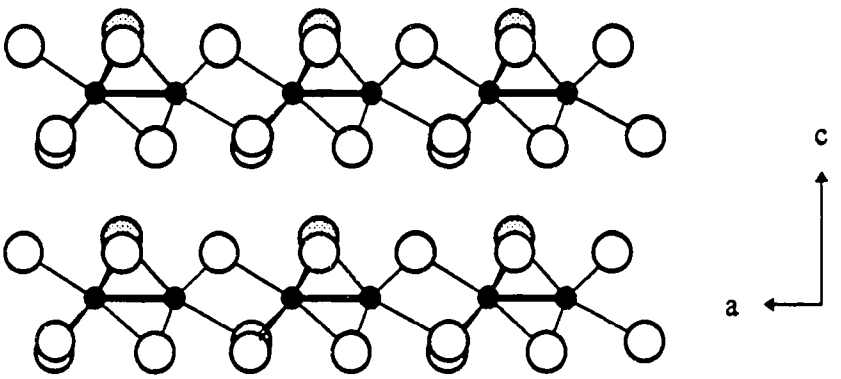

(b) [100] view of two (ferroelectric) ${}^{2}_{\infty}[M_3QX_7]$ slabs.

Figure 1-9. The M_3QX_7 structure. The triangular Nb_3 or Ta_3 clusters are highlighted by heavy bonds between the metal atoms (small black circles). The clusters are capped by a chalcogen (grey circles), and the remaining coordination sites are occupied by halides (open circles).

crystallographic site can be estimated within the context of Extended Hückel theory using Mulliken population analysis. Such calculations were performed by Miller on the compound α-Nb_3Cl_8.[42] Within each Nb_3X_8 slab, there are four crystallographically inequivalent anion sites (assuming C_{3v} cluster symmetry): 1) μ_3-X^i, cluster capping atom, 2) μ_2-X^i, cluster edge-bridging, 3) μ_2-X^a, two-cluster bridge, and 4) μ_3-X^a, three-cluster bridge. (The *i* and *a* superscripts refer to the *innen* and *ausser* notation developed by Schäfer and von Schnering.) The Mulliken populations calculated by Miller for these four sites in α-Nb_3Cl_8 are illustrated in Figure 1-10. His results showed the μ_3-X^i capping position to be the least electron-rich site of the four distinct anion positions. Consequently, the less electronegative element in a mixed anion should reside at this position, leaving the more electronegative atoms in the electron-richer sites. Since the (Pauling) electronegativities of the chalcogens S, Se, and Te are all less than that of the halogens Cl, Br, and I (see Table 1-3), the chalcogens choose the relatively electron-poor μ_3-X^i capping position, and the halogen atoms occupy the sites of greater electron density.

The seven M_3QX_7 structure types

The above structural descriptions apply to individual slabs only. For the full three-dimensional Nb_3X_8 and M_3QX_7 compounds, an endless variety of structure types (stacking variants or polytypes) is of course possible because of the limitless ways these slabs can stack upon one another. Structure type differences can result from adjacent slabs being shifted or rotated with respect to one another, or from an inversion of the slab, or both. These stacking variants have been sorted into two broad classes based on orientation of the M_3X_{cap} tetrahedron present in the slabs. When all M_3X_{cap} dipoles are oriented unidirectionally, the structure is termed "ferroelectric". Conversely, alternating M_3X_{cap} dipoles give "antiferroelectric" structures. Figure 1-11 illustrates these two categories.

Seven M_3QX_7 structure types have been characterized: α-Nb_3Cl_8, β-Nb_3I_8, Nb_3SBr_7, Ta_3SBr_7, Nb_3SeI_7, Nb_3TeBr_7, and *o*-Nb_3SI_7. Of these, five have trigonal or hexagonal symmetry. Only Ta_3SBr_7 (monoclinic) and *o*-Nb_3SI_7 (orthorhombic) have

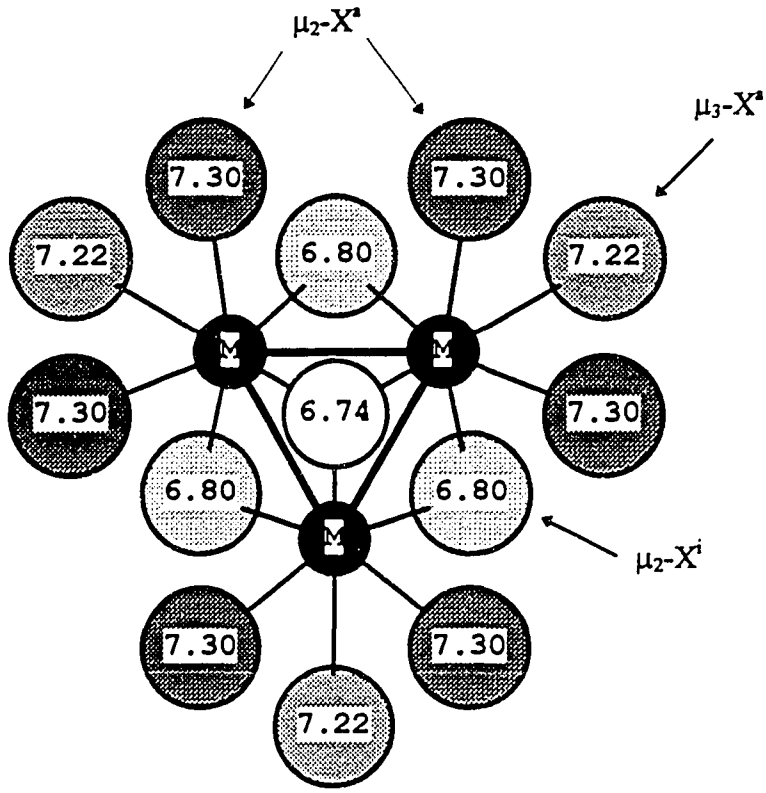

Figure 1-10. Calculated Mulliken populations in α-Nb_3Cl_8. Three of the four inequivalent crystallographic sites are labeled. Electron rich sites are shaded darker.

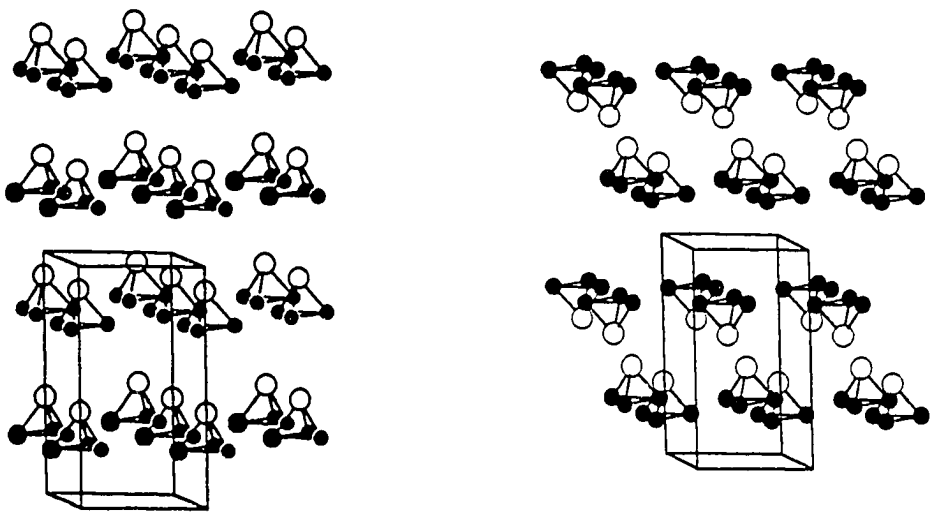

"Ferroelectric" "Antiferroelectric"

Figure 1-11. Orientation of the M_3X_{cap} units within the halide matrix leading to "ferroelectric" (unidirectional M_3X_{cap} units) and "antiferroelectric" (alternating M_3X_{cap} direction) stacking.

symmetries other than hexagonal. All are stacking variants built from the $^{2}_{\infty}[M_3QX_7]$ slabs discussed above, except for *o*-Nb_3SI_7, which contains undulating Nb_3SI_7 layers with a different connectivity of the clusters.

The α-Nb_3Cl_8 structure type

The $^{2}_{\infty}[M_3QX_7]$ adjacent slabs are oriented antiferroelectrically with respect to one another, and there are two slabs per unit cell. (In the binary halides of course, Q = X.) The structure is centrosymmetric and adopts the space group $P\bar{3}m1$. Each slab is related to the next via an inversion center located at (0, 0, 0). The stacking sequence of the anion layers is (...AB...), or (...*h*...). Lattice energy calculations have indicated that this stacking variant minimizes hard-core repulsions rather than electrostatic potential. This theoretical result is corroborated by the experimental observation that all "hard" chlorides known (Nb_3Cl_8, Nb_3TeCl_7 and Ta_3TeCl_7) adopt this structure type, whereas compounds containing "softer" bromides and iodides are more influenced by the Madelung term.[43] The α-Nb_3Cl_8 type is illustrated in Figure 1-12.

The β-Nb_3I_8 structure type

The rhombohedral β-Nb_3I_8 type (centrosymmetric, space group $R\bar{3}m$) is characterized by six-slab per unit cell stacking, with an anion layer stacking sequence of (...ABABCACABCBC...), or (...*hhcc*...). The orientation of the slabs is antiferroelectric. Only two compounds, β-Nb_3Br_8 and β-Nb_3I_8, adopt this type, illustrated in Figure 1-13.

The Nb_3SBr_7 structure type

The Nb_3SBr_7 type (Figure 1-14) is the simplest of all the 3-1-7 compounds, having only one slab per unit cell. As such, it is necessarily noncentrosymmetric and ferroelectric. The space group adopted is P3m1, and the anion stacking sequence is (...AB...), or

The α-Nb_3Cl_8 Type

Space group: $P\bar{3}m1$

- (...AB...) or (...*h*...) anion stacking sequence
- Centrosymmetric, antiferroelectric orientation of M_3X_{cap} units
- Two $^{2}_{\infty}[M_3QX_7]$ slabs per unit cell

(a) [001] view

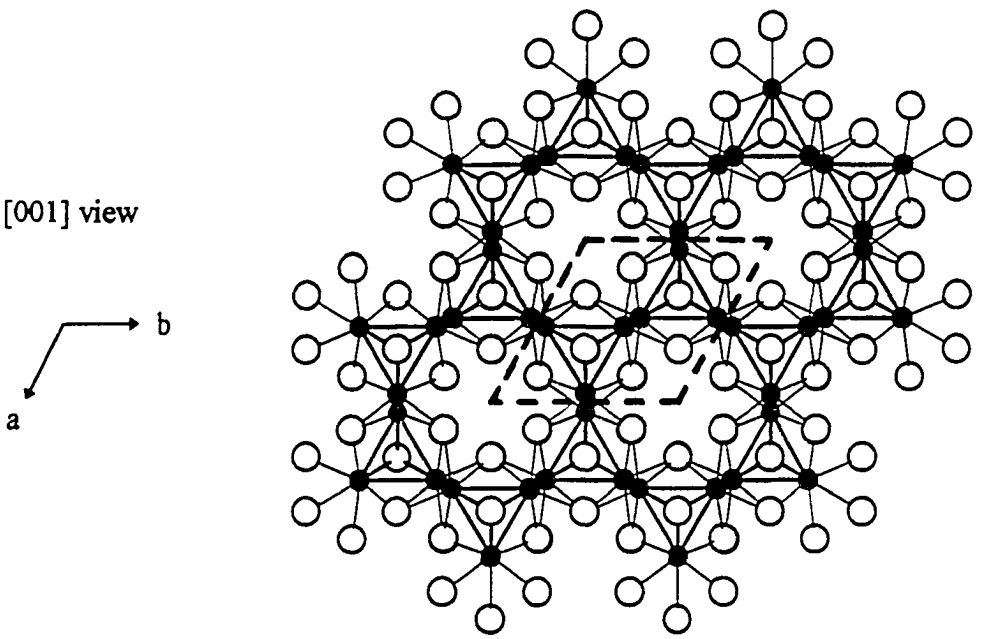

(b) [100] view

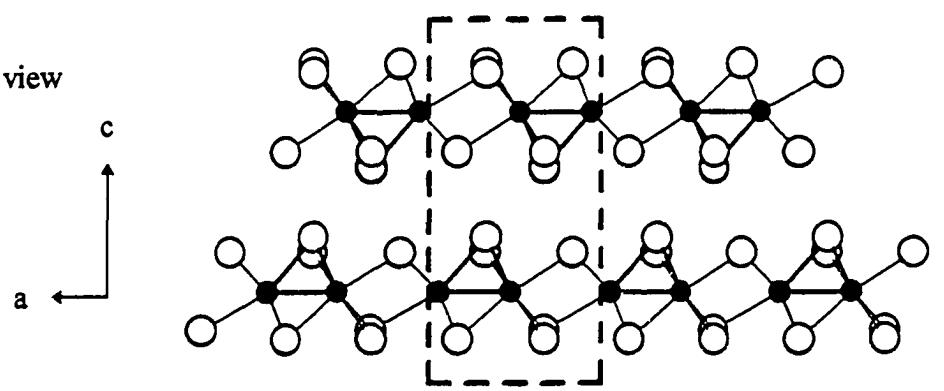

Compounds: α-Nb_3Cl_8 α-Nb_3Br_8, α-Nb_3I_8, Nb_3TeCl_7, Ta_3TeCl_7.

Figure 1-12. The α-Nb_3Cl_8 structure type.

The β-Nb_3I_8 Type

Space Group $R\bar{3}m$.

- (...ABCBCABABCAC...) or (...*hhcc*...) anion stacking
- Centrosymmetric, antiferroelectric orientation of Nb_3X_{cap} units
- Six $^{2}_{\infty}[Nb_3X_8]$ slabs per unit cell

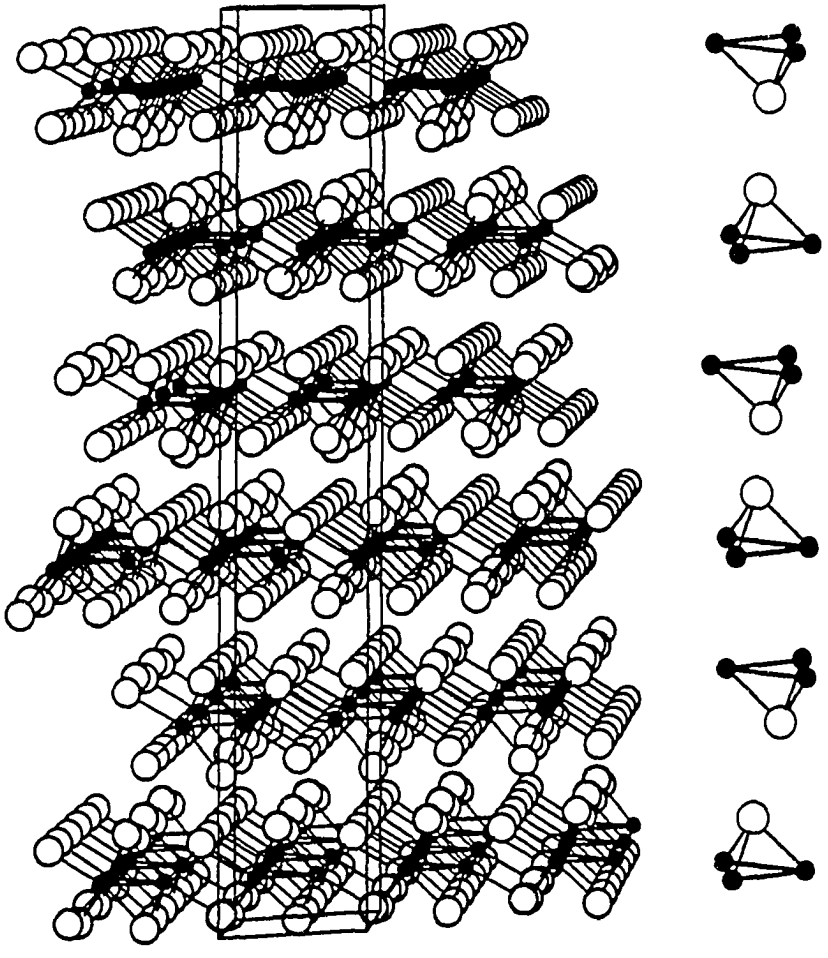

Compounds: β-Nb_3Br_8, β-Nb_3I_8

Figure 1-13. Perspective [100] view of the β-Nb_3I_8 structure type. Nb_3X_{cap} orientation in the slabs is indicated at right.

The Nb_3SBr_7 Type

Space Group: P3m1

- (...AB...) or (...*h*...) anion stacking sequence
- Non-centrosymmetric, ferroelectric orientation of the M_3Q_{cap} units
- One $^2_\infty$[M_3QX_7] slab per unit cell

(a) [001] view

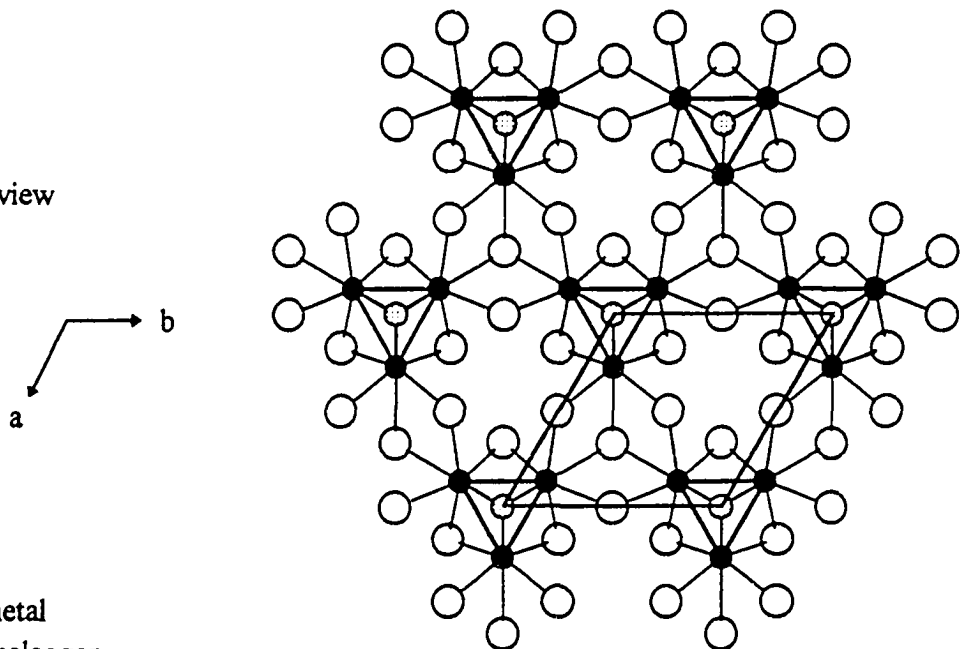

● = metal
⊙ = chalcogen
○ = halide

(b) [100] view of two slabs and the unit cell.

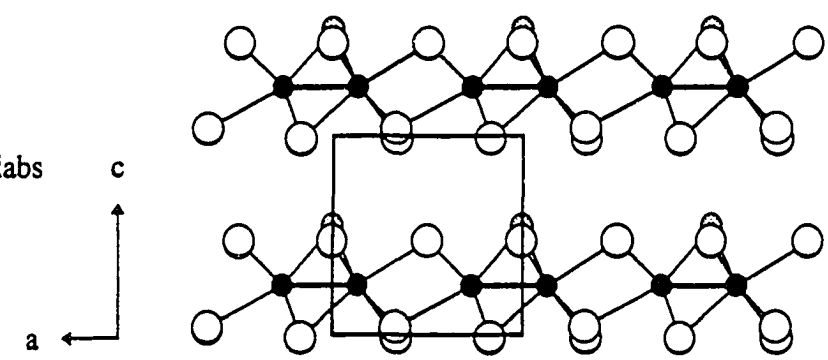

Compounds: Nb_3SBr_7, Nb_3SeBr_7, *h*-Nb_3TeI_7.

Figure 1-14. The Nb_3SBr_7 structure type.

(...*h*...), with adjacent slabs directly "superimposed" on one another (viewed down the stacking direction [001]). Nb_3SBr_7, Nb_3SeBr_7, *h*-Nb_3TeI_7, and the mixed metal derivative $Ta_{3-x}Nb_xTeI_7$ ($x \approx 2$) adopt this stacking type.

The Ta_3SBr_7 structure type

Ta_3SBr_7 is the sole example of this type, which is closely related to Nb_3SBr_7: a one-slab per unit cell, noncentrosymmetric and ferroelectric structure, with an anion layer stacking sequence of (...AB...), or (...*h*...). However in the Ta_3SBr_7 type adjacent $^2_\infty[Ta_3SBr_7]$ slabs are not "superimposed" on one another as they are in Nb_3SBr_7. The Ta_3SBr_7 structure can be derived from Nb_3SBr_7 by simply shifting alternate $^2_\infty[M_3QX_7]$ slabs by (½ *a*) relative to the hexagonal cell. This shift destroys the hexagonal symmetry of the Nb_3SBr_7 type: Ta_3SBr_7 is monoclinic, forming in space group Cm (Figure 1-15). Ta_3SBr_7 and Nb_3SBr_7 in fact represent the only two possible unique one-slab stackings of $^2_\infty[M_3QX_7]$ slabs - all other permutations result in at least a two-slab repeat unit. This is discussed in greater detail in Chapter 3.

The Nb_3SeI_7 structure type

The Nb_3SeI_7 type is a non-centrosymmetric, ferroelectric structure containing two $^2_\infty[M_3QX_7]$ slabs per unit cell. Adjacent slabs are related by a 6_3 screw axis (Figure 1-16). Anion layer stacking is (...ABCB...) or (...*hc*...). Only iodides have been observed to adopt this structure type: *hc*-Nb_3SI_7, *hc*-Ta_3SI_7, Nb_3SeI_7, Ta_3SeI_7, *hc*-Nb_3TeI_7, *hc*-Ta_3TeI_7 and *hc*-$Ta_{3-x}Nb_xTeI_7$ ($0 \leq x \leq 3$).

The Nb_3TeBr_7 structure type

This type, adopted only by its nominal compound, is a non-centrosymmetric, antiferroelectric, two slab stacking variant. The compound forms in space group P3m1, with an (...ABCB...) or (...*hc*...) anion sequence (Figure 1-17).

The Ta_3SBr_7 Type

Space Group: Cm

- (...AB...) or (...*h*...) anion stacking sequence
- Non-centrosymmetric, ferroelectric orientation of the Ta_3S_{cap} units
- One $^{2}_{\infty}[M_3QX_7]$ slab per unit cell

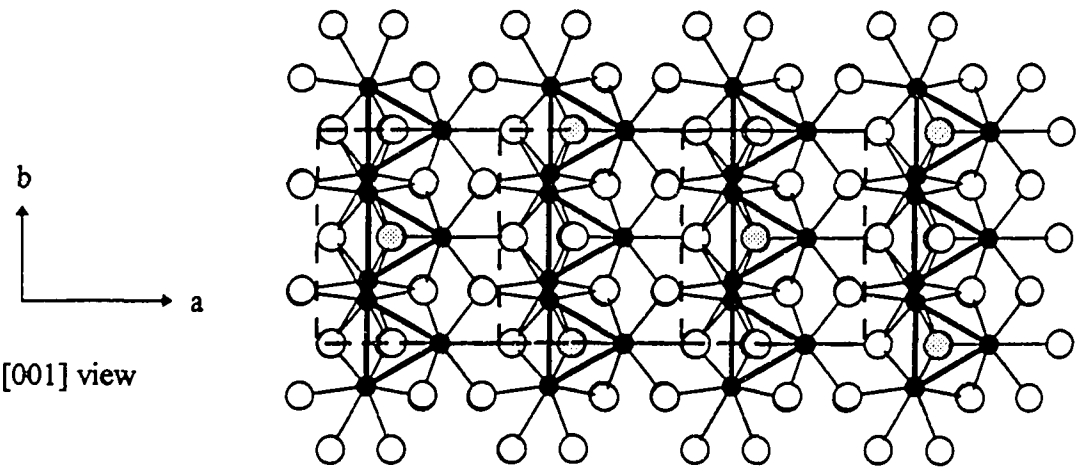

(a) [001] view

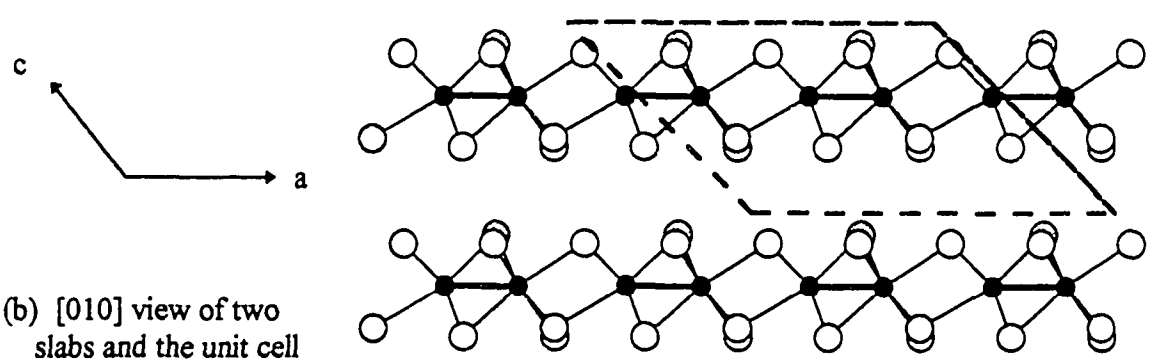

(b) [010] view of two slabs and the unit cell

Compounds: Ta_3SBr_7, $Ta_xNb_{3-x}SBr_7$ ($x \approx 2$)

Figure 1-15. The Ta_3SBr_7 structure type, in views (a) perpendicular to the slab stacking direction and (b) parallel to the stacking direction.

The Nb_3SeI_7 Type

Space Group: $P6_3mc$

- (...ABCB...) or (...*hc*...) anion stacking sequence
- Non-centrosymmetric, ferroelectric orientation of the M_3Q_{cap} units
- Two $^{2}_{\infty}[M_3QX_7]$ slabs per unit cell

(a) [001] view

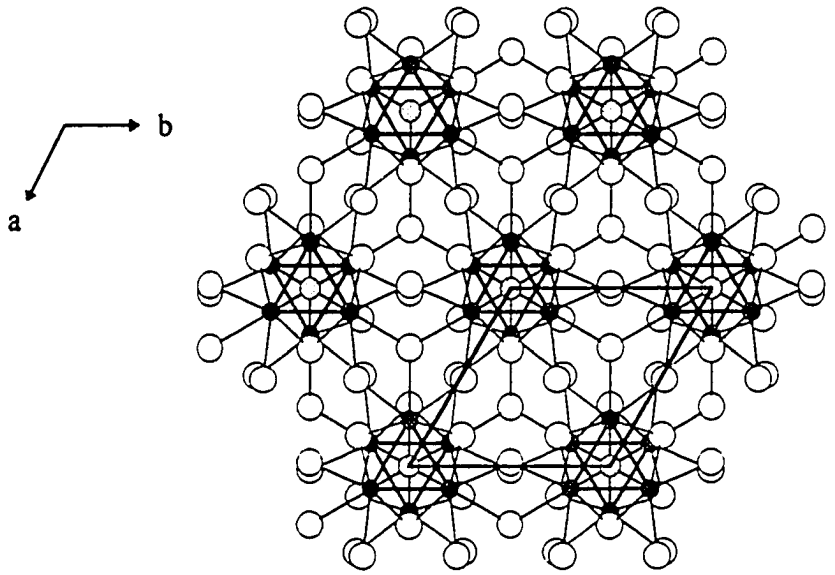

● = metal
○ = chalcogen
○ = halide

(b) [100] view of two slabs and the unit cell

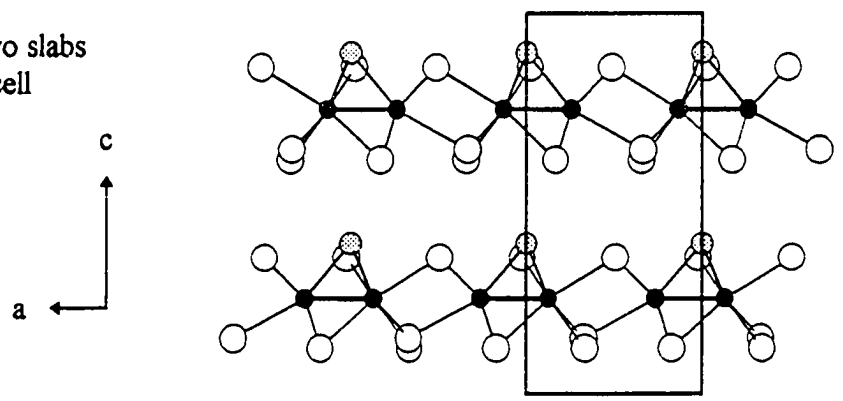

Compounds: *hc*-Nb_3SI_7, Nb_3SeI_7, Ta_3SeI_7, *hc*-Nb_3TeI_7, *hc*-Ta_3TeI_7
hc-$Nb_xTa_{3-x}TeI_7$ ($0 \leq x \leq 3$).

Figure 1-16. The Nb_3SeI_7 structure type.

The Nb_3TeBr_7 Type

Space Group P3m1

- (...ABCB...) or (...*hc*...) anion stacking sequence
- Non-centrosymmetric, antiferroelectric orientation of the Nb_3Te_{cap} units
- Two $^{2}_{\infty}[Nb_3TeBr_7]$ slabs per unit cell

(a) [001] view

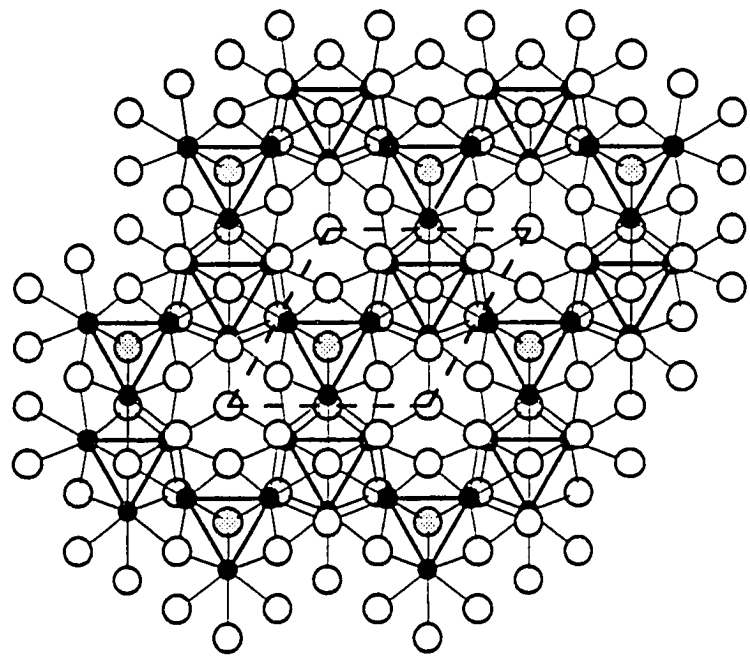

(b) [100] view of two slabs and the unit cell

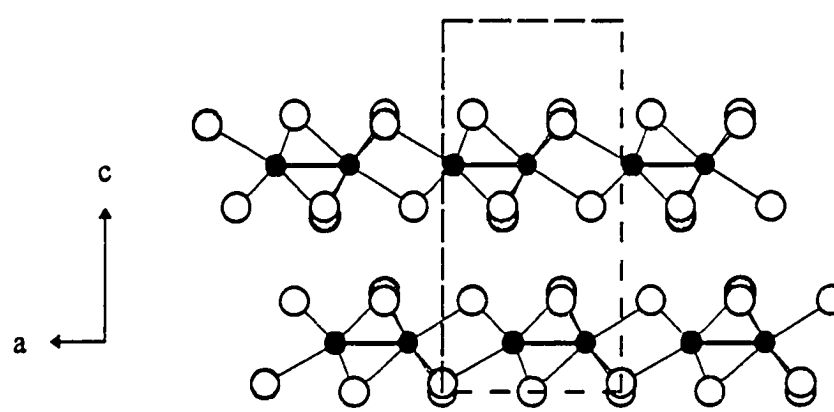

Compounds: Nb_3TeBr_7.

Figure 1-17. The Nb_3TeBr_7 structure type. Small black circles: Nb; larger grey circles, Te; open circles, Br.

The orthorhombic-*Nb_3SI_7 structure type*

Orthorhombic-Nb_3SI_7 is not a stacking variant. In this unusual structure, the ${}^{2}_{\infty}[Nb_3SI_7]$ slabs are not flat, but undulate along the crystallographic (*ab*) plane. The connectivity of the Nb_3X_{13} clusters is also different. The structure can be formulated $[NbS^{i-a}_{1/4}I^{i}_{2/2}I^{a-a}_{3/2}]_2[NbS^{i-a}_{2/4}I^{i}_{2/2}I^{a-a}_{2/2}]$, indicating two inequivalent sets of Nb atoms and an inter-cluster bridging role for the sulfur. One Nb is coordinated by two sulfur atoms trans to one another. The sulfur atom that caps the triangular Nb_3 cluster also serves as a bridge to the vertex of a neighboring cluster, as illustrated in Figure 1-18. The remainder of the Nb_3 coordination environment is analogous to the previous M_3QX_7 compounds. The symmetry of the cluster is C_s, with two short Nb-Nb bonds (2.96 Å) and one longer Nb-Nb bond (3.05 Å). From an anion-packing point of view, *o*-Nb_3SI_7 is a cubic close-packed arrangement of sulfide and iodide ions with Nb in 3/8 of the octahedral holes. The distribution of metal cations along the stacking direction has been described in terms of a concentration wave consisting of alternating 5/8 and 1/8 occupation of the octahedral holes.

Five of the structure types (α-Nb_3Cl_8, Nb_3SBr_7, Ta_3SBr_7, Nb_3SeI_7 and *o*-Nb_3SI_7) discussed above will figure prominently in the following thesis.

Electronic aspects: Molecular orbital picture / Band structure

Groundwork: Electronic structure calculations leading to an understanding of the molecular orbital diagram of discrete trinuclear cluster complexes of transition metals were first worked out in 1964 by Cotton and Haas.[61] Subsequently, molecular orbital calculations have been performed by diverse groups on a great range of trinuclear cluster compounds, both molecular and quasi-infinite.[62] As a precursor to the understanding of the electronic structure of trinuclear cluster-containing quasi-infinite solids, it is instructive to consider the MO results from such molecular systems. The conclusions so gained can then be broadened to include trinuclear clusters "condensed" into extended solids.

orthorhombic-Nb_3SI_7

(a)
Near-[010] view of two of the undulating layers and unit cell of *o*-Nb_3SI_7

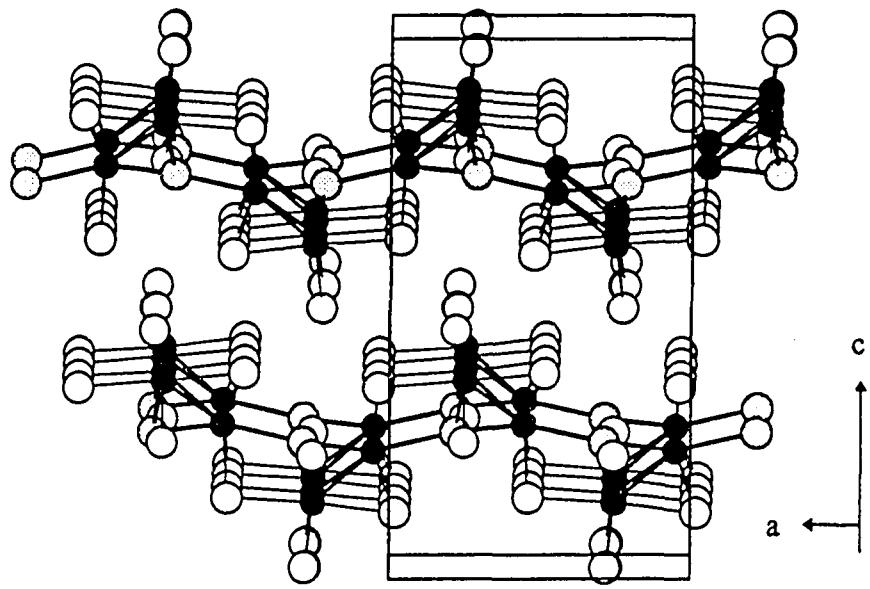

(b)
Cluster connectivity in
$[NbS^{i-a}_{1/4}I^{i}_{2/2}I^{a-a}_{3/2}]_2[NbS^{i-a}_{2/4}I^{i}_{2/2}I^{a-a}_{2/2}]$

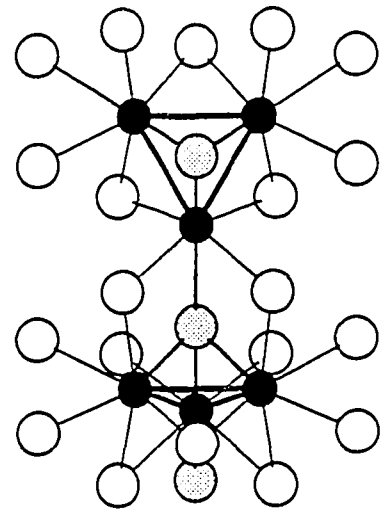

Compounds: *o*-Nb_3SI_7, *o*-Ta_3SI_7

Figure 1-18. The *o*-Nb_3SI_7 structure type. (a) View parallel to the undulating M_3SI_7 layers. (b) Illustration of the linkage of two clusters. In both pictures, the black circles are metal atoms, the grey circles are sulfurs, and the open circles are iodide.

Molecular orbital calculations have been done on transition metal systems beginning with bare M_3^{n+} clusters, then moving to partially ligated $M_3X_4^{n+}$ cluster cores, and finally to complete M_3X_{13} clusters.[12] Here the M_3X_{13} cluster is considered: this species represents a trinuclear cluster with the same coordination environment found in M_3QX_7. The orbital basis sets for these calculations consist of the transition metal s, p, and d orbitals, plus s and p orbitals of the ligands. Of primary interest here are the orbitals involved in metal-metal bonding, which bear directly on the stability and physical and electronic properties of the compound. Low-lying ligand lone pair orbitals and metal-ligand bonding orbitals are filled, where applicable. The molecular orbital diagram generated by these calculations is shown in the left-hand column of Figure 1-19. The HOMO was found to consist of a (1 + 2) set of three orbitals with contributions primarily from the metal d orbitals. The LUMO was found to be a slightly bonding orbital also primarily of metal character. In C_{3v} symmetry, which is the local symmetry of the M_3QX_{12} cluster fragments in M_3QX_7, these orbitals carry the labels a_1 + e (HOMO) and a_1 (LUMO). The predicted existence of this a_1 + e + a_1 scheme correlates nicely with bond distances observed from clusters with varying electron counts. Turning to Cotton's trinuclear cluster complexes, the $[Nb_3Cl_{10}(PH_3)_3]^-$ anion contains six cluster electrons $\{(3\cdot Nb \times 5e^-) - (10\cdot Cl \times 1e^-) + (1e^-/\text{monoanion})\}$, which occupy the a_1 + e orbital set. The Nb-Nb distance in this anion is 2.976(6) Å. According to the MO calculations the a_1 LUMO is also of bonding character, implying that occupation of this orbital should increase the bonding character in the cluster, and concomitantly decrease the Nb-Nb bond length. Cotton, et al., did synthesize the eight-electron compound $Nb_3Cl_7(PR_3)_6$, and indeed the Nb-Nb distance has shrunk to 2.832(4) Å, confirming the bonding character of this orbital. Other elements are known to form trinuclear clusters that can be described by the above treatment, with either six ($Zn_2Mo_3O_8$,[63] $Na_2Ti_3Cl_8$,[64] $[W_3Se_4(NCS)_9]^{5-}$[65]) or eight ($[Mo_3OCl_6(OAc)_3]^-$ [66]) cluster electrons.

The basic understanding of the electronic structure of these discrete molecular clusters carries over smoothly into an understanding of the electronic structure of the

Molecular orbital and energy band diagrams for $Nb_3X_{13}^{5-}$ clusters and Nb_3QX_7 solids

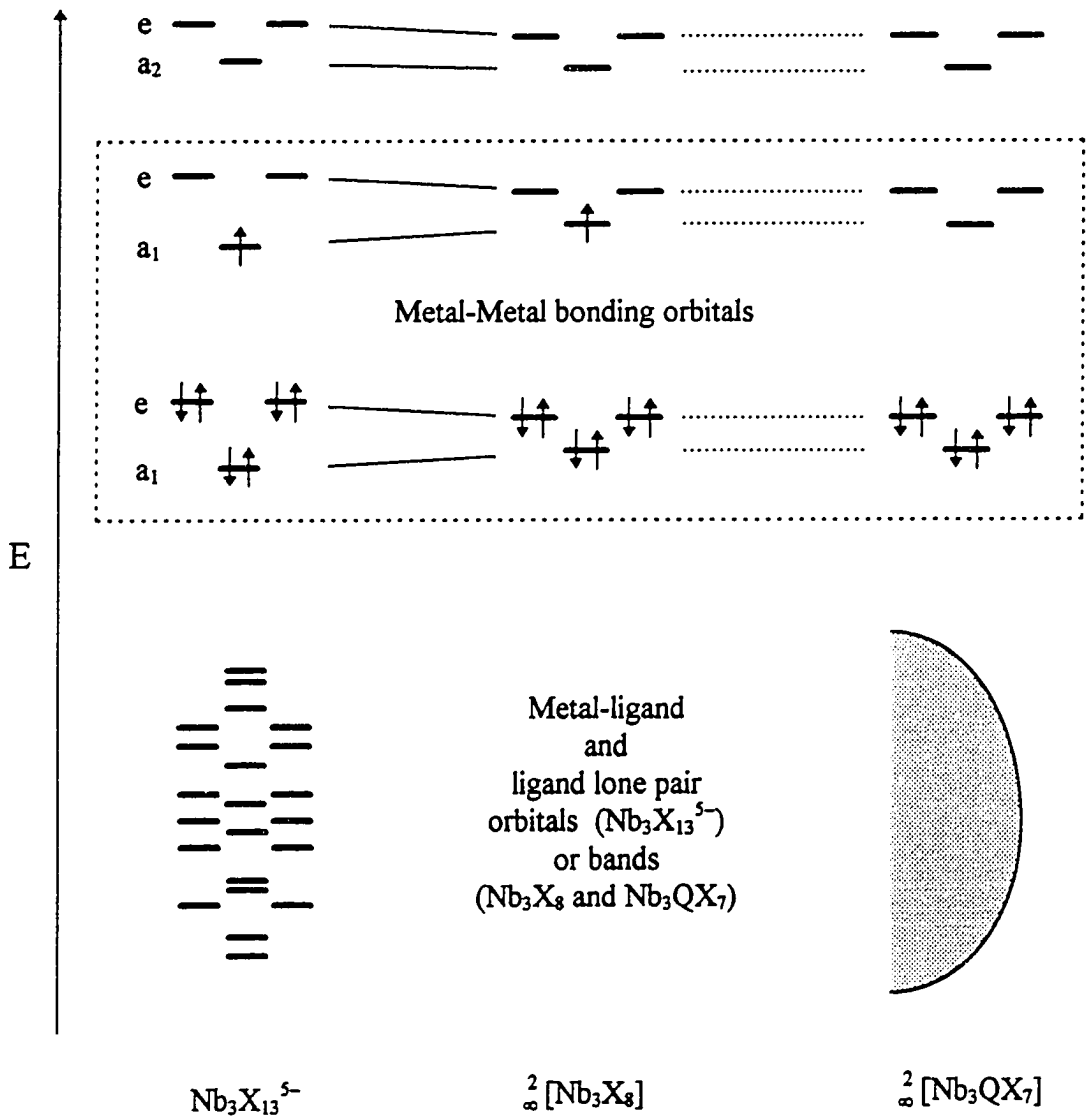

Figure 1-19. Qualitative orbital correlation diagram relating the molecular orbitals in a discrete $Nb_3X_{13}^{5-}$ cluster to the orbital bands in the extended solids Nb_3X_8 and Nb_3QX_7. A perturbation of the energy levels will occur on going from Nb_3X_8 to Nb_3QX_7; the magnitude will vary with Q. However, since the orbitals shown in the dashed box are all predominantly metal-metal in character, the change will be small.

trinuclear cluster-containing extended solids. Condensation of the discrete clusters into an extended solid results in a similar overall picture; however, in an extended solid, translational symmetry introduces additional symmetry elements and discrete orbitals broaden into bands consisting of a multitude of energy levels. Miller performed calculations on a hypothetical $Nb_3Cl_{13}^{5-}$ cluster and correlated this molecular scheme with ${}^{2}_{\infty}[Nb_3Cl_8]$ layers.[42] In ${}^{2}_{\infty}[Nb_3Cl_8]$, the intercluster interactions are mediated by bridging chloride atoms. However, near the Fermi level (the HOMO in a molecular system), the Nb-Cl interaction is weak, and consequently these bands remain quite narrow, behaving like localized molecular orbitals. Figure 1-19 shows a general orbital correlation diagram similar to that worked out by Miller.

Khvorykh, et al., have also done Extended Hückel MO calculations on the $Nb_3SBr_{12}^{5-}$ clusters in Nb_3SBr_7.[59] Their results reproduced the schemes of Cotton and Miller. The full band structure of β-Nb_3Br_8 was derived in 1994 by Meyer.[67]

In Nb_3X_8, seven electrons are available for cluster bonding. The a_1 + e bands are filled, and one electron resides in the singly degenerate a_1 band (Figure 1-19, middle column). This nicely explains the observed paramagnetism of these compounds, although the unusually low μ_{eff} values for β-Nb_3Br_8 and β-Nb_3I_8 suggest more complicated interactions. This understanding of the electronic structure of Nb_3X_8 clarifies the rationale behind the synthesis of M_3QX_7. If a divalent chalcogen is substituted for a halide, this leads to "oxidation" of the cluster by one electron, effectively emptying the upper a_1 band. The six remaining cluster electrons fill the a_1 + e set of orbitals (band) shown in the right-hand column of Figure 1-19.

Conclusions

The firm establishment of the crystal structures, physical properties, and electronic structures of the Nb_3QX_7 family seemed an encouraging precedent for the synthesis of analogous new tantalum cluster compounds. As demonstrated by the trend in the binary Ta and Nb halides, electron-richer (i.e., reduced) systems generally exhibit more extensive

M-M bonding, or higher nuclearity clusters. Fewer electrons available for cluster bonding might contravene the marked natural tendency of tantalum to form the higher nuclearity (hexanuclear) clusters so prevalent in tantalum halide chemistry. Therefore, although seven-electron tantalum halide clusters (e.g. Ta_3X_8) haven't been observed to form under any synthetic conditions to date, the six-electron cluster compounds Ta_3QX_7 might be attainable. After several early failures due to because the temperatures chosen (the temperature region of the synthesis of Nb_3QX_7, near 800°C) were too high, success was ultimately achieved at lower temperatures (< 550°C). Chapters Two through Five of this thesis detail the compounds discovered.

CHAPTER TWO

NEW TANTALUM CHALCOGENIDE IODIDES

Selenide and Telluride Iodides - Introduction

Three new tantalum chalcogenide iodide compounds have been discovered, adding to the three ($(TaSe_4)_2I$, $(TaSe_4)_3I$, $TaTe_4I$, see Chapter One) compounds previously known.

hc-Ta_3SeI_7 and *hc*-Ta_3TeI_7

Synthesis

Since *hc*-Ta_3SeI_7 and *hc*-Ta_3TeI_7 are prepared similarly and are isostructural with each other, they will be discussed together. The prefix "*hc*-" refers to the close-packed anion stacking sequence (i.e., ...ABCB...), and serves to distinguish these compounds from stacking variants, as discussed below.

hc-Ta_3QI_7 (Q = Se, Te) were prepared by stoichiometric reaction of Ta foil, chalcogen, and iodine in evacuated glass ampoules at 450°C for ca. one week, followed by rapid quenching to room temperature. Reactants were purified as far as possible before use as follows: Tantalum foil (Aesar, 0.027 mm thick, 99.99%) was cleaned with an $HF/HNO_3/H_2SO_4$ solution to remove surface impurities, then rinsed with ethanol and dried in vacuo at 500°C. Selenium powder (Alfa), and tellurium powder (Alfa) were both sublimed twice before introduction into the glove box. Iodine (Alfa, 99.9%, resublimed) was used as received. All purified reagents and products were subsequently handled in an Ar-filled glove box.

Crystals of *hc*-Ta_3SeI_7 and *hc*-Ta_3TeI_7 both readily form as shiny black hexagonal prisms, with a micaceous morphology. Whereas *hc*-Ta_3SeI_7 seems to form flatter, plate-like hexagonal prisms, *hc*-Ta_3TeI_7 is mostly found as long columns, in an amazing variety of shapes. Pyramids, proper prisms, bullet-shapes, etc. all form abundantly. Figure 2-1 shows SEM images of the two distinct crystal morphologies. The crystals are found

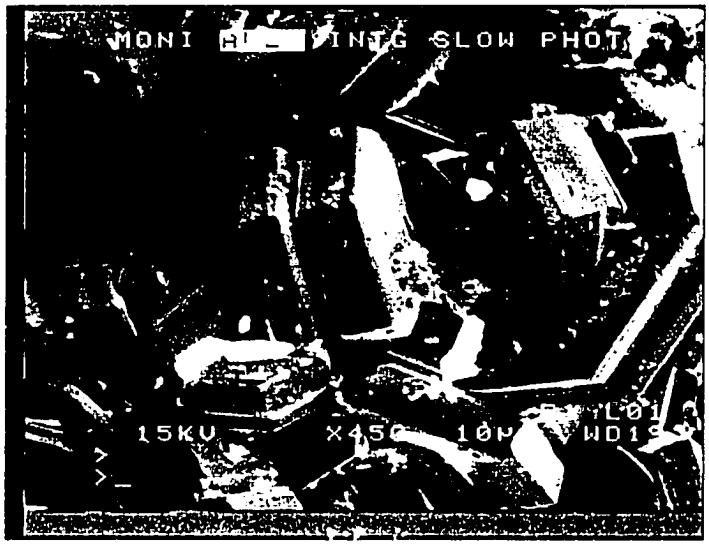

(a) SEM image (x450) of *hc*-Ta_3SeI_7 crystallites. *hc*-Ta_3SeI_7 formed as hexagonal drums, unlike *hc*-Ta_3TeI_7 (below), which crystallized as hexagonal prisms.

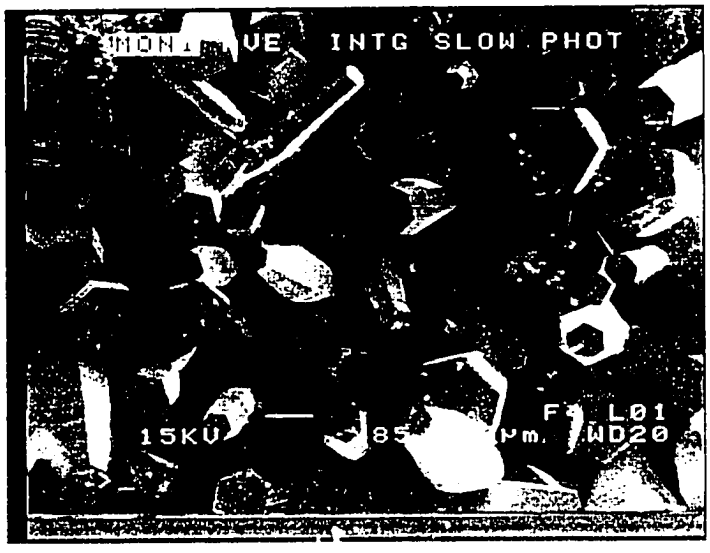

(b) SEM image (x85) of a field of *hc*-Ta_3TeI_7 crystals, showing the hexagonal prismatic morphology

Figure 2-1. SEM images of crystalline *hc*-Ta_3SeI_7 and *hc*-Ta_3TeI_7.

embedded in bulk powder as well as being transported to clean regions of the reaction tube. They are stable in air, water, and non-oxidizing acids indefinitely, but rapidly decompose in dilute HNO_3. Small hexagonal prisms suitable for x-ray diffraction cleave easily and cleanly from the longer columns - the larger, intact crystals usually are of poor quality for single crystal diffraction experiments. The best crystals can be grown from annealing reactions (transport reactions), conducted at 450°C for one to two weeks. It is not necessary to add a transport agent to the powdered starting compounds.

Products were identified by comparing observed Guinier powder x-ray diffraction patterns for Ta compounds to those obtained from analogous Nb compounds. Conditions for the formation and stability of Ta_3QI_7 indicate a lesser temperature stability range with respect to the Nb analogues, which survive up to ca. 900°C. Guinier powder X-ray diffraction of products from reactions conducted at temperatures from 350° to 900°C indicates an upper temperature limit of ca. 560°C for Ta_3QI_7. DTA data of *hc*-Ta_3TeI_7 corroborate these experimental observations, showing a large thermal event coupled to a ca. 50% mass loss near 565°C. The DTA plot is shown in Figure 2-2. The small mass loss over the range 250°C - 400°C is most likely due to impurities in the sample. Experimentally, at temperatures higher than ca. 560°C, only TaI_5 and Ta_6I_{14} can be identified in reaction tubes quenched rapidly from high temperature; the remaining product is amorphous to x-rays. With this information, it is likely that the mass loss observed in the DTA experiment is due to the volatilization of the decomposition product TaI_5.

Structure

Black reflective hexagonal prisms of *hc*-Ta_3TeI_7 (prism) and *hc*-Ta_3SeI_7 ("drum") from reactions at 450°C (two weeks) were selected for single crystal x-ray diffraction. In both cases, a hexagonal unit cell similar in size to the corresponding niobium compound was indexed using 25 reflections located by the diffractometer random search routine. Since the Nb_3SeI_7 structure type was indicated by the Guinier patterns, no additional unit cell size checks were performed. Subsequent solution of the structures in the Nb_3SeI_7 type provided final verification. Further data collection details are given in Table 2-1.

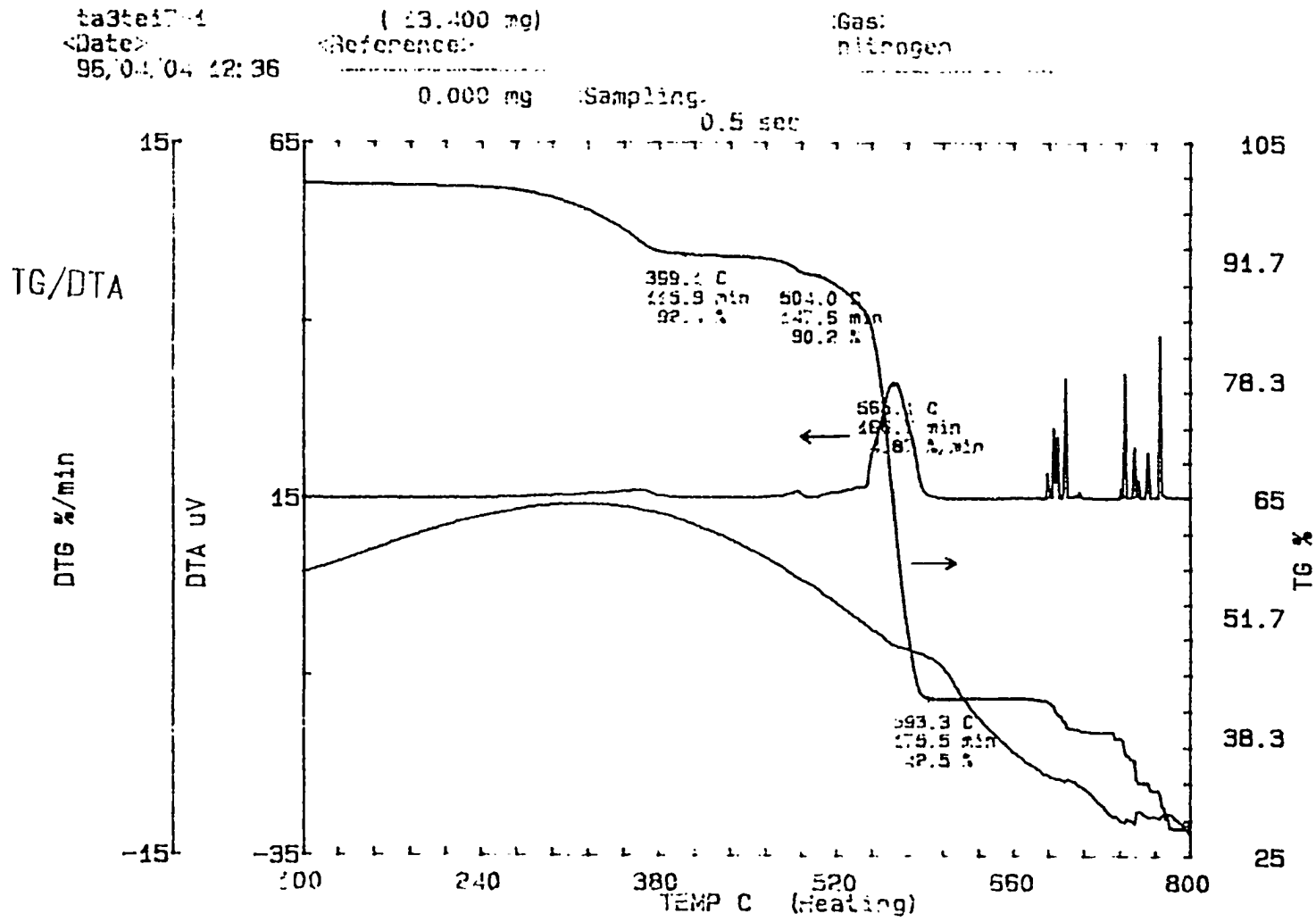

Figure 2-2. TG / DTA data for *hc*-Ta_3TeI_7. The approximately 50% mass loss centered at 565°C is due to decomposition of *hc*-Ta_3TeI_7. The small mass loss over the range 250°C - 400°C is less clear, but is most likely due to impurites in the sample.

Table 2-1. Crystallographic collection data for *hc*-Ta_3SeI_7 and *hc*-Ta_3TeI_7.

	hc-Ta_3SeI_7	*hc*-Ta_3TeI_7
Formula weight	1510.13	1558.78
Crystal system	hexagonal	hexagonal
Space group	$P6_3mc$ (no. 186)	$P6_3mc$ (no. 186)
Crystal Color	black	black
Crystal dimensions (mm)	0.22 x 0.22 x 0.1	0.12 x 0.12 x 0.2
Unit cell parameters (Å)		
a	7.541(1)	7.591(2)
c	13.590(3)	13.907(3)
Volume (Å^3)	669.90(20)	694.03(26)
Z	2	2
d_{calc} (g cm^{-3})	7.486	7.456
Diffractometer	CAD4	Rigaku AFC6R
Radiation, wavelength	Mo Kα, 0.71069 Å	Mo Kα, 0.71069 Å
Linear absorption coeff.	427.8 cm^{-1}	407.63 cm^{-1}
Data collection temp.	23°C	23°C
Scan method	ω-scan	ω-scan
2θ range	$2° \leq 2\theta \leq 60°$	$2° \leq 2\theta \leq 50°$
Range in *hkl*	$\pm h, \pm k, \pm l$	$+h, +k, +l$
Number of data collected	7814	1031
Observed ($I > 2\sigma I$)	3259	753
Unique	710	303
Parameters refined	24	24
Residuals		
R[a]	0.053	0.030
R_w[b]	0.046	0.031
Goodness-of-fit	1.11	1.30

[a] $R = \Sigma(|F_{obs}| - |F_{calc}|) / \Sigma |F_{obs}|$

[b] $R_w = \{\Sigma w(|F_{obs}| - |F_{calc}|)^2 / \Sigma |F_{obs}|^2\}^{1/2}$

where $w = 1/\sigma^2(F_{obs})$

Both structures were solved by direct methods using SHELXS-86 [68] and refined with the TEXSAN crystallographic package.[69] An empirical psi-scan absorption correction was applied to both data sets, followed by a DIFABS[70] correction to the isotropically refined atoms (unnormalized transmission ranges: Ta_3SeI_7, 0.8 - 1.1; Ta_3TeI_7, 0.9 - 1.1). All positions were then refined anisotropically. Atomic coordinates, isotropic thermal parameters and anisotropic displacement parameters are given in Table 2-2.

hc-Ta_3SeI_7 and *hc*-Ta_3TeI_7 are isostructural with Nb_3SeI_7 (and Nb_3TeI_7), which is described and illustrated in Chapter One, Figure 1-16.

Ta-Ta distances in *hc*-Ta_3SeI_7 and *hc*-Ta_3TeI_7 (2.955(2) Å and 3.007(2) Å, respectively), are comparable to those in Ta_6I_{14} (2.80 - 3.08 Å),[29] though slightly longer than in $[Ta_3Cl_{10}(PEt_3)_3]^-$ (2.932 Å),[12] presumably because of the latter's smaller halide. Ta-I and Ta-chalcogen distances are also typical. The Nb-Nb distances in the corresponding Nb analogues (3.02 Å for Nb_3SeI_7 and 3.04 Å for *hc*-Nb_3TeI_7)[71] are slightly longer than the Ta-Ta distances, which agrees with the concept of greater d-d orbital overlap in reduced Ta compounds due to the greater radial extent of the Ta 5d orbitals compared to Nb 4d. (Analogous niobium compounds usually show slightly longer bonds and lattice parameters than their Ta counterparts along directions in which metal-metal and metal-anion bonds predominate.) Bond distances and angles are given in Table 2-3.

X-ray photoelectron spectroscopy

Samples *hc*-Ta_3SeI_7 and *hc*-Ta_3TeI_7 were finely powdered in the glove box and transferred under inert atmosphere to a PHI 550 multi-technique surface analyzer, to obtain x-ray photoelectron spectra. The binding energies obtained for the Ta $4f_{7/2}$ peak (*hc*-Ta_3SeI_7, 23.4 eV; *hc*-Ta_3TeI_7, 23.4 eV after correction for charging using the adventitious C 1s peak, as recommended [72]) corroborate the highly reduced nature of the tantalum atoms in both compounds. Table 2-4 lists literature XPS Ta $4f_{7/2}$ values for other tantalum compounds.

Table 2-2. Atomic coordinates, isotropic and anisotropic displacement parameters for Ta_3SeI_7 and Ta_3TeI_7.

Ta_3SeI_7

Atom	x	y	z	B(eq)
Ta	0.8694(1)	-0.8694	1/4	0.73(1)
Se	0.0	0.0	0.3874(6)	0.8(2)
I(1)	0.3333	0.6667	0.6444(5)	0.9(1)
I(2)	0.8311(2)	-0.8311	0.6145(3)	0.82(3)
I(3)	0.4974(2)	-0.4974	0.3635(3)	0.94(3)

Atom	U_{11}	U_{22}	U_{33}	U_{12}	U_{13}	U_{23}
Ta	0.0084(4)	0.0084	0.0099(7)	0.0034(7)	0.0005(6)	-0.0005
Se	0.006(2)	0.006	0.017(6)	0.003	0.0	0.0
I(1)	0.009(1)	0.009	0.018(3)	0.004	0.0	0.0
I(2)	0.0085(8)	0.0085	0.014(1)	0.004(1)	0.0000(6)	-0.0000
I(3)	0.0111(7)	0.0111	0.013(1)	0.005(1)	0.0001(6)	-0.0001

Ta_3TeI_7

Atom	x	y	z	B(eq)
Ta	0.8680(1)	-0.8680	1/4	0.58(1)
Te	0	0	0.3996(4)	0.8(1)
I(1)	1/3	2/3	0.6459(4)	0.8(1)
I(2)	0.8298(2)	-0.8298	0.6184(2)	0.72(2)
I(3)	0.4979(2)	-0.4979	0.3603(2)	0.87(5)

Atom	U_{11}	U_{22}	U_{33}	U_{12}	U_{13}	U_{23}
Ta	0.0058(5)	0.0058	0.0105(6)	0.0028(7)	-0.0001(4)	0.0001
Te	0.008(2)	0.008	0.015(2)	0.004	0.0	0.0
I(1)	0.009(2)	0.009	0.015(2)	0.005	0.0	0.0
I(2)	0.005(1)	0.005	0.014(1)	0.000(1)	-0.0009(6)	0.0009
I(3)	0.0094(6)	0.0094	0.015(1)	0.006	0.0011(5)	-0.0009

$(U_{ij} = \exp(-2\pi^2(a^{*2}U_{11}h^2 + b^{*2}U_{22}k^2 + c^{*2}U_{33}l^2 + 2a^*b^*U_{12}hk + 2a^*c^*U_{13}hl + 2b^*c^*U_{23}kl))$

Table 2-3. Selected bond distances and angles in *hc*-Ta_3SeI_7 and *hc*-Ta_3TeI_7.

Bond (Å) or Angle (deg)	*hc*-Ta_3SeI_7	*hc*-Ta_3TeI_7
Ta-Ta	2.955(2)	3.007(2)
Ta-Q	2.528(7)	2.710(4)
Ta-I1 (μ_3-I^a)	3.010(3)	3.017(3)
Ta-I2 (μ_2-I^i)	2.723(3)	2.736(2)
Ta-I3 (μ_2-I^a)	2.904(3)	2.900(2)
Ta-Ta-Ta	60.00	60.00
Ta-Q-Ta	71.5(2)	67.4(1)
Ta-Ta-Q	54.3(1)	56.30(6)
Ta-I1-Ta	99.2(1)	98.9(1)
Ta-I2-Ta	65.86(9)	66.67(7)
Ta-I3-Ta	104.4(1)	104.46(9)
Ta-Ta-I3	142.21(7)	142.23(5)

Table 2-4. Reported tantalum $4f_{7/2}$ binding energies (eV) measured by x-ray photoelectron spectroscopy

Compound	Binding Energy (eV) Ta $4f_{7/2}$
Ta metal	21.6 - 21.9
$(NEt_4)_2[Ta_6Cl_{12}]Cl_6$	23.8
$[Ta_6Cl_{12}]Cl_2(H_2O)_4 \cdot 4H_2O$	25.8
$KTaO_4$	25.9
TaS_2	26.7
Ta_2O_5	26.7
$TaBr_5$	26.9
K_2TaF_7	29.4
hc-Ta_3SeI_7	23.4
hc-Ta_3TeI_7	23.4
Δ-Ta_3TeI_7	23.4
$Nb_xTa_{3-x}TeI_7$	23.4
Ta_3TeBr_7	23.5

Magnetic measurements and composition

Magnetic susceptibility measurements on powdered samples of many hand-picked small single crystals of both Ta_3SeI_7 and Ta_3TeI_7 display a weak paramagnetic signal, obeying the Curie-Weiss law (Ta_3SeI_7, 0.95 μ_B; Ta_3TeI_7, 0.60 μ_B). Plots of χ vs. T and of χ^{-1} vs. T for both compounds are shown if Figure 2-3 (Se) and Figure 2-4 (Te). In contrast, Nb_3SeI_7 and Nb_3TeI_7 show the diamagnetic behavior expected from formally closed-shell six-electron metal clusters. The precise origin of this magnetic moment is unknown, but two possibilities readily present themselves: 1) An extrinsic paramagnetic impurity, or 2) Iodine/chalcogen mixing or substitution is taking place, especially in the form of substitution of Se and Te by I on the cluster capping site. Such a substitution would create local paramagnetic "Ta_3I_8" regions, with seven-electron Ta_3 clusters. An estimate of the concentration of such regions in the Ta_3QI_7 framework (using a spin-only moment of 1.73 μ_B and diluting a pure Ta_3I_8 sample with diamagnetic Ta_3QI_7) yields a "Ta_3I_8 fraction" necessary to give rise to the observed moment. A hypothetical iodine-substituted Ta_3SeI_7 sample would require a Ta_3I_8 mole fraction of 0.55 (i.e. $Ta_3Se_{0.45}I_{7.55}$). For Ta_3TeI_7, the required mole fraction is 0.65 ($Ta_3Te_{0.35}I_{7.65}$). To address this possibility, electron microprobe quantitative analysis was performed on several crystals of both compounds. The electron microprobe instrument is very similar to the SEM, but is equipped with a wavelength-dispersive spectrometer (WDS) rather than the energy-dispersive (EDS) detector attached to the SEM. WDS is capable of much higher resolution of characteristic lines than is EDS, and therefore provides more accurate elemental compositions. This is an especially important point in a system containing tellurium and iodine, where the set of lines used for analysis (the Lα series) are very close together in energy (ΔE = 0.168 keV). The positions of these lines are: Tellurium Lα = 3.763 keV, Iodine Lα = 3.931 keV. The microprobe instrument requires elemental standards for all elements involved for precise compositional analysis. Tantalum and iodine standards were not available in the microprobe facilities used, so a sample of Ta_6I_{14} served as the standard source for both Ta and I. The Ta_6I_{14} was prepared in the same lab

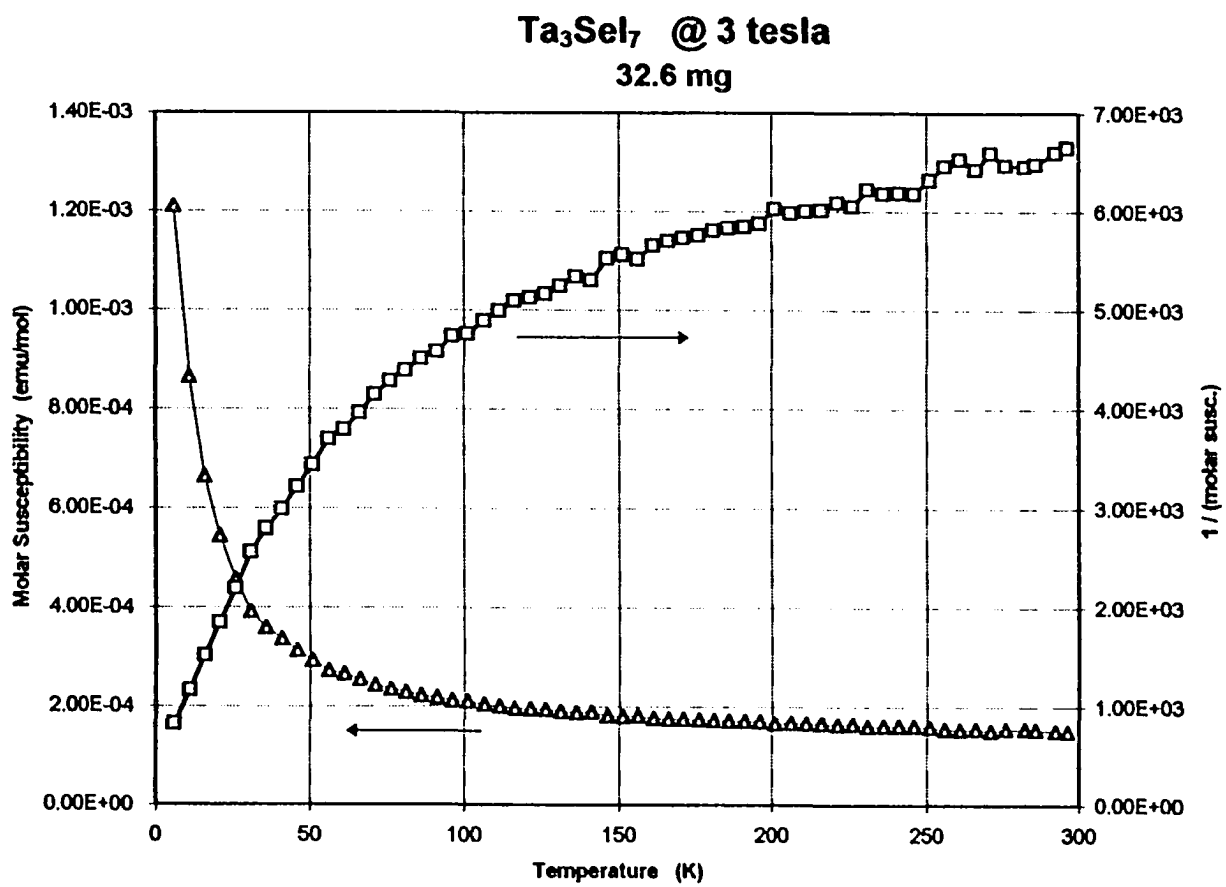

Figure 2-3. Magnetic susceptibility plot for *hc*-Ta_3SeI_7.

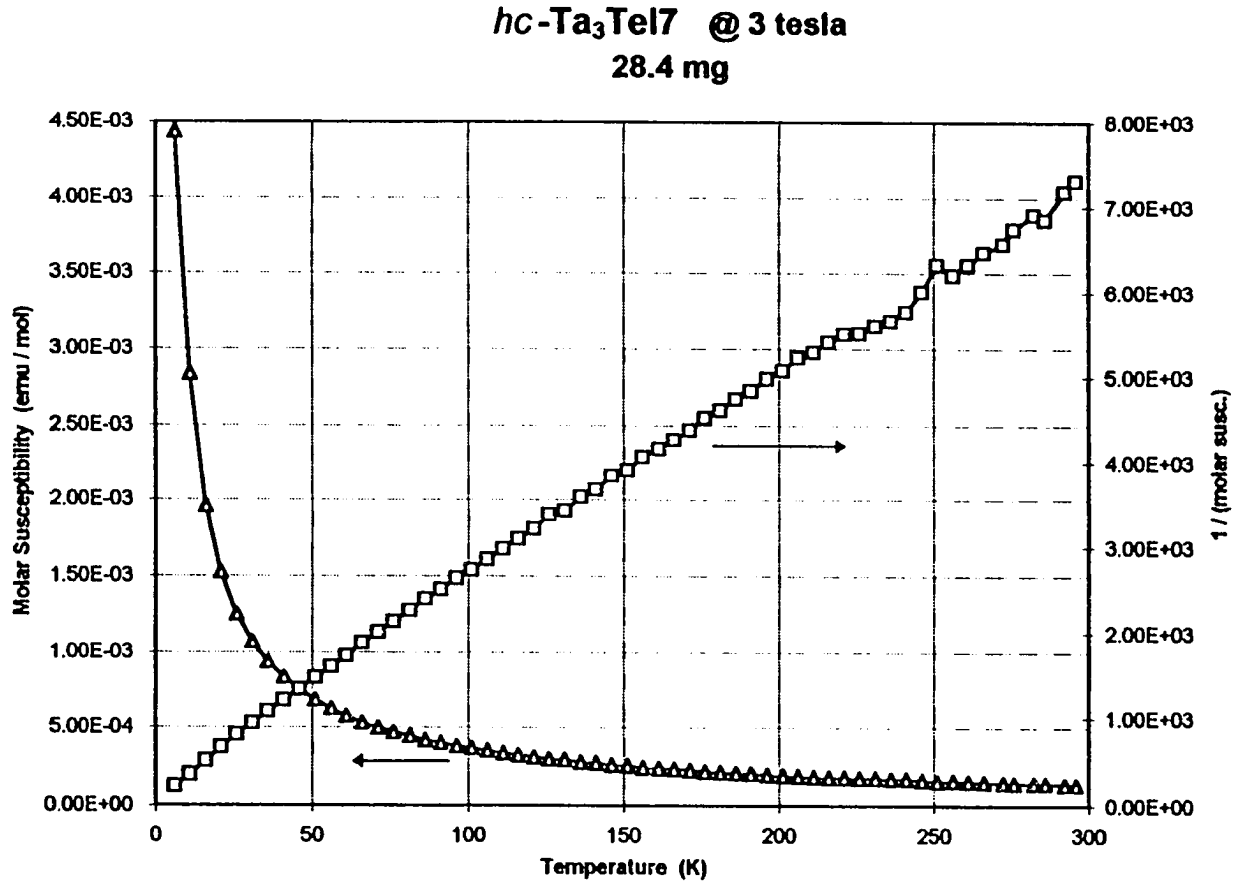

Figure 2-4. Magnetic susceptibility data for *hc*-Ta_3TeI_7.

as the Ta_3QI_7 samples, and its purity checked by Guinier diffraction. For tellurium, the element was used, which was available at the microprobe facilities.

The microprobe results confirmed the 3-1-7 stoichiometry in both cases. Also, at least in the case of the selenide, if such Se/I mixing were taking place, a dramatic effect in the μ_3-Q^i atom thermal parameter should be observed, but this is not the case.

The ...*hc*... variant is one of six different stacking variants discovered so far in the Nb_3X_8 and M_3QX_7 systems. The reason for the occurrence of the ...*hc*... modification over, for example, an ...*ABAB*... or ...*h*... anion layer stacking pattern, remains unclear. There would at first appear to be no great driving force for this particular stacking situation over any of the others, and the layered nature of these M_3QX_7 compounds might lead one to expect polymorphism in these layered systems as has been observed in the prototype compound CdI_2,[73] and in many other layered phases like TaS_2 [74] and other early transition metal dichalcogenides. Indeed, both the ...*hc*... and the ...*h*... variants have been observed in the Nb_3TeI_7 system[60]. In all the Ta_3SeI_7 reactions and re-heatings performed, though, only powders and crystals of the *hc*-type have been observed. However, polymorphism apparently exists in the Ta_3TeI_7 system, as discussed next.

Δ-Ta_3TeI_7

Introduction and synthesis

In addition to *hc*-Ta_3TeI_7 discussed above, another crystalline phase is frequently observed in "Ta_3TeI_7" reaction tubes. Large amounts of a material that is a highly reflective, well-faceted silver solid when crystalline, and dark grey when a powder, is found intermixed with (or sometimes instead of) *hc*-Ta_3TeI_7. Crystals of this compound have a trigonal morphology, with (visually) perfectly equilateral triangular faces. An SEM micrograph of crystals of this phase is shown in Figure 2-5. Because of this morphology, and because complete characterization of the compound remains elusive, it will be referred to as "Δ-Ta_3TeI_7". Generally the compound grows as densely intergrown large crystal chunks; occasionally loose, smaller crystals are found. The crystals grind with a lubricious

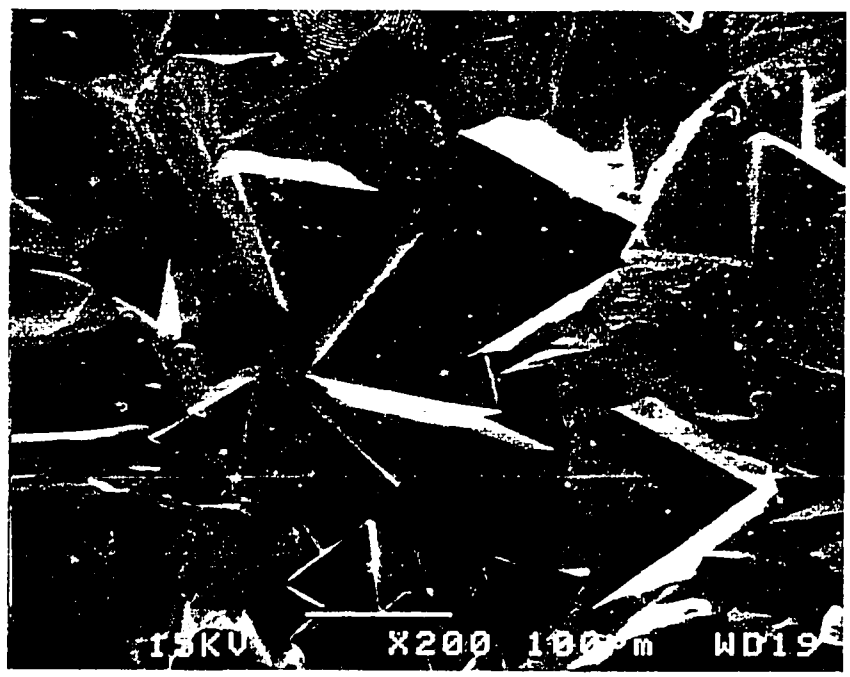

Figure 2-5. SEM micrograph of Δ-Ta_3TeI_7. Crystals of Δ-Ta_3TeI_7 form with a trigonal prismatic shape, whereas crystals of *hc*-Ta_3TeI_7 are hexagonal prismatic. The trigonal edges of the large crystallites in the center of the micrograph are approximately 125 μm.

feel in the mortar, indicating a layered nature similar to *hc*-Ta_3TeI_7. The compound's (non-) reactivity with air and moisture are similar to that of *hc*-Ta_3TeI_7, remaining unaffected indefinitely, but rapidly disappearing in dilute HNO_3.

Generally, Δ-Ta_3TeI_7 is observed from longer and hotter (to ~575°C) Ta_3TeI_7 reactions. However, the occurrence of this compound is unpredictable: Δ-Ta_3TeI_7 will sometimes form under conditions that previously gave only the *hc*- variant. *hc*-Ta_3TeI_7 was first discovered from two-week reactions at 450°C. When these experimental conditions were reproduced in subsequent reactions, the result was a mixture of phases with *hc*-Ta_3TeI_7 sometimes the majority, sometimes the minority phase. One reaction at 540°C, yielded 100% Δ-Ta_3TeI_7, but a repeat of this experiment gave both phases. Usually "Ta_3TeI_7" reactions produce both compounds simultaneously. Interestingly, upon annealing the *hc*- and Δ-phases do not seem to interconvert: annealing of a sample of pure *hc*- gives only *hc*-, and vice versa.

This unpredictability is most likely due to subtle, hard-to-control factors like the pressure in the reaction tube and temperature gradients and the effect they have upon similar (polymorphic?) compounds that differ only slightly in energy.

To attempt to quantify how to make one compound and not the other, several tubes were loaded and heated at different temperatures, with and without temperature gradients, for varying lengths of time, and with varying amounts of reactants in the tube. The reason for varying tube loading amount was to determine the effect of pressure on the final product, i.e. does a high pressure of vapor-phase species in the tube favor one phase? Unfortunately, no predictable pattern could be identified from these experiments.

X-ray diffraction

Guinier powder x-ray diffraction of both smaller "single"-like crystals as well as larger solid chunks of this compound immediately begins to show the characterization problems that plague better structural understanding of this phase. Many intense reflections in the powder pattern are very broad, over one degree in 2θ wide. Thorough grinding, or grinding with glass dust added to better homogenize the sample, does not

seem to help the quality of the powder pattern. The powder pattern of Δ-Ta_3TeI_7 is shown in Figure 2-6, alongside the pattern for *hc*-Ta_3TeI_7 for comparison. Some broad similarities to well-characterized 3-1-7 compounds exist here: the low-angle line (2θ = 12.8°), corresponding to the hexagonal *a* axis (100). Most telltale is the intense, fairly narrow line at 2θ = 48°. This line is present in all diffraction patterns of all 3-1-7 compounds discovered, as well as the related compounds Nb_3X_8.

Further characterization

Single crystal efforts A total of 35 single crystals of Δ-Ta_3TeI_7 have been examined on the Siemens P4 diffractometer. All exhibited very broad, asymmetric diffraction peaks, consistent with a poorly crystalline sample. However, the few crystals that have been good enough to measure diffraction positions have all corroborated one thing: hexagonal symmetry with a *c* axis length of near 21Å, and an *a* axis length of near 3.8 Å. On the crystal deemed best quality, 90 reflections were centered to gain the benefit of averaging many reflection angles to obtain better lattice constants. The lattice constants measured thusly by the diffractometer were 3.792(4) Å and 20.90(1) Å, hexagonal lattice.

Composition: Electron microprobe microanalysis To determine the composition of this phase, electron microprobe analysis was performed on a sample of Δ-Ta_3TeI_7, using the same preparative method described above for *hc*-Ta_3SeI_7 and *hc*-Ta_3TeI_7.

The microprobe sample was in the form of a large aggregation of triangular-faceted crystals, from a reaction at 540°C. The identity and purity of the sample were checked by Guinier powder diffraction before sample preparation. Only lines corresponding to Δ-Ta_3TeI_7 were observed in a small piece of the microprobe sample (i.e., no *hc*-Ta_3TeI_7, Ta_6I_{14}, etc.). The Δ-Ta_3TeI_7 was mounted in epoxy, and, after setting, buffed until a smooth sample surface was achieved. A total of 144 sampling points in several different regions of separate crystallites were measured by the probe. The average

(a) Upper: *hc*-Ta_3TeI_7.

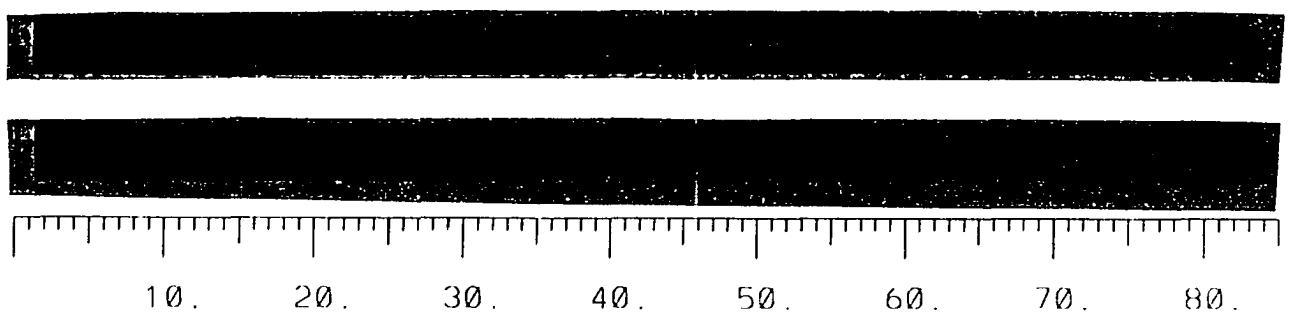

2θ (degrees)

(b) Lower: Λ-Ta_3TeI_7

Figure 2-6. Experimental Guinier diffraction patterns of *hc*-Ta_3TeI_7 and Λ-Ta_3TeI_7. Note the width of the intense Λ-Ta_3TeI_7 line (lower pattern) at $2\theta = 32^{\circ}$.

composition determined by the microprobe, with standard deviations, was "$Ta_{3.00}Te_{1.10(07)}I_{6.90(08)}$" (Ta defined as 3.00).

X-Ray photoelectron spectroscopy Samples of pure Δ-Ta_3TeI_7 were finely powdered in the glove box, and transferred under inert atmosphere to a PHI 550 multi-technique surface analyzer, to obtain x-ray photoelectron spectra. Information about the chemical states of the tantalum, tellurium and iodine atoms present could further link Δ-Ta_3TeI_7 with *hc*-Ta_3TeI_7 , giving further hints as to its structure. The tantalum binding energy so obtained is tabulated in Table 2-4, with experimental data for *hc*-Ta_3TeI_7 as well as reference (literature) data for relevant tantalum compounds. The binding energy of tantalum corresponds to a highly reduced Ta, and agrees well with the data for *hc*-Ta_3TeI_7. Tellurium and iodine binding energies are the usual expected for Te^{2-} and I^- species.

Magnetic susceptibility A crystalline aggregation of Δ-Ta_3TeI_7 was glued inside a plastic straw in air for magnetic susceptibility measurements. Its susceptibility was measured using a SQUID magnetometer, from 6 - 300 K at a field strength of 3 T. The results (Figure 2-7) show the same paramagnetic anomaly observed in *hc*-Ta_3TeI_7, the meaning of which has not been satisfactorily explained. A room temperature moment of 1.03 BM was measured.

Discussion

From the characterization experiments, even considering the lack of a high-quality single crystal, a reasonable hypothesis is that this phase is indeed a layered Ta_3TeI_7 compound, more precisely a polymorph consisting of a new stacking of the archetypal $^2_\infty[Ta_3TeI_7]$ slabs. The observed fact of a repeatable *c* axis length of ca. 21 Å measured from several different crystals corresponds nicely to a three-slab per unit cell polymorph.

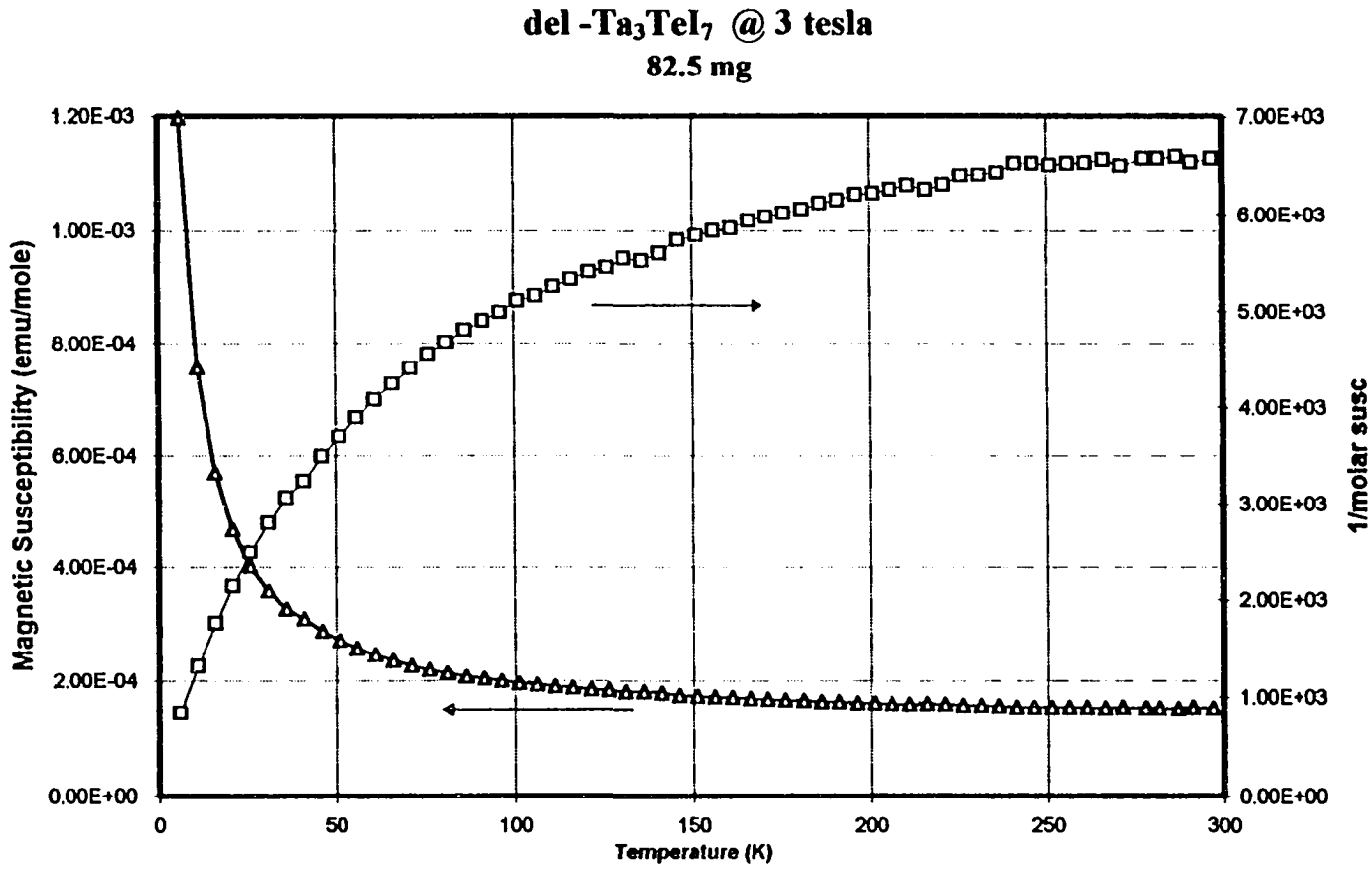

Figure 2-7. Magnetic susceptibility data for Δ-Ta_3TeI_7.

The broad diffraction peaks displayed by Δ-Ta_3TeI_7 point to disorder of some kind. Such disorder probably takes the form of misalignment of layered $^{2}_{\infty}[Ta_3TeI_7]$ domains, with some rotated (or inverted) relative to other domains in such a way that no long-range order is present.

Sulfide Iodides - Introduction

No tantalum sulfide iodide has ever been reported. Investigations into niobium sulfide iodide chemistry, though, have yielded four phases: Nb_6SI_9,[75] Nb_3SI_7 (actually $Nb_3S_{1-y}I_{7+y}$; $0 \leq y \leq 1$),[71] *o*-Nb_3SI_7 [71] and $Nb_7S_2I_{19}$.[76] The latter three compounds are closely related to the M_3QX_7 family, and show the Nb-S-I system to be the most prolific compound-former of all Nb_3QX_7 systems. Investigation into the Ta-S-I system was similarly fruitful, yielding three phases, with indications of even more.

hc-Ta_3SI_7

Synthesis

Despite the readiness with which *hc*-Nb_3SI_7 forms, the corresponding tantalum compound was not as forthcoming. Numerous stoichiometric reactions of the elements in the temperature region 350°C to 575°C did yield small amounts *hc*-Ta_3SI_7, but only as rare clumps of powder, usually constituting as minor a fraction of the total product as ca. 5%. Often, no *hc*-Ta_3SI_7 was found in a reaction tube at all. When the compound did form, it was observed to be a grey uniform polycrystalline material, which ground with a lubricating texture in the mortar. Generally, *hc*-Ta_3SI_7 formed as the "base" from which grew dense forests of Ta_4SI_{11} crystals (below). *hc*-Ta_3SI_7 was identified by its Guinier powder diffraction pattern, which is identical to that of *hc*-Nb_3SI_7. SEM micrographs of samples of this elusive phase are shown in Figure 2-8. This figure shows the rounded and smoothed corners of the hexagonal facets evident when the powder is magnified x330. The SEM instrument confirmed the presence of Ta, S and I in the sample.

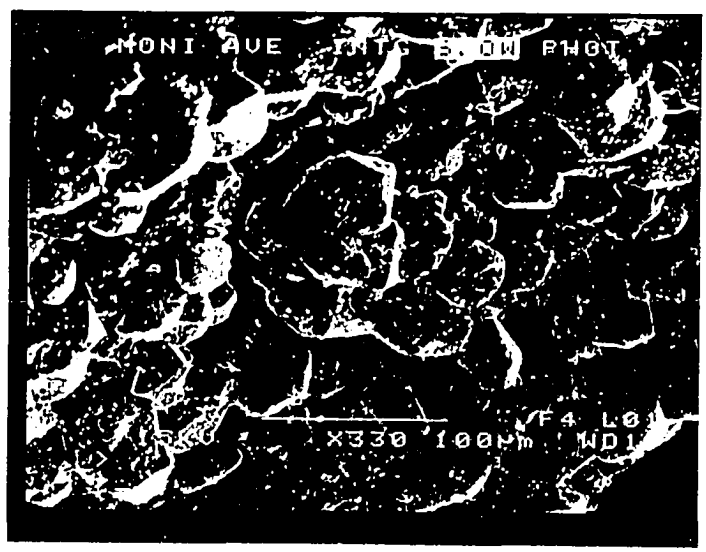

Figure 2-8. SEM micrograph of *hc*-Ta_3SI_7, showing the rounded and smoothed corners of the hexagonal facets (x330). The SEM instrument confirmed the presence of Ta, S and I in small sampling regions of the material.

Structural characterization. X-ray powder diffraction

After many attempts to improve yield and to grow crystals of *hc*-Ta_3SI_7 met with no success, the small amount of *hc*-Ta_3SI_7 available (ca. 0.25 g) was prepared for an x-ray powder diffraction experiment. The sample used was finely powdered in the glove box, and mounted onto a special cell designed for air-sensitive samples, in which a transparent thin plastic dome covers the flatbed sample stage and allows incident and diffracted x-ray beams to pass while protecting the sample from exposure to air. Data collection parameters are given in Table 2-5. The powder diffraction pattern so collected of *hc*-Ta_3SI_7 is shown in Figure 2-9. *hc*-Nb_3SI_7 was used as a structural model, and *hc*-Ta_3SI_7 could be successfully fit using this structural model. The observed and calculated profiles are shown in Figure 2-9, with the difference (Observed - Calculated) plotted below. A significant effect from preferred orientation was observed, as expected from highly anisotropic, low-dimensional compounds of a layered nature. Final R-factors are relatively high, R1 = 15.6% and wR = 18.1%, which may reflect the weak diffraction due to the small sample amount possible using the air-sensitive sample cell. Nevertheless, such R-factors are not unacceptable with x-ray data; they certainly do not indicate imposition of a grossly incorrect structure onto the data. However, detailed structural information such as bond distances and thermal parameters are certainly suspect from such data. Table 2-6 lists the lattice parameters and atomic coordinates output by this solution.

Table 2-5. Powder diffraction collection parameters for *hc*-Ta_3SI_7.

Instrument	Scintag XDS-2000
Radiation	Cu Kα, λ = 1.5406 Å
Angular range	$10° \leq 2\theta \leq 95°$
Scan type	Step scan, step width = 0.02°
# Data points collected	4250

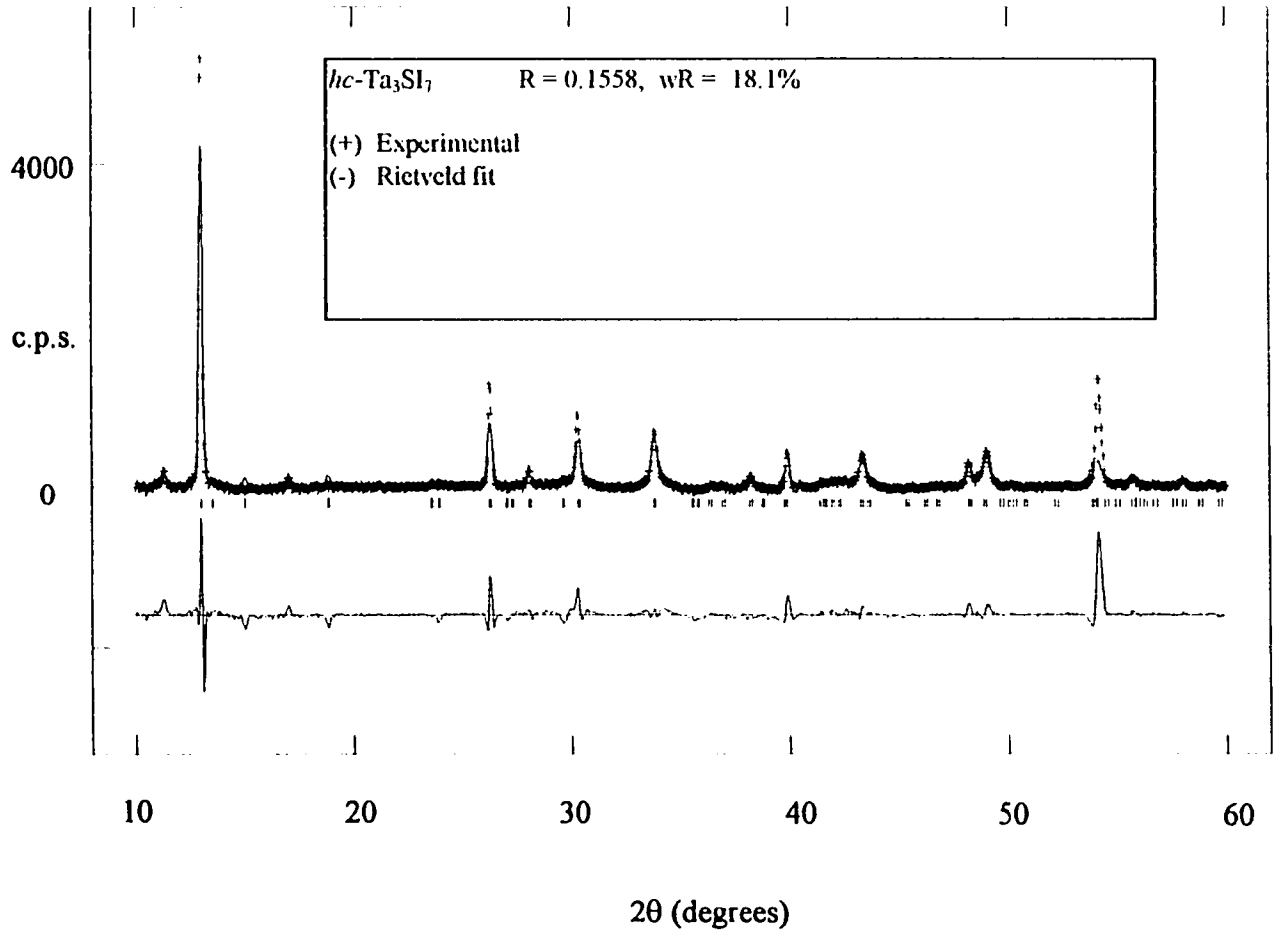

Figure 2-9. X-ray powder diffractogram for *hc*-Ta_3SI_7. *hc*-Nb_3SI_7 was used as an initial model. The difference plot (exper. - calc.) is shown below the powder pattern.

Table 2-6. Lattice parameters and atomic coordinates for *hc*-Ta_3SI_7 as refined from powder data.

Lattice parameters:	Space group $P6_3mc$, $a = 7.5498(2)$ Å, $c = 13.5702(4)$ Å		
Atom	x	y	z
Ta	0.8478	-x	0.2166
S	0.0	0.0	0.3518
I1	1/3	2/3	0.5870
I2	0.8361	-0.8361	0.5781
I3	0.4963	-0.4963	0.3357

Orthorhombic-Ta_3SI_7

Synthesis

By far the most abundant product formed from stoichiometric Ta_3SI_7 reactions is *orthorhombic*-Ta_3SI_7 (henceforth *o*-Ta_3SI_7). In fact, reactions often yield almost single phase *o*-Ta_3SI_7. The compound forms glistening grey powders and reflective black crystals with a rectangular plate or bar morphology from reactions in the temperature range 350°C to 500°C. The most abundant crystals, however, were obtained from a reaction loaded according to the stoichiometry "Ta_3SI_5". (This composition and several others were loaded in an effort to synthesize Ta_4SI_{11} (below), before its structure and composition were solved.) Typical reaction durations are one to three weeks. *o*-Ta_3SI_7 was initially identified from Guinier powder diffraction, on a sample of powder from a 450°C reaction. The powder pattern perfectly matched that of *o*-Nb_3SI_7, indicating the two are isostructural. A sample of this polycrystalline material was analyzed using a JEOL 6100 Scanning Electron Microscope, which verified the presence of Ta, S and I in the crystallites, and provided images. The rectangular bar or plate morphology of *o*-Ta_3SI_7 is plain from the SEM images shown in Figure 2-10.

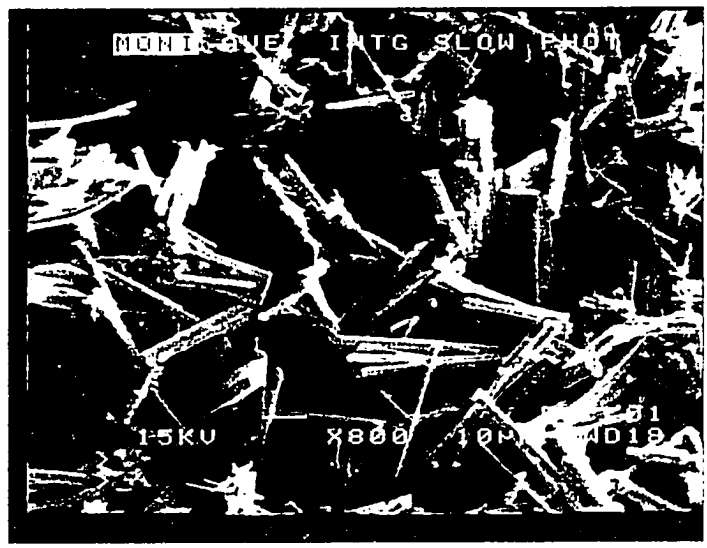

(a) x800 image of polycrystalline *o*-Ta_3SI_7, showing the longer bar morphology evident in powder samples of the compound.

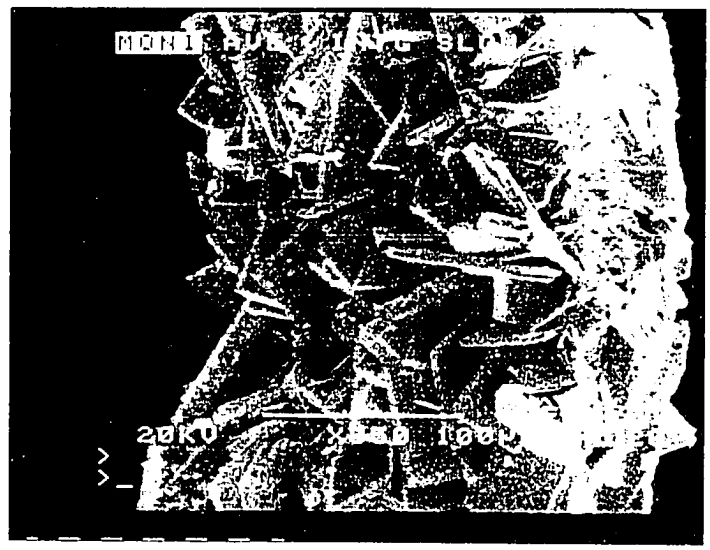

(b) x350 image of a larger aggregation of *o*-Ta_3SI_7 crystals, where the flat plate morphology is evident.

Figure 2-10. SEM images of *orthorhombic*-Ta_3SI_7.

Structural characterization

Several of the abundant single crystals from a Ta_3SI_5 reaction and from subsequent Ta_3SI_7 reactions were mounted on a Siemens P4 diffractometer for intensity data collection. All reproduced the information described next. From several reflections taken from a rotation photograph, an initial unit cell in the primitive orthorhombic crystal system, with a = 10.006(2) Å, b = 3.897(2) Å, c = 17.828(4) Å was indexed. This corresponds the the o-Nb_3SI_7 cell with b halved. Subsequently axial photographs (b axis) revealed weak interlayer spots indicating a doubling of the b axis was in order. Using the fractional search program on the Siemens (this routine searches for reflections with non-integral *hkl* values; if such are found that cannot be reconciled with the current unit cell, the reflections are re-indexed) a weak and broad reflection with k = 0.5 was located, necessitating a doubling of b. Using this new cell (a = 10.006(2) Å, b = 7.598(2) Å, c = 17.828(4) Å), which is nearly identical to o-Nb_3SI_7, several other reflections were found that would be inconsistent with the shorter b axis. However, all of these reflections were very weak (< 3 % of I_{max}), and also were noisy and broad, indications of problems to come. The primitive orthorhombic unit cell was refined using 45 reflections with $6° \leq 2\theta \leq 25°$, and subsequently 1775 data were collected, to $2\theta_{max}$ = 50°. Azimuthal ("psi") scans were performed on four inequivalent reflections, and applied to the data. The scans showed a wide variation of intensities, with transmission ranges T_{max}/T_{min} = 1.00/0.05, due to the flat bar morphology of the crystal. Of the 1775 collected data, 1207 were unique, and merged to R_{int} = 0.0643. At this point, severe problems became apparent. Systematic absence violations inconsistent with a centered lattice confirmed the primitive lattice type, and intensity statistics favored a centrosymmetric unit cell. However, the SHELX program could find no acceptable space group, due to the presence of systematic absence violations of above its tolerances. Inputting the space group of o-Nb_3SI_7 (Pmmn), and solving the structure using direct methods produced atomic positions that corresponded exactly to the the o-Nb_3SI_7 structure. Refining these positions yields the expected structure and bond distances and angles, but with unreasonable (negative) thermal motion ellipsoids, and high R-factors: R1 = 12% and wR2 = 35%. No

manipulation of the structure was found to remedy this problem. The same problems were observed from a total of twelve crystals grown from several independent reactions, ruling out an anomalous bad crystal. Interestingly, collecting a data set with *b* halved leads to a solution with R1 = 6%, but with too-short bond distances (Ta-Ta 0.8 Å), indicating a different (larger) unit cell.

Ta_4SI_{11}

Synthesis

Ta_4SI_{11} was first observed as an abundant (ca. 50% total product) side product from reactions of the elements in the ratio 3Ta:S:7I at 450°C in sealed, evacuated borosilicate glass tubes, designed to grow Ta_3SI_7 phases. After being unable to identify the compound from its Guinier powder diffraction pattern, a single crystal was selected and its structure solved (see below), yielding the composition "Ta_4SI_{11}". Tubes were then loaded at this stoichiometry, and heated at various temperatures to determine optimum conditions. Ta_4SI_{11} is best made by stoichiometric reaction of the elements at 430°C, for a duration of two weeks. Growth of the compound is sensitive to temperature gradients in the tube: highest (nearly quantitative) yields were obtained when the tube furnace was packed tightly with asbestos, to smooth out uneven temperature regions as much as possible. Heating a Ta_4SI_{11} mixture with an imposed temperature gradient leads to a mixture of phases, including hexagonal and orthorhombic Ta_3SI_7 (below), and Ta_6I_{14} in addition to Ta_4SI_{11}. Reagents used were: Tantalum "turnings" (Aesar, 99.99%, cleaned with an $HF/HNO_3/H_2SO_4$ solution to remove surface impurities, then rinsed with ethanol and dried in vacuo at 500°C), sulfur powder (Alfa, 99.9%, sublimed twice before use), and iodine (Alfa, 99.9%, resublimed). All purified reagents and products were handled in an Ar-filled glove box.

Ta_4SI_{11} crystallizes as long silver bars, which often aggregate in dense thickets, sprouting outward from a common point. Crystals are brittle and splinter easily along the long axis. Ta_4SI_{11} is sensitive to oxygen and moisture, decomposing to an uncharacterized white powder after several days. The compound appears to exist (in the absence of

oxygen, of course) up to temperatures of approximately 550°C, above which only Ta_6I_{14}, TaI_5 and TaS_2 are observed by x-ray powder diffraction.

Characterization

Scanning electron microscopy Verification of the presence of tantalum, sulfur and iodine in multiple single crystal samples of Ta_4SI_{11} was carried out using a JEOL 6100 Scanning Electron Microscope. Magnified images of Ta_4SI_{11} crystals are shown in Figure 2-11.

X-Ray Photoelectron Spectroscopy XPS spectra were measured using a PHI 550 multi-technique surface analyzer. Samples were prepared by finely powdering several larger single crystals of Ta_4SI_{11} in the glove box immediately before use. The samples were pressed onto indium foil in the glove box, and transferred to the XPS instrument under inert atmosphere. Binding energies were corrected for charging by using the C 1s peak of adventitious carbon (284.8 eV)[72] as an internal reference. However, no significant charging effects were observed, as C 1s always appeared at 284.8 eV. Additionally, large intact single crystals were mounted, and the surface etched by sputtered argon ions to removed any surface impurities introduced during handling, and probe the presumably pristine interior of the sample.

Magnetic Susceptibility Magnetic susceptibility measurements were performed with a SQUID magnetometer. Aggregations of Ta_4SI_{11} bars were loaded and sealed under inert atmosphere in fused silica tubes. The samples were kept in place by means of two tightly fitting fused silica rods on either side of the sample. The samples were chosen so that only larger single crystal aggregations were used, to avoid unwanted powder impurities and minimize the surface area susceptible to oxidation. Measurements were taken from 4 K to 300 K, at a field strength of 3T. The results are shown in Figure 2-12. A room temperature moment of 1.53 BM was measured, reproducible over three separate runs.

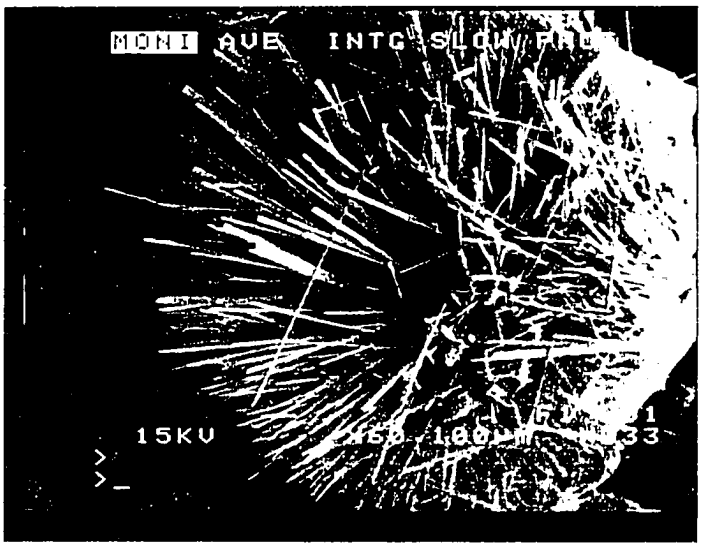

(a) SEM image of a typical spiny ball formation of Ta_4SI_{11} crystals.

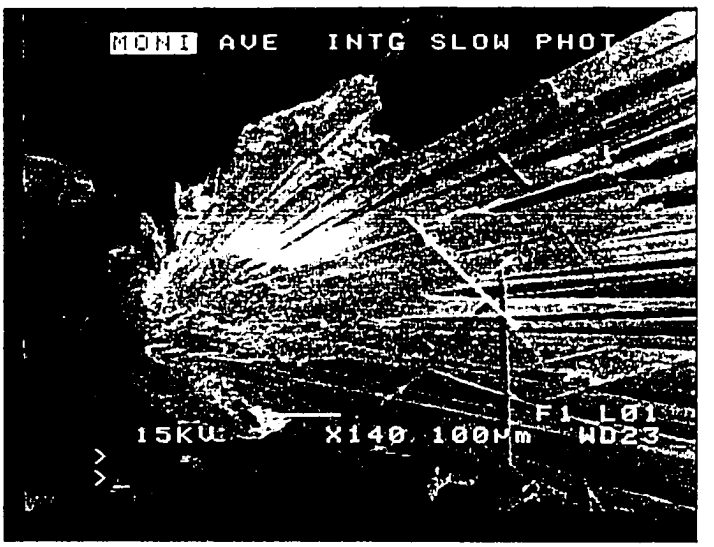

(b) SEM image of a fan of Ta_4SI_{11} crystals with a common nucleation point.

Figure 2-11. SEM images of Ta_4SI_{11}.

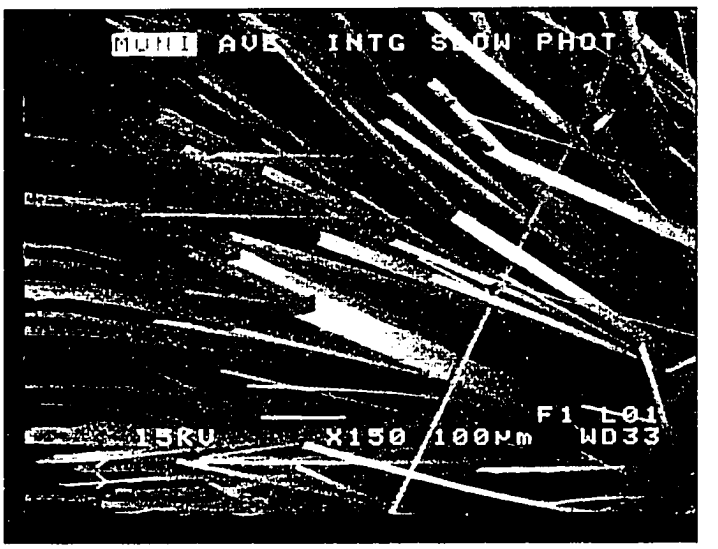

(c) Rectangular bar morphology of Ta_4SI_{11} crystals.

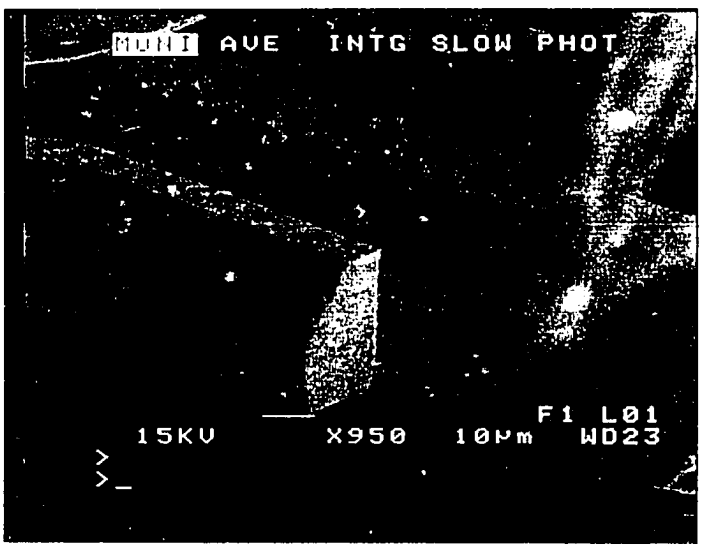

(d) Higher magnification of the end of a crystal.

Figure 2-11 (continued). SEM images of Ta_4SI_{11}.

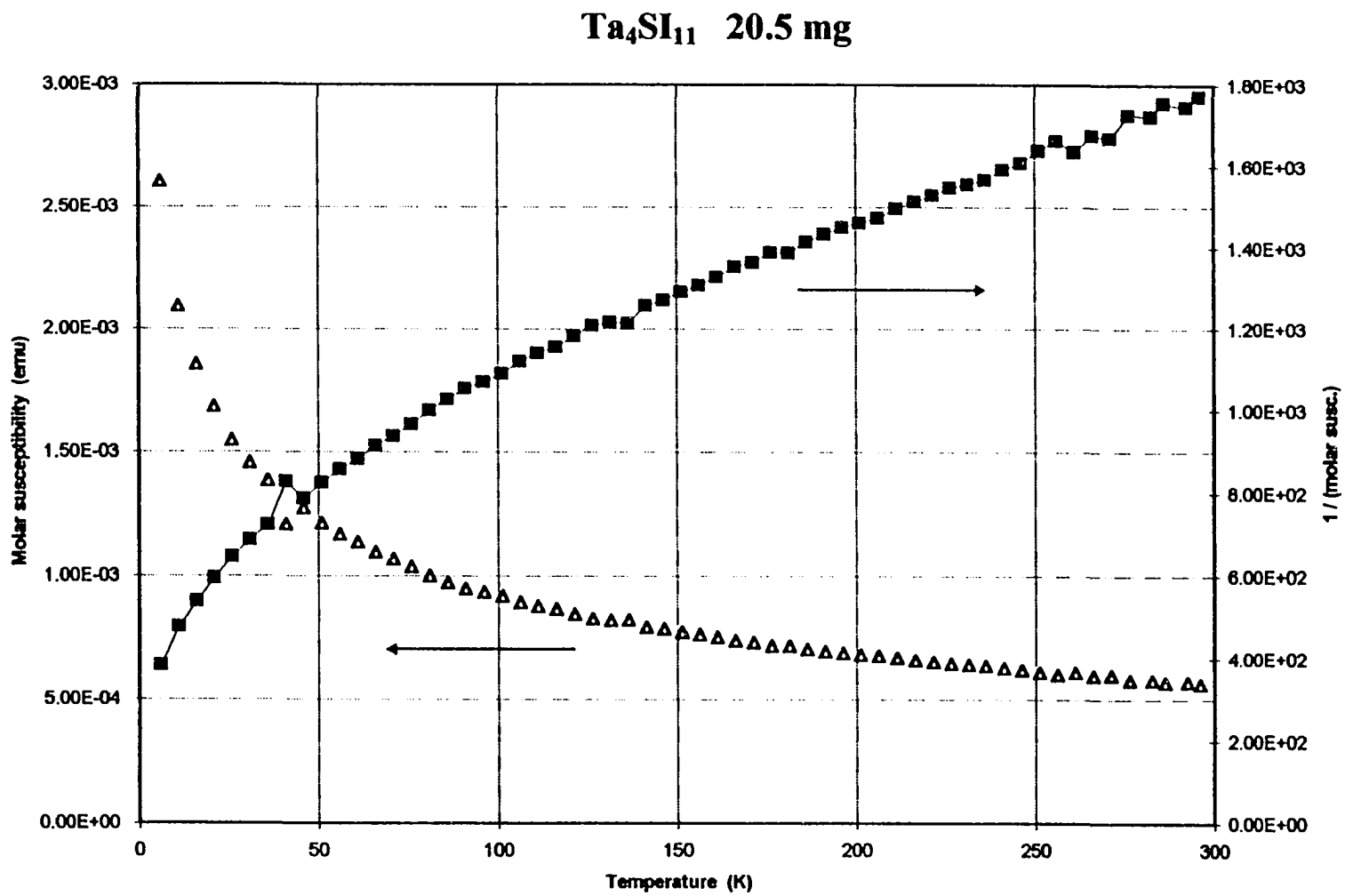

Figure 2-12. Magnetic susceptibility data for Ta_4SI_{11}. A curve fit for T > 100 K gives μ_{eff} = 1.53 BM.

Crystallography

A small silver bar (0.02 x 0.03 x 0.12 mm) was sealed inside a glass capillary under argon, and mounted on a Siemens P4 diffractometer. A primitive orthorhombic unit cell with dimensions a = 16.135(3) Å, b = 3.813(1) Å and c = 8.131(2) Å was indexed and refined on the basis of 45 reflections in the range $6° \leq 2\theta \leq 25°$. Axial photographs confirmed these lattice metrics. 2629 reflections were collected to $2\theta_{max} = 55°$, of which 685 were unique, 533 unique observed ($I > 2\sigma I$), and $R_{int} = 0.0498$. An empirical absorption correction was applied to the data, using the average of six complete "psi-scans" measured in well-separated regions of reciprocal space. The structure was solved using direct methods (SHELX-86 [68]) and refined with the SHELXL-93 crystallographic package.[77] Complete data collection details, atomic positions and isotropic thermal parameters, and anisotropic displacement factors are given in Tables 2-7, 2-8, and 2-9, respectively.

Structure description

Figure 2-13 shows Ta_4SI_{11} viewed parallel to the short b axis. The compound can be viewed as a close-packed structure similar to the M_3QX_7 compounds, but with a different metal atom distribution. In Ta_4SI_{11}, approximately close-packed layers of composition "SI_{11}" stack parallel to the (302) family of lattice planes in cubic close-packed ((...ABC...) or (...*c*...)) fashion, at an angle of 37.25° from the a axis. However, instead of a pattern of interstitial site occupation by the metal atoms that generates parallel slabs, as in the layered M_3QX_7 compounds, in Ta_4SI_{11} the occupation of these close-packed layer holes defines an undulating sheet structure with a period of 16.135 Å. Ta_4SI_{11} can still be viewed as a "layered" structure, since the undulating Ta_4SI_{11} layers are separated by a van der Waals gap.

The nature of the distibution of tantalum atoms within the layers is not straightforward. The structure solution gives rise to two distinct tantalum positions. Full occupation of these sites would lead to butterfly Ta_4 clusters that bend at the turns of the

Table 2-7. Summary of crystallographic data for Ta_4SI_{11}.

Formula weight	2151.76
Crystal system	Orthorhombic
Space group	Pmmn (No. 59)
Color of crystal	silver
Dimensions of crystal (mm)	0.02 x 0.03 x 0.12
Lattice parameters (Å)	
a	16.135(3)
b	3.813(1)
c	8.131(2)
Vol. (Å^3)	500.2(2)
Z	1
d_{calc} (g cm^{-3})	7.143
Diffractometer	Siemens P4
Radiation	Mo Kα, λ = 0.71071 Å
Linear absorption coefficient	38.854 mm^{-1}
Transmission ranges	0.96 - 0.57
Temperature of data collection	23°C
Scan method	2θ-ω scan
Range in *hkl*	$-20 \le h \le 20$
	$-4 \le k \le 4$
	$-10 \le l \le 10$
$2\theta_{max}$ (deg)	55.00
Number refl. measured	2629
No. unique	685
No. unique observed ($I > 2\sigma_I$)	533
R(int)	0.0498
No. parameters refined	38
Difference map (e$^-$/Å^3)	
Largest peak	2.15
Largest hole	-2.16
Residuals[a]	
R (observed, all data)	0.0322, 0.0503
R_w (observed, all data)	0.0695, 0.0762
GoF (all data)	1.054

[a] $R = \Sigma||F_o| - |F_c||/\Sigma|F_o|$; $R_w = [\Sigma w(|Fo| - |Fc|)^2/\Sigma w(F_o)^2]^{1/2}$; $w = 1/\sigma^2(F_o)$.

Table 2-8. Atomic positions, site occupation factors (sof), and U_{eq} for Ta_4SI_{11}.

Atom	x	y	z	sof	U_{eq}
Ta1	3/4	0.8568(3)	0.68160(13)	0.510	0.0116(4)
Ta2	0.60860(7)	1/4	0.87665(14)	0.517	0.0127(4)
I1	0.58153(6)	3/4	0.63999(13)	1.0	0.0181(3)
I2	3/4	1/4	0.4229(2)	1.0	0.0282(5)
I3	0.58430(7)	3/4	0.12070(13)	1.0	0.0234(3)
I4	1/4	3/4	0.1050(4)	0.534	0.0127(11)
S	1/4	3/4	-0.9311(32)	0.466	0.0127(11)

Table 2-9. Anisotropic displacement factors for Ta_4SI_{11}. I4 and S were refined as a split position with the constraint U_{ij} (I4) = U_{ij} (S).

Atom	U_{11}	U_{22}	U_{33}	U_{23}	U_{13}	U_{12}
Ta1	0.0125(5)	0.0096(6)	0.0127(5)	0.0002(4)	0.0	0.0
Ta2	0.0098(5)	0.0140(7)	0.0143(6)	0.0	0.0005(4)	0.0
I1	0.0152(5)	0.0168(5)	0.0223(6)	0.0	0.0002(4)	0.0
I2	0.0215(7)	0.0116(8)	0.0514(11)	0.0	0.0	0.0
I3	0.0328(6)	0.0175(6)	0.0199(5)	0.0	0.0080(4)	0.0
I4	0.0160(11)	0.0123(12)	0.0101(3)	0.0	0.0	0.0
S	0.0160(11)	0.0123(12)	0.0101(3)	0.0	0.0	0.0

$$U_{ij} = \exp(-2\pi^2(a^{*2}U_{11}h^2 + b^{*2}U_{22}k^2 + c^{*2}U_{33}l^2 + 2a^*b^*U_{12}hk + 2a^*c^*U_{13}hl + 2b^*c^*U_{23}kl))$$

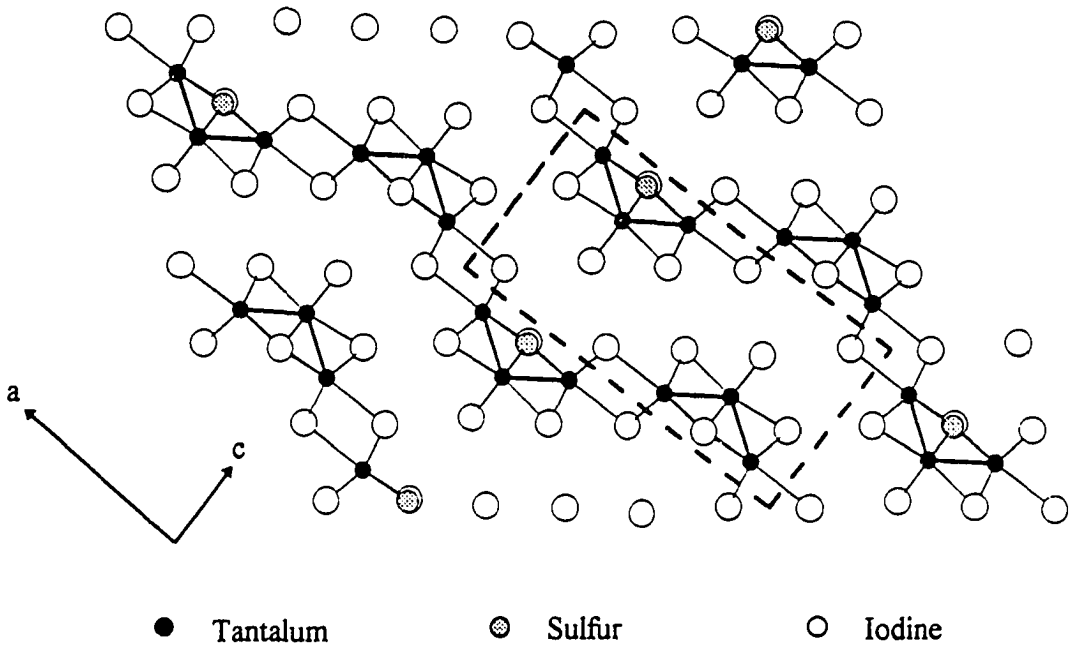

Figure 2-13. Projection of the structure of Ta_4SI_{11}, viewed down the *b* axis. The approximately close-packed mixed anion layers can be viewed as stacking parallel to the (302) family of lattice planes (horizontal in the figure). The occupation of octahedral interstices between the cp layers defines an undulating layer structure.

undulating anion layers. However, the site occupation factors of both metal sites each refine to near 50%. An additional complication is the atomic position that resides inside the cradle or elbow of the apparent bent cluster, and seemingly "bridges" all four metals. This site refines as a 50:50 sulfur-iodine split position. Figure 2-14 shows a [001] view of what the crystallographic experiment sees, which is an average over the entire crystal. This Figure also includes a view of the apparent butterfly cluster, showing the split S/I position. The question now becomes how the metal atoms are distributed throughout the structure, and how this correlates with the split S/I position. For the tantalum atoms, two feasible possibilities spring to mind immediately: 1) 4-member "butterfly" clusters of tantalum disordered throughout the structure, or 2) a mixture of Ta_3 clusters and isolated Ta atoms. The solution to this problem cannot be conclusively determined based on the x-ray diffraction experiment, which measures average electron density over the entire crystal and cannot elucidate the precise local situation; independent characterization methods are required.

X-ray photoelectron spectroscopy

To help clarify more details about the structure, X-ray photoelectron spectroscopy spectra were measured. The XPS spectrum of any tantalum atom produces a doublet signal, corresponding to the $4f_{7/2}$ (lower binding energy) and $4f_{5/2}$ (higher binding energy). These peaks are always separated by 1.91 eV. This constant separation facilitates deconvolution of overlapping peaks due to non-equivalent atoms. The reported binding energies are for the Ta $4f_{7/2}$ peaks. The Ta_4SI_{11} spectrum showed two peaks, at 23.8 eV and 26.3 eV, suggesting two different oxidation states for Ta. The Ta $4f_{7/2}$ binding energy of 23.8 eV indicates a highly reduced metal center, and suggests the presence of triangular clusters having an average oxidation state of +3. As reported earlier in Chapter Two, the binding energies of Ta in the Ta_3 cluster containing species *hc*-Ta_3SeI_7 and *hc*-Ta_3TeI_7 are 23.4 eV. For comparison, the literature XPS values for tantalum in other compounds is given in Table 2-4.

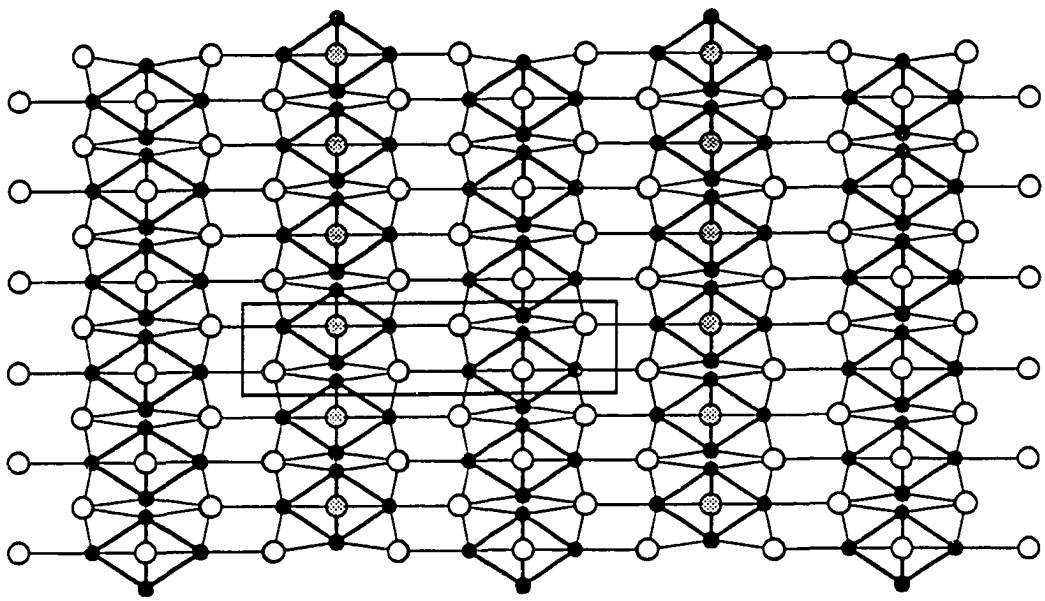

(a) [001] view of the crystallographically averaged structure of Ta_4SI_{11}; small black circles, Ta; large grey circles, the S/I split position, large open circles, I.

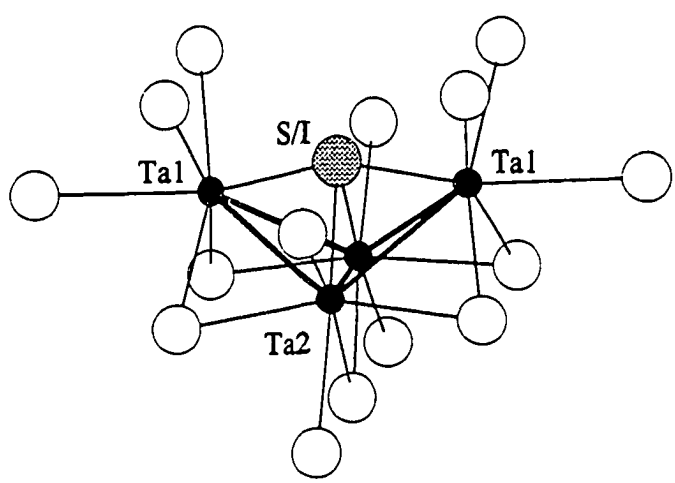

(b) The apparent butterfly cluster that results from the averaged Ta_4SI_{11} solution. Distances are: Ta1-Ta2, 3.157(2) Å, Ta2-Ta2, 2.999(3) Å. Ta2-S, 2.328(2) Å and Ta1-S, 2.524(2) Å. Ta-I distances range from 2.7 to 3.2 Å.

Figure 2-14. Structural features of the crystallographically averaged structure of Ta_4SI_{11}.

It is tempting to assign the B.E. peaks at 26.3 eV to oxygen contamination of the sample, and not to a mixed-valence effect. Oxygen contamination of the crystalline samples used would be limited to surface oxidation though, since all products were handled under inert atmosphere. To explore this possibility, samples of single crystals were etched in the XPS instrument by sputtering with Ar ions. Etching removes contaminated surface layers, and exposes the unoxidized, presumably pristine interior of the sample. After etching, the peak at 26.3 eV persisted, which suggests this peak is characteristic of the sample, and not due to surface oxidation. Additionally, the Ta $4f_{7/2}$ peak of Ta_2O_5 appears at slightly higher binding energy (26.7 eV, Table 2-4). Figure 2-15 shows the deconvoluted analysis of the peaks, after etching. This Figure shows the total Ta signal (solid line) and the constituent peaks from the two different tantalum atoms. The reference Ta $4f_{7/2}$ peaks from the two distinct tantalum atoms are shown as the dotted line, with their attendant Ta $4f_{5/2}$ peaks at +1.91 eV as the long-dashed curve.

The two binding energies suggest a mixture of Ta_3 trinuclear clusters and tantalum atoms in a higher oxidation state. It is not likely that the two peaks result from chemical inequivalencies within the trinuclear cluster itself (local symmetry C_s), as the 2.8 eV difference between the two is much too large to support this contention. The distortion of the Ta_3 clusters away from perfect equilateral geometry is moderate, with Ta-Ta distances of 3.157(2) Å and 2.999(2) Å, and angles of 56.70(1)° and 61.65(1)°. A formulation of Ta_4SI_{11} consistent with the crystallographic, magnetic, and x-ray photoelectron spectroscopic data is "$(Ta^{3+})_3(Ta^{4+})(S^{2-})(I^-)_{11}$"; a 1:1 mixture of Ta_3 clusters and isolated tantalum centers in the +4 oxidation state. These two metal units must be randomly distributed throughout the three-dimensional structure to give the apparent average structure solved from the x-ray data. While it is possible (but unverifiable) that some kind of ordering of the trinuclear clusters and isolated atoms exists within each undulating layer, certainly no ordering or registry can exist between the Ta_4SI_{11} layers, otherwise a different symmetry or unit cell size would be found.

The assignment of the split sulfur-iodine position goes as follows: When a trinuclear cluster occurs, sulfur is the capping atom. Conversely then, when the single

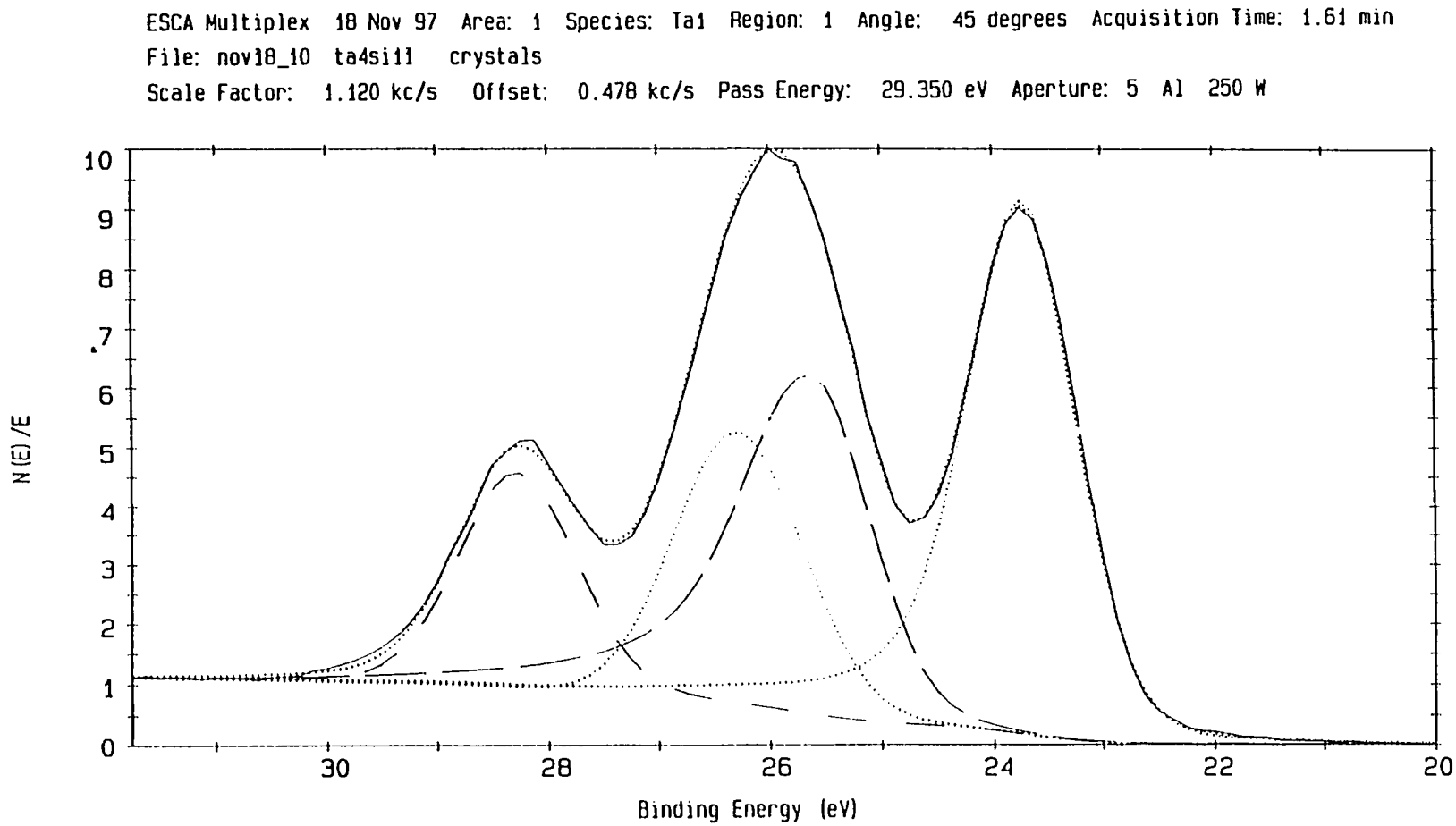

Figure 2-15. Deconvoluted analysis of the Ta $4f_{7/2}$ peaks, after etching. The total (sum) Ta signal is plotted as the solid curve. The reference Ta $4f_{7/2}$ peaks from the two different tantalum atoms (23.8 eV and 26.3 eV) are shown as the dotted lines, and the Ta $4f_{5/2}$ peaks at +1.91 eV from $4f_{7/2}$ as the long-dashed curve.

tantalum atom occurs, it is surrounded by a coordination environment of entirely iodine. This assignment accounts for the amount of each species present, as well as being the most reasonable placement of the sulfur in light of the behavior of the chalcogen in the similar compounds Ta_3QX_7; that is, always capping a trinuclear cluster. Figure 2-16 shows the metal coordination environments in Ta_4SI_{11}, and lists the important bond distances. This assignment, though, requires a short Ta-I4 bond length of 2.324(2) Å, coordinating the Ta^{4+} ions. However, with all the disorder and fractional occupancy present throughout the structure, such a distance could be a false artefact forced upon the structure as a consequence of averaging. Examining the anisotropic displacement parameters listed in Table 2-9, no unusual motion is manifest in the S or I4 U_{ij} values. In fact, the only noticeably large U_{ij} value is U_{33} for I2, apparently elongated into the van der Waals gap.

Extended Hückel calculations were carried out on three models (illustrated in Figure 2-17) of the Ta_4SI_{11} structure, using atomic orbital parameters given in Table 2-10. The purpose of these calculations was to determine the total energies of various metal atom distribution possibilities. Due to the disorder, all atomic positions within the unit cell needed to be specified. The three models used in the calculations follow the guidelines for possible tantalum atom distribution enumerated earlier (p. 77):

1. "Butterfly" Ta_4 clusters, distributed over the three-dimensional structure as shown in Figure 2-17 (a). Along the [010] direction of each undulating Ta_4SI_{11} layer, a Ta_4 cluster is fully occupied, with the adjacent Ta_4 set unoccupied. For this model, the sulfur was positioned in the crook of the cluster, coordinated to all four Ta atoms.

2. A 50:50 mixture of Ta_3 clusters and isolated Ta atoms. There are two possible unique distributions in this case: (i) such that the Ta_3 clusters are all parallel throughout the structure (along [010]), or (ii) the Ta_3 clusters alternate orientation, following the undulating layers (Figure 2-17 (b)).

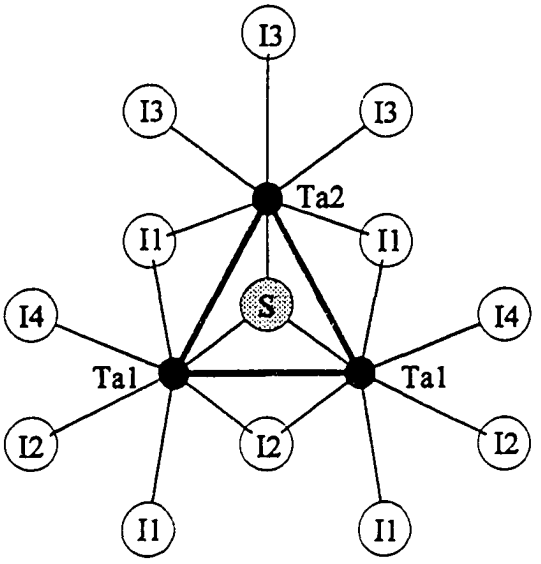

Distances in the Ta_3SI_{12} cluster (Å)

Ta1-Ta1	2.999(2)
Ta1-Ta2	3.157(2)
Ta1-S	2.52(2)
Ta2-S	2.324(5)
I1-Ta1	2.769(1)
I1-Ta2	2.744(1)
I2-Ta1	3.127(2), 2.583(2)
I3-Ta2	2.780(1), 3.112(2)
I4-Ta1	2.892(2)

(a) The Ta_3 cluster and its coordination environment.

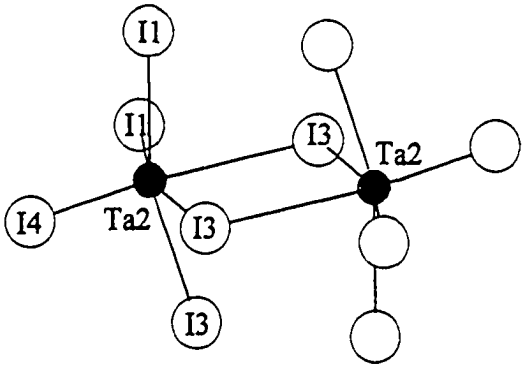

Bond Distances (Å)

Ta2-Ta2	4.467(2)
I1-Ta2	2.744(1)
I3-Ta2	2.780(1)
I4-Ta2	2.324(5)

(b) Coordination environment around the Ta^{4+} centers.

Figure 2-16. Tantalum coordination environments in Ta_4SI_{11}. (a) Surrounding the Ta_3 cluster. (b) Surrounding the isolated Ta atoms.

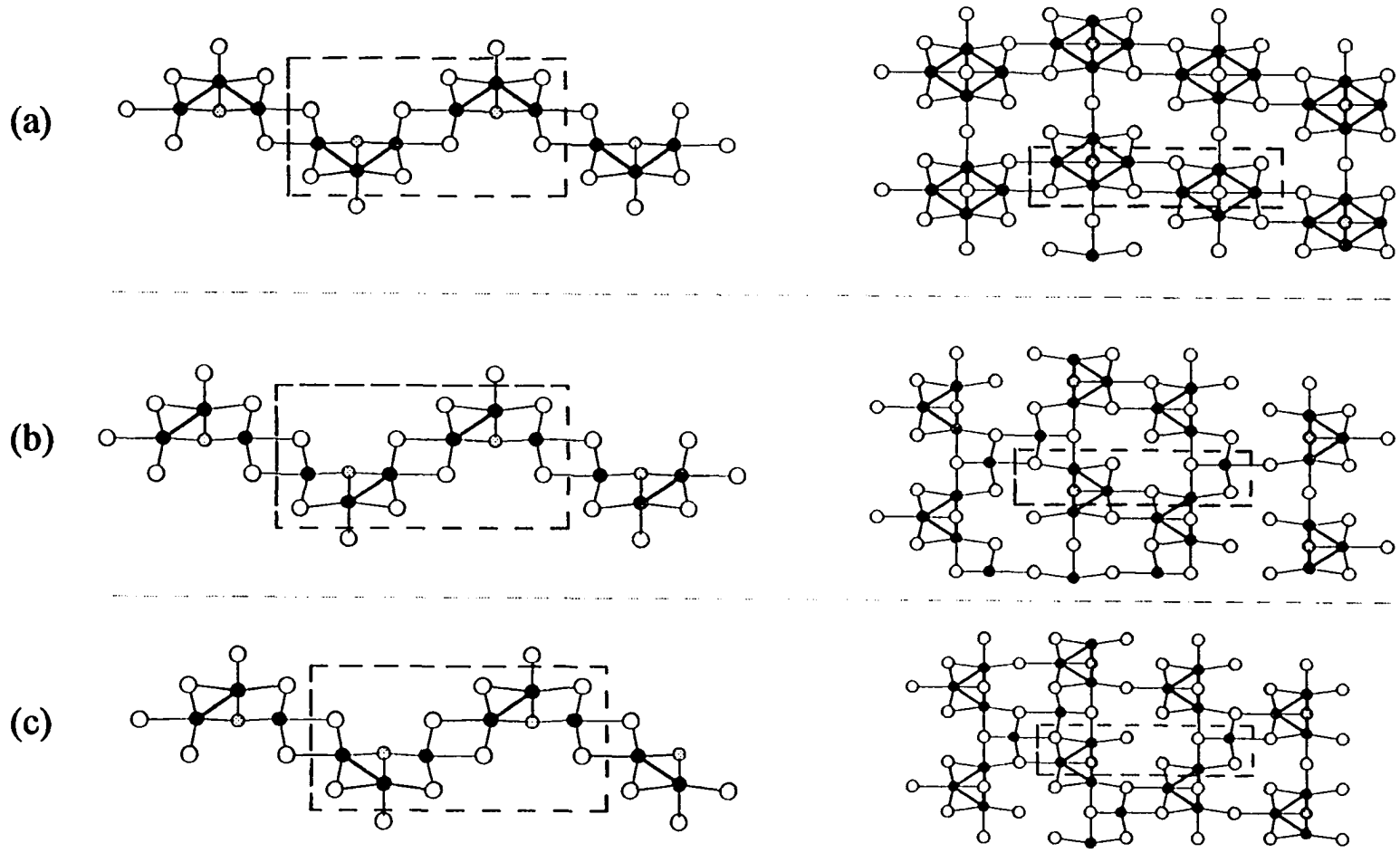

Figure 2-17. The three model Ta_4SI_{11} structures used in Extended Hückel calculations. Left column: [010] view. Right column: [001] view. Structures (b) and (c) were determined to have nearly equivalent total energies, and both were 0.27 eV (per formula unit) lower in energy than the upper model structure.

Table 2-10. Atomic orbital parameters used in Ta_4SI_{11} Extended Hückel calculations.

Atom	Orbital	H_{ii} (eV)	ζ_1	C_1	ζ_2	C_2
	6s	-8.96	2.28			
Ta	6p	-4.99	2.24			
	5d	-9.83	4.76	0.6104	1.94	0.6104
S	3s	-20.00	2.12			
	3p	-13.30	1.83			
I	5s	-18.00	2.66			
	5p	-12.72	2.32			

The calculations showed a significant energetic separation of the two broad cases: The total energies of the two Ta_3 + Ta cases were found to be quite similar, differing by only 0.05 eV (per formula unit) from one another. However, both of these cases were clearly stabilized relative to the butterfly clusters. The total energy of this possibility was found to be +0.27 eV relative to the trinuclear and isolated atom distribution.

Ta_4SI_{11} bears a close structural resemblance to *o*-Ta_3SI_7, which, although poorly characterized, is almost certainly isostructural with *o*-Nb_3SI_7 (see Chapter 1). Both structures contain undulating mixed sulfur-iodine layers, with the metal atoms defining a similar undulating layer structure. Within both undulating layer structures, Ta_3 clusters are capped by a sulfur atom, generating local Ta_3X_{13} type clusters. In *o*-Ta_3SI_7, the Ta_3 cluster coordination environment involves an additional sulfur atom; this second coordinating S provides a bridge to another Ta_3 cluster. Coordination of the Ta_3 units is then "$Ta_3S_2I_{11}$". In Ta_4SI_{11}, the sulfur atom is not shared between separate clusters, and the Ta_3 coordination is "Ta_3SI_{12}". Because of these structural similarities, and considering the crystallographic difficulties encountered in the solutions of both structures, one might raise the possibility of whether Ta_4SI_{11} and *o*-Ta_3SI_7 may be the same compound, but somehow a disorder mechanism falsely (but reproducibly) produces two different solutions. The Guinier x-ray powder diffraction patterns of Ta_4SI_{11} and *o*-Ta_3SI_7 are reproduced in Figure 2-18. (These are actually theoretical patterns generated from single

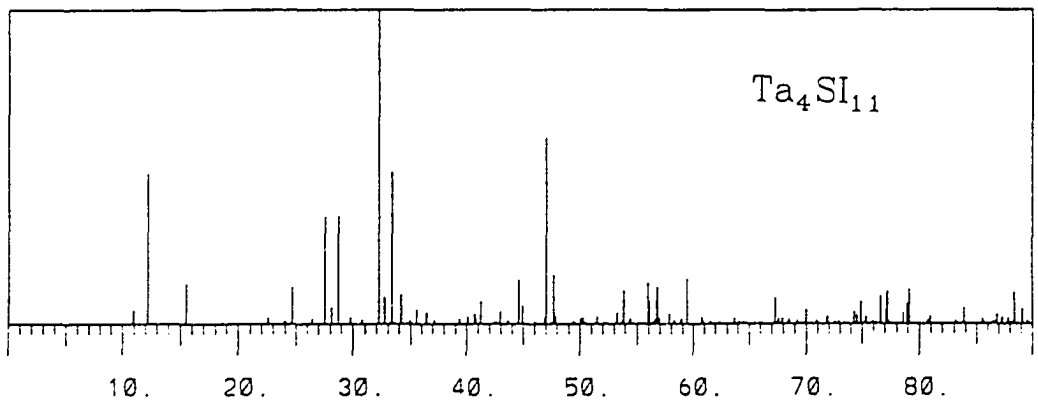

2θ (degrees)

(a)

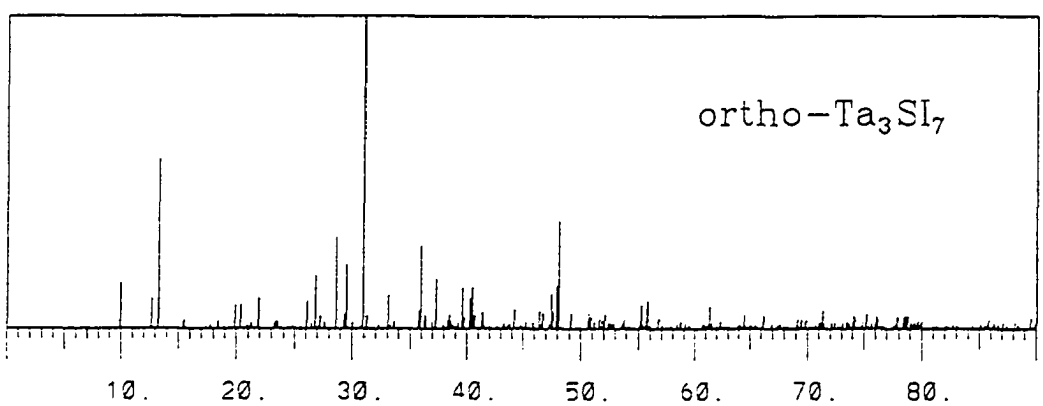

2θ (degrees)

(b)

Figure 2-18. Guinier powder diffraction patterns of (a) Ta_4SI_{11} and (b) o-Ta_3SI_7.

crystal data (in the case of *o*-Ta_3SI_7, the *o*-Nb_3SI_7 atomic positions were used), to take advantage of the greater clarity of these plots compared to Guinier photographic filmstrips reproduced onto paper. The positions and intensities of the lines in these theoretical patterns exactly match the experimental patterns.) Consideration of these powder patterns, which eliminate the troublemaking effects of multiply-crystalline samples, definitely establishes the uniqueness of the two phases. It is clear that the patterns are significantly different, reflecting the different structures that emerge from the single crystal work.

The available data support the contention of a mixed-valent, disordered sulfide iodide. The problem of the short Ta-I4 distance remains, and is a disturbing one. Other attempts at characterizing the sample have been attempted: Various mass spectrometry techniques (electron impact ionization, chemical ionization in positive and negative ion modes) have been employed, but the compound is not sufficiently volatile to produce any vapor-phase fragments that could illuminate structural details. The compound is not soluble in anything, and therefore other ionization techniques (electrospray, etc.) cannot be used. The potential of a superstructure undetected by conventional diffractometer technique exists. In particular, the split position might be "frozen" or resolved into one position, giving rise to an ordered structure. Several attempts at cooling crystals to -80°C, though, did not reveal any indication of a different unit cell.

CHAPTER THREE

SYNTHESIS AND CHARACTERIZATION OF THREE NEW TANTALUM CHALCOGENIDE BROMIDES

Background: Nb_3QBr_7 (Q = S, Se, Te)

Nb_3TeBr_7, Nb_3SeBr_7, and Nb_3SBr_7 have all been reported. Nb_3TeBr_7, the first M_3QX_7 compound to be made, was prepared in 1988 by Furuseth and Hönle from a reaction of the elements at 800°C for two weeks. Solution of the structure was not straightforward, and required analysis of data from a twinned crystal. The structure has already been described and illustrated in Chapter One, Figure 1-17. Nb_3SeBr_7 and Nb_3SBr_7 can also be synthesized by stoichiometric combination of the elements at elevated (ca. 800°C) temperature. Both adopt the Nb_3SBr_7 type, which is the simplest M_3QX_7 structure type. Details of this structure can also be found in Chapter One, Figure 1-14.

Tantalum chalcogenide bromides, Ta_3QBr_7 (Q = S, Se, Te)

General note on synthesis of Ta_3QBr_7

All reactions were done by stoichiometric combination of the elements, according to Equation (1):

$$3\ Ta + Q + 7/2\ Br_2 = Ta_3QBr_7 \qquad (1)$$

For all syntheses, the following reagents were used: Tantalum (foil or "turnings", 99.95%, Aesar). The tantalum was cut into manageable strips (usually about 1-2 cm long by 1-5 mm wide) and washed with a concentrated $HF/HNO_3/H_2SO_4$ solution to remove surface impurities, then dried in vacuo at 1000°C. Sulfur (Alfa), selenium (Alfa), and tellurium (Alfa) were all sublimed and then powdered under an inert atmosphere before use. The Ta strips and the chalcogen powder were loaded into the reaction ampoule (either pyrex or fused silica, depending on the reaction temperature to be used) in an

Ar-filled glove box, then taken out of the box and attached to a vacuum line for transfer of Bromine. Br_2 (Fisher) was deoxygenated by several freeze-pump-thaw cycles before distilling onto P_2O_5 for drying and storage - subsequently the appropriate amount of Br_2 was vacuum-transferred from its volumetric storage tube directly into the reaction ampoule containing Ta and Q. This mixture was then frozen solid with liquid nitrogen, evacuated to ca. 10^{-3} torr, and flame-sealed under vacuum. The tubes were then placed in horizontal tube furnaces and heated to the desired reaction conditions.

Ta_3TeBr_7

Synthesis

Ta_3TeBr_7 can be synthesized according to Equation (1) at temperatures of up to 550°C. Complete conversion of starting materials is accomplished by heating at temperatures of 500 to 550°C for a duration of two weeks. Lower temperatures or shorter reaction times leave unreacted tantalum metal along with $TaTe_2$ and copious amounts of Ta_6Br_{15} and $TaBr_5$. At the proper conditions, crystalline Ta_3TeBr_7 grows profusely, forming black, reflective, hexagonal-shaped crystals with a plate morphology which are usually massed together as densely intergrown bunches. Generally, these large aggregations are found transported to the far end of the reaction tube. In fact, Ta_3TeBr_7 can be purified by heating powdered samples in a temperature gradient in evacuated tubes. Various gradients have been found to transport the pure solid, but heating in a gradient of 550 - 425°C, yielded excellent transport (visual estimate of transported pure compound yield: 75%). The crystal bunches are transported to the cooler end of the tube, though polycrystalline compound may still be present at the hot end. Ta_3TeBr_7 appears to be stable in air for at least several months, though after such time surfaces of crystals are no longer mirror-smooth, but dull and textured. It is unaffected by water and by weak, non-oxidizing acids, but is quickly consumed in even dilute HNO_3. Crystals of Ta_3TeBr_7 grind to a dark grey, possibly red-brown-tinged powder with a lubricating feel in the mortar, indicating the expected layered structure.

Characterization

Scanning electron microscopy A sample of black crystals was mounted on a JEOL 6100 scanning electron microscope, for compositional analysis and to obtain magnified images that might reveal morphological information. Energy Dispersive Analysis (EDS) clearly showed the presence of only Ta, Te, and Br in several different sampled crystals. The SEM also provided images illustrating the poorly crystalline nature of Ta_3TeBr_7. Figure 3-1 shows an SEM micrograph of a sample of crystalline Ta_3TeBr_7, showing curving, ruffling, twisting, and separation of sections within individual Ta_3TeBr_7 crystals. Such severe stacking faults are usually an indication that proper crystal growing conditions have not been found yet, and that the compound may be crystallizing too fast. To find optimum crystal-growing conditions, samples of pre-made Ta_3TeBr_7 were subjected to further heating, under chemical transport conditions. Samples of pure Ta_3TeBr_7 were ground to fine powders under inert atmosphere, and sealed under vacuum in glass tubes. In Appendix A is a comprehensive summary of all the heating conditions employed in these reaction and re-heating experiments, and the results in each case. Even extended heating through a minimal temperature gradient (e.g., six weeks at 505 - 495°C) failed to yield well-crystallized material, though the same conditions produced excellent crystals of Ta_3SBr_7.

This poorly crystalline nature illustrated by the SEM micrographs of course also manifests itself in the lack of single crystals of suitable quality for x-ray diffraction, and is echoed in the report of Nb_3TeBr_7, where a twinned crystal had to be used. Examination of more than 50 single crystals of Ta_3TeBr_7 failed to turn up even one collectable crystal due to very broad, asymmetric diffraction peaks. Several crystals were nonetheless indexed (but not collected) in the hexagonal system, and gave axis lengths of a = 7.15 Å, and c = 13.17 Å. These cell parameters are very approximate, though, due to the difficulty in precisely centering diffraction peaks sometimes as broad as 1.5° in omega. However, they are quite similar to the reported Nb_3TeBr_7 lattice constants of a = 7.174 Å and c = 13.166 Å, indicating Ta_3TeBr_7 may be isostructural with Nb_3TeBr_7.

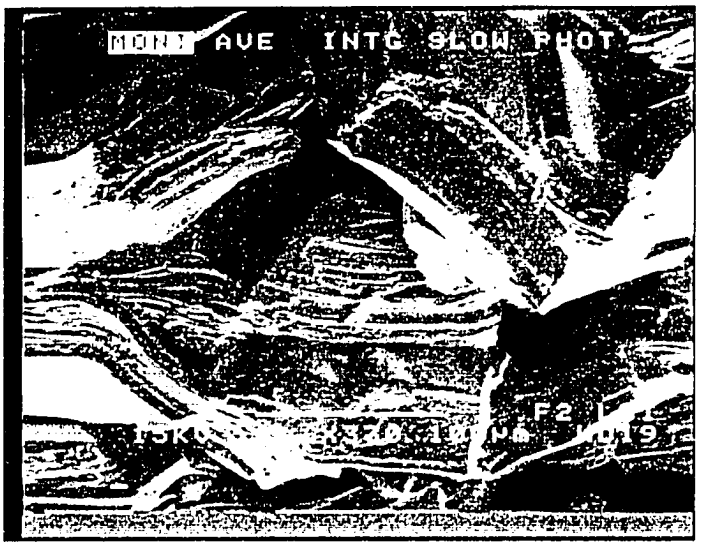

(a) x330 image.

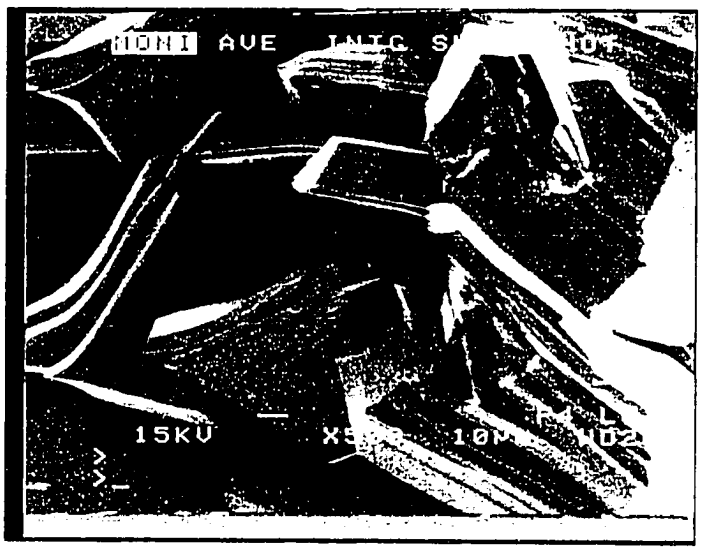

(b) x500 image.

Figure 3-1. SEM images of Ta_3TeBr_7 showing the intergrowth, bending and misstacking responsible for the poor quality of all Ta_3TeBr_7 crystals examined.

X-ray powder diffraction The x-ray powder diffractogram of Ta_3TeBr_7 is shown in Figure 3-2.

Magnetic susceptibility Magnetic susceptibility measurements were made on a large crystalline chunk of Ta_3TeBr_7, which was glued inside a plastic straw in air. Measurements were made with a SQUID magnetometer operating at a field strength of 3 T, at temperatures of 6 to 300 K. Figure 3-3 shows the magnetic data. A relatively large paramagnetic signal was observed (room temperature moment, μ_{eff} = 1.41 BM).

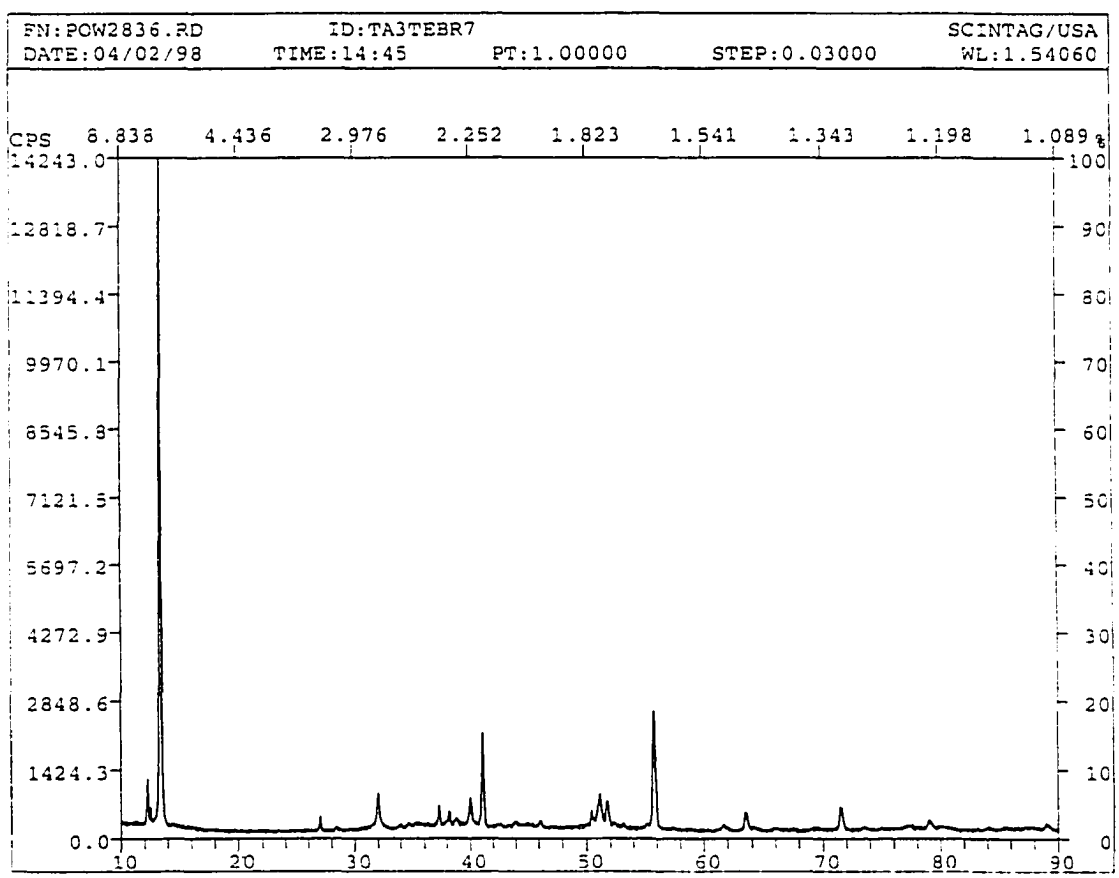

2θ (degrees)

Figure 3-2. The x-ray powder diffraction pattern of Ta_3TeBr_7.

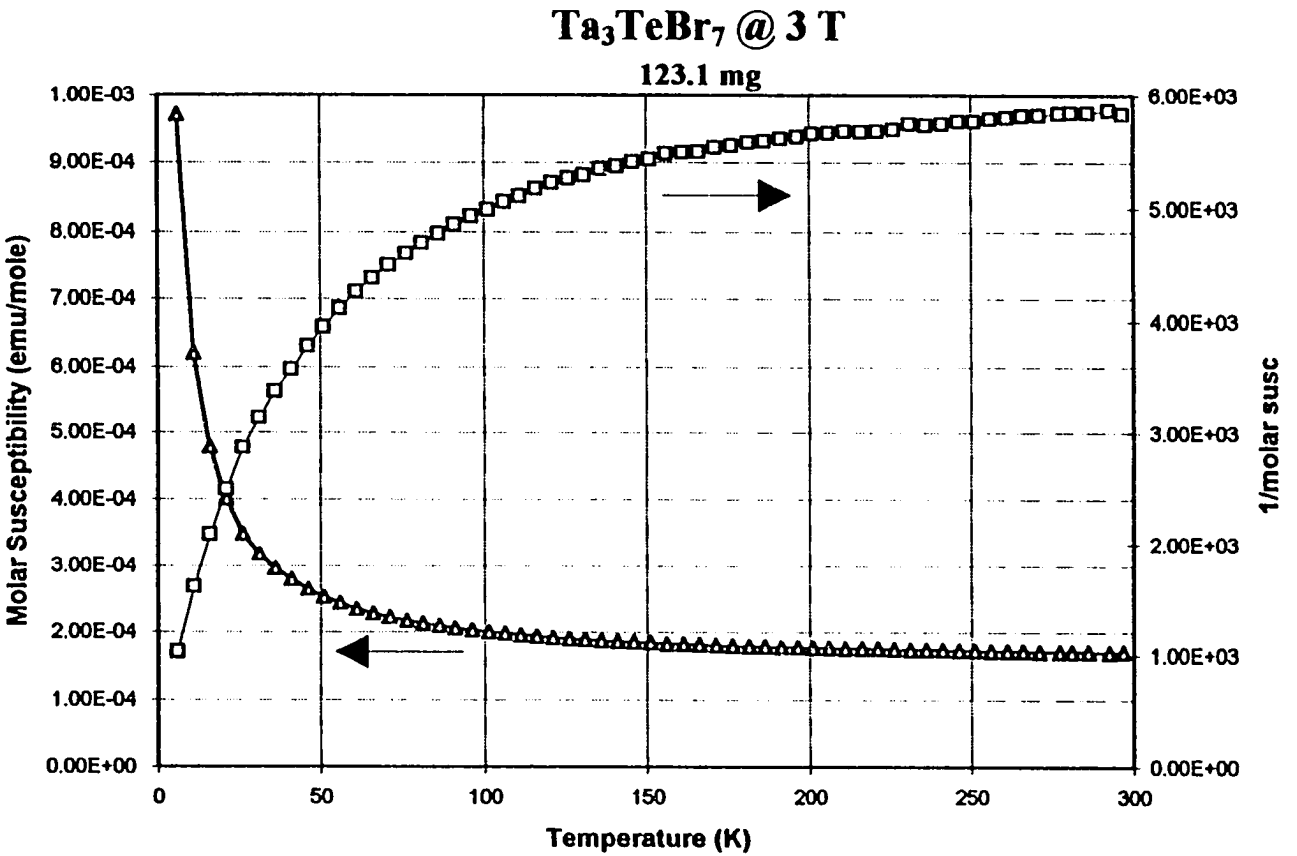

Figure 3-3. Magnetic susceptibility data for Ta_3TeBr_7.

Ta_3SeBr_7

Synthesis

The conditions for preparation of Ta_3SeBr_7 are quite similar to those for Ta_3TeBr_7. The compound forms at temperatures of up to ca. 550°C, above which it is unstable with respect to Ta_6Br_{15}, $TaBr_5$ and $TaSe_2$. Single-phase yield has not been achieved, and Ta_3SeBr_7 is always accompanied by some Ta_6Br_{15} and $TaBr_5$. Ta_3SeBr_7 does not form crystals as readily as Ta_3TeBr_7 does, but remains in largest amount as a powder or thin coating of the tube wall. Crystals can be grown by heating premade Ta_3SeBr_7 (or, more precisely, mixed powders of Ta_3SeBr_7, Ta_6Br_{15} and $TaBr_5$) in a temperature gradient of 550 - 425°C for approximately two weeks. The yield of crystals thus transported in still quite small (visual estimate ~ 5 %). A summary of the results of all Ta_3SeBr_7 reactions and re-heating of pre-reacted powders is given in Appendix A.

Ta_3SeBr_7 forms a dark grey powder which grinds with a lubricating feel in the mortar, indicative of a layered structure. The Guinier powder diffraction pattern of Ta_3SeBr_7 is quite similar to that of Ta_3SBr_7 (below), but with line positions shifted toward smaller two-theta (larger *d*-spacing) by about a degree. The magnitude of the line position shift corresponds with what is expected when replacing S with Se in a similar structure. A shift of this magnitude is also observed in the series Nb_3SI_7 / Nb_3SeI_7. Crystalline Ta_3SeBr_7 appears to be stable in air for a period of at least several months. Further tests of reactivity could not be performed due to lack of pure sample.

Characterization

Scanning electron microscopy A sample of crystalline Ta_3SeBr_7 was analyzed by EDS using a JEOL scanning electron microscope. Figure 3-4 shows two SEM micrographs of Ta_3SeBr_7: (a) is an image of a typical bunch of crystals, and (b) is a higher magnification of a side of one of these crystals. EDS identified Ta, Se, and Br to be the only elements present in the samples. There is the question of ambiguity here though, since the characteristic lines of Se ($L\alpha$, 1.65 keV) and Br ($L\alpha$, 1.78 keV) are

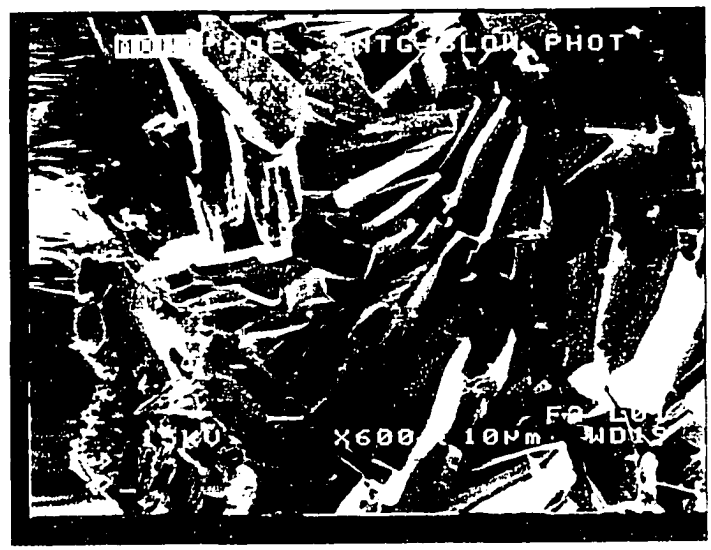

(a) x600 image of an aggregation of Ta_3SeBr_7 crystallites (approximate average size 10-20 µm x 30-40 µm).

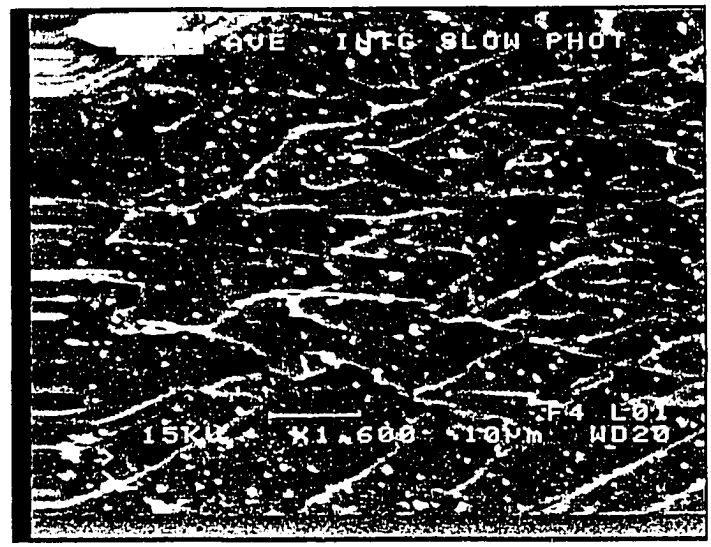

(b) Higher (x1600) magnification of a rough side of a crystallite.

Figure 3-4. SEM images of Ta_3SeBr_7.

separated by only 0.13 keV on the energy scale. However, the SEM instrument could resolve a small shoulder appearing on the side of the large Br peaks, clearly due to selenium. In contrast to Ta_3TeBr_7, which forms large, sprawling plate crystals, crystalline Ta_3SeBr_7 grows as rough columnar pieces, with a trigonal morphology. Like Ta_3TeBr_7, good single crystals of Ta_3SeBr_7 are not forthcoming. The compound doesn't grow crystals readily to begin with, and of the twenty or so examined, all exhibited very broad and noisy diffraction maxima, or even powder rings in the rotation photographs. This is again reminiscent of Nb_3SeBr_7, whose structure was solved from powder diffraction data, presumably due to lack of a suitable single crystal. Comparison of the experimental powder pattern of Ta_3SeBr_7 to the pattern generated from the reported data for Nb_3SeBr_7 opens the possibility (probability?) that the two compounds are isostructural. On the other hand, Ta_3SBr_7 is not isostructural with Nb_3SBr_7, but their structures are so similar that, in practice, their powder patterns are indistinguishable. A similar possibility exists, then for Ta_3SeBr_7 (and for Ta_3TeBr_7).

The refusal of Ta_3SeBr_7 and Ta_3TeBr_7 to grow suitable single crystals is puzzling, and underscores how little is known about crystal nucleation mechanisms in these systems.

Ta_3SBr_7

Synthesis

Polycrystalline Ta_3SBr_7 was synthesized by stoichiometric reaction of the elements in evacuated, flame-dried pyrex tubes at 550°C for two weeks, according to Equation (1). The reaction tubes (typically 10cm x 8mm i.d.) were then placed in horizontal tube furnaces packed with asbestos to smooth out temperature gradients, and heated to 550°C for 12 days. The product from this step was a coarse-textured black solid that ground with a lubricating feel, and a small amount of orange $TaBr_5$. Subsequently, the black solid was ground to a fine powder in an Ar-filled glove box and loaded into another pyrex tube, evacuated and sealed, and placed in a 505-495°C temperature gradient. After six weeks, several small clumps of black, reflective, dagger-shaped crystals were found throughout the tube, but predominantly at the hot end. The majority of the product remained

powdered. Crystals of Ta_3SBr_7 appear to be air- and moisture-stable for at least several weeks. SEM micrographs of Ta_3SBr_7 crystals are shown in Figure 3-5.

Structure solution

A small black dagger crystal was epoxied in air onto a thin glass fiber, and, after an initial crystal-quality check using the Weissenberg technique, aligned on a Siemens P4 diffractometer. The initial unit cell and symmetry of Ta_3SBr_7 were determined on the basis of six reflections taken from a rotation photograph. Subsequently 40 reflections of varying intensities located between 22° and 25° in 2θ were used to refine the cell. Axial photographs were taken of all three axes to verify the unit cell lengths. Due to its small size, the crystal was then moved to a Rigaku AFC6R diffractometer to take advantage of the greater intensity offered by the rotating anode instrument. 1118 data were collected with no centering restrictions, of which 509 were observed ($I > 3\sigma_I$). Systematic absences confirmed a C-centered lattice and positively ruled out a *c*-glide operation, leaving three space groups; C2, C2/m, and Cm. Of these, C2/m was eliminated on the basis of intensity statistics, which strongly indicated noncentrosymmetry. Since an axial photograph of the *b* axis taken before data collection clearly showed mirror symmetry, space group Cm was chosen. Subsequent failed attempts to solve the structure in C2 verified this assignment. The structure was solved by direct methods using SHELXS-86. [68] All atoms were easily located from Fourier map peaks, reasonable Ta-Ta, Ta-S, and Ta-Br distances, and structural similarities of Ta_3SBr_7 to other M_3QX_7 compounds. Psi-scans of six reflections were averaged and applied to the data to correct for absorption and, after isotropic refinement,[69] a DIFABS correction was applied.[70] All atoms were then refined anisotropically. The final residuals converged at $R = 0.027$, $R_w = 0.032$. Further crystallographic information is listed in Table 3-1. Atomic coordinates and isotropic displacement parameters are given in Table 3-2. Anisotropic displacement parameters are given in Table 3-3.

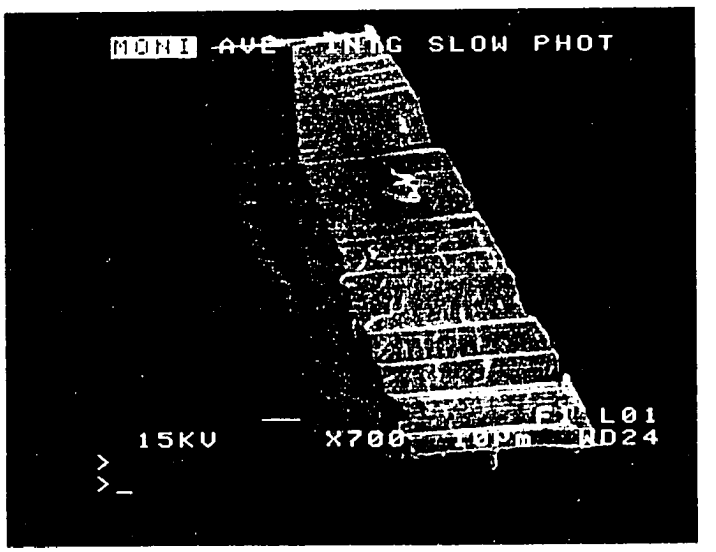

(a) x700 image.

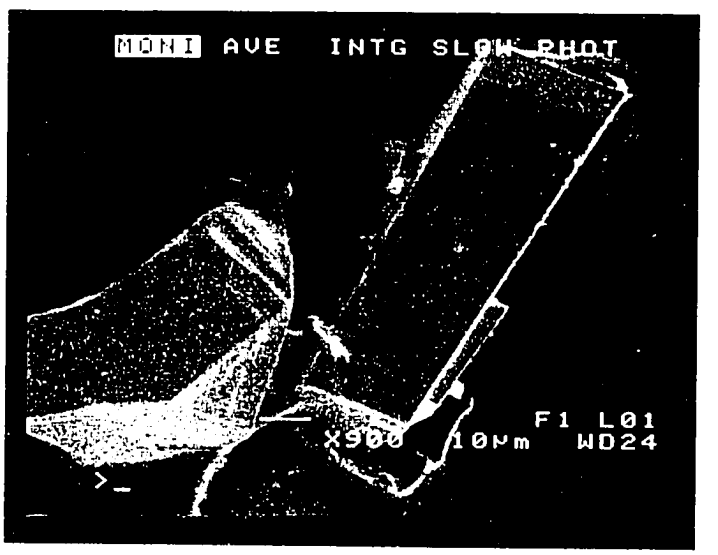

(b) x900 image.

Figure 3-5. SEM images of larger crystalline Ta_3SBr_7 samples.

Table 3-1. Crystallographic data for Ta_3SBr_7

Formula weight	1134.23
Crystal system	Monoclinic
Space group	Cm (no. 8)
Color of crystal	black
Dimensions of crystal (mm)	0.03 x 0.04 x 0.2
Lattice parameters (Å)	
a	12.249(2)
b	7.071(2)
c	8.829(2)
β (deg)	134.421(8)
Vol. (Å^3)	546.16(23)
Z	2
d_{calc} (g cm^{-3})	6.896
Diffractometer	Rigaku AFC6R (Mo Kα)
Linear absorption coefficient	55.13 mm^{-1}
Transmission ranges	0.87-1.0
Temperature of data collection	23°C
Scan method	2θ-ω scan
Range in *hkl*	$0 \le h \le 14$
	$0 \le k \le 8$
	$-10 \le l \le 7$
$2\theta_{max}$ (deg)	50
Number refl. measured	1118
No. observed	1067
No. unique observed ($I > 3\sigma_I$)	509
R(int)	0.1193
No. parameters refined	57
Largest ΔF peak, e$^-$/Å^3	2.0
Residuals[a]	
R	0.0267
R_w	0.0322

[a] $R = \Sigma||F_o| - |F_c||/\Sigma|F_o|$; $R_w = [\Sigma w(|Fo| - |Fc|)^2/\Sigma w(F_o)^2]^{1/2}$; $w = 1/\sigma^2(F_o)$.

Table 3-2. Atomic coordinates and isotropic displacement parameters for Ta_3SBr_7.

Atom	Position	x	y	z	B_{eq}[a]
Ta1[b]	2a	0.9643	0	0.6138	0.65(6)
Ta2	4b	0.1662(2)	0.2025(1)	0.6129(3)	0.63(4)
Br1	2a	0.6553(7)	0	0.393(1)	0.8(2)
Br2	2a	0.7111(7)	0	0.8380(8)	1.0(2)
Br3	2a	0.1327(7)	0	0.3444(8)	1.1(2)
Br4	4b	0.9638(5)	-0.2537(8)	0.8384(6)	1.0(1)
Br5	4b	0.8799(5)	-0.2539(8)	0.3454(5)	1.0(1)
S	2a	0.243(2)	0	0.886(2)	0.7(4)

Table 3-3. Anisotropic displacement parameters for Ta_3SBr_7.

Atom	U_{11}[c]	U_{22}	U_{33}	U_{12}	U_{13}	U_{23}
Ta1	0.009(1)	0.0087(8)	0.010(1)	0.0	0.0075(9)	0.0
Ta2	0.0088(6)	0.0074(5)	0.0112(6)	-0.0012(6)	0.0082(5)	-0.0007(6)
Br1	0.013(3)	0.011(3)	0.016(2)	0.0	0.013(2)	0.0
Br2	0.021(3)	0.010(3)	0.013(2)	0.0	0.014(3)	0.0
Br3	0.019(3)	0.013(3)	0.018(3)	0.0	0.016(3)	0.0
Br4	0.011(2)	0.014(2)	0.014(2)	0.005(2)	0.009(2)	0.0058(6)
Br5	0.011(2)	0.013(2)	0.014(2)	-0.006(2)	0.009(2)	-0.0069(5)
S	0.009(7)	0.009(6)	0.015(6)	0.0	0.010(6)	0.0

[a] $B_{eq} = (8\pi^2/3)\Sigma_i\Sigma_j U_{ij} a_i^* a_j^* \mathbf{a}_i \mathbf{a}_j$.
[b] Ta1 positional parameters fixed in x, z.
[c] $U_{ij} = \exp(-2\pi^2(a^{*2}U_{11}h^2 + b^{*2}U_{22}k^2 + c^{*2}U_{33}l^2 + 2a^*b^*U_{12}hk + 2a^*c^*U_{13}hl + 2b^*c^*U_{23}kl))$

Theoretical calculations

Extended Hückel electronic structure calculations[77] within the tight-binding approximation[78] were performed on the observed structures of Ta_3SBr_7 as well as on a hexagonal (Nb_3SBr_7 type) model structure. Default atomic orbital parameters[79] were iterated to charge consistency, and are listed in Table 3-4. Lattice energy calculations were performed which included two terms, the Madelung energy, U_{MAD}, and the Born-Mayer repulsion energy, U_{BM}. These terms can be expressed as follows:

$$U_{MAD} = 14.40 \sum_{ij} q_i q_j / r_{ij} \qquad (2)$$

$$U_{BM} = b \sum_{ij} (1 + q_i / r_i(0) + q_j / r_j(0)) \exp(-r_{ij} / \rho) \qquad (3)$$

Summations were carried out over all pairs of atoms $\{ij\}$ except when $i = j$. The scale factor b in the Born-Mayer term is determined by assuming the lattice energy calculated for each structure to be a minimum with respect to the shortest anion-cation distance R_0, i.e., $(\partial U_{LAT}/\partial R)|_{R=R_0} = 0$. As discussed later, twelve structures were investigated.

Table 3-4. Atomic orbital parameters for extended Hückel calculations on M_3SBr_7 (M = Nb, Ta).

Atom	Orbital	H_{ii} (eV)	ζ_1	C_1	ζ_2	C_2
	5s	-8.96	1.89			
Nb	5p	-4.99	1.85			
	4d	-9.83	4.08	0.6401	1.64	0.5516
	6s	-8.96	2.28			
Ta	6p	-4.99	2.24			
	5d	-9.83	4.76	0.6104	1.94	0.6104
S	3s	-20.00	2.12			
	3p	-13.30	1.83			
Br	4s	-22.07	2.59			
	4p	-13.10	2.13			

Since the scale factors for all twelve were nearly identical, an average value was calculated and used for all twelve. *r(0)* values are the "basic radii" for ions as defined by Bevan and Morris.[80] These values are: Ta, 0.72 Å; S, 1.84 Å; Br, 1.96 Å. Finally, ρ = 0.345 Å. The Madelung energy was evaluated using the Ewald method.[81]

Results and Discussion

Ta_3SBr_7 crystallizes in a new structure type, and is the first Ta compound in the M_3QX_7 system not isostructural with its Nb counterpart. However, the basic structural motifs present in Ta_3SBr_7 are quite similar to other 3-1-7 compounds. Figure 3-6 shows an approximate [010] view of two Ta_3SBr_7 slabs with the unit cell and anion sheet stacking sequence. Ordered, nearly close-packed mixed-anion sheets pack in an ...AB..., or ...*h*..., fashion, the same general anion stacking pattern observed in Nb_3SBr_7. The sulfur atoms occur only in every other mixed-anion layer (the "B" layer in Figure 3-6), and order in a hexagonal pattern commensurate with the location of the metal clusters. This ordering pattern is shown in Figure 3-7. Tantalum atoms reside in 3/4 of the octahedral holes in alternate layers, and cluster together to form the trinuclear clusters that hallmark all M_3QX_7 compounds. The Ta_3 clusters are always situated directly beneath, and so are capped by, the sulfur atoms. In Ta_3SBr_7, all of these Ta_3S "tetrahedra" are oriented in the same direction ([001]) throughout the structure, an arrangement which automatically precludes centrosymmetry.

As noted above, in both Nb_3SBr_7 and Ta_3SBr_7 the mixed anion layers pack in an ...AB... (...*h*...) fashion, with one M_3SBr_7 slab per unit cell. However, because of the presence of the triangular metal clusters, coupled with the suifur-bromine ordering in the anion layers, a shift in the stacking of successive Ta_3SBr_7 slabs causes the adoption of the new structure type in the tantalum system while maintaining the same general anion layer stacking sequence found in Nb_3SBr_7. In fact, as discussed in more detail later in this section, the Nb_3SBr_7 and Ta_3SBr_7 structure types represent the only two unique ways to stack M_3QX_7-type slabs while maintaining one slab per unit cell and ...AB... packing. The

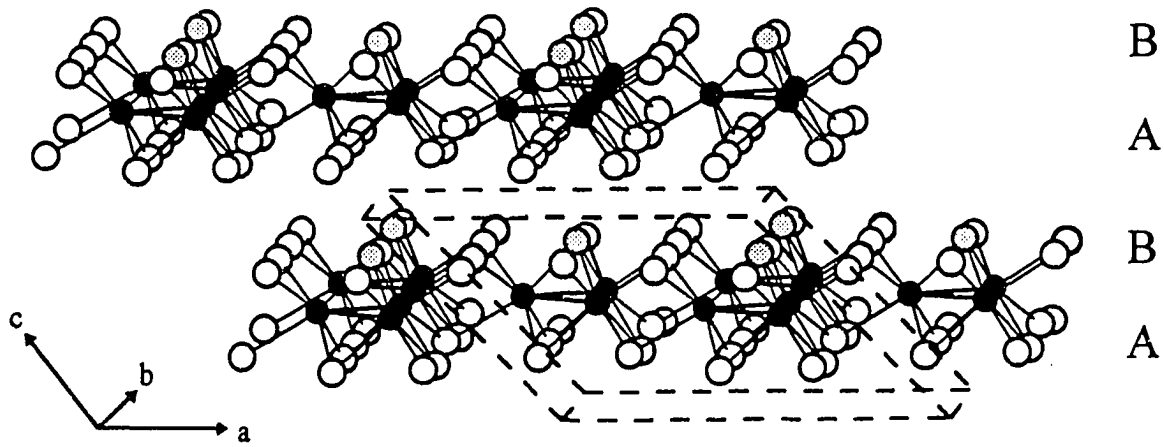

Figure 3-6. Approximate [010] view of two Ta_3SBr_7 slabs and the unit cell. The mixed-anion sheet stacking sequence is indicated also. Dark circles, Ta; Grey circles, S; open circles, Br.

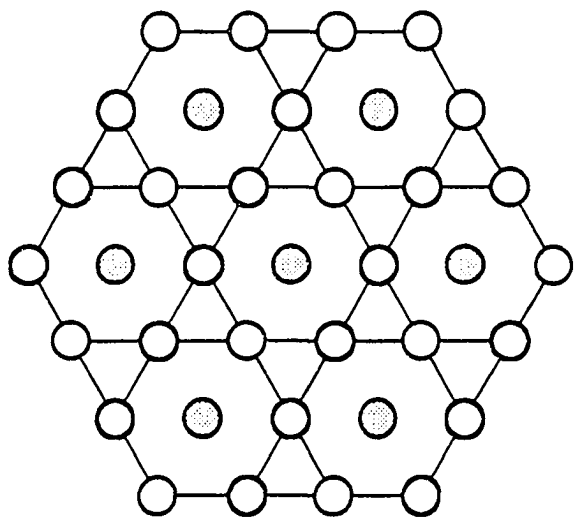

Figure 3-7. Ordering pattern formed by the anion layers in M_3QX_7. The positions of S or Br1 within the anion layers in Ta_3SBr_7 are shown as shaded circles.

construction of these two types is now described. Figure 3-8 shows one M_3QX_7 slab viewed down the stacking direction ([001]). The large dark circles constitute an "A" anion sheet, and the large open circles a "B" sheet. The unique atom (S) at the centers of the hexagonal spaces formed by the surrounding anion matrix are labeled, and the metal atoms are shown as small black circles. Bonds are omitted for clarity. The two one-slab structures are generated as follows:

1. Perfect superposition of like ordered anion sheets: each A (or B) sheet stacks directly over all other A (or B) sheets (perfect ...ABAB... pattern). Referring to Figure 3-8, and focusing on any sulfur atom in a "B" sheet, this corresponds to all sulfur atoms in every "B" sheet stacking directly above the sulfur atoms in all other "B" sheets. In essence, the sulfurs "line up" along the stacking direction, [001]. This stacking sequence generates the previously discovered Nb_3SBr_7 type. Successive Nb_3SBr_7 slabs are related to one another simply by a lattice translation in the stacking direction (see Figure 1-14, Chapter One).

2. Shifting of every other slab such that the "A" and "B" sheets in alternating slabs have moved to any one of the six available nearest neighbor "A" and "B" sites, respectively (ABA'B'). Again referring to Figure 3-8 and focusing on any sulfur atom in a "B" sheet, this corresponds to sulfur atoms in alternate slabs being situated above any one of the six adjacent "B" sites (light atoms) specified by arrows. The Ta_3 clusters follow the position of the sulfur. (Conceptually "moving" the appropriate layers in any of the six directions specified by the arrows in Figure 3-8 yields the same three-dimensional structure, but with a different relative orientation of the unit cell.) This stacking sequence generates the new monoclinic Ta_3SBr_7-type, where the cluster pattern is such that successive slabs are related to one another by the stacking vector [1/2 b + c], with two formula units per unit cell. Figure 3-9 shows two Ta_3SBr_7 slabs viewed down [001], with the projection of the unit cell.

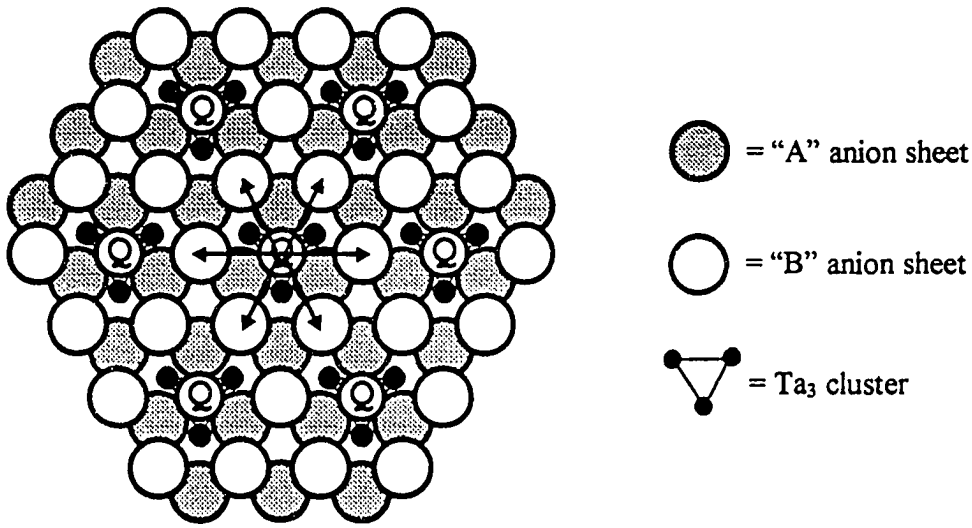

Figure 3-8. [001] view of a single $^{2}_{\infty}[M_3QX_7]$ slab. Large grey circles: "A" sheet (Br1, Br3, Br5). Large open circles: "B" sheet (Br2, Br4, S (= Q, labeled)). Small black circles: Ta_3 clusters.

Arrows indicate shifts of alternate slabs that generate the Ta_3SBr_7 structure while maintaining overall ...AB... stacking. (i.e., stacking an identical slab on top of the one shown so that the Q atom is at the terminus of one of the arrows results in the Ta_3SBr_7 structure.) See text for complete description.

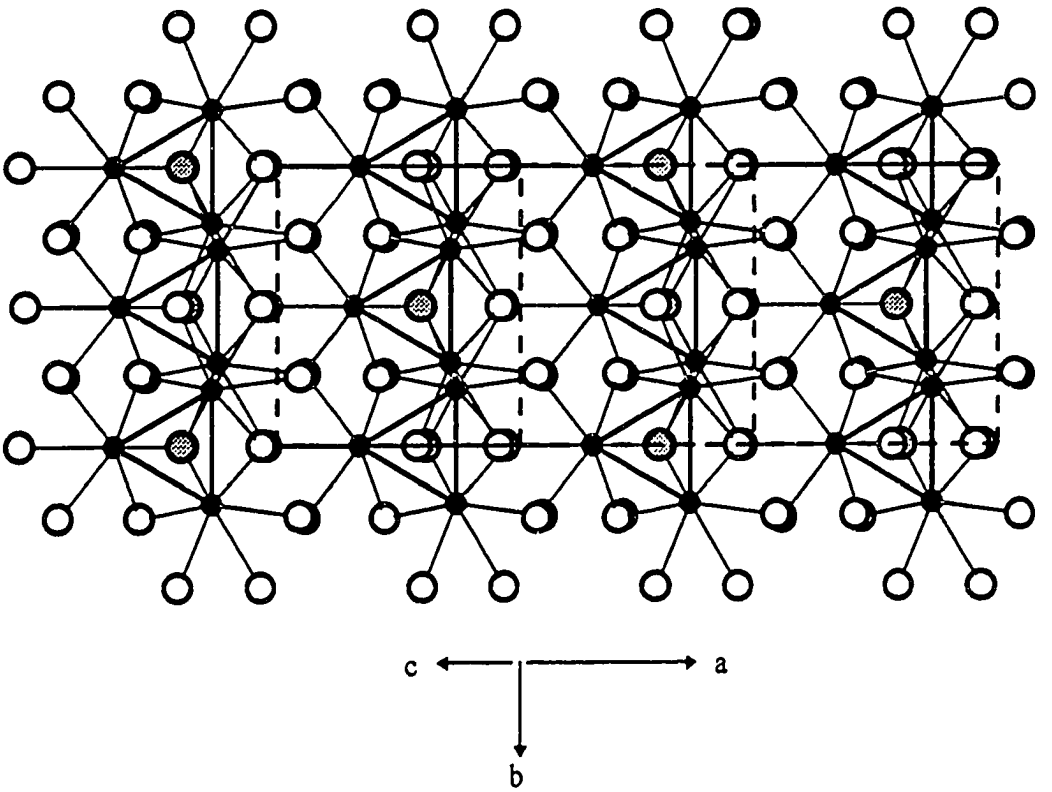

Figure 3-9. [001] view of Ta_3SBr_7. Ta, black circles; Br, open circles; S, grey circles.

A multitude of stacking modes involving multi-slab stacking and alternate orientations of the Ta_3Q_{cap} fragment is of course possible, but *within the constraint of one slab per unit cell*, these ordered sheets can stack only in the two unique ways described above. All other stacking possibilities result in a structure containing at least two slabs per unit cell. Why this is so can be seen by considering the following requirements for a one-slab M_3QX_7 structure, which both must be satisfied simultaneously:

1. (...AB...) stacking of the anion sheets. Clearly, more complicated stacking patterns (e.g. ABAC, ABCB) require a larger repeat unit.

2. Non-centrosymmetry. For M_3QX_7 systems, this implies unidirectional orientation of all M_3Q_{cap} fragments. If the M_3Q_{cap} fragments alternate direction throughout the structure, again the repeat unit must incorporate fragments from at least two slabs.

The simplicity of having only two stacking type choices obviously disappears when the possibility of more than one slab per unit cell and alternate orientations of the M_3Q_{cap} fragments are allowed. Allowing two slab per unit cell stacking, the number of possible structure types increases to 24. This number includes the one-slab Nb_3SBr_7 and Ta_3SBr_7 types, which can be thought of as a special subset of the larger two-slab set. Only three two-slab structures have been found: the Nb_3SeI_7, Nb_3TeBr_7, and α-Nb_3Cl_8-types. In a manner similar to how the structure of Ta_3SBr_7 was derived from that of Nb_3SBr_7 (see above), the structures of these 24 variants can also be derived. As proof of the existence of the 24 two-slab types, consider the following. Six non-equivalent sites surround each anion sheet atom. Two orientations of the Ta_3Q_{cap} units relative to those in the adjacent slabs ("ferroelectric" and "antiferroelectric") are possible. Finally, there are two possible unique rotational conformations of the slabs relative to one another (identity + six-fold rotation of the adjacent slab). Thus, 6 x 2 x 2 = 24 possible types. Of these 24, 12 display chemically unreasonable anion stacking sequences, involving directly superimposed atom sheets (i.e. an AA sequence), giving rise to trigonal prismatic sites in the van der Waals

gap. Such stacking has never been observed in these systems, or indeed in any system without an atom in the trigonal prismatic holes to hold the layers in this position (e.g., MoS_2). After discarding the 12 structures with ABBA, ABBC, or ABCA stacking, 12 feasible types remain. Representations of these 12 types are given in Figure 3-10. In this figure, only the spatial relationship of two metal triangles situated in adjacent slabs is shown in projection down the stacking direction [001]. A hexagonal unit cell is indicated in dashed line for comparison with Nb_3SBr_7. The anion sheet stacking sequence is given next to each projection, and the projections are divided into two classes, ferroelectric (unidirectional orientation of the Ta_3Q_{cap} dipole), and antiferroelectric (the Ta_3Q_{cap} dipole alternates direction from slab to slab).

In order to compare the relative energies of the possible two-slab structures, lattice energy calculations were performed. The Madelung energies were evaluated, and Born-Mayer repulsion terms were included to probe for small repulsive interactions between tantalum atoms which might drive adoption of a particular type. The hypothetical structures mimic actual M_3QX_7 slabs as far as reasonably possible. Within the slabs, however, slight deviations from the observed bond lengths were introduced due to the use of perfect close-packed anion sheets in the calculations. Actual M_3QX_7 compounds show slight disruptions due to metal clustering, as discussed further later. Ta-Ta and Ta-S distances were set equal to those observed in Ta_3SBr_7, and all others were within 0.1 Å of the observed distances. The distance between slabs (the van der Waals gap) was taken from that observed in Ta_3SBr_7. These slabs were then "stacked" to produce the twelve structures investigated. Since the slabs are identical, the calculated energies reflect interactions through the van der Waals gap rather than within the slabs.

Initially, Madelung energies alone were evaluated. These are listed in Figure 3-10. The results show a clear sorting of the structures into two classes, ferroelectric and antiferroelectric. In all cases, the six ferroelectric structures were favored (more negative Madelung energies). Such an arrangement maximizes the distance between the sulfurs,

Ferroelectric			Antiferroelectric		
Stacking	Structure	E_{Mad} (eV)	Stacking	Structure	E_{Mad} (eV)
ABCB (Nb_3SeI_7 type)	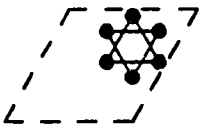	-138.453	ABCB	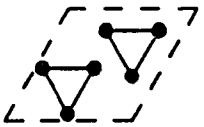	-137.763
ABAB (Nb_3SBr_7 type)	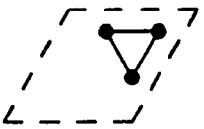	-138.266	ABAC	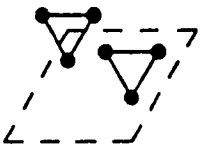	-137.763
ABAC	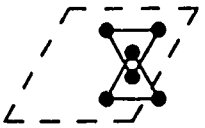	-138.240	ABAB (α-Nb_3Cl_8 type)	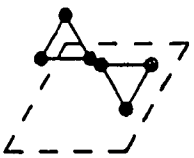	-137.682
ABAB (Ta_3SBr_7 type)	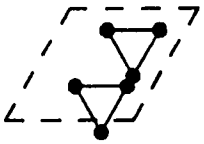	-138.096	ABAC	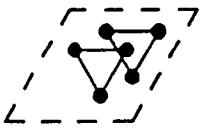	-137.650
ABCB	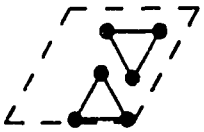	-138.062	ABCB	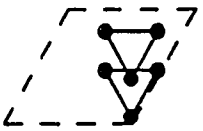	-137.650
ABAC	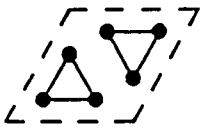	-137.923	ABAB	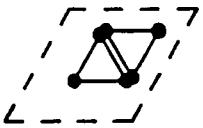	-137.641

Figure 3-10. Partial [001] projections of the twelve structures used in lattice energy calculations. Positions of the metal cluster sites in adjacent slabs are shown. Anion stacking sequences are given to the left of each projection, and calculated Madelung energies to the right.

reducing strong repulsion between the "hard" S^{2-} anions. Further inspection of the six favorable ferroelectric structures also suggests a preference for the slabs to align such that the more highly charged chalcogen anion to be as near as possible to the metal cations in the adjacent slab. Interestingly, the only observed M_3QX_7 compounds forming with an antiferroelectric structure are M_3QCl_7 (M = Nb, Ta; Q = Se, Te), implying greater importance of the Madelung term for the bromides and iodides, as suggested earlier.[42] The failure of the calculations to predict the Ta_3SBr_7 type as the most favorable of the twelve structures is not too disturbing, since the six lowest energy ferroelectric structures are separated by at most only 0.5 eV.

Next, the Born-Mayer repulsion term was taken into account. Including this term changed the energetic ordering of the structures, and is clearly the more important term for bromides. Ta_3SBr_7 is now the most favored of the observed structure types. Results are given in Figure 3-11.

Additionally, a series of extended Hückel calculations designed to determine relative energies of the two stacking variants and possibly rationalize the preference for monoclinic versus hexagonal stacking were carried out. A perfectly hexagonal M_3SBr_7 model slab was generated starting with the published Nb_3SBr_7 lattice parameters and atomic coordinates. However, to account for the slightly smaller lattice metrics and bond distances in Ta_3SBr_7, these Nb_3SBr_7 lattice parameter values were adjusted (shortened), and atomic coordinates were tuned until average Ta-Ta, Ta-S, and Ta-Br distances were achieved. From this model slab, the two different three-dimensional structures were built by specifying appropriate stacking vectors to give the hexagonal or monoclinic variants. The number of **k**-points was the same (32) in all calculations. The calculated total energy for the observed monoclinic structure was -1110.21 eV, and the total energy for the hypothetical Nb_3SBr_7-type hexagonal Ta_3SBr_7 was -1110.25 eV. Clearly, the calculation results show only negligible energetic differences (0.04 eV on scale of roughly 1000 eV) between the hexagonal and monoclinic stacking modes.

Ranking	Anion Stacking Sequence	[001] projection of the Ta_3 units	$E_{MAD} + E_{BM}$	Slab orientation
1.	ABAC	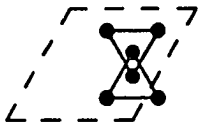	-80.102 eV	Ferroelectric
2.	ABCB	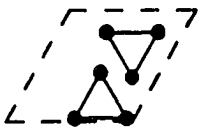	-80.031 eV	Ferroelectric
3.	ABAC	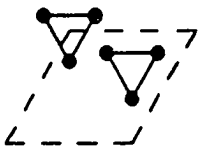	-79.796 eV	Antiferroelectric
4.	ABAB (Ta_3SBr_7 type)	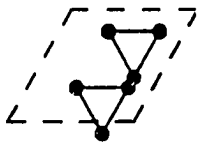	-79.766 eV	Ferroelectric
5.	ABAB (α-Nb_3Cl_8 type)	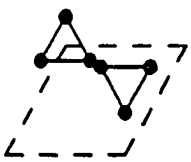	-79.717 eV	Antiferroelectric
6.	ABAB (Nb_3SBr_7 type)	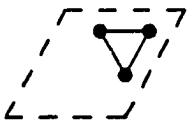	-79.299 eV	Ferroelectric
8.	ABCB (Nb_3SeI_7 type)	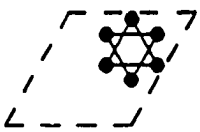	-79.039 eV	Ferroelectric

Figure 3-11. Energetic ranking of the important structures as derived from the lattice energy calculations. The energies in the fourth column represent the sum of the Madelung term and the Born-Mayer term.

The stacking mode in Ta_3SBr_7 prohibits the possibility of hexagonal symmetry. The three-fold axis and two of the three mirror planes centered on the M_3SBr_7 cluster unit in the hexagonal case are lost: the local cluster point symmetry drops from C_{3v} to C_s, with the one remaining mirror plane dividing the cluster into two sets of crystallographically inequivalent atoms. The cluster unit and atom labeling scheme are shown in Figure 3-12. However, within or very close to being within experimental error, all Ta-Ta and Ta-S bond distances are equal: Ta1-Ta1, 2.862(2) Å; Ta1-Ta2, 2.864(2) Å; Ta1-S, 2.44(2) Å; Ta2-S, 2.36(1) Å. Ta-Br distances follow this trend also. The triangular cluster is still nearly equilateral: ∠Ta1 = 60.04(6)°, ∠Ta2 = 59.98(3)°. Other relevant bond distances and bond angles are listed in Table 3-5.

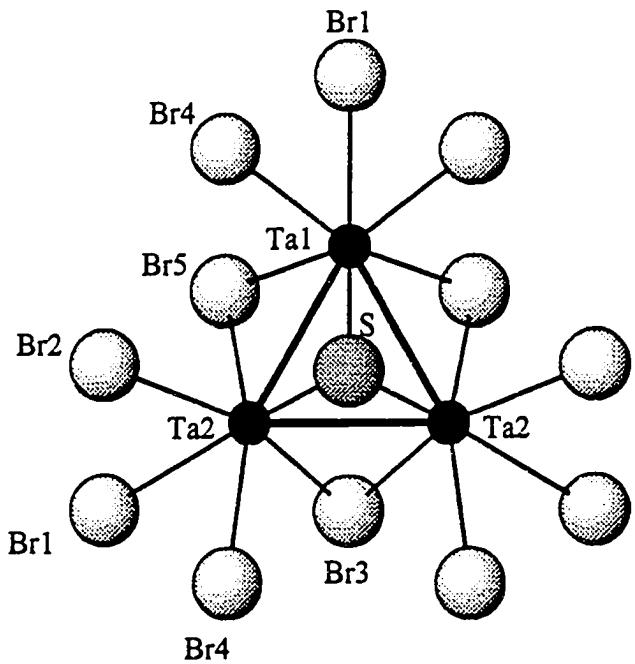

Figure 3-12. Ta_3SBr_7 cluster atom labeling scheme, view down [001]. A mirror plane bisects Br1, Ta1, S, Br3. Small black circles, Ta; large grey circle, S; large open circles, Br.

Table 3-5. Comparison of bond distances in Ta_3SBr_7 and Nb_3SBr_7 (Å), and selected bond angles in Ta_3SBr_7 (deg).

Ta_3SBr_7		Nb_3SBr_7	
Ta1 - Ta2	2.862(2)	Nb - Nb	2.896
Ta2 - Ta2	2.864(2)		
Ta1 - S	2.44(2)	Nb - S	2.410
Ta2 - S	2.36(1)		
Ta1 - Br1	2.793(7)	Nb - Br1	2.804
Ta2 - Br1	2.801(4)		
Ta1 - Br5	2.545(5)		
Ta2 - Br5	2.532(4)	Nb - Br2	2.544
Ta2 - Br3	2.545(5)		
Ta1 - Br4	2.678(5)		
Ta2 - Br4	2.681(5)	Nb - Br3	2.687
Ta2 - Br2	2.673(3)		

(Horizontal dashed lines separate sets of bonds rendered inequivalent when compared to Nb_3SBr_7 by the lower symmetry of Ta_3SBr_7)

Bond Angles in Ta_3SBr_7

Ta2 - Ta1 - Ta2	60.04(6)	Ta1 - Br1 - Ta2	97.6(2)
Ta1 - Ta2 - Ta2	59.98(3)	S - Ta1 - Br1	165.1(4)
Ta1 - S - Ta2	73.2(4)	S - Ta2 - Br1	162.7(3)
Ta2 - S - Ta2	74.7(4)	Br4 - Ta2 - Br5	162.1(1)
Ta1 - Br5 - Ta2	68.6(1)	Br4 - Ta1 - Br5	162.2(2)
Ta2 - Br3 - Ta2	68.5(1)		

To probe for possible electronic reasons for the small deviations from trigonal symmetry, extended Hückel calculations were carried out on a hypothetical monoclinic Ta_3SBr_7 where the slight crystallographic inequivalencies were removed, and individual slabs were restored to hexagonal symmetry. The complete three-dimensional structure still has monoclinic symmetry because of the slab stacking mode. The overlap populations of all Ta-Ta and Ta-S bonds in this hypothetically undistorted monoclinic Ta_3SBr_7 were exactly equivalent, implying that the slight distortions away from C_{3v} cluster symmetry result from a mild (in fact nearly negligible) "relaxation" of the structure when hexagonal symmetry constraints are removed upon lowering to monoclinic symmetry.

In order to approach each other closely enough to achieve the Ta-Ta bond distances mentioned above, the tantalum atoms are displaced from the centers of their octahedral sites toward the centroid of the resultant cluster. These displacements affect the surrounding anion layer network: The atom in the anion layer ("B" sheet) directly above the three clustered metals (the capping chalcogen atom) is "squeezed" up into the van der Waals gap to minimize repulsion from the tightly bound triangle beneath it. Simultaneously, a halide (Br1) is drawn into the metal atom layer in compensation for the space left by the displaced metal atoms. The result of these anion displacements (driven by the formation of the metal triangle) is a topographical pattern of elevations on the top side of each M_3QX_7 slab and indentations on the underside. These corrugations occur in all M_3QX_7 compounds, as well as in Nb_3X_8. In the parent $Cd(OH)_2$ structure, of course, no metal-metal bonding exists; each Cd atom sits exactly in the center of its octahedral hole, and the anion layers are flat. Atomic Force Microscopy (AFM) experiments performed on the binary halides Nb_3X_8 (X = Cl, Br, I) yielded images of one surface of a slab, probably the surface containing the X_{cap} atom, where a similar elevation of the capping halide was observed.[82]

In Ta_3SBr_7, the sulfur atoms lie 0.297 Å above the surrounding Br2 + Br4 layer, and Br1 is lifted 0.302 Å into the metal layer. It is interesting to note that in Ta_3SBr_7, successive slabs are stacked so that the "bumps" caused by the protruding S atoms on the top side of a slab correlate with the indentations caused by the lifting of Br1 into the

underside of the adjacent slab. However, it is unlikely that this is the reason for the particular stacking mode in Ta_3SBr_7. Nb_3SBr_7 shows the same bumps/depressions, but crystallizes so that the sulfurs directly abut a flat surface. Furthermore, no preferred fitting is observed even in compounds where, because of different relative sizes of chalcogen and halide, the bumps and depressions are even more pronounced. For example, in Ta_3TeI_7, the large Te^{2-} anions protrude 0.55 Å above the surrounding iodide layer, yet no correlation of these contours is observed. In Nb_3TeCl_7 [42] and Ta_3TeCl_7 (see Chapter Four), where the chalcogen/halogen size ratio is largest, a centrosymmetric structure forms where the elevated Te atoms share the same van der Waals gap space.

The above considerations underscore the subtlety of the factors governing the formation of particular polytypes: the effect of entropic terms and hard-to-control experimental details like pressure in the reaction tube, or unwanted (but everpresent) temperature gradients, lack of knowledge about nucleation and crystal-growth mechanisms, all of which are difficult to quantify. Most likely, an interplay between very small energetic and entropic effects beyond the scope of our calculations determines the various stackings of the weakly interacting M_3QX_7 slabs in such layered compounds. This suggests that, upon finding the right conditions, polymorphism may be observed in these systems. In an attempt to investigate temperature effects on the formation of different polytypes, crystals of Nb_3SBr_7 were grown in our lab at temperatures of 450°C, 600°C, and the reported 800-750°C transport conditions. Nb_3SBr_7 was chosen because Ta_3SBr_7 thermally decomposes into Ta_6Br_{15}, $TaBr_5$ and TaS_2 above ca. 575°C, so its temperature stability region offers less flexibility than does Nb_3SBr_7. Several Nb_3SBr_7 crystals from each reaction temperature were chosen. All reproduced the published hexagonal structure, as determined by single crystal x-ray diffraction.

Tantalum and niobium are well-known for their often indistinguishable behavior at moderate temperatures, and the departure of Ta_3SBr_7 from the structural model set by Nb_3SBr_7 is unusual. This sulfide bromide pair offers an interesting opportunity for a mixed-metal study, namely $Ta_{3-x}Nb_xSBr_7$ ($0 \leq x \leq 3$). Which of the two structures will be preferred? Will the relative amounts of each metal play a role? Although a tantalum-rich

system might be expected to adopt the Ta_3SBr_7 structure and a niobium-rich system the Nb_3SBr_7 structure, a composition around $Nb_{1.5}Ta_{1.5}SBr_7$ might yield unexpected results. Such a system was explored, and the results are given in Chapter Five of this thesis.

CHAPTER FOUR
NEW TANTALUM CHALCOGENIDE CHLORIDES

Introduction

Chlorine is the smallest and most electronegative halogen under consideration here, and chloride compounds should be expected to differ from the larger halide compounds in that the chloride will introduce more hard ionic character into the compound. "Ionic" here refers to a greater degree of charge localization due to the greater electronegativity of Cl, and a greater separation of energy levels (larger band gap). Chlorides seem to be less readily incorporated into complicated structures, possibly due to the greater relative stability of binary alternative products. Systems composed of increasingly "hard" anions (S/Cl > Se/Cl > Te/Cl > Q/Br > Q/I) show a much greater proportion of simple binary phases to more structurally "delicate" ternary ones.

α-Nb_3Cl_8 and Nb_3TeCl_7 are the chloride phases reported for niobium most relevant to this thesis. Both adopt the α-Nb_3Cl_8 structure, described in Chapter One and in greater detail below. Nb_3SCl_7 and Nb_3SeCl_7 apparently have not been synthesized.

Tantalum chalcogenide chlorides, Ta_3QCl_7 (Q = S, Se, Te)

General note on synthesis of Ta_3QCl_7

Due to handling inconveniences associated with gaseous elemental chlorine and the ease and equal suitability of using $TaCl_5$ in this research, the latter was employed as the halide source in all syntheses of tantalum chalcogenide chlorides described below. Purification of commercial $TaCl_5$ is essential due to inevitable contamination by oxides and oxychlorides. $TaCl_5$ was separated from common impurities like $TaOCl_3$ and Ta_2O_5 by repeated sublimations at 150°C in a static vacuum. The purifed $TaCl_5$ was then handled in an Ar-filled glove box exclusively.

The general reaction to form the chalcogenide chlorides is:

$$8\ Ta + 7\ TaCl_5 + 5\ Q = 5\ Ta_3QCl_7 \quad (Q = S, Se, Te) \qquad (1)$$

The $TaCl_5$ is reduced by elemental Ta in the presence of chalcogen at the appropriate temperature to yield the ternary phase.

Ta_3TeCl_7

Synthesis and characterization

The highest yields of pure Ta_3TeCl_7 can be obtained by reactions according to Equation (1) at temperatures from 500°C to ca. 550°C, for a duration of two weeks. Nearly quantitative conversion of the starting materials is achieved using these conditions. Ta_3TeCl_7 will form at lower temperatures, but reaction time necessary to produce a good yield of Ta_3TeCl_7 is increased significantly, and transport of the pure crystalline solid is diminished. 550°C appears to be the upper stability limit of Ta_3TeCl_7. Above ca. 550°C, Ta_3TeCl_7 is not observed; instead, the binaries $TaCl_5$, Ta_6Cl_{15} and $TaTe_2$ are the only compounds observable by x-ray powder diffraction.

Ta_3TeCl_7 generally forms as large batches of black, reflective, densely intergrown crystals that grow prodigiously at the far (presumably cooler) end of the reaction tube. Such transport occurs even when efforts to smooth out temperature gradients are made. Since the exercise of trying to remove any magnitude of temperature gradient is one of utter futility, efforts were made only to minimize such thermal inhomogeneities as much as possible. Indeed a small gradient helps separate the pure crystalline solid from starting materials and intermediate phases, and Ta_3TeCl_7 can be purified by "sublimation". Grinding crude Ta_3TeCl_7 and then heating the powdered sample in vacuo through a small temperature gradient (within ±25°C of 500°C, with a 5 to 10° imposed temperature gradient) nicely transports pure crystalline solid. Ta_3TeCl_7 crystals display a clear hexagonal morphology, forming as flat, reflective, hexagonal plates. Figure 4-1 shows SEM micrographs of crystalline Ta_3TeCl_7. Single crystals can grow to quite large

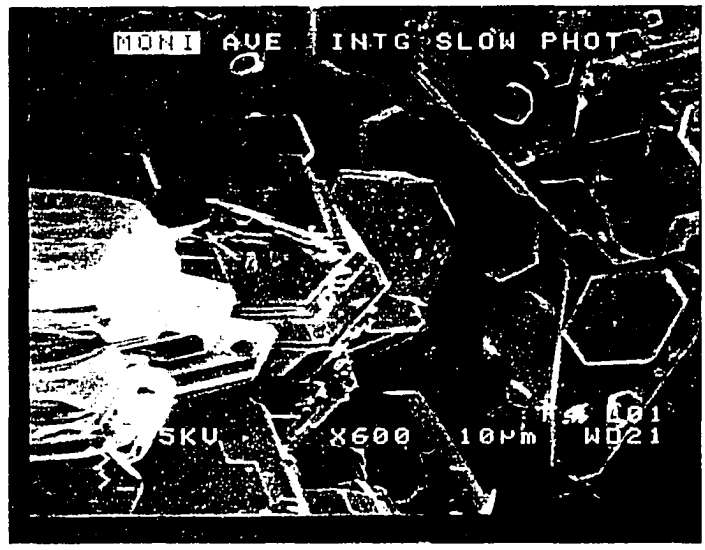

(a)

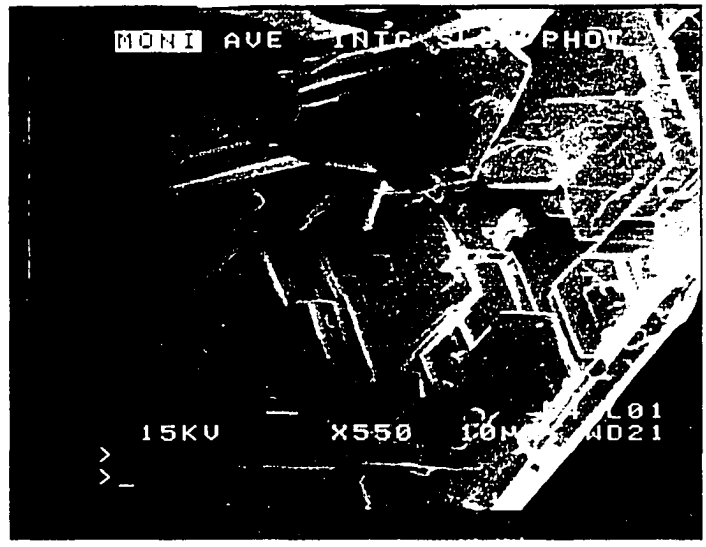

(b)

Figure 4-1. Two SEM images of Ta_3TeCl_7 , showing the broad, flat hexagonal plate morphology, and the stacking of crystallites.

dimensions, up to 3 mm across. Though such large crystals as well as the bulk solid both appear black, Ta_3TeCl_7 is actually dark green. Crystals of the compound become transparent olive-green when extremely thin. Interestingly, Nb_3Cl_8 is reported to be a dark green color; no mention is made of the color of Nb_3TeCl_7. Ta_3TeCl_7 grinds with a lubricating feel to a green powder. Ta_3TeCl_7 is air-stable apparently indefinitely, and is also unaffected by immersion in water and organic solvents. Non-oxidizing acids act slowly on the compound, eventually decomposing it to an uncharacterized white powder after a few days. Oxidizing acids decompose the compound immediately.

The Guinier powder diffraction pattern of Ta_3TeCl_7 indicated it to be isostructural with Nb_3TeCl_7. However, notwithstanding the readiness with which Ta_3TeCl_7 will form single crystals, high-quality crystals of Ta_3TeCl_7 were difficult to come by. The best crystal was obtained from a reaction at 500°C for two weeks. Many other efforts, incuding initial reactions and heating powders of pure, premade Ta_3TeCl_7 under a wide set of conditions also yielded numerous single crystals. Most of these diffracted poorly, exhibiting broad, poorly-shaped diffraction maxima (greater than 1° wide, asymmetric), indicative of misstacked, poorly aligned sections of the crystals. A suitable crystal was finally selected, mounted in a capillary, and aligned on a Siemens P4 diffractometer for intensity data collection. The diffraction peak widths ranged from 0.4° to 1°, but were Gaussian in shape. Unit cell parameters were determined by indexing 35 reflections with $9° \leq 2\theta \leq 25°$. 792 reflections were collected, to $2\theta_{max} = 45°$ at a temperature of 296 K. No significant decay in intensity was observed. The data were corrected for Lorentz and polarization effects during the data reduction process, and later an empirical correction for absorption using azimuthal ("psi") scans of several reflections was applied. The structure was easily solved using direct methods[68] and refined using SHELXL-93.[83] Structure solution was straightforward, using isostructural Nb_3TeCl_7 as a model.[42] Table 4-1 contains a summary of the crystallographic data relevant to structure determination and refinement. Atomic positional parameters and isotropic displacement parameters are given in Table 4-2. More accurate lattice constants were achieved by refining Guinier powder diffraction data. A sample of Ta_3TeCl_7 was ground thoroughly in an Ar-filled glove box,

Table 4-1. Summary of crystallographic data for Ta_3TeCl_7

Formula weight	918.60
Crystal system	Trigonal
Space group	$P\bar{3}m1$ (No. 164)
Color of crystal	black
Dimensions of crystal (mm)	0.2 x 0.2 x 0.05
Lattice parameters (Å)	
a	6.851(10)
c	12.661(3)
Vol. (Å^3)	514.6(2)
Z	2
d_{calc} (g cm^{-3})	5.928
Diffractometer	Siemens P4
Radiation	Mo Kα, λ = 0.71071 Å
Linear absorption coefficient	36.34 mm^{-1}
Transmission ranges	0.87-1.0
Temperature of data collection	23°C
Scan method	ω scan
Range in *hkl*	$-1 \leq h \leq 7$
	$-7 \leq k \leq 1$
	$-1 \leq l \leq 13$
$2\theta_{max}$ (deg)	45.00
Number refl. measured	704
No. observed ($I > 2\sigma_I$)	296
No. unique observed	219
R(int)	0.0800
No. parameters refined	26
Difference map (e$^-$/Å^3)	
Largest peak	2.033
Largest hole	-1.671
Residuals[a]	
R	0.0374
R_w	0.0686
GoF	1.120

[a] $R = \Sigma||F_o| - |F_c||/\Sigma|F_o|$; $R_w = [\Sigma w(|Fo| - |Fc|)^2/\Sigma w(F_o)^2]^{1/2}$; $w = 1/\sigma^2(F_o)$.

Table 4-2. Atomic coordinates and isotropic displacement parameters for Ta_3TeCl_7.

Atom	Position	x	y	z	U_{eq}
Ta	6i	0.52716(10)	-x	0.75982(10)	0.0069(4)
Te	2d	2/3	1/3	0.5909(3)	0.0097(9)
Cl1	2d	1/3	2/3	0.8668(10)	0.007(3)
Cl2	6i	0.8322(5)	-x	0.8855(6)	0.008(2)
Cl3	6i	0.1662(5)	-x	0.6609(6)	0.010(2)

with silicon powder added as an internal standard. Ground glass was also added to aid in the powdering process. Using the angular positions of 25 lines measured from a Guinier film, the lattice constants of Ta_3TeCl_7 were refined. The results are given in Figure 4-2, along with the powder diffraction pattern generated from the single crystal solution. The lattice constants and Guinier pattern of α-Nb_3Cl_8 and Nb_3TeCl_7 are also given in this Figure.

Further characterization: Magnetic susceptibility

One large solid crystalline sample of Ta_3TeCl_7 was glued in air inside a straw for magnetic susceptibility measurements. The susceptibility was measured using a SQUID magnetometer, from 6 - 300 K at a field strength of 3 T. The sample showed the same weak paramagnetic signal observed in all M_3QX_7 compounds, the meaning of which has not been satisfactorily explained. A room temperature moment of 1.91 BM was measured. The magnetic susceptibility data are shown in Figure 4-3.

Structure description

Ta_3TeCl_7 is isostructural with Nb_3TeCl_7, adopting the centrosymmetric α-Nb_3Cl_8 structure in which nearly close-packed mixed anion sheets stack in an ...AB..., or ...*h*... fashion, and triangular tantalum clusters interleave alternate sheets. Both structures can

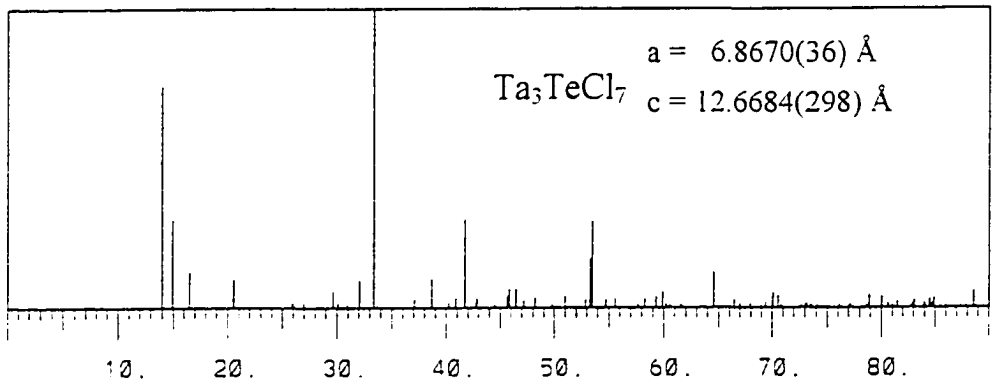

(a)

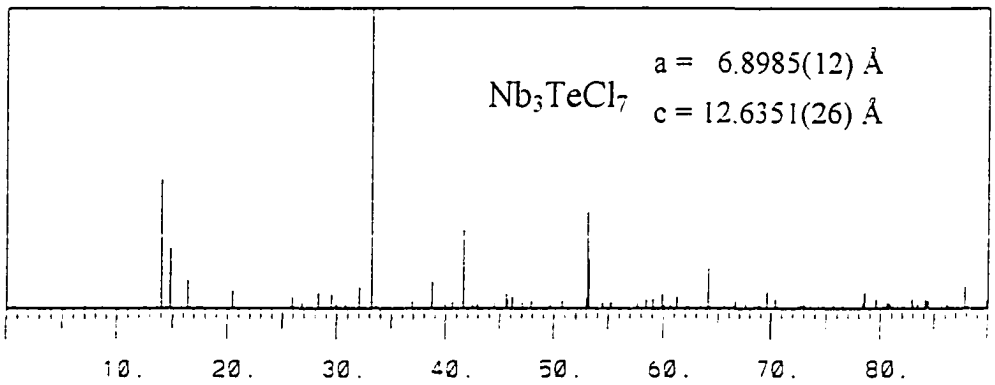

(b)

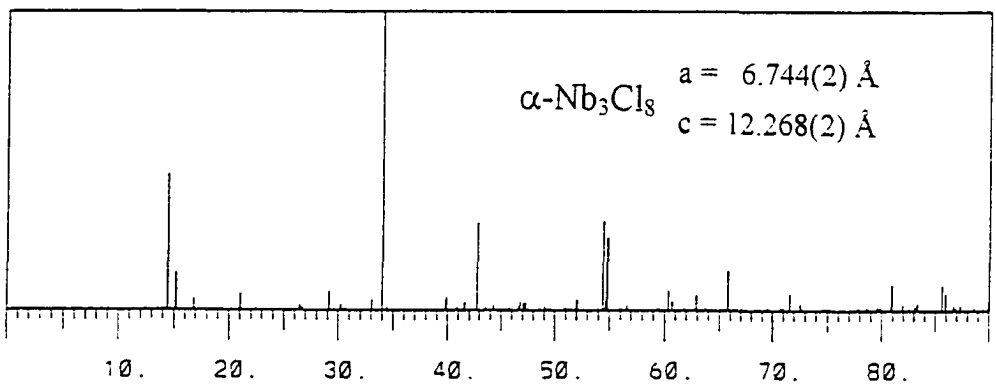

(c)

Figure 4-2. (a) Generated powder pattern for Ta_3TeCl_7, with lattice parameters as refined from powder data. (b) Powder pattern and refined lattice parameters for Nb_3TeCl_7. (c) α-Nb_3Cl_8 powder pattern and lattice parameters. The abscissa corresponds to degrees 2θ.

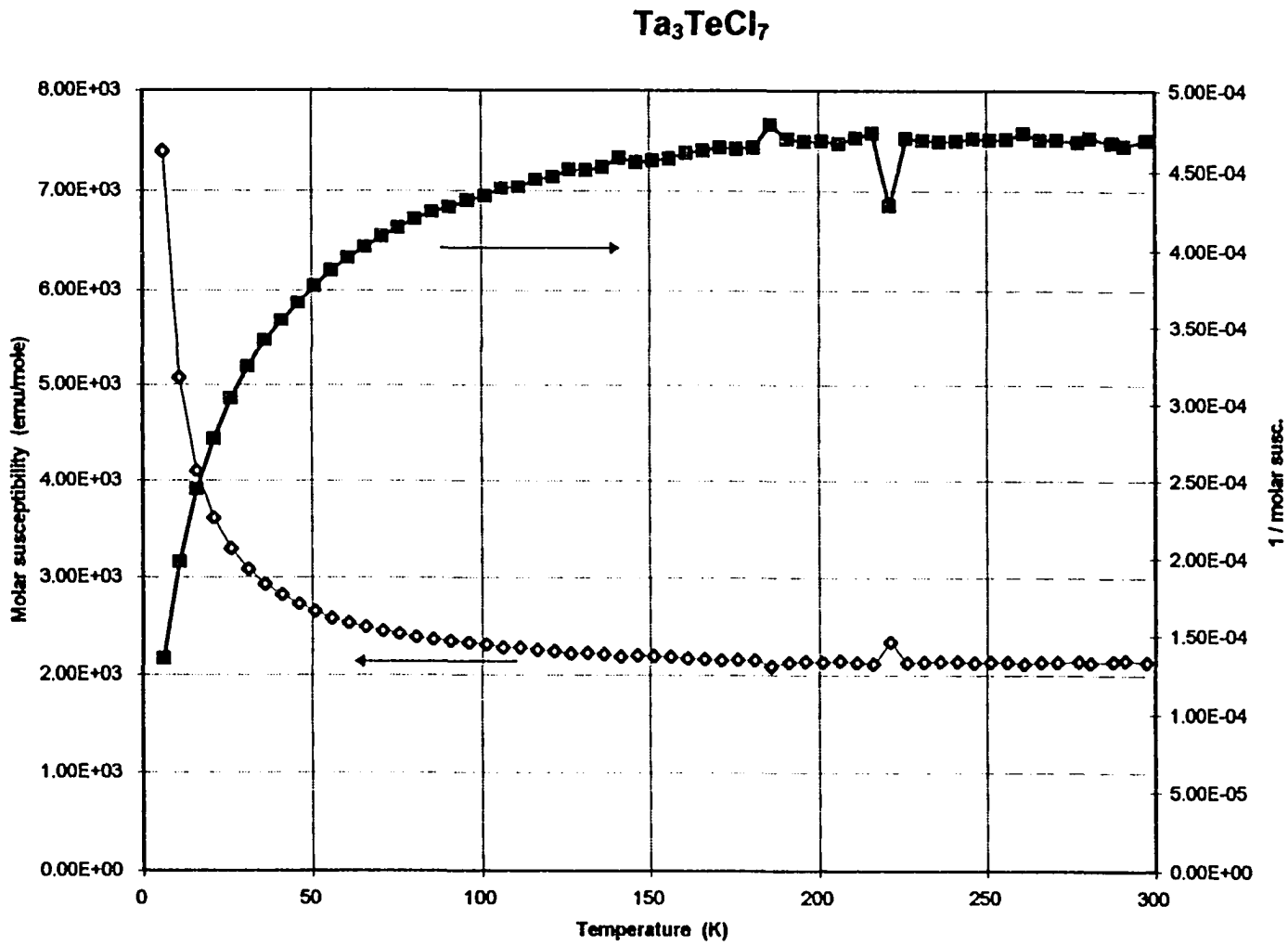

Figure 4-3. Magnetic susceptibility data for Ta_3TeCl_7.

be viewed as chalcogen-substituted α-Nb_3Cl_8 derivatives. In Ta_3TeCl_7, the anion sheets stack such that two adjacent layers are mixed Te/Cl sheets, then the next two sheets consist of only chloride, then two more mixed sheets, and so on. The metal clusters are sandwiched between a mixed sheet and an unmixed sheet, and follow the position of the tellurium atom, which always acts as the cluster capping atom. In the mixed Te/Cl sheets, the telluriums are surrounded by six Cl atoms, never by another Te. The chloride anions are arranged in a Kagome net (the same pattern described in reference to Ta_3SBr_7, Chapter Three, Figure 3-7), the large hexagonal spaces of which are occupied by Te. Structural diagrams of the α-Nb_3Cl_8 type can be found in Chapter One, Figure 1-12. As occurs in all M_3QX_7 compounds and also in Nb_3X_8, the cluster capping atom situated above the clusters and the $\mu_3{}^a$ anion situated below the clusters are both displaced above their respective surrounding anions as a response to clustering. In Ta_3TeCl_7, the tellurium atoms are pushed up by a distance of 0.887 Å. This is the largest capping chalcogen displacement of any of these compounds, and is due to the large anion size mismatch. Elevation of the large Te^{2-} anions is enhanced by the surrounding dense network of hard Cl^- ions. Cl1 is displaced 0.237 Å, pulled into the metal layer. Due to the centrosymmetric stacking in Ta_3TeCl_7, these protruding Te atoms share the same van der Waals space, at a minimum distance of 4.577 Å from each other. The other van der Waals gap is bookended by the sheets containing Cl1 and Cl3 atoms, and features indentations caused by the displacement of Cl1 into the metal layers.

The Ta-Ta distance in Ta_3TeCl_7, 2.867(2) Å, is the shortest of any 3-1-7 compound characterized yet. This is clearly a halide matrix effect, with the small size of the chlorides allowing closer proximity of the tantalum atoms. When embedded in a matrix of larger anions, like iodides as in *hc*-Ta_3TeI_7, the Ta-Ta distance is 3.004(2) Å. Ta-Ta, Ta-Te and Ta-Cl bond distances are listed in Table 4-3, with selected bond angles. Bond distances in Nb_3TeCl_7 are also given, and reflect the usual trend in isostructural niobium and tantalum compounds: tantalum-tantalum distances are slightly shorter than the corresponding niobium-niobium distances, while metal-anion distances are similar.

Table 4-3. Bond distances (Å) and selected bond angles (deg) for Ta_3TeCl_7. Distances in Nb_3TeCl_7 are included for comparison.

Ta-Ta	2.867(2)	Nb-Nb	2.898(1)	Ta-Ta-Ta	60.00
Ta-Te	2.704(3)	Nb-Te	2.700(1)	Ta-Te-Ta	64.03(9)
Ta-Cl1	2.669(6)	Nb-Cl1	2.672(1)	Ta-Ta-Te	57.98(4)
Ta-Cl2	2.425(5)	Nb-Cl2	2.416(1)	Ta-Cl2-Ta	72.5(2)
Ta-Cl3	2.496(4)	Nb-Cl3	2.515(1)	Ta-Cl1-Ta	96.5(3)

Ta_3SeCl_7

Synthesis and characterization

Several reactions according to Equation (1), and re-heatings of the products of these reactions were carried out, in the temperature range 450 to 575°C. Details of the experimental conditions of all these reactions are tabulated in Appendix A. By far the most abundant material left in all Ta_3SeCl_7 tubes is unreacted Ta metal and $TaCl_5$. $TaSe_2$ and Ta_6Cl_{15} were also observed. Ta_3SeCl_7 forms in low yield as a thin grey coating of the tube wall, at temperatures of 500 to 550°C. This material was initially identified by Guinier powder x-ray diffraction. The powder pattern is identical to that of Ta_3TeCl_7, but the diffraction line positions are shifted to greater 2θ, indicating the material has a structure similar to Ta_3TeCl_7, but with a smaller unit cell. This analysis is consistent with what would be expected upon replacing Te with the smaller chalcogen Se. A sample of the grey film that gave the Ta_3SeCl_7 powder pattern was analyzed for elemental content using SEM. The SEM confirmed the presence of Ta, Se and Cl and provided magnified images of the crystallites that make up the film. These are shown in Figure 4-4. Small areas of individual crystallites were sampled to insure the elemental identification was from a pure sample and not contributions from $TaSe_2$ and Ta_6Cl_{15}. The trigonal morphology of the crystallites is evident from the micrographs.

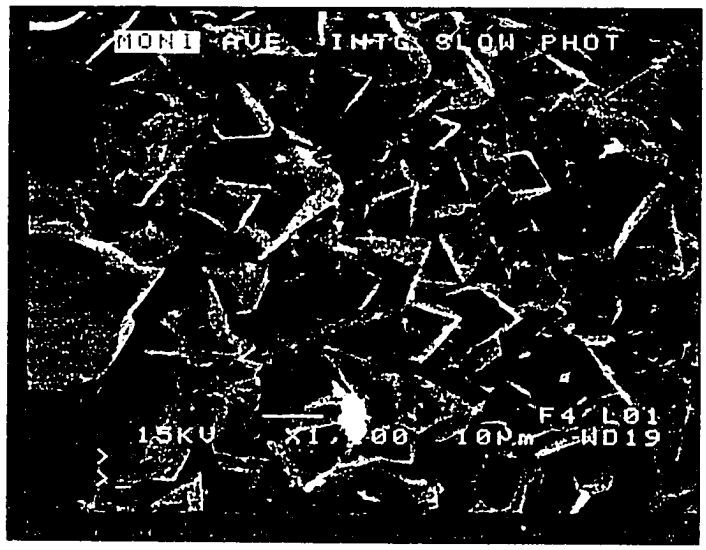

(a) 1100x magnification of a Ta_3SeCl_7 film, showing the trigonal morphology of the crystallites.

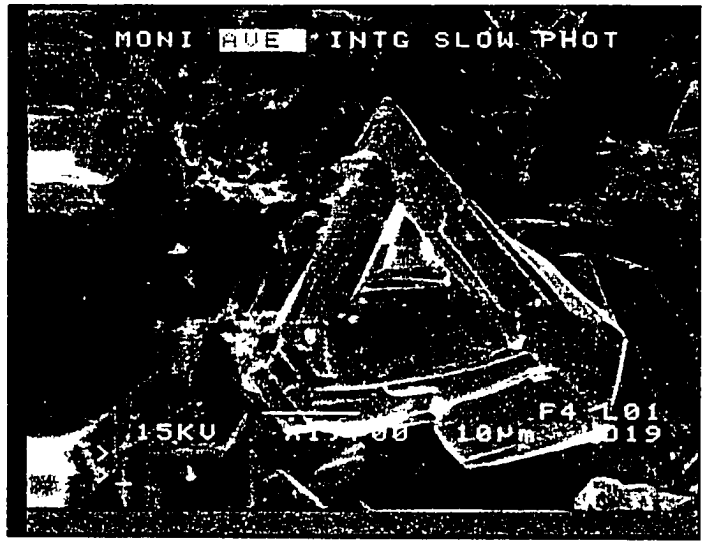

(b) Higher magnification of a Ta_3SeCl_7 crystallite.

Figure 4-4. SEM images of Ta_3SeCl_7 synthesized at 500°C.

Ta_3SeCl_7 crystal-growing efforts: All attempts were via high-temperature annealing or transport, starting from finely ground products from initial Ta_3SeCl_7 reactions. Samples were heated both with and without an imposed temperature gradient. Despite many such efforts, Ta_3SeCl_7 refused to to grow larger crystals or even larger amounts of bulk powder.

Ta_3SCl_7

There is no evidence at all for Ta_3SCl_7. Several reactions according to Equation (1) in the usual temperature range (400 to 550°C) yield only $TaCl_5$, Ta_6Cl_{15}, TaS_2, Ta metal, and an air-sensitive yellow-orange solid. Appendix A lists all reactions and re-heatings of composition Ta_3SCl_7 attempted. The identity of the yellow-orange solid has not been determined. All reports of "$TaSCl_3$" (Chapter One) mention it to be an air-sensitive yellow powder; however all efforts to grow crystals by slow-cooling or extended heating failed. The material appears to be amorphous, as it does not yield a Guinier diffraction pattern, which at least could be compared to the suggested structural models for "$TaSCl_3$" ($NbOCl_3$ and $MoOBr_3$, see Chapter One). No attempts to further characterize this phase were made.

CHAPTER FIVE
TANTALUM-NIOBIUM MIXING STUDIES

Introduction

There have been several diverse Ta-Nb mixing studies reported.[14, 84-93] These studies often show a complete substitutional range of metals, but some systems have shown definite limits to the amount of one metal that can be substituted into the system. Most interesting are changes in structure that can occur upon substitution, notwithstanding the close similarities of behavior of Ta and Nb. The system $Nb_xTa_{1-x}Te_4$ has received much attention,[84] and belongs to the class showing complete solubility of one metal onto the other (i.e. $x \in (0,1)$). The end-member phases $NbTe_4$ and $TaTe_4$ are both known, and form tetragonal structures that can be assigned to space group P4/ncc (subcells). Of interest in these systems is the superstructure, which differs. At room temperature, $NbTe_4$ forms an incommensurately modulated superstructure, while $TaTe_4$ forms a commensurately modulated one. The mixed system $Nb_xTa_{1-x}Te_4$ shows a complete range of solubility between $NbTe_4$ and $TaTe_4$, and the average structure (the subcell) is that of the binaries. The superstructure that results in the mixed-metal system has been shown to be composition dependent, with the Nb-rich end adopting the $NbTe_4$ superstructure, and vice versa. An example of a system which is not stable over all compositional ranges is $Nb_xTa_{2-x}Te_3$. Harbrecht, et al., studied the stability limits of the system $Nb_xTa_{2-x}Te_3$ after their discovery of the binary telluride Ta_2Te_3. They found that niobium could be stabilized in the structure to a limiting composition $NbTaTe_3$ ($x = 1$).[85] Attempting to incorporate more niobium led to formation of $NbTe_2$ and Nb_3Te_4 as side products, along with $Nb_xTa_{2-x}Te_3$. Nb_2Te_3 is still unknown. A substantial part of the Ta-Nb substitutional chemistry known is due to Franzen, et al., who have studied several metal-rich compounds in the tantalum-niobium-sulfur system.[14, 86-89] Several Ta-Nb-S phases were synthesized at extremely high temperatures in an arc melter, and also subsequently annealed at high (up to ~1400°C) temperature. The compounds were found

to adopt structures with extensive metal-metal interactions, often containing elemental bcc-like metal cluster fragments with Ta and Nb mixed onto the same crystallographic sites. However, in these systems, the distribution of Nb and Ta over the various metal positions in these sometimes complex structures was not completely random. Preferential segregation of Nb and Ta over crystallographically and chemically different sites was observed, ascribed to stronger metal-metal bonding between Ta atoms than between Nb-Ta and Nb-Nb. The layered compound $Ta_{3.28}Nb_{1.72}S_2$ consists of S-M-M'-M"-M'-M-S slabs separated by van der Waals gaps, where M refers to a mixed Ta-Nb site. The Ta atoms congregate in the interior on the layers, where the coordination sphere of an atom is composed entirely of other metals, thus maximizing metal-metal interactions. Nb atoms are found in greater abundance near the sulfur-rich surface layers, where metal atoms are coordinated by both sulfur and metal. In $Ta_{3.28}Nb_{1.72}S_2$, metal sites further into the metal-rich interior (M") showed compositions of 88.3 % Ta and 11.7 % Nb, whereas metal sites on the outer edge of a slab (M') had 62.7 % Nb, 37.3 % Ta.[14]

The Ta-Nb substitutional studies above have been divided into the following two categories:[86]

1. When the mixed Ta-Nb phase results in the stabilization of a entirely new structure; i.e., one that does not exist for either binary niobium or tantalum compound. For example, the $Ta_{3.72}Nb_{1.28}S_2$ phase mentioned above has no "M_5S_2" analog in Nb or in Ta binary sulfide chemistry. Other examples include $Ta_{6.08}Nb_{4.92}S_4$ ($M_{11}S_4$),[88] $Ta_{5.26}Nb_{6.74}S4$ ($M_{12}S_4$),[89] $Ta_{1.05}Nb_{0.95}S$ (M_2S),[86] $Ta_{1.40}Nb_{0.60}S$,[90] and $Ta_3Nb_5N_9$.[91]

2. The simple substitution of Nb or Ta into a structure where a corresponding (isostructural) pure binary compound is known. Examples of this category are legion, including $Nb_xTa_{1-x}Te_4$,[84] $Nb_xTa_{2-x}Te_3$ (Ta_2Te_3 type),[85] $Ta_{6.18}Nb_{14.92}S_8$ ($Nb_{21}S_8$ type),[87] $Ta_{1.79}Nb_{0.21}S$ (Ta_2S type),[87] $Ta_{1.376}Nb_{1.126}As_{0.897}$ (Ti_3P type, with Nb_3As and Ta_3As),[92] and Cu_3NbTaO_8 (= $Cu_3Ta_2O_8$ and $Cu_3Nb_2O_8$).[93]

Mixing the two metals together provides a system where subtle forces are in competition, and might lead to unexpected and interesting structural chemistry.

Mixed-metal studies in the Ta_3QX_7 system

The family of compounds Ta_3QX_7, where the three ternary elements neatly segregate onto distinct crystallographic positions, offers an inviting potential for substitutional chemistry. Three clear possibilities exist:

1. Ta-Nb substitution at a cluster site, similar to the examples described above. This option can be further broken down by specifying the elements to be mixed have either the same valence electron count as Ta (i.e. V and Nb, maybe Bi?), or a different valence electron count than Ta (Mo or Hf for example). An element other than Ta or Nb (or V) would of course change the cluster electron count. The ramifications of varying the cluster electron count have been discussed earlier (Chapter One), and bear directly on the bond lengths and magnetic properties of the substituted compounds.

2. Substitution onto the capping (chalcogen) site. This of course is the origin of the Nb_3QX_7 family, which resulted from the substitution of a chalcogen for a halogen in the binary halides Nb_3X_8. For the present purposes, this option refers mainly to chalcogen-chalcogen mixing, but also, to a lesser degree, halogen-chalcogen mixing at the capping site.

3. Substitution onto a halide position. Three crystallographically inequivalent halide positions exist in the hexagonal 3-1-7 compounds, and different Mulliken populations have been calculated for each position (see Chapter One). An interesting opportunity for experimentally studying the site-adoption preference of the various elements in these compounds is thereby offered, further probing the importance of the correlation of site electron density and atom electronegativity posited by Miller to explain the position of Te in Nb_3TeCl_7.[42]

The various Ta_3QX_7 substitutional studies that are described below were undertaken to answer several questions, the most basic of which is obviously: Is it even possible to substitute one element for another on the various sites described in the section above? Other questions are: Will substitution take place while maintaining the structure of the pure ternary being substituted, or will a new structure type result? To what extent can additional elements be mixed into the structures? Here two general possibilities can be enumerated:

1. Solid-solution behavior, where a complete substitutional range is observed, i.e., any composition can be made simply by loading according to the desired stoichiometry and heating at the appropriate temperature.

2. The formation of only discrete compositions. This case would indicate a direct correlation with the structural features of these 3-1-7 compounds. An example of the second possibility is demonstrated by considering mixing of Ta and Nb onto the metal cluster site of a 3-1-7 compound. Structures could conceivably form with all triangular clusters made up of a definite Ta:Nb ratio, for instance "$TaNb_2$". On the other hand, all substitutional permutations could be present in the metal clusters, making the overall structures a mixture then of Ta_3, Ta_2Nb $TaNb_2$, and Nb_3 clusters, with the relative populations of these five cluster compositions ultimately determining the overall composition of the crystal.

The system $Ta_{3-x}Nb_xTeI_7$ $(0 \leq x \leq 3)$

Prologue: Synthesis of *h*-Nb_3TeI_7, the first M_3QX_7 polytype

Many of the niobium-rich mixed-metal systems discussed below form in the Nb_3SBr_7 structure type. This structure type, discussed in Chapter One of this thesis, has been heretofore unreported for any iodides. During the course of research into the Nb_3TeI_7 system designed to hunt for polymorphs, a stacking variant of Nb_3TeI_7 adopting

the Nb_3SBr_7 type was discovered. The preparation and characterization of this new polytype will now be described. Nb_3TeI_7 was reported in 1988 by Hönle and Furuseth.[59] Under the reported synthetic conditions (reaction of the elements at 800°C in evacuated silica tubes for seven days), Nb_3TeI_7 is observed to form in the Nb_3SeI_7 structure type, also described in Chapter One of this thesis. Briefly, this structure is composed of mixed Te / I anion layers that stack in an (...ABCB...) or (...*hc*...) fashion with Nb_3 clusters in every other layer. The Nb_3 clusters are always capped by the Te atoms, and each successive Nb_3TeI_7 slab is related to the adjacent slab by a 6_3 screw axis. There are two Nb_3TeI_7 slabs per unit cell and the structure is necessarily non-centrosymmetric, forming in space group $P6_3mc$. Because of the (...ABCB...) or (...*hc*...) anion layer stacking sequence, and to distinguish this compound from the new polytype reported here, the earlier $P6_3mc$ Nb_3TeI_7 will be henceforth referred to as *hc*-Nb_3TeI_7, and the new stacking variant reported below will be labeled *h*-Nb_3TeI_7 in reference to its anion stacking pattern.

hc-Nb_3TeI_7

A complete structure determination of *hc*-Nb_3TeI_7 has never been reported, only the structure assignment and lattice constants.[58] Crystals of *hc*-Nb_3TeI_7 were proliferate in the Nb_3TeI_7 studies discussed here, therefore a full structure determination is now given. Intensity data from a hexagonal prism selected from a 600°C reaction were collected on a Siemens P4 diffractometer. After correcting the 1488 collected reflections ($2\theta_{max}$ = 60°) for absorption (psi-scans), the structure was easily solved by direct methods.[68] Further crystallographic information is listed in Table 5-1. Atomic coordinates and isotropic displacement parameters are given in Table 5-2. More details of the structure will be discussed in reference to *h*-Nb_3TeI_7.

h-Nb_3TeI_7

h-Nb_3TeI_7 was discovered from a series of reactions of the elements in the ratio 3Nb:Te:7I at seven temperatures: 350°, 400°, 500°, 600°, 650°C, 700°, 800°. No Nb_3TeI_7 phases were observed in reactions at 900° and 1025°. All reactions were carried

Table 5-1. Summary of crystallographic data for *hc*-Nb_3TeI_7

Formula weight	1294.63
Crystal system	Hexagonal
Space group	$P6_3mc$ (No. 186)
Color of crystal	black
Dimensions of crystal (mm)	0.15 x 0.15 x 0.30
Lattice parameters (Å)	
a	7.6300(10)
c	13.800(3)
Vol. (Å^3)	695.8(2)
Z	2
d_{calc} (g cm^{-3})	6.180
Diffractometer	Siemens P4
Radiation	Mo Kα (λ = 0.71073 Å)
Linear absorption coefficient	19.967 mm^{-1}
Transmission range, max / min.	0.741 / 0.344
Temperature of data collection	23°C
Scan method	2θ-ω scan
Scan speed	Variable: 3 to 60°/min. in ω
hkl ranges	$-1 \le h \le 10$
	$-10 \le k \le 1$
	$-1 \le l \le 19$
$2\theta_{max}$ (deg)	60.00
Number refl. measured	1488
No. unique	383
No. observed ($F_o \ge 4\sigma(F_o)$)	283
R_{int}	0.1114
Weighting scheme	$w^{-1} = \sigma^2(F_o^2) + 0.0399F_c^2$
No. parameters refined	25
Residuals[a]	
$F_o \ge 4\sigma(F_o)$	R1 = 0.0520; wR2 = 0.0959
All data	R1 = 0.0799; wR2 = 0.1065
GoF, All data[b]	1.071
Largest difference peak, e$^-$/Å^3	2.501
Largest difference hole, e$^-$/Å^3	-2.789

[a] $R1 = \Sigma||F_o| - |F_c|| / \Sigma|F_o|$; $wR2 = [\Sigma[w(F_o^2-F_c^2)^2] / \Sigma[w(F_o^2)^2]]^{1/2}$

[b] $GoF = S = [\Sigma[w(F_o^2 - F_c^2)^2] / (n - p)]^{1/2}$, where n = # reflections, p = total # parameters refined.

Table 5-2. Positional parameters and isotropic displacements parameters for *hc*-Nb_3TeI_7

Atom	x	y	z	U_{eq}
Nb	0.8667(2)	-x	1/4 (fixed)	0.0112(7)
Te	0	0	0.1022(5)	0.0122(11)
I1	2/3	1/3	0.3563(6)	0.0142(13)
I2	0.1694(2)	-x	0.3814(4)	0.0128(6)
I3	0.4979(2)	-x	0.1375(5)	0.0147(6)

out in evacuated pyrex or fused silica tubes, and the products identified by powder Guinier and single-crystal x-ray diffraction. The temperatures used, and the products identified at each temperature are given in Table 5-3. The new polytype *h*-Nb_3TeI_7 was first observed from the 700°C reaction. This tube contained crystals of two visually dissimilar morphologies. The majority of the crystals were six-sided chunks, clearly of hexagonal symmetry. However, many crystals from this tube had a trigonal, or triangular prismatic morphology. The Guinier pattern of samples of these crystals clearly differed from the pattern of the known phase *hc*-Nb_3TeI_7, most diagnostically by the absence of one intense diffraction line. Theoretical Guinier powder patterns generated from single-crystal solutions of *hc*-Nb_3TeI_7 and *h*-Nb_3TeI_7 are compared in Figure 5-1.

Structure of h-Nb_3TeI_7

Triangular prismatic shaped crystals were of *h*-Nb_3TeI_7 were eventually located in the reactions at 600°, 650°C, and 700°C. A crystal from the 650°C reaction was selected, mounted in a glass capillary, and aligned on a Siemens P4 diffractometer. The initial unit cell was determined on the basis of several reflections located with the aid of a rotation photograph. Axial photographs confirmed the cell edge lengths, and subsequently the unit cell was refined using 40 reflections from $6° \leq 2\theta \leq 25°$. *h*-Nb_3TeI_7 forms in the trigonal system, Laue symmetry 3m1, with a = 7.642(1) Å, c = 6.897(1) Å, and V = 348.82(8) Å^3.

Table 5-3. Identification of products from Nb_3TeI_7 reactions at various temperatures.

Temp. (°C)	Products (Guinier)	Sample info.
350	*hc*-Nb_3TeI_7 + unknowns	powder only
400	*hc*-Nb_3TeI_7	powder, few crystals
500	*hc*-Nb_3TeI_7	powder and crystals
600	*h*-Nb_3TeI_7 (minor) + *hc*-Nb_3TeI_7	Several crystals
650	*h*-Nb_3TeI_7 + *hc*-Nb_3TeI_7	Crystalline pieces
700	*h*-Nb_3TeI_7 + *hc*-Nb_3TeI_7 + Nb_3I_8	Crystals
800	*h*-Nb_3TeI_7 + *hc*-Nb_3TeI_7	Crystals
900	No Nb_3TeI_7 phases. Nb_3Te_4 + unknowns	powder
1025	No Nb_3TeI_7 phases. Nb_3Te_4 + unknowns	powder

694 reflections were collected to $2\theta_{max} = 50°$, of which 316 were observed. Psi-scans of several reflections for an empirical absorption correction were collected, and later applied to the data. The stucture was easily solved by direct methods using SHELXS-86,[68] and refined with SHELXL-93.[83] Table 5-4 summarizes other relevant crystallographic data.

h-Nb_3TeI_7 is the first example of polytypism discovered in the M_3QX_7 system. *h*-Nb_3TeI_7 forms in the Nb_3SBr_7 structure type, space group P3m1, with one Nb_3TeI_7 slab per unit cell. The mixed Te-I anion layer stacking sequence is (...ABAB...), or (...*h*...), from which derives the nomenclatural choice. Unlike *hc*-Nb_3TeI_7, where each successive Nb_3TeI_7 slab is related to the next by a 6_3 screw axis, in *h*-Nb_3TeI_7, successive layers are directly "superimposed" on top of one another. Near-[100] and [001] views of this simple structure type are shown in Chapter One, Figure 1-14. Atomic coordinates and isotropic displacement parameters are listed in Table 5-5. Bond distances and angles for *h*-Nb_3TeI_7 are listed in Table 5-6, and as expected are quite similar to those in *hc*-Nb_3TeI_7, also in Table 5-6.

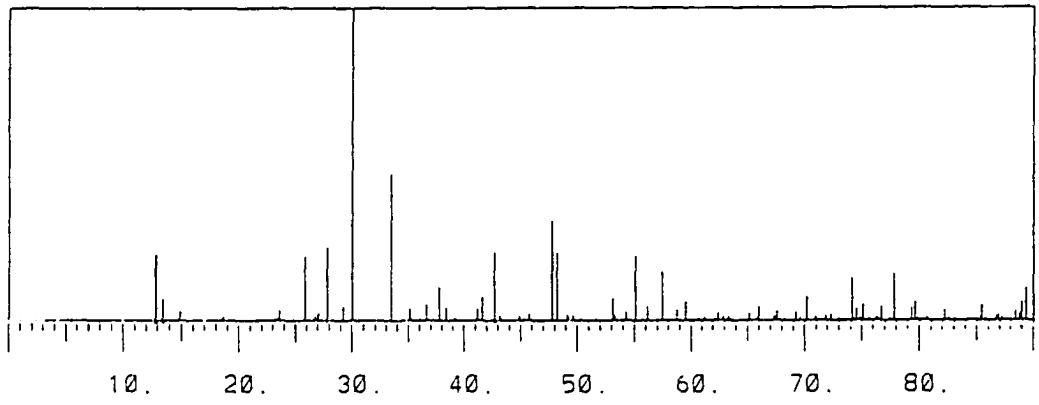

2θ (degrees)

(a) *hc*-Nb_3TeI_7.

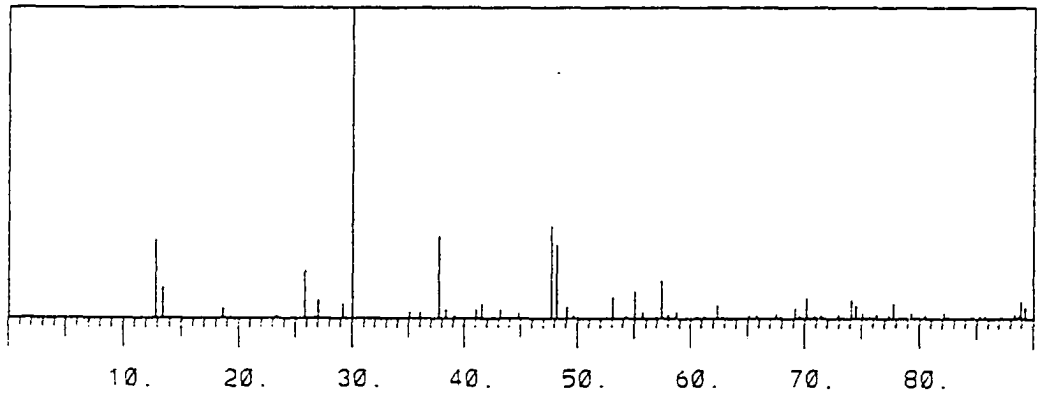

2θ (degrees)

(b) *h*-Nb_3TeI_7.

Figure 5-1. Comparison of the Guinier powder diffraction patterns of *h*-Nb_3TeI_7 and *hc*-Nb_3TeI_7. The strong line present at $2\theta \approx 33.4°$ in only the *hc*-Nb_3TeI_7 pattern is the 203 reflection.

Table 5-4. Summary of crystallographic data for *h*-Nb_3TeI_7.

Formula weight	1294.63
Crystal system	Trigonal
Space group	P3m1 (No. 164)
Color of crystal	black
Dimensions of crystal (mm)	0.1 x 0.1 x 0.2
Lattice parameters (Å)	
a	7.642(1)
c	6.897(1)
Vol. (Å^3)	348.82(8)
Z	1
d_{calc} (g cm^{-3})	6.163
Diffractometer	Siemens P4
Radiation	Mo Kα (λ = 0.71073 Å)
Linear absorption coefficient	19.913 mm^{-1}
Transmission range, max / min.	0.922 / 0.815
Temperature of data collection	23°C
Scan method	ω scan
Scan speed	Variable; 2 to 45°/min. in ω
hkl ranges	$-1 \le h \le 8$
	$-9 \le k \le 1$
	$-1 \le l \le 8$
$2\theta_{max}$ (deg)	50.00
Number refl. measured	694
No. unique	323
No. observed ($F_o \ge 4\sigma(F_o)$)	316
R_{int}	0.0439
Weighting scheme	$w^{-1} = \sigma^2(F_o^2) + 0.0317F_c^2$
No. parameters refined	25
Residuals[a]	
$F_o \ge 4\sigma(F_o)$	R1 = 0.0264; wR2 = 0.0588
All data	R1 = 0.0268; wR2 = 0.0590
GoF, All data[b]	1.211
Largest difference peak, e$^-$/Å^3	1.26
Largest difference hole, e$^-$/Å^3	-3.183

[a] $R1 = \Sigma||F_o| - |F_c|| / \Sigma|F_o|$; $wR2 = [\Sigma[w(F_o^2-F_c^2)^2] / \Sigma[w(F_o^2)^2]]^{1/2}$

[b] $GoF = S = [\Sigma[w(F_o^2 - F_c^2)^2] / (n - p)]^{1/2}$, where n = # reflections, p = total # parameters refined.

Table 5-5. Atomic coordinates and isotropic displacements parameters for *h*-Nb_3TeI_7.

Atom	x	y	z	U_{eq}
Nb	0.86658(9)	-x	1/2 (fixed)	0.0095(3)
Te	0	0	0.2015(4)	0.0104(4)
I1	2/3	1/3	0.7129(3)	0.0115(4)
I2	0.16938(8)	-x	0.7637(3)	0.0121(3)
I3	0.49855(7)	-x	0.2747(3)	0.0135(3)

Table 5-6. Bond distances (Å) and selected bond angles (deg) in *h*- and *hc*-Nb_3TeI_7.

Bond	*h*-Nb_3TeI_7	*hc*-Nb_3TeI_7
Nb-Nb	3.059(2)	3.052(5)
Nb-Te	2.713(2)	2.695(6)
Nb-I1 (μ_3^a-I)	3.0262(15)	3.023(5)
Nb-I2 (μ_2'-I)	2.737(2)	2.731(4)
Nb-I3 (μ_2^a-I)	2.9122(12)	2.911(4)
Angle		
Nb-Nb-Nb	60.00	60.00
Nb-Te-Nb	68.64(6)	69.0(2)
Nb-I1-Nb	98.45(5)	98.5(2)
Nb-I2-Nb	67.94(6)	67.9(2)
Nb-I3-Nb	103.80(6)	103.7(2)
Te-Nb-I1	159.65(7)	159.9(2)
Te-Nb-I2	110.54(4)	110.39(11)
Te-Nb-I3	86.43(5)	86.55(15)

It is tempting to speculate on the effect of temperature on the distribution of the two Nb_3TeI_7 polytypes, since a dependence on temperature is observed (Table 5-3). To wit, *h*-Nb_3TeI_7 seems to be favored at higher temperatures, as it was not observed at temperatures of below 600°C. A question of how to assign relative abundances of the two polytypes in these mixtures is apt. Visual estimates are clearly dubious, since the phases

often form as large, solid silver plugs whose morphology is not evident, and because taking powder patterns of every bit of material in the tube is impractical. A more sinister complication is how to determine if samples of *hc*-Nb_3TeI_7 contain any *h*-Nb_3TeI_7: because the simpler *h*-Nb_3TeI_7 pattern is virtually identical to the *hc*-Nb_3TeI_7 pattern except for the absence of a particular line (see Figure 5-1), *hc*-Nb_3TeI_7 can always be conclusively identified, whereas *h*-Nb_3TeI_7 cannot. If the *h*-Nb_3TeI_7 pattern is superimposed onto the *hc*-Nb_3TeI_7 pattern, it will be undetectable. In order to minimize this problem, small single crystal samples were used whenever possible, but because of their small size, often several crystals or larger samples less likely to be homogeneous were used. Because of this problem, estimates of which phases form at which temperatures are probably skewed in favor of *hc*-Nb_3TeI_7.

$Ta_{3-x}Nb_xTeI_7$ $(0 \leq x \leq 3)$

Synthesis of $Ta_{3-x}Nb_xTeI_7$

To investigate the questions posed in the Introduction section concerning mixing, we chose first the telluride iodide system $Ta_{3-x}Nb_xTeI_7$ to study, partially due to the fact that iodide systems seem to form the highest-quality crystals most readily. This is important since single-crystal x-ray diffraction will be the first and most important characterization tool.

$Ta_{3-x}Nb_xTeI_7$ were prepared according to Equations (1) and (2):

$$(3\text{-}x)\ Ta + x\ Nb + Te + 7/2\ I_2 = Ta_{3-x}Nb_xTeI_7 \qquad (1)$$

$$2\ Ta_3TeI_7 + Nb_3TeI_7 = 3\ Ta_2NbTeI_7 \qquad (2)$$

$Ta_{3-x}Nb_xTeI_7$ reactions from the elements were done at x = 1, 1.5 and 2 (Equation (1)). Also, reaction of the pure ternary compounds was done, at a 2:1 Ta_3TeI_7 : Nb_3TeI_7 ratio (Equation (2)). Reagents used were: Nb foil (0.025 mm thick, cut in small strips; Alfa, 99.99%); Ta (Alfa, 99.995%. Foil, 0.127 mm, cut in approx. 2 mm x 20 mm strips),

Te (Alfa); I_2 (Alfa, resublimed, 99.99%). Both metal foils were cleaned with an HF/HNO_3 mixture to remove surface impurities, then dried in vacuo at T > 500°C before use. The tellurium was thrice-sublimed at 450°C under dynamic vacuum and stored in the glove box.

Initial reactions were carried out at 450°C, the optimum temperature for preparation of *hc*-Ta_3TeI_7. Higher temperatures were avoided due to the apparent instability of pure *hc*-Ta_3TeI_7 above ca. 560°C. Subsequently, re-heating, or "annealing" steps were performed at temperatures of 450°C and under chemical transport conditions through a temperature gradient of 545-505°C. The latter conditions were found to be optimum for growth of the best $Ta_{3-x}Nb_xTeI_7$ crystals, which were always found transported to the cooler end of the tube. In all cases reported below, the same batch of sample was carried through all steps, i.e., the product from the initial reaction was ground, re-loaded and used for the re-heatings. The purpose of these re-heating steps was both to grow more and better crystals than what was available from the initial reactions, and to determine if re-grinding and reheating samples would result in the same Ta:Nb mixing ratio observed in antecedent reactions.

Characterization of $Ta_{3-x}Nb_xTeI_7$

Initially, the question of whether Nb and Ta would even mix in this system was conclusively answered using the independent characterization tool of scanning electron microscopy. Multiple single crystals from the each of the various reactions (x = 1, 1.5, 2, and premade ternary, all temperatures) mentioned above were studied using a JEOL 6100 scanning electron microscope. The simultaneous presence of both niobium and tantalum in all samples was clear from the strong characteristic emission peaks for tantalum at 1.710 keV (Mα) and for niobium at 2.164 keV (Lα), which appeared in all spectra. The SEM also verified the presence of Te and I in all samples as well.

For a more quantitative analysis of the Ta/Nb content, samples from the x = 1, 1.5 and 2 reactions were studied using x-ray photoelectron spectroscopy. A PHI 550 Multi-Technique surface analyzer instrument was used, and all samples were prepared, mounted,

and transferred to the instrument under inert atmosphere. In all cases, pristine, crystalline samples from a reaction at 545-505°C, were used, after identifying the product by x-ray powder diffraction. Along with confirming the mixed composition, the XPS experiment provided binding energies corresponding to reduced metal atoms: Nb $5d_{3/2}$, 203.6 eV; Ta $4f_{7/2}$, 23.4 eV. The tantalum binding energy agrees very well with that measured for the pure Ta_3TeI_7 phases (Chapter Two, Table 2-4).

Several crystals from each system and reaction were studied by single crystal x-ray diffraction using a Siemens P4 diffractometer. Since the x-ray scattering factors of Nb and Ta are quite different due to the wide separation in atomic numbers between the two elements, single-crystal x-ray diffraction is an excellent method for the determination of the relative content of each metal in a given crystal. In addition to single-crystal work, careful Guinier powder diffraction studies of most reactions were performed to at least qualitatively identify polytypes formed from each set of conditions that may not have yielded diffraction-quality single crystals.

Tables 5-7 through 5-10 gather together the results of all single-crystal solutions from the Ta_2NbTeI_7, $Ta_{1.5}Nb_{1.5}TeI_7$, $TaNb_2TeI_7$ and 2 Ta_3TeI_7 + Nb_3TeI_7 reactions and re-heatings. These tables list selected data collection information, hexagonal lattice parameters, R-factors, and the refined composition determined from all the crystals. Lattice parameters for pure Nb_3TeI_7 and Ta_3TeI_7 are also given, in Table 5-7.

Ta_2NbTeI_7 ($x = 1$)

16 solutions from three reactions are in Table 5-7. All single crystals formed the *hc*-type stacking variant (Nb_3SeI_7 structure, space group $P6_3mc$, *c* axis length near 13.9 Å). Metal compositions refined from the single-crystal data range from $Ta_{1.74}Nb_{1.26}$ to $Ta_{2.69}Nb_{0.31}$. Most, however, were very near "Ta_2Nb". Interestingly, the first annealing reaction (45 days at 450°C) yielded compositions on average higher in Ta than either the initial 450°C reaction or the subsequent 500-475°C reaction. The XPS experiments corroborated the compositions refined from single crystal data. The average metal ratio from several samples of large crystals from this reaction was found to be "$Ta_{1.80}Nb_{1.20}$".

Table 5-7. Summary of crystallographic results for "Ta_2NbTeI_7" reaction products.

Crystal ID	Lattice Parameters (Å) *a*	*c*	R(int)	# Data	Unique	Observed (>2σF$_o$)	R1 Fo>4σFo	wR2	Refined Composition [a]
	Initial reaction, 450°C, 2 wks.					All data sets collected to $2\theta_{max}$ = 50.00°.			
250-5	7.598(1)	13.866(3)	0.0613	1188	288	278	0.0370	0.0839	$Ta_{1.94}Nb_{1.06}TeI_7$
362-2	7.590(1)	13.897(3)	0.0832	1189	287	250	0.0277	0.0493	$Ta_{2.67}Nb_{0.33}TeI_7$
	Annealed, 450°C, 45 d.					All data sets collected to $2\theta_{max}$ = 50.00°.			
405-3	7.584(1)	13.894(3)	0.1022	1185	286	248	0.0379	0.0618	$Ta_{2.50}Nb_{0.50}TeI_7$
405-4	7.590(1)	13.886(3)	0.0588	1185	286	267	0.0344	0.0786	$Ta_{2.39}Nb_{0.61}TeI_7$
405-5	7.587(1)	13.889(3)	0.0522	1185	286	267	0.0399	0.0935	$Ta_{2.20}Nb_{0.80}TeI_7$
406-3	7.590(1)	13.888(3)	0.0809	1185	285	255	0.0392	0.0794	$Ta_{2.41}Nb_{0.59}TeI_7$
406-4	7.586(1)	13.892(3)	0.0956	1185	286	244	0.0354	0.0634	$Ta_{2.45}Nb_{0.55}TeI_7$
406-5	7.589(1)	13.885(3)	0.1028	1185	286	245	0.0432	0.0864	$Ta_{2.43}Nb_{0.57}TeI_7$
	Annealed in gradient, 500 - 475°C, 14 d.					All data sets collected to $2\theta_{max}$ = 50.00°.			
456-1a	7.601(1)	13.883(3)	0.0526	1184	289	274	0.0305	0.0653	$Ta_{1.97}Nb_{1.03}TeI_7$
456-2	7.599(1)	13.883(3)	0.0689	1192	289	280	0.0349	0.0803	$Ta_{1.96}Nb_{1.04}TeI_7$
458-4	7.600(1)	13.880(3)	0.0404	1185	289	282	0.0240	0.0630	$Ta_{1.73}Nb_{1.27}TeI_7$
459-2	7.600(1)	13.882(2)	0.0608	1193	289	279	0.0220	0.0518	$Ta_{2.07}Nb_{0.93}TeI_7$

[a] The esd on the metal compositions in all cases is ≤ 0.01, i.e., $Ta_{2.07(1)}Nb_{0.93(1)}$ is the upper error limit.

Table 5-8. Summary of crystallographic results from "$Ta_{1.5}Nb_{1.5}TeI_7$" reactions.

Crystal ID	Lattice Parameters (Å) *a*	*c*	R(int)	Data	Unique	Observed (>2σF$_o$)	R1 Fo>4σF$_o$	wR2	Refined Composition [a]
Annealed in gradient, 545 - 505°C, 30d						All data sets collected to $2\theta_{max}$ = 50.00°.			
525-1	7.620	6.913	0.0285	692	321	320	0.0228	0.0603	$Ta_{1.34}Nb_{1.66}TeI_7$

Table 5-9. Summary of crystallographic results from "$TaNb_2TeI_7$" reactions.

Crystal ID	Lattice Parameters (Å) *a*	*c*	R(int)	Data	Unique	Observed (>2σF$_o$)	R1 Fo>4σF$_o$	wR2	Refined Composition [a]
485-1	7.624(1)	6.905(1)	0.0411	964	512	486	0.0279	0.0629	$Ta_{0.88}Nb_{2.12}TeI_7$
485-2	7.624(1)	6.901(1)	0.0518	1232	656	612	0.0308	0.0759	$Ta_{0.86}Nb_{2.14}TeI_7$
485-3	7.624(1)	6.905(1)	0.0434	963	512	487	0.0259	0.0558	$Ta_{0.80}Nb_{2.20}TeI_7$
485-6	7.622(1)	6.905(1)	0.0574	964	512	510	0.0271	0.0702	$Ta_{0.82}Nb_{2.18}TeI_7$
485-7	7.622(1)	6.902(1)	0.0358	686	318	317	0.0232	0.0552	$Ta_{0.86}Nb_{2.14}TeI_7$

[a] In all cases, the esd of the metal compositions are ≤ 0.01, i.e., $Ta_{0.86(1)}Nb_{2.14(1)}$ is the upper error limit.

Table 5-10. Summary of crystallographic results from "2 Ta_3TeI_7 + Nb_3TeI_7" reactions.

Crystal ID	Lattice Parameters (Å) *a*	*c*	R(int)	Data	Unique	Observed (>2σF_o)	R1 Fo>4σFo	wR2	Refined Composition [a]
Annealed in gradient, 545 - 505°C, 30d						All data sets collected to $2\theta_{max}$ = 50.00°.			
490-1	7.599(1)	13.880(3)	0.0738	1190	289	271	0.0250	0.0509	$Ta_{1.90}Nb_{1.10}TeI_7$
490-2	7.601(1)	13.886(3)	0.0560	1190	289	275	0.0239	0.0562	$Ta_{1.89}Nb_{1.11}TeI_7$
490-4	7.599(1)	13.892(3)	0.0523	1194	289	286	0.0228	0.0512	$Ta_{1.97}Nb_{1.03}TeI_7$
490-5	7.604(1)	13.888(3)	0.0528	1185	289	273	0.0270	0.0508	$Ta_{1.91}Nb_{1.09}TeI_7$
490-8	7.597(1)	13.892(3)	0.0497	1193	289	277	0.0229	0.0516	$Ta_{1.78}Nb_{1.22}TeI_7$

[a] In all cases, the esd for the metal compositions is ≤ 0.01, i.e., $Ta_{1.78(1)}Nb_{1.22(1)}$ is the upper error limit.

The *h*-polytype was observed by Guinier powder diffraction from a reaction at 545-505°C, but no XRD-quality single crystals of "*h*-Ta_2NbTeI_7" were ever found. The *h*-polytype from this reaction formed only as a microcrystalline solid in very low yield, and was not subjected to XPS analysis.

$Ta_{1.5}Nb_{1.5}TeI_7$ ($x = 1.5$)

Crystals from this system were not abundant. An acceptable solution was obtained from only one crystal, from an annealing reaction heated in a 545-505°C gradient for 4.5 weeks (Table 5-8). Reactions generally yielded large chunks of crystalline solid. The one crystal adopted the *h*-type, with a metal composition of "$Ta_{1.33}Nb_{1.67}$". Both the *h*- and the *hc*-polytypes were observed by Guinier patterns, however. Suitable single crystals of the *hc*-type never formed from $x = 1.5$ reactions. Two poor solutions of the *hc*-types indicated an Ta:Nb ratio of about 1:2. XPS results from a large single crystal sample gave "$Ta_{1.26}Nb_{1.74}$" as the metal ratio. No indications of a tantalum-rich sample were found from XPS or single crystal work.

$TaNb_2TeI_7$ ($x = 2$)

Both the *h*- and *hc*-types were observed in the Guinier patterns, though high-quality crystals, and thus single-crystal solutions were limited to only the *h*-type. The refined compositions from five crystals of *h*-$Ta_{3-x}Nb_xTeI_7$ from the same reaction are all within ± 0.04 moles of "$Ta_{0.84}Nb_{2.16}$" (Table 5-9). To determine the composition (metal ratio) of the *hc*-type found in the $TaNb_2$ system, XPS was done on large *hc*-type crystals. The XPS gave a metal composition of "$Ta_{0.66}Nb_{2.34}$". Interestingly, a few *hc*-type crystals were collected on the Siemens P4. The refined compositions were very Ta-rich, near "Ta_2Nb". This data is very suspect, however. Even though there was little indication of poor crystal quality during pre-collection searching or during the collection (Narrow, gaussian peak profiles, straightforward indexing of the Nb_3SeI_7-type cell), these crystals turned out to be of poor quality, exhibiting many large systematic absence violations of the

c-glide operation in the space group $P6_3mc$. Crystals defective in this way are common from all Ta_3QX_7 systems that adopt the *hc*-Nb_3SeI_7 structure type.

2 Ta_3TeI_7 + Nb_3TeI_7

Both polytypes were observed from Guinier diffraction. Four single crystals of the *hc*-type were found to be suitable XRD quality. Their compositions are narrowly distributed around "$Ta_{1.9}Nb_{1.1}$". A crystallographic summary from these four crystals is given in Table 5-10. XPS corroborated these results, yielding a metal composition of "$Ta_{1.87}Nb_{1.13}$".

Conclusions

Though only three $Ta_{3-x}Nb_xTeI_7$ points (x = 1, 1.5, and 2) were studied, several conclusions can be drawn. First, niobium and tantalum readily mix onto the metal site over at least the substitutional range $0.31 \leq x \leq 2.20$, but probably over the complete range $x \in (0,1)$. Furthermore, both *h*- and the *hc*-type stacking variants were observed at all values of x. However, the distribution of these types was not random in any given system. This is especially demonstrated by the $NbTa_2TeI_7$ system, where only a small amount of the *h*-type was ever identified. At the same time, large quantities of the *hc*-type were readily made. This implies a preference for Ta-rich systems to adopt the *hc*-type. Niobium-rich systems, on the other hand, formed both types readily. There seems to be a tendency of decent crystals to form only when the metal content is right. Nb-rich favors the *h*-type, and will not form good crystals in the *hc*-type, and vice versa. The most interesting reaction from this point of view is the equimetallic x = 1.5 case. We know that both types will form. The question this system could answer is: will the metal content correlate with structure type? Evidence to the contrary exists only from the Nb_2Ta case, which yielded abundant crystals of the *h*-type only. However, XPS results on the *hc*-type gave a similar composition as refined from single crystal data, implying any metal ratio could form in any structure type.

For crystals and crystalline samples unsuitable for single-crystal x-ray diffraction, x-ray photoelectron spectroscopy was used to determine the Ta:Nb ratio. These XPS experiments generally provided tantalum and niobium compositions that agreed well with the loaded stoichiometry, regardless of structure type.

Since only the structure types corresponding to the those of the known ternary phases were observed, it appears clear that upon Ta-Nb mixing the tantalum and niobium atoms are distributed throughout the structures in such a way that the x-ray diffraction experiment can detect no ordering. The identity of the atoms within individual M_3 clusters in the ${}^{2}_{\infty}[M_3TeI_7]$ slabs, though, is uncertain, and cannot be determined crystallographically. Conceivably, the observed *h*- and *hc*-types could contain randomly distributed mixtures of homonuclear Nb_3 and Ta_3 clusters, randomly distributed mixtures of heteronuclear "Ta_2Nb" and "$TaNb_2$" clusters, or mixtures of all four cluster types, and so long as the relative abundances of the various cluster species add up to the observed composition, the result would be the same to x-rays. However, all attempts to elucidate the local cluster bonding picture using other characterization techniques were unsuccessful. Solid-state NMR (the quadrupolar nuclei ^{93}Nb, ^{181}Ta, and ^{125}Te could all theoretically be used) was an encouraging candidate because of the high relative receptivity of the ^{93}Nb nucleus, indicative of an atom that produces a strong signal. Unfortunately, the relaxation times were apparently too short on the NMR timescale to measure a signal, probably due to the tightly bound, eight-coordinate environment of the metal atoms providing abundant relaxation pathways. Atomic Force Microscopy was also tried, and although this technique did verify the hexagonal *a* lattice constants and the surface corrugations on both sides of the ${}^{2}_{\infty}[M_3TeI_7]$ slabs, features below the anion surface (in the metal layers) remained shrouded.

The system $Nb_{1.5}Ta_{1.5}SI_7$

Motivation

As discussed in Chapter Two, despite numerous reaction attempts a well-crystallized hexagonal Ta_3SI_7 has not been synthesized. Instead, the new ternaries Ta_4SI_{11} and *o*-Ta_3SI_7 form abundantly. The impetus for this mixing sudy was to stabilize tantalum in a hexagonal form. Note: the prefix "*hc*-" again refers to the anion stacking sequence (...ABCB..., or ...*hc*...), and serves to specify the Nb_3SeI_7 structure type (space group $P6_3mc$, two slabs per unit cell), as described in Chapter One.

hc-$Ta_{3-x}Nb_xSI_7$

Synthesis

Synthesis of *hc*-$Ta_{3-x}Nb_xSI_7$ can be achieved from stoichiometric reaction of the purified or cleaned elements in sealed, evacuated pyrex or fused silica tubes from 400 to 550°C for ca. two weeks, according to Equation (3):

$$(3-x)\ Ta(foil) + x\ Nb(foil) + 1/8\ S_8 + 7/2\ I_2 = Ta_{3-x}Nb_xSI_7 \qquad (3)$$

Such reactions yield plentiful hexagonal pyramidal black reflective crystals, as well as polycrystalline material. The powder patterns of Ta_4SI_{11}, and *o*-M_3SI_7 can also be identified by Guinier diffraction, but these are minor constituents. By visual estimate, the Ta_4SI_{11} and *o*-M_3SI_7 together amounted to less than 15% total product. The best *hc*-$Ta_{3-x}Nb_xSI_7$ crystals were found in tubes heated either in a temperature gradient of 545-505°C for a few weeks, or at 500°C for two weeks, and are transported to the opposite end of the tube. They vary in size from near-microcrystalline to a few millimeters in length. In reactions conducted above 550°C, the only products identifiable by Guinier powder diffraction are TaS_2, Ta_6I_{14}, and TaI_5.

Characterization

Guinier powder diffraction of several individual samples of the hexagonal pyramid crystals indicate adoption of the Nb_3SeI_7 structure type. This might be the expected result since both Nb_3SI_7 and Ta_3SI_7 have been observed in this type, though only small amounts of polycrystalline Ta_3SI_7 have been synthesized. Additionally, several single crystals were analyzed with a JEOL 6100 scanning electron microscope for elemental content, which showed the presence of only Nb, Ta, S, and I in all samples.

Structure and composition

Four hexagonal pyramidal crystals from two reactions (500°C for 13 days and a sample that was ground and re-heated in a temperature gradient of 545-505°C for 4 weeks) were mounted on a Siemens P4 diffractometer for intensity data collection. Collection information common to all data sets in given in Table 5-11. The structures were solved by direct methods and refined using SHELX,[68, 83] after applying a psi-scan

Table 5-11. Crystallographic data for common to all $Ta_{3-x}Nb_xSI_7$ solutions.

Crystal system	Trigonal
Space group	$P6_3mc$ (No. 186)
Crystal color, habit	black, hexagonal pyramids
Lattice parameters (average, Å)	
a	7.553(1)
c	13.540(3)
Vol. (Å^3)	669.53(10)
Z	2
d_{calc} (g cm^{-1})	6.599
Diffractometer	Siemens P4
Radiation	Mo Kα, λ = 0.71071 Å
Temperature of data collection	23°C
Scan method	ω scan
Range in *hkl*	$-1 \leq h \leq 7$
	$-7 \leq k \leq 1$
	$-1 \leq l \leq 13$
$2\theta_{max}$ (deg)	50.00

absorption correction to the data. Structure solution was straightforward using *hc*-Nb_3SI_7 as a model. A summary of each solution is given in Table 5-12. A description of a typical structure solution now follows. Initially, the sulfur and iodine positions were kept fully occupied and the mixed-metal site was allowed to refine, indicating a metal composition slightly Nb-rich, at "$Ta_{1.4}Nb_{1.6}$". At this point problems with the capping (sulfur) site became apparent, as the sulfur isotropic thermal parameter shrank to zero when refined as fully occupied by sulfur, indicating greater electron density on this site. This effect was attributed to partial S/I mixing. Refinement of the capping site as a mixed sulfur-iodine position was carried out by fixing all occupancy and thermal parameters except the sulfur site occupation factor. The sulfur SOF rose to 1.28 upon doing this. Assuming the extra electron density comes from partial iodine mixing, the SOF indicated a S/I ratio of ~90% S to 10% I. The atomic ratio was then set at this value and allowed to refine, constrained to a total occupancy of 100%. The final percentages were: 89% S, 11% I. R-factors dropped significantly as a result, from 0.030/0.065 to 0.027/0.057 (R1/wR2). Subsequently, isotropic thermal parameters were included in the refinement. Eventually, all thermal parameters and occupancies were allowed to refine anisotropically, with the S and I constrained as equal. Throughout all refinement steps, the *z*-coordinate for the mixed S/I capping site was kept as one coordinate and not split into two positions, even though the distances from the cluster to the sulfur and iodine should be different. This is reflected in the U_{33} displacement factor, which is about three times larger than the U_{11} / U_{22} values. Consequently the M-cap distance reported below is an average distance consisting of an 88% contribution from the M-S length and a 12% contribution from M-I_{cap}. Atomic coordinates, isotropic thermal parameters and site occupation factors for a representative "$Ta_{1.40}Nb_{1.60}S_{0.85}I_{7.15}$" solution are given in Table 5-13. Anisotropic displacement parameters are given in Table 5-14, and average bond distances and angles from the four essentially identical solutions are given in Table 5-15.

Table 5-12. Summary of $Ta_{3-x}Nb_xSI_7$ single crystal results.

	from initial reaction, 500°C, 13d		Reheated, 545 - 505°C, 30 d	
Crystal ID	515-1	516-1	630-1	630-2
Absorption coeff. (mm^{-1})	29.71	26.10	29.78	29.81
Number refl. measured	1237	1238	1232	1201
No. observed ($I > 2\sigma_I$)	1155	1155	1152	1125
No. unique	278	278	278	278
No. unique observed	276	277	277	277
R(int)	0.0533	0.0473	0.0418	0.0528
No. parameters refined	28	28	28	28
Data-parameter ratio	10	10	10	10
Largest difference peak	0.99	0.79	0.69	0.96
Largest difference hole	-2.14	-0.87	-1.30	-0.94
Residuals[a]				
R (observed)	0.0210	0.0188	0.0183	0.0235
R_w	0.0408	0.0443	0.0435	0.0459
GoF	1.205	1.119	1.170	1.105
Refined Composition	$Ta_{1.410(5)}Nb_{1.590(5)}S_{0.859(2)}I_{7.141(2)}$	$Ta_{1.376(5)}Nb_{1.624(5)}S_{0.840(2)}I_{7.160(2)}$	$Ta_{1.347(4)}Nb_{1.653(4)}S_{0.892(2)}I_{7.108(2)}$	$Ta_{1.436(5)}Nb_{1.564(5)}S_{0.883(2)}I_{7.117(2)}$

[a] $R = \Sigma||F_o| - |F_c||/\Sigma|F_o|$; $R_w = [\Sigma w(|F_o| - |F_c|)^2/\Sigma w(F_o)^2]^{1/2}$; $w = 1/\sigma^2(F_o)$.

Table 5-13. Atomic coordinates, site occupation factors (SOF), and isotropic thermal parameters for a representative "$Ta_{1.5}Nb_{1.5}SI_7$" crystal. (Refined composition $Ta_{1.41}Nb_{1.59}S_{0.86}I_{7.14}$, crystal "515-1" in Table 5-12).

Atom	x	y	z	U_{eq}	SOF
Ta	0.8695	-x	1/4	0.0093(3)	0.470(5)
Nb	0.8695	-x	1/4	0.0093(3)	0.530(5)
S	0	0	0.3864	0.026(2)	0.859(2)
I_{cap}	0	0	0.3864	0.026(2)	0.141(2)
I1	1/3	2/3	0.6438	0.0115(4)	1.0
I2	0.8310	-x	0.6135	0.0137(4)	1.0
I3	0.4970	-x	0.3649	0.0122(3)	1.0

Table 5-14. Anisotropic displacement parameters in $Ta_{1.41}Nb_{1.59}S_{0.86}I_{7.14}$ (Crystal "515-1" in Table 5-12).

Atom	$U_{11}= U_{22}$	U_{33}	$U_{23} = -U_{13}$	U_{12}
Ta, Nb	0.0080(3)	0.0125(4)	0.0000(2)	0.0044(3)
S, I_{cap}	0.010(2)	0.059(5)	0.000	0.0049(10)
I1	0.0088(5)	0.0168(8)	0.000	0.0044(3)
I2	0.0114(5)	0.0177(6)	0.0024(2)	0.0051(4)
I3	0.0097(4)	0.0163(5)	-0.0012(2)	0.0043(4)

$$U_{ij} = \exp(-2\pi^2(a^{*2}U_{11}h^2 + b^{*2}U_{22}k^2 + c^{*2}U_{33}l^2 + 2a^*b^*U_{12}hk + 2a^*c^*U_{13}hl + 2b^*c^*U_{23}kl))$$

Table 5-15. Average bond distances (Å) and selected bond angles (deg) in $Ta_{1.5}Nb_{1.5}SI_7$. The average of the four data sets is given. Values for Nb_3SI_7 are given for comparison.

Bond	$Ta_{1.4}Nb_{1.6}S_{0.85}I_{7.15}$	Nb_3SI_7
M-M	2.959(1)	2.995
M-S	2.517(5)	2.404
M-I1 (μ_3^a-I)	3.020(1)	2.993
M-I2 (μ_2^i-I)	2.730(1)	2.737
M-I3 (μ_2^a-I)	2.917(1)	2.906
Angle		
M-M-M	60.0	60.0
M-S-M	72.0(2)	72.7
M-I1-M	99.17(4)	98.8
M-I2-M	65.62(4)	67.1
M-I3-M	104.04(5)	103.6

Discussion

Tantalum can be readily stabilized in the *hc*-Nb_3SeI_7 structure type in the mixed-metal compound $Ta_{3-x}Nb_xSI_7$ ($x \approx 1.6$). Although only one point on the $Ta_{3-x}Nb_xSI_7$ continuum was studied ($x = 1.5$), results from the $Ta_{3-x}Nb_xTeI_7$ study (above) imply a full Ta-Nb substitutional range is probably possible.

Along with the Ta-Nb mixing, the metal triangle μ_3^i capping position appears to be occupied by a mixture of sulfur and iodine, to the extent of about 90% S, 10% I. This phenomenon has a precedent in the studies of the system $Nb_3S_{1-y}I_{7+y}$ by Miller and Lee.[94] They found that iodine and sulfur mixed readily on the capping site over the complete range of y, and that a structure type dependence on y occurred. Compounds having $y > 0.5$ (iodine-rich) adopted the Nb_3I_8 structure (Chapter One), and those with $y < 0.5$ (sulfur-rich) adopted the Nb_3SI_7 structure (Nb_3SeI_7 type). The $Ta_{3-x}Nb_xSI_7$ system appears to follow this trend also, adopting the *hc*-Nb_3SI_7 structure at the sulfur-rich composition studied. No attempts to synthesize a $Ta_{3-x}Nb_xS_{1-y}I_{7+y}$ phase with lesser sulfur content were made.

The system $Nb_{1.5}Ta_{1.5}SBr_7$

Motivation

The sulfide bromide pair Ta_3SBr_7 and Nb_3SBr_7 offers an interesting opportunity for a mixed-metal study, because of the different structures adopted by the two. These structures have been discussed at length in Chapter Three. This pair in fact represents the only Ta-Nb analogues discovered thus far in the M_3QX_7 system that are not isostructural with each other. In a mixed $Ta_{3-x}Nb_xSBr_7$ system, which of the two structures will be preferred? Will the relative amounts of each metal play a role? The equimetallic case (x = 1.5) was investigated in an attempt to answer these questions, and the results are discussed below.

Results

Synthesis

Stoichiometric reaction of the elements according to Equation (4) at 475°C in

$$1.5\ Ta\ (foil) + 1.5\ Nb\ (foil) + 1/8\ S_8 + 7/2\ Br_2 = Nb_{1.5}Ta_{1.5}SBr_7 \qquad (4)$$

evacuated pyrex or fused silica tubes for four weeks yields reflective black pyramidal crystals and polycrystalline material whose Guinier diffraction pattern matches Ta_3SBr_7 and Nb_3SBr_7.

Characterization

Black irregular prismatic crystals were mounted in air onto glass fibers, and aligned on a Siemens P4 diffractometer. After centering several reflections located with the aid of a rotation photograph, a C-centered monoclinic unit cell was indexed, corresponding to the Ta_3SBr_7 type. Both axial photographs as well as the Siemens P4 search routine designed to check for different symmetry or unit cell size confirmed the monoclinic cell. This cell was then refined with 45 more reflections in the angular range $14° \leq 2\theta \leq 27°$.

The final diffractometer-determined lattice constants are: a = 12.256(2) Å; b = 7.075(1) Å, c = 8.775(2) Å, β = 133.93(3)°. Complete intensity data sets (sphere, collected with the lattice centering restriction only) were collected for several such crystals. The structure was easily solved in the space group Cm using Ta_3SBr_7 as a model, and allowing the metal sites to refine as a mixture of Ta and Nb. The solutions, although not of high quality, were enough to verify the adoption of the Ta_3SBr_7 structure type and to determine a rough tantalum-niobium content in the crystals.

All $Nb_{1.5}Ta_{1.5}SBr_7$ single crystals have given only tantalum-rich refinements. The best solution, refined to a composition "$Ta_{2.28}Nb_{0.72}SBr_7$". The other data sets gave similar metal ratios. Although the R-factors are high (R1 = 6.58%, wR2 = 16.97%), the data do at least indicate a significantly greater percentage of tantalum, even though the reaction stoichiometry was 1:1.

CHAPTER SIX
GENERAL CONCLUSIONS

Several new tantalum chalcogenide halide compounds, most with the general formula Ta_3QX_7 (Q = S, Se, Te; X = Cl, Br, I), have been synthesized and characterized. These compounds represent the first examples of trinuclear clusters of tantalum discovered by traditional high-temperature solid-state chemistry techniques. Of these, *hc*-Ta_3TeI_7, *hc*-Ta_3SeI_7, Ta_3SBr_7, Ta_3TeCl_7 have been thoroughly structurally characterized with single crystal x-ray diffraction methods. The five compounds *hc*-Ta_3SI_7, *o*-Ta_3SI_7, Ta_3TeBr_7, Ta_3SeBr_7, and Ta_3SeCl_7, while certainly known, are limited to powder diffraction characterization and are less well understood structurally and synthetically. A new structure type, the mixed-valent compound Ta_4SI_{11}, was discovered in the Ta-S-I system. The structure of this unusual compound could not be determined solely by x-ray diffraction methods due to extensive disorder. Additionally, the elements tantalum and niobium were shown to substitute readily for each other in the systems $Ta_{3-x}Nb_xTeI_7$, $Ta_{3-x}Nb_xSI_7$, and $Ta_{3-x}Nb_xSBr_7$, though whether the bonding within the trinuclear clusters is heterometallic or homometallic remains unclear.

Ta_3QX_7 and Ta_4SI_{11} all show similar temperature stability ranges, surviving to a maximum temperature of ca. 550°C, before decomposing to the pentahalides, hexanuclear cluster compounds and unknown products (presumably involving the chalcogen, though the fate of Q was only rarely detected using x-ray diffraction). This property distinguishes the chemistry of Ta_3QX_7 from the analogous niobium compounds Nb_3QX_7, which were synthesized and are stable towards thermal decomposition at temperatures as great as 900°C. It is uncertain exactly why the tantalum phases seem less thermally hardy, but the reason may be a reflection of the greater tendency of tantalum to engage in metal-metal bonding, which might favor the formation of the Ta_6X_{14} and Ta_6X_{15} compounds observed so frequently during the various syntheses.

The facility with with these compounds were made and the variety of structures found point to a potentially very rich chemistry. The absence of such ternary cluster

chemistry heretofore when compared to similar elements, especially niobium, is almost certainly due to a lack of detailed study in the proper temperature region, and not to an inherent unreactivity of the element itself. A particular problem in preparing new tantalum cluster phases might be the tendency to use as a synthetic starting point the chemistry of niobium. These two elements, rightfully notorious for being chemically similar, in actuality often behave quite differently. In the present case, initial investigations into the Ta-Q-X systems failed because the reaction temperatures chosen were too high.

Synthesis, characterization, and purification of all Ta_3QX_7 compounds (and Ta_4SI_{11}) benefitted greatly from chemical vapor transport. The nature of the vapor-phase species responsible for transport is uncertain, though tubes viewed in the furnace when still hot and during the cooling process visually deposit large amounts of the tantalum pentahalides, implicating this volatile species. Chemical transport is quite useful when separating the pure Ta_3QX_7 material (and selecting crystals) from bulk powders, as the transport of most Ta_3QX_7 products is achieved and controlled readily. Large amounts of the pure crystalline solid can often be transported to the cooler end of the tube, over a timescale of a few days to a couple weeks.

Chemically, these compounds are relatively fragile with respect to oxidation and reduction, and if induced to react usually do so at the expense of the cluster-containing layered structure. Various attempts to intercalate small atoms into the van der Waals gap resulted either in no reaction (in the case of neutral molecules like pyridine or water) or in destruction of the Ta_3QX_7 framework, as in the case of diverse reactions with alkali and alkaline earth metals, alkali metal salts, polychalcogenide fluxes and others. Appendix C contain a thorough record of all such reactions attempted and the products obtained.

Some puzzling aspects of tantalum halide cluster chemistry remain, though, especially in light of the ready formation and stability of the trinuclear clusters in Ta_3QX_7, as demonstrated by this thesis. In particular, Ta_3X_8, the tantalum analogues of Nb_3X_8, do not form even in the temperature regions that so readily gave Ta_3QX_7. Several attempts to make these elusive binary halides were carried out, with only Ta metal, Ta_6X_{14} or Ta_6X_{15} and TaX_5 as the result. The absence of Ta_3X_8 might be correlated with the refusal

of Ta_3QX_7 to be intercalated by one-electron donors, since supplying an electron to the LUMO of the six-electron metal-metal bonding system makes Ta_3QX_7 isoelectronic with Ta_3X_8.

The investigation into the Ta-Q-X system was quite fruitful: "turning down the heat" expanded the solid-state cluster chemistry of tantalum significantly, and again demarcated this element from its lighter group member niobium with respect to the formation of new structure types (Ta_3SBr_7, Δ-Ta_3TeI_7(?) and Ta_4SI_{11}). Hints of an even richer chalcogenide halide chemistry arose from these studies as well, with some minor side products giving a tantalizing glimpse into further tantalum chalcogenide halide possibilities. Appendix B contains these exciting discoveries.

APPENDIX A: SUMMARY OF ALL Ta-Q-X REACTIONS ATTEMPTED, AND PRODUCT IDENTIFICATION.

Numbers indicate separate reactions; multiple temperatures means the product from the previous line was re-loaded and annealed at the conditions indicated. In order from lowest temperature to highest.

IODIDES

Ta-Te-I:

Reaction / annealing temperature	Products identified by Guinier powder diffraction	page # and notebook
Ta_3TeI_7		
1. 300°C, 13d	Ta + $TaTe_2$ + Ta_6I_{14} + TaI_5	p219nb3
2. 400°C, 10.5d	Ta + $TaTe_2$ + Ta_6I_{14} + TaI_5	p220nb3
3. 425°C, 4wks	Δ-Ta_3TeI_7 + *hc*-Ta_3TeI_7 + Ta_6I_{14}/TaI_5 + Ta	p9nb5
4. 450°C, 15d	*hc*-Ta_3TeI_7 + "$Ta_6Te_{4-x}I_{10+x}O$" + $TaTe_2$ + TaI_5	p231,270nb3
5. 450°C, 17d	Ta + *hc*-Ta_3TeI_7 + Δ-Ta_3TeI_7 + TaI_5	p276nb3
6. 450°C, 14d (Ta powder)	$TaTe_2$ + *hc*-Ta_3TeI_7 + TaI_5	p27nb4
7. 450°C, 7d	Ta + *hc*-Ta_3TeI_7 + Ta_6I_{14}/TaI_5	p35nb4
8. 450°C, 14d	Δ-Ta_3TeI_7 + *hc*-Ta_3TeI_7 + Ta_6I_{14}/TaI_5 Ta + $TaTe_2$	p44nb4
9. 450°C, 7 wks	*hc*-Ta_3TeI_7 + Δ-Ta_3TeI_7 (quantitative)	p133nb4
10. 450°C, 14d	Ta + Δ-Ta_3TeI_7 + "$Ta_6Te_{4-x}I_{10+x}O$"	p29nb4
575°C, 9d	Δ-Ta_3TeI_7 xtals + *hc*-Ta_3TeI_7 xtals + Ta_6I_{14}	p169nb4
540 - 500°C	Δ-Ta_3TeI_7 + Ta_6I_{14} + $TaOI_2$	p37nb5
11. 450°C, 3wks	*hc*-Ta_3TeI_7 + Δ-Ta_3TeI_7 + Ta_6I_{14}/TaI_5	p6nb4
450 - 440°C, 9d	Δ-Ta_3TeI_7 xtals + *hc*-Ta_3TeI_7 xtals	p188nb4
450 - 425°C, 10d	Δ-Ta_3TeI_7 xtals + *hc*-Ta_3TeI_7 xtals	p188nb4
625°C, 17d	Ta_6I_{14} + Ta_2O_5 + Nb_3Te_4-like pattern	p65nb5
485°C, 16d	*hc*-Ta_3TeI_7 + Δ-Ta_3TeI_7 + orange unk.	p117nb5

12. 500°C, 2 wks	Ta + Δ-Ta_3TeI_7 + *hc*-Ta_3TeI_7 (minor) + Ta_6I_{14}	p283nb3
13. 540 - 440°C, 5d	Ta + Δ-Ta_3TeI_7 + Ta_6I_{14} + TaI_5	p51nb4
14. 540°C, 21d	Quantitative yield Δ-Ta_3TeI_7 (large scale)	p187nb4
15. 540°C, 9d	Ta + *hc*-Ta_3TeI_7 + Ta_6I_{14}/TaI_5	p37nb4
16. 600°C, 9d	TaI_5 + Ta_6I_{14} + unknown***	p112nb3
17. 700°C, 9d	TaI_5 + unknown***	p112nb3
18. 800°C, 9d	TaI_5 + unknown black powder (strong)***	p112nb3
19. 850 - 800°C, 10d	TaI_5 + unknown***	p5nb3

***Same unknown: a velvety black nonlustrous powder, chalky feel in mortar.

Ta_4TeI_7

Rationale: incorporation of more Ta into the vacancy site??
Reactions:

1. 435°C, 10d	Ta, *hc*- + Δ-Ta_3TeI_7	p57nb7
500°C, 14d	Ta, *hc*-Ta_3TeI_7, Δ-Ta_3TeI_7, Ta_6I_{14}.	p77nb7

Ta_3TeI_6

Rationale: To prepare a chalcogen-substituted hexanuclear Ta_6X_{12}-containing phase
Reactions:

1. 675°C, 9.5d	Ta_6I_{14} + unknown***	p160nb4
500°C, 25d	Δ-Ta_3TeI_7 + Nb_3Te_4-like pattern + TaI_5	p206nb4

$Ta_3Te_2I_5$

Rationale: Attempt to make "$Ta_6Te_{4-x}I_{10+x}O$" (see Appendix B).
Reactions:

1. 675°C, 10.5d	$TaTe_2$ + unknown***	
2. 470 - 430°C, 10d	"much unreacted stuff, no visible mC xtals"	p81nb4
675 - 650°C, 10.5d	Ta_6I_{14}/TaI_5 + Ta_2O_5 + unknown***	

These two reactions were combined, and then heated as below:

827°C, 10d	TaI_5 + Nb_3Te_4-like pattern (diff. unknown)	p237nb4
3. 450°C, 17d	*hc*-Ta_3TeI_7 + Δ-Ta_3TeI_7 + $TaTe_2$	p102nb4

$TaTeI_2$

Rationale: Attempt to make ZrI_3-type Ta-Te-I phase seen as side product in an earlier reaction ($Ta_6Te_6I_8O$, 432°C, 17d; p15nb5)

Reactions:

1. 430°C, 21d	*hc*-Ta_3TeI_7 + Δ-Ta_3TeI_7 + $TaTe_2$ + TaI_5	p19nb7

Ta-Se-I:

Reaction / annealing temperature	Products identified by Guinier powder diffraction	notebook & page #
Ta_3SeI_7		
1. 500°C, 18d	*hc*-Ta_3SeI_7 + Ta_6I_{14}	p284nb3
450°C, 20d	*hc*-Ta_3SeI_7 xtals transported	p19nb4
2. 450°C, 14d	*hc*-Ta_3SeI_7 + Ta_6I_{14} + unknown**	p28nb4
3. 550 - 450°C, 14d	*hc*-Ta_3SeI_7 + Ta_6I_{14} only. Good transport.	p92nb4
4. 450°C, 16d	*hc*-Ta_3SeI_7 + Ta_6I_{14}	p232nb3
450°C, 2wks	*hc*-Ta_3SeI_7 + unknowns	p114nb4
5. 450°C, 3wks	Ta + *hc*-Ta_3SeI_7 + Ta_6I_{14}/TaI_5	p277nb3
6. 450°C, 3wks	*hc*-Ta_3SeI_7 + Ta_6I_{14} + TaI_5	p7nb4
575°C, 9d	*hc*-Ta_3SeI_7 + Ta_6I_{14} + unknown**	p170nb4
827°C, 10d	Tube attack: TaO/Ta_2Si + unknowns**	p237nb4

$Ta_3Se_{1.6}I_7$

Rationale: Error in loading led to excess Se in these reactions.

Reactions:

1. 450°C, 7d	*hc*-Ta_3SeI_7 + Ta_6I_{14} + unknown**	p34nb4
2. 540°C, 9d	Ta_6I_{14} + unknown**	p36nb4
3. 450°C, 14d	*hc*-Ta_3SeI_7 + unknown** + TaI_5	p45nb4
4. 530 - 440°C, 5d	Ta + *hc*-Ta_3SeI_7 + unknown** + TaI_5	p48nb4

Ta_3SeI_6

Rationale: To prepare a chalcogen-substituted octahedral Ta_6X_{12}-containing phase

Reactions:

1. 675°C, 9.5d	unknown** + TaI_5 + Ta_2O_5	p161nb4
500°C, 25d	*hc*-Ta_3SeI_7 + Ta_6I_{14} + TaI_5 + unknown**	p205nb4

Ta_4SeI_{11}

Rationale: Attempt to make selenium analogue of Ta_4SI_{11}

Reactions:

1. 425°C, 17d	*hc*-Ta_3SeI_7 + Ta_6I_{15} + Ta_6I_{14}/TaI_5 + unknown**	p133nb5
500°C, 24d	*hc*-Ta_3SeI_7 + Ta_6I_{14} + TaI_5 + couple weak lines?	p55nb7

Ta-S-I:

Note: Frequently the same unknown phase, identified below as unknown "A" was observed. This phase was a non-lustrous, black powder that diffracted poorly (broad peaks, weak pattern).

Reaction / annealing temperature	Products identified by Guinier powder diffraction	notebook & page #
Ta_3SI_7		
1. 400°C, 13.5d	*hc*-Ta_3SI_7 + *o*-Ta_3SI_7 + Ta_4SI_{11} + TaI_5	p191nb4
440°C, 17d	maj. *o*-Ta_3SI_7 + Ta_6I_{14}	p71nb7 (II)
2. 425°C, 2 wks	*o*-Ta_3SI_7 + Ta_6I_{14} + little Ta_4SI_{11}	p8nb5
545 - 505°C,		p23nb8
3. 430°C, 15d	*o*-Ta_3SI_7 + Ta_6I_{14}/TaI_5 + unknown "A"	p85nb7
4. 440°C, 17d	maj. *o*-Ta_3SI_7 + Ta_4SI_{11} + Ta_6I_{14}	p71nb7 (I)
505 - 485°C,		p23nb8
5. 450°C, 16d (#1)	*o*-Ta_3SI_7 + Ta_6I_{14} + TaI_5	p233nb3
450°C, 17d	*o*-Ta_3SI_7 + Ta_6I_{14}/TaI_5 + $TaOI_2$	p89nb4
6. 450°C, 14d	*hc*-Ta_3SI_7 + Ta_4SI_{11} + Ta_6I_{14}/TaI_5 + unknown "A"	p23,32nb4

7. 450°C, 14d	*hc*-Ta_3SI_7 + Ta_4SI_{11} + Ta_6I_{14}/TaI_5 + unknown "A"	p26nb4
8. 450°C, 7d	*o*-Ta_3SI_7 + Ta_6I_{14}/TaI_5	p33nb4
9. 450 - 350°C, 9d	Ta_4SI_{11} + Ta_6I_{14}/TaI_5	p100nb4
10. 450 - 350°C, 14d	Ta_4SI_{11} + Ta_6I_{14}/TaI_5 + unk. "A"	p91nb4
450°C, 10d	Ta_4SI_{11} + Ta_6I_{14}/TaI_5 + unk. "A"	p131nb4
11. 450°C, 3.5d	*o*-Ta_3SI_7, Ta_6I_{14}/TaI_5	p174nb4
450 - 440°C, 10d	*hc*-Ta_3SI_7 + *o*-Ta_3SI_7 + Ta_4SI_{11} + Ta_6I_{14}/TaI_5	p174nb4
12. 500°C, 16d	*o*-Ta_3SI_7 + *hc*-Ta_3SI_7 + Ta_6I_{14}	p285nb3
575°C, 9d	Ta_6I_{14}/TaI_5 + $TaOI_2$ + unknown "A":	
13. 525°C, 17d	Ta_6I_{14} + TaI_5 + unk. "A" (black powder)	
14. 530 - 440°C, 5d	Ta + Ta_4SI_{11} + Ta_6I_{14}/TaI_5 + unknown "A"	p47nb4
15. 675°C, 10.5d	TaI_5 + few unknowns (TaO?)	p164nb4
16. 675 - 650°C, 10.5d	TaS_2 + Ta_6I_{14}	p165nb4
440°C, 17d	Ta_6I_{14}/TaI_5 + unknown "A"	p73nb7
550 - 440°C,	unopened	p25nb8

$Ta_3S_2I_7$

1. 430°C, 15d	*o*-Ta_3SI_7 + Ta_6I_{14}/TaI_5 + unknown "A"	p85nb7

Ta_3SI_6

1. 675°C, 10d	Ta_6I_{14}/TaI_5 + unknown! (*not* "A")	p162nb4

Ta_3SI_5

1. 432°C, 17d	*o*-Ta_3SI_7 + unknown "A" (black powder)	p19nb5
2. 432°C, 20d	*o*-Ta_3SI_7 + Ta_4SI_{11} + unknown (weak)	p71nb5
525°C, 16d	Ta_6I_{15} + at least two unknowns (not "A")	p119nb5
430°C, 17d	No transport, starting powder	p57nb6
545 - 505°C, 30d	Ta_6I_{14} + unknown ("A" ?)	p43nb7
3. 430°C, 15d	*o*-Ta_3SI_7 + Ta_6I_{14} +unknown "A"	p87nb7

The above three products combined into 4. :

4. 550 - 440°C,	unopened	p23nb8

Ta_2SI_4

1. 430°C, 15d	Ta_4SI_{11} + Ta + unknown "A"	p87nb7

Ta_2SI_3

1. 432°C, 17d	Ta metal + Ta_4SI_{11} (big xtals) + unk. "A"	p17nb5

Ta_2SI_2

1. 430°C, 15d	*o*-Ta_3SI_7 + Ta_4SI_{11} + unknown "A" + other unknowns	p89nb7

Ta_2SI

1. 450°C, 7d	Ta metal + unknown "A" (large yield)	p208nb4
535°C, 20d	Ta metal + TaS_2 (MoS_2) + unknown "A"	p83nb5
2. 500°C, 13d	2H-TaS_2 + I_2 + Ta_6I_{14}	p93nb5

TaS_2I

1. 450°C, 7d	TaS_2 + I_2	p209nb4

$TaSI_2$

1. 450°C, 7d	TaS_2 (MoS_2 type) + TaI_5	p210nb4

Ta_4S_6I

1. 432°C, 17d	Unknown grey fibers! + TaS_2 + I_2	p21nb5
535°C, 20d	TaS_2 + weak lines (unknown "A")	p79nb5
2. 500°C, 13d	TaS_2 (MoS_2 type) + I_2 + unknown (not "A")	p95nb5

Ta_4SI_{11}

1. 432°C, 20d	Ta_4SI_{11} + trace Ta_6I_{14}/TaI_5 + unknown "A"	p73nb5
2. 450°C, 14d	*o*-Ta_3SI_7 + Ta_4SI_{11} + Ta_6I_{14}/TaI_5 + unknown "A"	p70nb7

$Ta_7S_2I_{19}$

1. 470 - 430°C, 17d	Ta + Ta_4SI_{11} + Ta_6I_{14}/TaI_5 + unknown "A"	p101nb4
2. 400°C, 13.5d	*o*-Ta_3SI_7 + Ta_6I_{14} / TaI_5	p191nb4

BROMIDES

Ta-Te-Br:

Ta_3TeBr_7

Reaction / annealing temperature	Products identified by Guinier powder diffraction	notebook & page #
1. 450°C, 8d	Ta + $TaTe_2$ + Ta_3TeBr_7 + $TaBr_5$	p24nb4
450°C, 21d	Ta_3TeBr_7 + $TaBr_5$	p73nb4
2. 550°C, 12.5d	Ta_3TeBr_7 + Ta_6Br_{15} + Ta_6Br_{14} + $TaBr_5$	p84nb4
3. 500°C, 20d	Ta_3TeBr_7 xtals (major) + $TaOBr_2$	p194nb4
Combined prod. from 2 & 3:		
550 - 450°C,	good transport, large crystal mass	p23nb8
4. 500°C, 18d	Ta_3TeBr_7 + Ta	p60nb4
505 - 495°C, 6 wks	Starting powder, little $TaBr_5$	p203nb4
515 - 500°C, 10d	Unchanged powder, No crystal transport	p222nb4
530 - 500°C, 14d	Rough Ta_3TeBr_7 crystals, $TaOBr_2$	p256nb4
575 - 500°C, 14d	No crystals	p63nb6
575 - 550°C, 14d	Transport of many XRD candidates	p63nb6
5. 550 - 450°C, 14d	Ta + Ta_3TeBr_7 + Ta_6Br_{15} + Ta_6Br_{14}	p87nb4
545 - 505°C, 3d	Ta_3TeBr_7 + $TaOBr_2$ + weak lines	p25nb5
550 - 425°C, 21d	Good Ta_3TeBr_7 xtal transport	p17nb6

Ta-Se-Br:

Ta_3SeBr_7

Reaction / annealing temperature	Products identified by Guinier powder diffraction	notebook & page #
1. 450°C, 8d	Ta + $TaSe_2$ (?) + $TaBr_5$	p31nb4
450°C, 21d	Ta + polycrystalline Ta_3SeBr_7 + $TaBr_5$	p74nb4
550 - 425°C, 21d	Good transport. Ta_3SeBr_7 XRD xtals.	p17nb6
575 - 500°C, 2 wks	Transport of intergrown Ta_3SeBr_7	p63nb6
575 - 550°C, 30d	Ta_3SeBr_7 xtals + Ta_6Br_{15} + $TaBr_5$	p13nb7
2. 500°C, 15.5d	Ta + Ta_3SeBr_7 + ?	p288nb3
3. 500°C, 18d	Ta_3SeBr_7 xtals (CR260) + Ta + TaBr5 +	p61nb4
4. 500°C, 20d	Ta_3SeBr_7 + Ta_6Br_{15}	p195nb4
5. 550°C, 12.5d	Ta_3SeBr_7 + Ta_6Br_{15}	p83nb4
505 - 495°C, 6wks	Ta_3SeBr_7 + $TaBr_5$ + Ta_6Br_{14}	p202nb4
515 - 500°C, 14d	No crystal transport	p222nb4
530 - 500°C, 14d	Ta_3SeBr_7 xtals + $TaOBr_2$ + $TaBr_5$	p202nb4
6. 550 - 450°C, 14d	Ta + Ta_3SeBr_7 + Ta_6Br_{15} + $TaBr_5$	p86nb4
545 - 505°C, 3d	Starting powder + $TaOBr_2$ + $TaBr_5$	p27nb5

Ta-S-Br:

Ta_3SBr_7

Reaction / annealing temperature	Products identified by Guinier powder diffraction	notebook & page #
1. 450°C, 8d	Ta + Ta_3SBr_7 + $TaBr_5$ + unknown	p30nb4
450°C, 20d	Ta + Ta_3SBr_7 + Ta_6Br_{15} + $TaBr_5$	p75nb4
550 - 425°C, 21d	Rounded Ta_3SBr_7 pieces + crystals.	p19nb6
575 - 500°C, 14d	Excellent Ta_3SBr_7 crystals	p63nb6
575 - 550°C, 4wks	Ta_3SBr_7 crystals + $TaBr_5$ + Ta_6Br_{14}	p13nb7
2. 500°C, 18d	Ta_3SBr_7 + Ta_6Br_{15} + Ta + $TaBr_5$	p62nb4

3. 550°C, 12.5d	$Ta_3SBr_7 + Ta_6Br_{15} + TaBr_5$	p82nb4
505 - 495°C, 6wks	1st Ta_3SBr_7 crystals + $Ta_6Br_{15} + TaBr_5$	p201nb4
4. 550 - 450°C, 14d	$Ta_3SBr_7 + Ta_6Br_{15} + Ta_6Br_{14} + TaBr_5 + Ta$	p85nb4
505 - 495°C, 37d	unopened	p29nb5

CHLORIDES

Ta-Te-Cl:

Ta_3TeCl_7

Reaction / annealing temperature	Products identified by Guinier powder diffraction	notebook & page #
1. 300°C, 4wks	$Ta + TaTe_4 + Ta_3TeCl_7 + TaCl_5$	p129nb2
2. 450°C, 16d	weak $Ta_3TeCl_7 + TaTe_2 + TaCl_5 + Ta$	p234nb3
3. 500°C, 18d	Ta_3TeCl_7 (best xtal) + $TaTe_2 + Ta + TaCl_5$	p58nb4
4. 550°C, 12.5d	(tube cracked) $Ta_3TeCl_7 + Ta_2O_5 + Ta + Ta_6Cl_{15}$	p76nb4
5. 550 - 450°C, 10d	mostly Ta_3TeCl_7 + Ta + white solid	p97nb4
6. 500°C, 15.5d	$Ta_3TeCl_7 + Ta_6Cl_{15}$	p286nb3
500°C, 39d	$TaTe_2 + Ta_6Cl_{15}$ + unknown!	p121nb4
7. 500°C, 3 wks.	Ta_3TeCl_7	p127nb6
550 - 450°C, 3d	Bad. Domes of rounded flakes.	p21nb8

Ta-Se-Cl:

Ta_3SeCl_7

Reaction / annealing temperature	Products identified by Guinier powder diffraction	notebook & page #
1. 500°C, 15.5d	$Ta_3SeCl_7 + Ta + Ta_6Cl_{15} + TaCl_5$ (small)	p287nb3
500°C, 39d	Ta_6Cl_{15} + unknown	p122nb4
2. 500°C,	Ta, thin grey film, brown solid	p39nb4
3. 500°C, 18d	$TaSe_2 + Ta + TaCl_5$ + little Ta_3SeCl_7	p58nb4

4. 550 - 450°C, 10d	Ta_3SeCl_7 + Ta + $TaCl_5$	p98nb4
515 - 500 °C, 10d	No transport	p222nb4
530 - 500°C, 14d	No transport	p256nb4
550 - 425°C, 21d	Thin grey film transported + starting powder	p19nb6
575 - 500°C, 30d	Thin grey film transported + starting powder	p19nb6
575 - 550°C, 14d	Tiny crystals transported + starting powder	p19nb6
5. 550°C, 12.5d	Ta + Ta_3SeCl_7 + Ta_6Cl_{15} + $TaCl_5$	p77nb4

Ta_3SCl_7

Reaction / annealing temperature	Products identified by Guinier powder diffraction	notebook & page #
1. 475°C, 25 d	Ta, yellow solid, grey film (transported)	p125nb6
700°C, 7 d; 475°C, 2 wks	loaded,	p9nb8
2. 500°C	Ta, yellow-orange solid, grey thin film	p39nb4
500°C, current		
3. 500°C, 18d	TaS_2 + Ta + yellow-orange air-sensitive solid	p57nb4
4. 550 - 450°C, 10d	Ta_6Cl_{15} + TaS_2 + Ta + $TaCl_5$	p99nb4
5. 550°C, 12.5d	Ta + $TaCl_5$ + Ta_3SCl_7 / TaS_2 (? - unclear)	p78nb4
500°C, 39d	Ta_6Cl_{15} + unknown	p123nb4

APPENDIX B. ADDITIONAL DISCOVERIES

The purpose of this Appendix is to relate information about some very interesting compounds inadvertently discovered during the course of the diverse investigations of the Ta-Q-X and related systems (mixed-metal, quaternary), that formed the subject of this thesis. These compounds are not included in the main part of the thesis because their synthesis is not always reproducible, and/or because characterization is not complete due to difficulties in making enough of the pure material. However, discussing such enticing gems provides a glimpse into the possibilities of the relatively unexplored Ta-Q-X system, and a starting point for possible future research.

I. $Ta_6Te_{4-x}I_{10+x}Z$. (x unknown, Z probably oxygen).

Initial discovery: from "Ta_3TeI_7" reactions using tantalum foil treated with HF/HNO_3 before use. A few rectangular bar crystals formed in the tube, visually quite different from the abundant hexagonal or trigonal *hc*-Ta_3TeI_7 and Δ-Ta_3TeI_7 crystals. Guinier powder diffraction showed a very unusual, highly distinctive pattern, reproduced below from a single crystal solution (Figure B1).

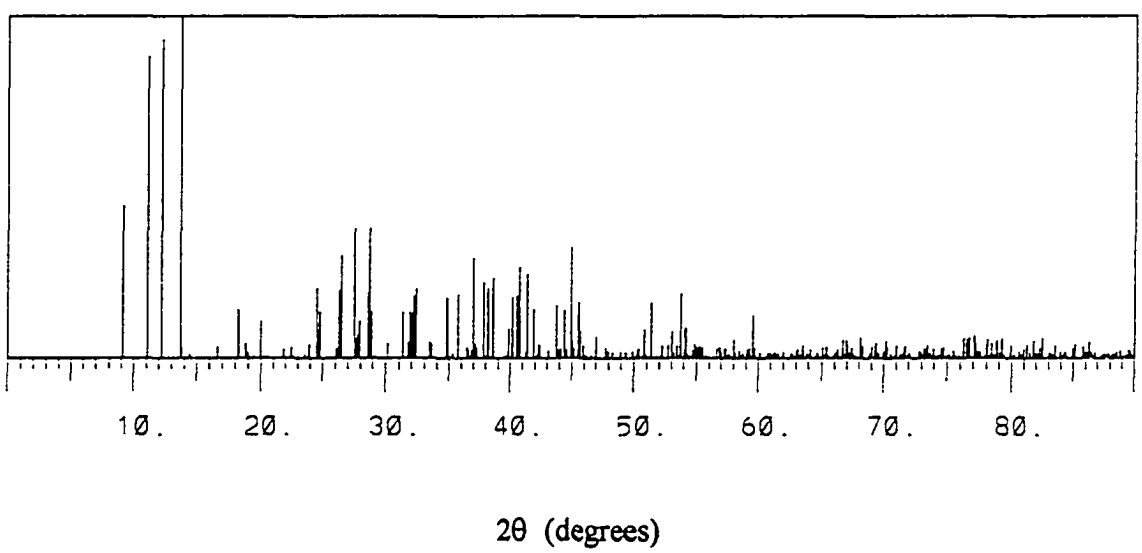

Figure B-1. The Guinier diffraction pattern of "$Ta_6Te_{4-x}I_{10+x}O$".

Acceptable single crystals of this phase were selected, and its structure solved from intensity data collected on the Siemens P4. A summary of important crystallographic information is given in Table B1.

Table B-1. Available crystallographic information for "$Ta_6Te_{4-x}I_{10+x}O$"

Space group	C2/m
Unit cell dimensions (Å, °)	
a	16.831(3)
b	12.244(2)
c	7.640(2)
β	108.31(3)
Volume	1494.7(5)
Z	2
Data ($2\theta_{max}$ = 50°)	1384 total, 1184 observed (> 2σ)
R_{int}	0.0253
R1 / wR2 (observed)	0.0358 / 0.0834
GoF	1.079
Fourier map	2.21 and -1.95 e^- / $Å^3$

Atomic positions and isotropic thermal parameters

Atom	x	y	z	U_{iso}
Ta1	0.0	0.18087(6)	0.5	0.0163(2)
Ta2	0.08190(3)	0.38001(5)	0.62626(7)	0.0167(2)
I1	0.03824(9)	0.0	0.2981 (2)	0.0236(3)
I2	0.13725(9)	0.5	0.9653 (2)	0.0291(4)
I3	0.16602(7)	0.18227(8)	0.7556 (2)	0.0320(3)
I4	0.22024(9)	0.5	0.5780 (3)	0.0349(3)
Te	-0.05444(6)	0.30416(8)	0.7371 (1)	0.0224(3)
"O"	0.0	0.5	0.5	0.032 (5)

Structure: The structure of this phase consists of centered, planar Ta_6 clusters, linked together to form one-dimensional chains by four bridging atoms. These chains run parallel to the crystallographic *b* axis. The Ta_6 clusters can be viewed as two trinuclear clusters joined together by two Ta-Ta bonds linking two vertices of each trinuclear cluster fragment. The square formed by such a linkage is apparently centered by a small atom. Each trinuclear cluster fragment is bicapped (above and below) by an atom, and coordinated by eight other anions. Each metal atom is eight-coordinate, and has a similar coordination environment as the tantalum atoms in Ta_3QX_7: distorted octahedral coordination by the anions with one face of the octahedron opened to accomodate two metal-metal bonds. Two structural views are shown below (Figures B2 and B3), with bond lengths and angles.

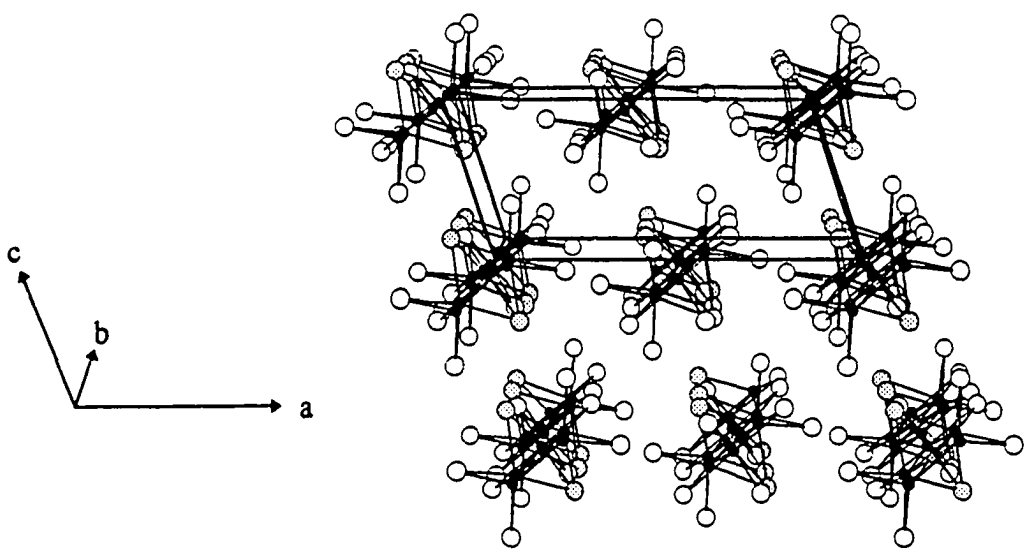

Figure B-2. View of the packing of the one-dimensional chains running parallel to the *b* axis.

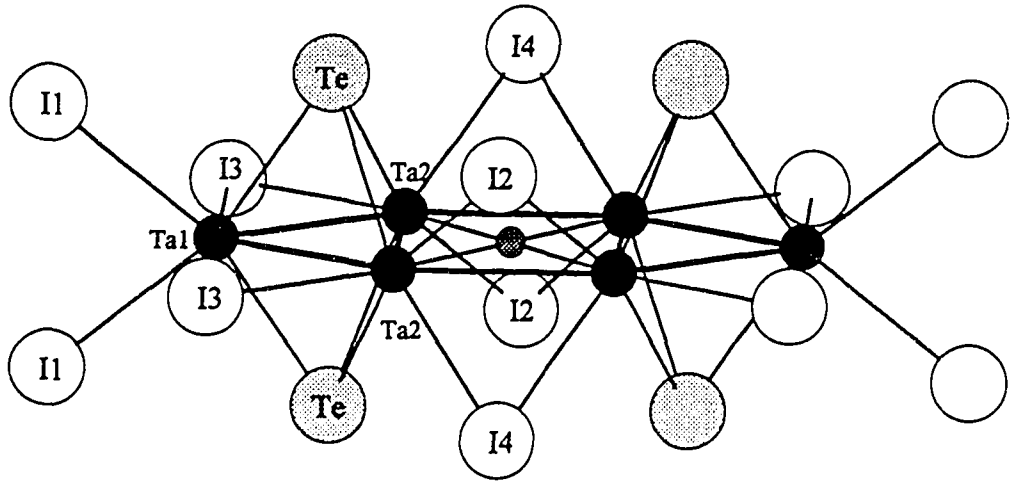

Bond Distances (Å) and Angles (°)

Ta1-Ta2	2.818(1)	Ta2-Ta1-Ta2	60.17(3)
Ta2-Ta2	2.825(2) (triangle)	Ta1-Ta2-Ta2	59.92(2)
Ta2-Ta2	2.938(1) (square)	Ta2-Ta2-Ta2	90.0
Ta1-Te	2.728(1)	Ta2-O-Ta2	87.75(4) (tri)
Ta1-I1	2.884(1)	Ta2-O-Ta2	92.25(4) (sq)
Ta1-I3	2.862(1)	Ta1-Te-Ta2	60.97(3)
Ta2-Te	2.824(2)	Ta2-Te-Ta2	59.83(4)
Ta2-I2	2.867(1)	Ta2-I2,4-Ta2	61.58(4)
Ta2-I4	2.873(1)	Ta1-I3-Ta2	59.43(3)
Ta2-"O"	2.038(1)	Ta1-I1-Ta1	100.30(5)

Figure B-3. The cluster unit, with bond distances and angles. The small dark grey atom, assigned as oxygen, sits on a crystallographic inversion center. The I1 atoms provide bridges to the Ta1 atoms in other clusters.

Problems: There are three major problems hindering full understanding of this phase:

1. The tellurium / iodine problem: X-ray diffraction cannot distinguish between Te and I due to similar scattering factors. Both Te and I have been verified in the structure from x-ray photoelectron spectroscopy, but the distribution of the two is only speculative. Several synthetic attempts to solve this problem by systematically varying the Te / I ratio over all possibilities failed (see 3., below). In the solution above, the tellurium atoms have been placed in role of the trinuclear cluster capping atom, by analogy to Ta_3TeX_7, and because iodine has never been observed in this role.
2. The nature of the small atom in the center of the square of Ta atoms caused by the "joining" of the two Ta_3 units. The bond distance from this site to the four surrounding tantalum atoms is 2.0380(7) Å. This is a reasonable length for an element in the first or second period only: H through F. The XPS experiment did not detect any elements other than C and O, which unfortunately are always present in samples. The detection of these elements, then, could be real or simply the usual adventitious presence of C and O. Another, more insidious possibility, is that the electron density building up on this site is a crystallographic artefact, and is not due to a real atom. This site is a special position (0,0,0) and is located at the center of four heavy tantalum atoms. However, if this atom is removed, a peak of near 10 $e^-/Å^3$ registers in the Fourier map. This is rather large, and indicates a valid scattering source.
3. Non-reproducible synthesis. This compound has only been found as a very minor side product in certain Ta_3TeI_7 and Ta_2NbTeI_7 tubes. Numerous attempts to make the compound in larger yield have all failed. These attempts were carried out by systematically varying the Te / I ratio, that is, varying the x in "$Ta_6Te_{4-x}I_{10+x}O$" from 4 to -10 ($Ta_6I_{14}O$ to $Ta_6Te_{14}O$), and heating at 450°C for two weeks. Also, all reasonable small atoms were tried: H (TaH source), B, C, N (TaN source), O (Ta_2O_5 source), F (CaF_2 source). Although these various reactions did lead to the discovery of some new compounds (below), the target phase never formed.

Interestingly, the one "clue" to this compound is that it only formed when one particular batch of Ta metal was used: Ta foil, 0.127 mm thick, which was washed with an HF / HNO_3 solution and dried in air in a drying oven (120°C) before use. When Ta metal pre-treated with the proper $HF/HNO_3/H_2SO_4$ cleaning solution is used, no compound formation was observed. The reason for this is unknown.

II. $TaTe_xI_{3-x}$ ($x \approx 1$).

One of the many systematic reactions designed to grow the $Ta_6Te_{4-x}I_{10+x}O$ cluster phase discussed above was "$Ta_6Te_6I_8O$", which resulted in the discovery of another new tantalum chalcogenide halide compound. Reaction between Ta foil, Ta_2O_5, Te and I_2 according to Equation (1),

$$28\ Ta\ (foil) + Ta_2O_5 + 30\ Te + 20\ I_2 = 5\ \text{“}Ta_6Te_6I_8O\text{”} \qquad (1)$$

at 430°C for ca. two weeks in evacuated pyrex tubes yielded brittle, reflective black solid chunks with distinct hexagonal facets. This was a minor phase (visual estimate 3-5% total product), the majority products being Ta_3TeI_7, $TaTe_2$, $TaOI_2$, Ta_6I_{14} and TaI_5. X-ray photoelectron spectroscopy verified the presence of Ta, Te and I in two independent samples, and gave a composition of "$TaTe_{0.87}I_{2.17}$" The Guinier powder pattern of the black solid was simple, sharp, and could be matched exactly to the ZrI_3-type structure. This structure has generated controversy over the years, initially being solved in the hexagonal system, but later assigned to primitive orthorhombic symmetry on the basis of a few extremely weak reflections.[95] Crystals of "$TaTe_xI_{3-x}$" were obtained by chipping small pieces from the larger chunks that formed in the reaction tubes, using a scalpel. Data sets were collected on both the Siemens P4 and on an AFC6R diffractometer equipped with a rotating anode. On both diffractometers, a primitive hexagonal cell was easily indexed using several of the narrow, intense peaks. There was no indication of a different cell on either diffractometer, from axial photographs or from any of the search

routines available. However, this is reminiscent of the problems with ZrI_3, where the orthorhombic cell was chosen based on weak spots appearing in a Weissenberg photograph exposed for 40 hours; the cell could not be found even on a rotating anode diffractometer using a large crystal. With these previous ZrI_3 work in mind, intensity data sets of $TaTe_xI_{3-x}$ were also collected after manually transforming to the corresponding orthorhombic cell: a = 12.180(2) Å, b = 6.480(1) Å, c = 7.028(1) Å.

Based on the powder patterns and on the single crystal solution, $TaTe_xI_{3-x}$ is grossly isostructural with ZrI_3. Briefly, this structure is built up of one-dimension chains of face-sharing $Ta(Te/I)_{6/2}$ octahedra running parallel to the hexagonal c-axis. Within the chains, the metal atoms alternate short and long distances, due to Ta-Ta dimer formation. Structural views are shown in Figure B-4. Crystallographic information is in Table B-2.

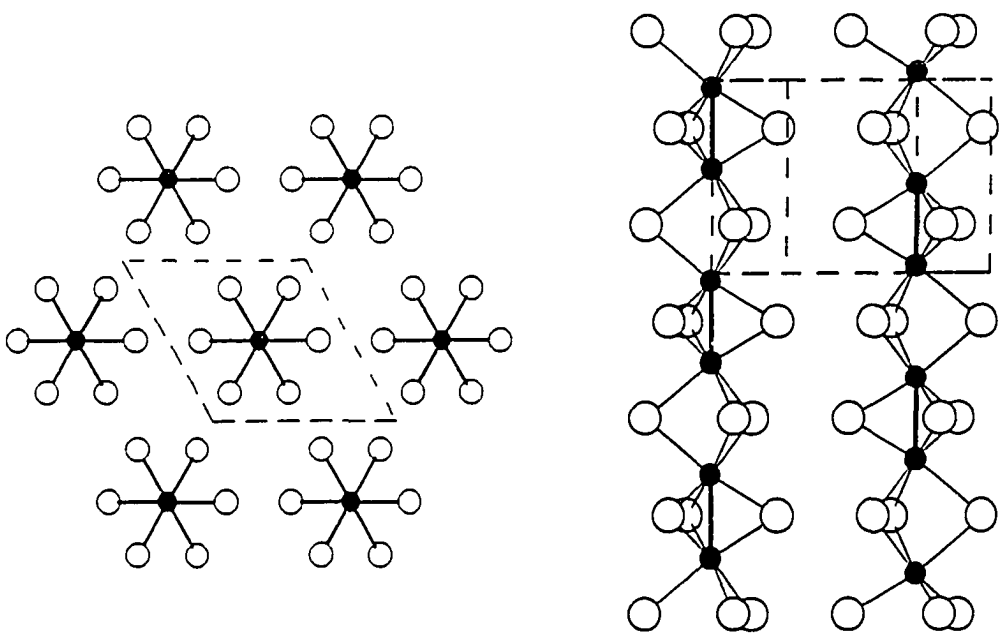

(a) [001] view

(b) view of the Ta-Ta dimers within the $TaTe_xI_{3-x}$ chains

Figure B-5. Structural views of $TaTe_xI_{3-x}$. Black circles, Ta; Open circles, Te/I.

Table B-2. Available crystallographic information for "$TaTe_xI_{3-x}$"

Space group	$P6_3/mcm$
Unit cell dimensions (Å)	
a	7.029(1)
c	6.479(1)
Volume (Å^3)	277.22(7)
Z	2
Data ($2\theta_{max}$ = 55°)	676 total, 134 unique
R_{int}	0.0588
R1 / wR2 (all)	0.0304 / 0.0565
GoF	1.234
Fourier map	1.103 and -1.250 e$^-$/Å^3

Atomic positions and isotropic thermal parameters

Atom	x	y	z	U_{iso}
Ta	0.0	0.0	0.0396(2)	0.0195(5)
Te/I	0.0	0.3228(1)	0.25	0.0227(4)

Anisotropic displacement parameters

Atom	U_{11}	U_{22}	U_{33}	U23	U13	U12
Ta	0.0200(4)	0.0200(4)	0.0185(13)	0.0	0.0	0.0100(2)
Te/I	0.0319(6)	0.0212(4)	0.0188 (5)	0.0	0.0	0.0159(3)

The best solution was obtained in the space group $P6_3/mcm$ (see Table B-2). This high symmetry space a mirror plane at $z = 0$. The metal atoms therefore are constrained to the centers of their octahedral holes (i.e. 0,0,0), resulting in a uniform Ta-Ta distance. Refining the structure this way results in large U_{33} thermal displacement factors for the Ta atoms and high R-factors, both of which indicate the true structure involves dimerization. This problem was circumvented and the pairing of the metals was included by refining the metal positions as half-occupied split positions. The Ta *z*-coordinate is slightly off-center of (0,0,0), a position which generates an extra Ta-Ta dimer in the space where the long

Ta-Ta length should be in the correct structure. The structure was solved by allowing both the tantalum *z*-coordinate and the site occupation factor to vary. This approach led to an exactly half-occupied Ta position, with $z = 0.0399$. The resulting bond distances (d(Ta-Ta) = 2.725(2), 3.242(2) Å) are very reasonable for a strongly bound Ta-Ta dimer. Of course, the Te/I content cannot be resolved from the x-ray diffraction experiment, but based on the XPS data, the anion matrix is presumably roughly 2:1 I:Te.

Attempts were made to solve the structure in the reported orthorhombic setting, after manual transformation of the hexagonal cell. A complete sphere of data were collected (triclinic symmetry, no restrictions), and the solution was attempted using the ZrI_3 orthorhombic cell shape and atomic positions. The results were puzzling: The data (which could be solved to R1/wR2 = 0.0277/0.0557 in $P6_3/mcm$), would not solve acceptably in the orthorhombic system, even though Ta-Ta and Ta-I bond distances were very close to those obtained from the hexagonal solutions. Also, attempts to synthesize this phase from the elements by loading stoichiometric "$TaTeI_2$" yielded only binaries and Ta_3TeI_7 compounds.

III. "Ta_6I_{18}"

Under the pretense that the small atom in the center of the Ta_6 cluster might be fluorine (HF is used to clean the metal before use), reactions using CaF_2 were carried out. (No TaF_5 was available at the time.) The reaction described by Equation (2) was carried

$$0.5\ CaF_2 + 3\ Ta\ (foil) + Te + 7.5\ I_2 = Ca_{0.5}Ta_3TeI_7F \qquad (2)$$

out at 450°C for two weeks in an evacuated pyrex tube. The majority of the product was identifiable material (*hc*-Ta_3TeI_7, Ta_6I_{15}, CaF_2), but a few small reflective black well-faceted crystals formed, transported to the opposite end of the tube. An insufficient amount of the material formed for any characterization methods besides SEM and x-ray diffraction. The Guinier pattern was similar to that of Ta_6I_{15}, but with each Ta_6I_{15} line split into three. SEM showed strong Ta and I; no other elements (e.g. Ca) were unambiguously detected. A few crystals of the material were chipped from the larger

brittle chunks, and intensity data were collected. A summary of important crystallographic information is listed in Table B-3.

Structure: This compound apparently contains discrete Ta_6I_{18} clusters based on the $[Ta_6I_{12}]$ unit, with an additional six "terminal" iodides at the metal vertex positions. The hexanuclear metal core is not octahedral, but flattened slightly in the crystallographic *c*-direction. These cluster units pack as shown in Figure B-4. An expanded view of the Ta_6I_{18} cluster is shown in Figure B-5, with bond distances. All Ta-Ta and Ta-I bond distances are all reasonable, in fact very similar to those in Ta_6I_{14} and Ta_6I_{15}.

Table B-3. Available crystallographic information for "Ta_6I_{18}"

Space group	$R\bar{3}$
Unit cell dimensions (Å)	
a	17.011(2)
c	9.615(2)
Volume (Å^3)	2409.6(6)
Z	3
Data ($2\theta_{max}$ = 50°)	1263 total, 922 unique
R_{int}	0.0544
R1 / wR2 (all)	0.0609 / 0.0886
GoF	1.328
Fourier map	2.188 and -1.832 e$^-$/Å^3

Atomic positions and isotropic thermal parameters

Atom	x	y	z	U_{iso}
Ta	0.23159(5)	0.68020(5)	0.03177(8)	0.0139(3)
I1	0.01603(8)	0.13827(8)	0.1732 (1)	0.0179(3)
I2	0.07393(8)	0.56484(8)	0.1699 (1)	0.0184(3)
I3	0.26360(9)	0.23516(9)	0.1858 (1)	0.0244(4)
Q1[a]	1/3	2/3	1/6	
Q2[a]	0.1112(14)	0.6977(14)	0.3118(24)	

[a] Small peaks corresponding to these atomic positions appear in the Fourier map. If assigned to calcium, both refine to site occupation factors of ~ 0.2 Ca.

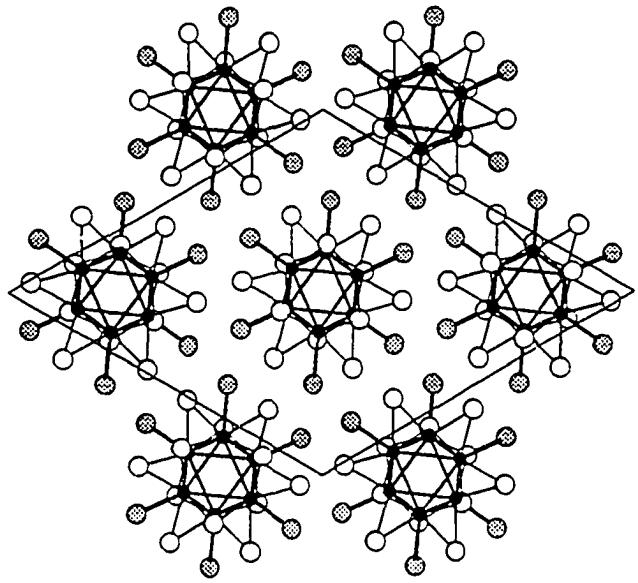

(a)

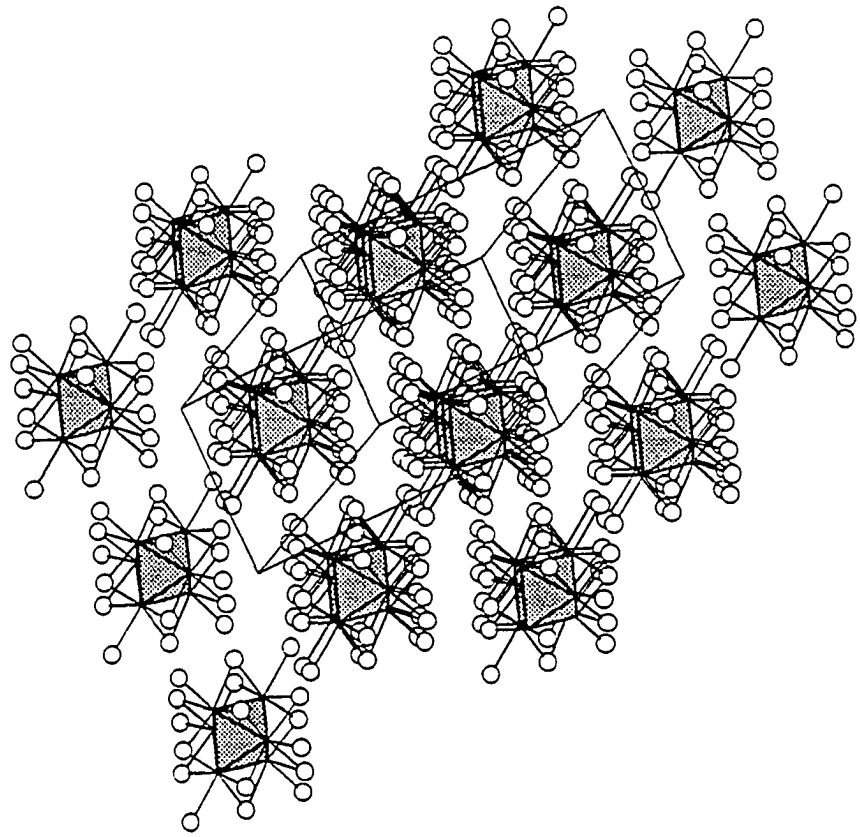

(b)

Figure B-4. Two views of the packing of the "Ta_6I_{18}" clusters. (a) View down [001], with the "terminal" atoms (I3) in grey. (b) Another view of the packing. Ta_6 clusters are shaded.

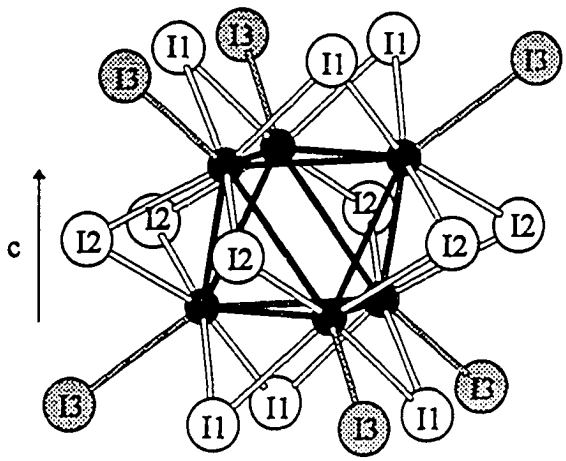

Bond distances in the Ta_6I_{18} clusters (Å)

Ta-Ta	3.190(1) ([001])
Ta-Ta	3.216(1) (*ab* plane)
Ta-I1	2.769(2), 2.773(2)
Ta-I2	2.758(1)
Ta-I3	2.960(2)

Figure B-5. Expanded view of a Ta_6I_{18} cluster.

In addition to the well-defined Ta_6I_{18} clusters, two additional peaks arise in the Fourier map, as shown in Table B-3. The first (Q1: 1/3, 2/3, 1/6), centers the Ta_6 cluster (d(Ta-Q1) = 2.2648(8) Å), and the second (Q2: 0.1112, 0.6977, 0.3118), is stuffed in between the Ta_6I_{18} clusters, d(Q2-I) = 2.44(2) - 3.39(2) Å, d(Q2-Ta) = 3.53(2) Å. These peaks are small, and if assigned to a calcium atom, both refine as ~20% occupied, giving "$Ca_{1.25}Ta_6I_{18}$". However, the identity (or even the veracity) of these peaks is uncertain.

A more serious problem with this phase is that of reproducibility. The few crystals obtained came from the first "$Ca_{0.5}Ta_3TeI_7F$" reaction attempted. Subsequent attempts to repeat the same experiment did not produce any of the compound, though the same reagents and synthetic conditions were used. Additionally, several other reactions involving Ca, and/or CaF_2 were done ($CaTa_6I_{18}$, $CaTa_3TeI_7$, $CaTa_3TeI_7F_2$, $CaTa_6Te_4I_{10}F_2$), all without success.

APPENDIX C:
OTHER MIXING STUDIES AND QUATERNARY AND INTERCALATION CHEMISTRY

Introduction

Along with the tantalum-niobium mixing studies discussed in Chapter Five, several other mixing studies were undertaken to explore the substitutional possibilities of the M_3QX_7 system. The studies discussed in this appendix are categorized as follows:

I. Chalcogen mixing. Simple substitution of one chalcogen for another, presumably at the capping site. This is particularly interesting is the case of sulfur, where the substitution of sulfur into an easily formed compound like *hc*-Ta_3TeI_7 could present another example of the stabilization of sulfur into a hexagonal Ta_3QX_7 phase (*hc*-Ta_3SI_7 does not form readily, *viz.* Chapter Two). For all chalcogen mixing studies discussed below, the iodide system was chosen due to the readiness with which the ternary iodides formed single crystals, leading to ease of characterization of the materials. Additionally, equimolar chalcogen ratios were chosen in all cases, i.e., all studies were carried out on "$Ta_3Q^a_{0.5}Q^b_{0.5}I_7$" systems.

II. Halogen mixing. A mixed-halogen matrix is especially interesting with a view toward the theoretical site-preference studies within the 3-1-7 framework discussed in Chapter One. The question to be addressed here is whether the halogens will sort themselves onto the various crystallographic sites by electronegativity, as the chalcogen apparently does. Two tantalum systems were chosen for study, $Ta_3TeI_3Cl_4$ and $Ta_3SeI_3Br_4$. In these compounds, using the various Mulliken populations calculated for Nb_3Cl_8 (Chapter One), the chalcogen should still occupy the cluster capping site. The halides, if the trend holds, should segregate (order) with the less electronegative

iodine occupying the least electron-rich site, the $\mu_3{}^a$ three-cluster bridging site. The second halide should occupy the remaining two crystallographic sites.

III. Other mixed-metal halides and chalcogenide halides. The understanding of the electronic structure of the Nb_3X_8 and M_3QX_7 systems suggests the possibility of incorporating a metal from another group of the periodic table into the trinuclear cluster. Especially considering the ease with which niobium was substituted into the various tantalum phases, substitution of a similar metal (Hf, Zr, Mo, eg.) is reasonable, and offers a tuning of the electron count at the cluster.

I. Chalcogen Mixing

$Ta_3Se_xTe_{1-x}I_7$ ($x = 0.5$)

Synthesis and Characterization

Smooth substitution of selenium and tellurium onto the cluster capping site was verified by the synthesis of $Ta_3Se_xTe_{1-x}I_7$, with $x \approx 0.5$ in high yield, using the same conditions that form the ternary selenide and telluride iodides.

The mixed selenide-telluride compound "$Ta_3Se_{0.5}Te_{0.5}I_7$" can be made readily by stoichiometric combination of the elements in the same temperature range as the corresponding ternaries Ta_3SeI_7 and Ta_3TeI_7, i.e., 450 to 550°C. Reaction times are also the same - one to two weeks, with quantitative conversion achieved in two to three weeks. The compound grows long hexagonal prism crystals, more similar to the morphology of *hc*-Ta_3TeI_7 than to *hc*-Ta_3SeI_7. Abundant single crystals can be grown by reaction of the elements, or by reheating premade powders, in a temperature gradient of 545-505°C, for several days. The Guinier x-ray powder diffraction pattern of "$Ta_3Se_{0.5}Te_{0.5}I_7$" showed the mixed compound to be isostructural with the two ternary endmembers ($x = 0$ and $x = 1$). Lattice constants and the exact chalcogen content were determined using single crystal

x-ray diffraction, on several crystals from a 545-505°C re-heating step. The single crystal data also confirmed the isostructurality of the mixed phase with Ta_3SeI_7 and Ta_3TeI_7. All data sets were collected in an identical manner, which information is given in Table C-1. Results of the solutions are also shown in Table C-1. In all cases, the refinement yielded Te:Se ratio near 0.6 : 0.4, slightly tellurium-rich. The lattice constants reflect the expected trend due to the different sizes of the two chalcogens, with the mixed compound having lattice constants midway between the pure ternaries. The mixed position was refined as a single site, and not as a split position consisting of selenium and tellurium at different distances from the Ta_3 cluster. The Ta-Q bond lengths therefore represent an average bond length, comprised of ca. 40% Ta-Se and 60% Ta-Te contributions. In all cases the Ta-Q length was determined to be 2.652(4) Å, again midway between the Ta-Se length in Ta_3SeI_7 (2.528(7) Å) and *hc*-Ta_3TeI_7 (2.710(4) Å).

Table C-1. Crystallographic summary for $Ta_3Se_{0.38}Te_{0.62}I_7$ (representative solution).

Space group	$P6_3mc$
Unit cell dimensions (Å)	
a	7.569(1)
c	13.770(3)
Volume (Å^3)	683.19(9)
Z	2
Data ($2\theta_{max}$ = 50°)	1222 total, 284 unique
R_{int}	0.0602
R1 / wR2 (all data)	0.0340 / 0.0611
GoF	1.167
Fourier map	1.70 and -1.78 e$^-$ / Å^3
Results	
Composition (average of four solutions)	$Ta_3Se_{0.38}Te_{0.62}I_7$

$Ta_3S_xTe_{1-x}I_7$ ($x = 0.5$) and $Ta_3S_xSe_{1-x}I_7$ ($x = 0.5$)

Synthesis and Characterization

Partial substitution of sulfur onto the capping site is perhaps more appealing than the Se-Te compound reported above. The possibility of incorporation of sulfur into the hexagonal phase is one reason; another is the incorporation of selenium and tellurium into the sulfide iodide compounds that have no counterpart in ternary Se or Te chemistry, i.e. Ta_4SI_{11} and *o*-Ta_3SI_7.

The mixed sulfur-tellurium and sulfur-selenium compounds $Ta_3S_xQ_{1-x}I_7$ (Q = Se, Te) can be synthesized in high yield by stoichiometric combination of the elements from 450 to 550°C, for a duration of a few days to quantitative conversion in ca. three weeks. Both compounds form glistening grey powders which grind in the mortar with a lubricating feel. Guinier powder diffraction indicates adoption of the *hc*-Nb_3SeI_7 type, as the mixed Se/Te compound did. Unfortunately, no single crystals of either of these compounds were ever grown, despite attempting reactions at different temperatures, and also attempting to re-heat, or anneal, the premade powders under a variety of conditions. The Guinier powder diffraction patterns were thus the sole characterization method for these compounds. This method is sufficient, though, to answer the question of whether the powders that form consist of one single mixed-chalcogen phase, or of a mixture of the ternary compounds. The lattice parameters of the two ternary phases possible in each mixed-chalcogen system are similar of course, but are sufficiently different to permit the distinguishing of phases. Using $Ta_3Se_xTe_{1-x}I_7$ as an example, the intense 203 and 205 lines of *hc*-Ta_3SeI_7 and *hc*-Ta_3TeI_7 are separated by ca. 0.5° in 2-theta, more than enough to distinguish these two phases using these two lines. The situation is analogous for *hc*-Ta_3SI_7 compared to *hc*-Ta_3SeI_7 and *hc*-Ta_3TeI_7. Therefore, a powder pattern containing two closely spaced sets of lines will indicate the coexistence of two phases.

The Guinier diffraction patterns of both the "$Ta_3S_xSe_{1-x}I_7$" and "$Ta_3S_xTe_{1-x}I_7$" powders indicate the presence of only one phase, presumably a mixed chalcogen phase, based on the evidence that only one diffraction pattern appears. No splitting of lines was observed. Furthermore, the patterns of the sulfur-doped systems showed the expected shifts relative to the known ternary selenide and telluride patterns, indicating mixing. In both cases, the lines in the sulfur-doped patterns were shifted toward larger 2θ values (smaller *d*-spacings) relative to the pure *hc*-Ta_3SeI_7 and *hc*-Ta_3TeI_7 patterns. This is the expected result when the unit cell of a system has been reduced in size due to incorporation of a smaller element.

II. Halogen Mixing

$Ta_3TeI_3Cl_4$ and $Ta_3SeI_3Br_4$

Synthesis and Characterization

Synthesis of the mixed halide compounds $Ta_3TeI_3Cl_4$ and $Ta_3SeI_3Br_4$ was carried out according to Equations (1) and (2), respectively:

$$11\ Ta\ (foil) + 4\ TaCl_5 + 5\ Te + 7.5\ I_2 = 5\ Ta_3TeI_3Cl_4 \qquad (1)$$

$$3\ Ta\ (foil) + Se + 1.5\ I_2 + 4\ Br_2 = Ta_3SeI_3Br_4 \qquad (2)$$

Reagents were loaded into flame-dried quartz tubes in a glove box, and sealed under vacuum. The temperature chosen was 500°C, and the reactions were allowed to proceed for two weeks. At the end of this time, each tube contained two distinct products: a black powder, and a reflective silver solid, which was transported to the opposite end of the tube. This solid has a distinct layered "micaceous" morphology, and ground with a lubricating feel in the mortar. Guinier powder patterns of the transported crystalline solid resembled 3-1-7 compounds, especially Nb_3SBr_7. SEM verified the presence of all four elements in each case. However, the solid forms as large pieces, and no suitable crystals of either phase could ever be removed. Solution of the structures via x-ray powder diffraction was not attempted.

III. Other

MTa_2I_8 (M = Zr, Hf)

A hypothetical compound MTa_2I_8 with M = four-valence-electron Zr or Hf would have six metal-metal bonding electrons per cluster, as with Ta_3QX_7. All attempts to synthesize these enticing compounds were carried out by reactions of the elements at 450° to 550°C, in evacuated glass tubes. For all "hetero-metal" reactions, the result was the same: Zr or Hf was not incorporated into a Ta-I compound. The ultimate fate of group IV metals were the brightly colored tetraiodides, ZrI_4 and HfI_4. The Ta-I in the tube formed predominantly Ta_6I_{14}, tantalum metal, and some TaI_5.

Ta_2MoTeI_7, $Ta_2MoTe_3I_5$

Molybdenum likewise could not be induced into the Ta_3QX_7 framework. Reactions of the elements in the usual temperature range according to the above formulae led to formation of MoI_2, $MoTe_2$, and known tantalum iodide and telluride iodide products.

Intercalation of Ta_3QX_7

Intercalation of tantalum compounds

Previous studies intercalating TaS_2 with sodium, ammonia and even large organometallic moieties have been well-documented.[96] The layered nature of Ta_3QX_7 raises the possibility of intercalation chemistry. Fundamental structural chemistry has been discussed at length in this thesis already: Important to be reminded of here is the energetically "accessible" and slightly Ta-Ta bonding MO (Figure 1-19 and attendant discussion in Chapter One) present in Ta_3QX_7 that might be able to accept electrons from the intercalate without structural decomposition.

Intercalation of binary layered halide compounds of the $CdCl_2$ or CdI_2 types has never been observed; stirring the layered compounds in solution with the intercalate

candidate leads rather to dissolution of the host, driven by solvation to form a metal coordination complex. For example, the formation of $Cd(NH_3)_6^{2+}$ is observed instead of NH_3 intercalation during studies of $CdCl_2$. [97] The reason for this is the lack of stabilizing metal-metal interactions within the layered framework, and the lesser lattice energy compared with the non metal-metal bonded Group V dichalcogenides that do exhibit intercalation chemistry. (greater ionic charges = greater lattice energy).

Intercalation chemistry has, however, been observed in layered halides that do have extensive stabilizing metal-metal bonding. Corbett, et al., have intercalated ZrX (X = Cl, Br), layered compounds containing double metal layers sandwiched by halide. These phases could handle up to one mole of hydrogen ($ZrXH_{1.0}$) without undergoing structural decomposition.[98] The strongly bound metal double-layer network apparently increases the lattice energy of the compound and prevents solvation of the metal ions.

In 1991, Simon, et al, succeeded in intercalating α-Nb_3Cl_8 with sodium to give $Na_xNb_3Cl_8$ by reacting Nb_3Cl_8 with a solution of sodium benzophenone in tetrahydrofuran.[99] The overall structure of Nb_3Cl_8 underwent a change in anion stacking pattern from hcp to ccp, and the Nb-Nb bond length decreased slightly, consistent with population of an M-M bonding orbital (see Chapter One). Also, the compound changed color from green to red upon intercalation.[100]

With a view towards studying the reactivity and chemical properties of Ta_3QX_7, the intercalation of Nb_3Cl_8 is an encouraging precedent. This is particularly true for Ta_3TeCl_7, which adopts the Nb_3Cl_8 structure type and can be made readily in pure form.

Synthetic approaches to intercalation of Ta_3QX_7:

A. High-temperature solid-state reactions between pure ternary Ta_3QX_7 compounds and the chosen intercalates. See also end of this appendix, "Quaternary reactions" for quaternary synthetic attempts.

B. $(NaK)_x$(benzophenone) + Ta_3TeCl_7: Direct analogy to $Na_xNb_3Cl_8$.

C. Refluxing the powdered Ta_3QX_7 compounds in an organic solvent, at room and elevated temperatures.

A. High-temperature solid-state reactions.

Several reactions of various Ta_3QX_7 "hosts" with various proposed intercalate species with were attempted. In general, reactions were carried out using standard evacuated glass tube method, at a variety of temperatures. Occasionally a Ta or Al_2O_3 crucible was used to guard against reactions of extremely active alkali metals or alkaline earths with the glass container (at least for the initial reaction, until the active metal was completely consumed). As well as investigating the potential intercalation chemistry of these phases, the following reactions also constituted an attempt to prepare quaternary derivatives of Ta_3QX_7 compounds. A reference to the page number in the lab notebook is given (p159nb4 = page 159 in notebook four).

I. Hydrogen, Alkali metals

Hydrogen

- $H_2 + Ta_3TeCl_7$

Conditions: Flow system: ultra pure carrier grade H_2 (>99.999%) used. The Ta_3TeCl_7 was XRPD pure, and finely powdered. Placed at bottom of a self-made reaction vessel, inserted into a tube furnace for heating.

Reactions:

1.	200°C, 4h	No change. Unaffected Ta_3TeCl_7 (XRPD)
	400°C, 6h	Te (s) sublimed to cooler part of reaction vessel. XRPD shows Ta_3TeCl_7 left, as well as Ta_2O_5. Oxygen source unknown. Gas/Si grease/glass?
	500°C, several hours	Stronger Ta_2O_5, weaker Ta_3TeCl_7.

Sodium

- $Ta_3TeCl_7 + Na$ (p159nb4, p223nb4, p57nb5, p31nb7)

Reactions:

1.	105°C, 1h / 475°C, 3h	Unreacted Na + Ta_3TeCl_7 + NaCl + bright green powder. Distinctive powder pattern.
	500°C, 3 wks	NaCl + bright green solid + unknown crystals, hexagonal vertices. Unsuccessful XRD
	480 - 460°C, 5 wks	Same unknown crystals, bright green powder. NaCl
	925°C, 1d / 750°C, 21d	$TaTe_2$ + steel-wool texture grey fibers: low 2θ line. (also seen in $SrTa_3TeCl_7$, $Li_2Ta_3TeCl_7$, etc., below)

- $(NaK)_2$(benzophenone) + Ta_3TeCl_7 (p75nb6, p49nb7)

Conditions: Periodically refreshed purple $(NaK)_2$(bzph) solution (in thf) decanted onto Ta_3TeCl_7 powder, stirred @ room temp, 1d. Solid product filtered, washed with thf till clear washings, dried in vacuo. Handled in glove box.

Results:	Finely divided grey powder, unreacted silver alkali metal piece. SEM: K, Ta, Te Cl present. <u>*No Na.*</u> XRPD: Weak & broad diffraction lines. Unmatchable - not similar to Ta_3TeCl_7.
Annealing (500°C, 35d):	Tube attack. Grey powder. Weak diffraction, unidentifiable.

- Na + Ta_3TeI_7 (p158nb4, p221nb4, p55nb5, p35nb7)

Reactions:

1.	105°C, 1h / 450°C, 12h	Ta_3TeI_7 + Ta_6I_{14} + NaI
	500°C, 3 wks	*hc*-Ta_3TeI_7 + Ta_6I_{14} + NaI
	480 - 460°C, 5 wks	Ta_6I_{14} + NaI only (?) - can't locate Te by XRPD
	727°C, 1d / 575°C, 21d	TaI_5 + NaI + $TaOI_2$ + *hc*-Ta_3TeI_7 + low 2θ line.

- 2Na + Nb_3TeI_7 (p157nb4, p224nb4, p107nb5, p35nb7)

Reactions:

1.	105°C, 1h / 475°C, 3h	Nb_3TeI_7 + NaI
	500°C, 3wks	Nb_3TeI_7 + NaI + 2 unknown phases
	700°C, 6 wks	Nb_5Te_4 (film on wall) + Nb_6I_{11} + NaI
	925°C, 1d / 750°C, 21d	Nb_3I_8 + Nb_3TeI_7 + Nb_3I_8 + Nb_5Te_4 + NaI + intense line at low 2θ.

II. Alkali and Alkaline Earth Chalcogenides

- Na_2S + Ta_3SI_7 (p7nb5)

Reactions:

1.	500°C, 5d	NaI / Na_2S + extremely hard solid, unknown

- (Na_2S / 0.5 S_8) + Ta_3SI_7 (p228nb4)

Purpose: Dissolve Ta_3SI_7 in a "reactive polychalcogenide flux" of Na_2S_5.

Reactions:

1.	400°C, 3.5d	NaI / Na_2S + two unknowns: Crystals and very hard solid.

- 5 Na_2Se_5 (flux) + Ta_3SeI_7 (p226nb4, p4nb6, p53nb5, p27nb7)

Reactions:

1.	400°C, 3.5d	NaI + $TaSe_3$ + Se + unknowns
	450°C, 30d	No XRPD, more $TaSe_3$ ribbon, prob. Se
	480 - 460°C, 5 wks	NaI + $TaSe_3$
	510°C, 30d	NaI + $TaSe_3$

III. Miscellaneous

Tin

- 11 Sn (flux) + Δ-Ta_3TeI_7 (p231nb4, p63nb5, p23nb7)

Reactions:

1.	350°C, 2.5d; furnace off	Sn + SnI_2 + Ta_3TeI_7
	625°C, 17d	Sn + SnI_2 + SnTe + intense unknown lines
	1000°C, 2d / slow cool to 700°C, furnace off	Sn + SnI_2 + SnTe + 2 unknowns + Ta_2O_5

Gallium

- 6.6 Ga + *hc*-Ta_3TeI_7 (p229nb4, p35nb5, p115nb5, p29nb7)

Reactions:

1.	350°C, 2.5d; furnace off	Ta_3TeI_7 + Ga_2I_4
	450°C, 21d	Ga_2I_4 + silver cotton-candy stuff + black powder
	525°C, 16d	Ga_2I_4 + silver threads/black powder (= identical patterns)
	510°C, 30d	Silver fibers / grey powder. Still unknown!

Silver

- 6 Ag + Ta_3TeI_7 (p230nb4, p33nb5, p121nb5)

Reactions:

1.	400°C, 3.5d	no entry
	450°C, 21d	weak Ta_6I_{14} + strong unknown (AgI?)
	525°C, 16d	Ta_6I_{14} + hex-AgI (?) (same unknown as above)

Quaternary Systems: $A_xTa_3QX_7$

The reactions tabulated below in outline form present a summary of the reactions designed to investigate the potential quaternary chemistry of the Ta_3QX_7 system. Such a quaternary chemistry has been discovered in niobium chemistry where, as alluded to in Chapter One, Rb and Cs have been put into the Nb-S-Br system. The compounds $Rb_3Nb_6SBr_{17}$ [9] and $CsNb_3SBr_7$ [101] retain obvious structural similarities to the "parent" Nb_3SBr_7 structure, but each forms its own new and unique structure. Such phases might constitute encouragement enough to pursue the same chemistry for tantalum; also, considering the readiness with which Ta-Q-X systems yielded such diverse and abundant ternary compounds once the proper temperature region was found, it almost seems likely that incorporation of a fourth element into a Ta-Q-X system might occur.

General: Reaction carried out using standard evacuated glass tube method. A reference to the page number in the lab notebook is given (p180nb4 = page 180 in notebook four).

I. Hydrogen, Alkali metals

Hydrogen

- $H_2Ta_3TeCl_7$ (p180nb4, p49nb5)

Equation: $4TaH + 2TaCl_5 + TeCl_4 + Te$

Reactions:

1. 450°C , 9d: $TaOCl_2$, unknowns?
   480 - 460°C, 5 wks: Uncertain: Ta_6Cl_{15} and Ta_3TeCl_7 likely

- $H_2Ta_3TeI_7$ (p178nb4, p51nb5)

Equation: $Ta + 2TaH + Te + 7/2\ I_2$

Reactions:

1. 450°C, 9d: $TaOI_2$ + unreacted Ta/TaH. Unidentified powder
   480 - 460°C, 5 wks: prob. *hc*-Ta_3TeI_7, Δ-Ta_3TeI_7.

- HTa_3TeI_7 (p57nb7)

Equation: $Ta + TaH + Te + 7/2\ I_2$

Reactions:

1. 435°C, 10d: Ta/TaH + hc-Ta_3TeI_7 + $TaTe_2$-like pattern + Ta_6I_{14}/TaI_5 + unknown

Lithium

- $Li_2Ta_3TeCl_7$

with Li metal:

Equation: $10Li + 8Ta + 5Te + 7TaCl_5 = 5Li_2Ta_3TeCl_7$ (p123nb5, p33nb7)

Reactions:

1. 500°C, 14d: $Ta_6Cl_{15} + TaTe_2$
   727°C, 1d / 575°C, 21d: Ta_2Si/TaO (indistinguishable patterns) + $TaTe_2$ + low 2θ pattern (unknown).

with LiCl:

Equation: $2LiCl + 2Ta + Te + TaCl_5 = Li_2Ta_3TeCl_7$ (p125nb5, p33nb7)

Reactions:

1. 500°C, 14d: $Ta_6Cl_{15} + TaTe_2$ + LiCl + low 2θ pattern seen in $Na+Ta_3TeCl_7$ reaction
   925°C, 1d / 750°C, 21d: $TaTe_2$ + low 2θ pattern + Ta_2Si

- $Li_2Ta_3TeI_7$

Equation: $2Li + 3Ta + Te + 7/2\ I_2$ (p139nb5, p21nb7)

Reactions:

1. 425°C, 17d: *hc*-Ta_3TeI_7 + Δ-Ta_3TeI_7 + LiI + junk
   430°C, 17d: Δ-Ta_3TeI_7 + $TaTe_2$* + LiI-like pattern + little $TaOI_2$.
   *$TaTe_2$ lines shifted to lower 2θ

Sodium

- $Na_2Ta_3SI_7$ (p11nb7, p47nb7)

Equation: $Na_2S + 3Ta + 7/2\ I_2$

Reactions:

1. 425°C, 16d: $Ta_4SI_{11} + Ta_6I_{14}$ + o-Ta_3SI_7 + NaI/Na_2S (same pattern)
   500°C, 35d: $Ta_6I_{14} + Na_2S/NaI$ + intense inknowns

- $Na_2Ta_3Se_6I_7$ (p129nb5, p27nb7)

Equation: $Na_2Se_5 + 3Ta + Se + 7/2\ I_2$

Reactions:

1. 500°C, 14d: $NaI + TaSe_2$
   510°C, 30d: $NaI + TaSe_2 + I_2$

Potassium, Rubidium:

- No reactions attempted.

Cesium

- $CsTa_3SI_7$ (p15nb7, p51nb7)

Equation: $CsI + 3Ta + 1/8\ S_8 + 3\ I_2$
Reactions:
1. 430°C, 20d — $Cs_2TaI_6 + Ta_6I_{14}/TaI_5 + o\text{-}Ta_3SI_7$
   500°C, 24d — $Cs_2TaI_6 + Ta_6I_{14}$ + unknowns

- $Cs_4Ta_3SI_7$ (p67nb7)

Equation: $4CsI + 3Ta + 1/8\ S_8 + 3/2\ I_2$
Reactions:
1. 435°C, 10d — Ta metal + $CsI + Cs_2TaI_6$

- $CsTa_3SeI_7$ (p15nb7, p53nb7)

Equation: $CsI + 3Ta + Se + 3\ I_2$
Reactions:
1. 430°C, 20d — $Ta_3SeI_7 + Cs_2TaI_6$ + prob. Ta_6I_{14}
   500°C, 24d — $Cs_2TaI_6 + Ta_6I_{14}$ + "other intense lines"

- $CsTa_3TeI_7$ (p17nb7, p53nb7)

Equation: $CsI + 3Ta + Te + 3\ I_2$
Reactions:
1. 430°C, 20d
   500°C, 24d — Cs_2TaI_6 + *hc*-Ta_3TeI_7 + strong unknown

II. Alkaline Earth Metals

Be, Mg

- No reactions attempted.

Calcium

- $CaTa_3TeI_7$ (p131nb5, p7nb7, p79nb7)

Equation: $Ca + 3Ta + Te + 7/2\ I2$
Reactions:
1. 425°C, 17d — *hc*-Ta_3TeI_7 + Δ-$Ta_3TeI_7 + Ta_6I_{14}$. No sign of Ca!
   430°C, 17d — *hc*-Ta_3TeI_7 + many unknown lines.
   500°C, 35d — *hc*-Ta_3TeI_7 + Δ-Ta_3TeI_7 + unknown powder.

Strontium

- $SrTa_3TeCl_7$ (p127nb5, p31nb7)

Equation: $SrCl_2 + 2Ta + Te + TaCl_5$

Reactions:

1.	500°C, 14d:	$TaTe_2 + Ta_6Cl_{15} + SrCl_2$
	925°C, 1d / 750°C, 21d	$TaTe_2 + SrCl_2$ + grey fiber weave - low 2θ lines like Nb_3Te_4

Barium

- $BaTa_3SI_7$ (p137nb5, p47nb7)

Equation: $BaS + 3Ta + 7/2\ I_2$

Reactions:

1.	425°C, 17d	Ta metal, Ta_6I_{14} + mixture of *hc*-Ta_3SI_7, o-Ta_3SI_7, Ta_4SI_{11} (unsure - weak patterns) + weak, complicated unknown pattern.
	500°C, 35d	$Ta_6I_{14} + TaOI_2$ + at least two unknowns

III. Other

Zinc

- $Zn + 3Ta + Te + 7/2\ I_2$ (p168nb4, p207nb4, p67nb5, p25nb7)

Reactions:

1.	450°C, 10d	Δ-Ta_3TeI_7 + grey unknown & white unknown.
	500°C, 3 wks	Δ-Ta_3TeI_7+ Ta_6I_{14} + dirty white unknown, like "ZnI_2/ZnTe"
	625°C, 17d	Unknowns + TaI_5 + Ta_2Si/TaO
	1000°C, 2d / slow cool to 700°C, furnace off	Ta_2O_5 + Ta_2Si/TaO + unk. + Nb_3Te_4-like pattern

Zirconium

- $ZrTa_3SI_7$ (p11nb7, p49nb7)

Equation: $ZrS + 3Ta + 7/2\ I_2$

Reactions:

1.	425°C, 16d	$ZrI_4 + Ta_6I_{14}$ + ? + simple unknown crystalline phase (all crystals bad)
	500°C, 35d	$ZrI_4 + Ta_6I_{14}$

REFERENCES CITED

[1] H. Boehland and F. M. Schneider, *Z. Chem.*, **1972**, *12*, 28.

[2] G. W. A. Fowles, R. J. Hobson, D. A. Rice and K. J. Shanton, *J. Chem. Soc., Chem Commun.*, **1976**, 552.

[3] W. Tremel, *Chem. Ber.*, **1992**, *125*, 2165.

[4] H. F. Franzen, W. Hönle and H. G. von Schnering, *Z. Anorg. Allg. Chem.*, **1983**, *497*, 13.

[5] H. G. von Schnering, H. Wöhrle and H. Schäfer, *Naturwissenschaften*, **1961**, *48*, 159.

[6] V. E. Fedorov, V. K. Evstaf'ev, S. D. Kirik and A. V. Mishchenko, *Russ. J. Inorg. Chem*, **1981**, *26*, 1447.

[7] H. Ben-Yaich, J. C. Jegaden, M. Potel, M. Sergent, A. K. Rastogi and R. Tournier, *J. Less-Common Metals*, **1984**, *102*, 9.

[8] H.-J. Meyer and J. D. Corbett, *Inorg. Chem.*, **1991**, *30*, 963.

[9] H. Womelsdorf and H.-J. Meyer, *Angew. Chem. Int. Ed. Eng.*, **1994**, *33(19)*, 1943.

[10] A. Broll, A. Simon, H. G. von Schnering and H. Schäfer, *Z. Anorg. Allg. Chem.*, **1969**, *367*, 1.

[11] A. Simon and H. G. von Schnering, *J. Less-Common Metals*, **1966**, *11*, 31 (β-Nb_3X_8)
S. S. Berdonosov and A. V. Lapitskii, *Russ. J. Inorg. Chem.*, **1965**, *10*, 2812 (α-Nb_3Br_8).

[12] F. A. Cotton, M. P. Diebold, X. Feng and W. J. Roth, *J. Am. Chem. Soc.*, **1988**, *27*, 3413.

[13] N. N. Greenwood and A. Earnshaw, *Chemistry of the Elements*, Pergamon Press, New York, (1984).

[14] X. Yao and H. F. Franzen, *J. Am. Chem. Soc.*, **1991**, *113*, 1426.

[15] A. Zalkin and D. E. Sands, *Acta Cryst.*, **1958**, *11*, 615.

[16] S. S. Berdonosov, A. V. Lapitskii, D. G. Berdonosova and L. G. Vlasov, *Russ. J. Inorg. Chem.*, 1963, **8**, 1315
R. Rolsten, *J. Am. Chem. Soc.*, **1958**, *80*, 2952.

[17] U. Müller, *Acta Cryst.*, 1979, **B35**, 2502
R. Rolsten, *J. Am. Chem. Soc.*, **1958**, *80*, 2952.

[18] F. A. Cotton, P. A. Kibala, M. Matusz and R. B. W. Sandor, *Acta Cryst.*, **1991**, *C47*, 2435
W. Hönle and H.-G. von Schnering, *Z. Krist.*, **1990**, *191*, 139;
A. Zalkin and D. E. Sands, *Acta Cryst.*, **1958**, *11*, 615.

[19] W. Hönle, S. Furuseth and H.-G. von Schnering, *Z. Naturforsch.*, **1990**, *45B*, 952
U Müller and P. Klingelhöfer, *Z. Naturforsch.*, **1983**, *38B*, 559 (β).

[20] B. Krebs and D. Sinram, *Z. Naturforsch.*, **1980**, *35B*, 12
W. Litke and G. Brauer, *Z. Anorg. Allg. Chem.*, **1963**, *325*, 122.

[21] E. A. Pisarev, D. V. Drobot and I. V. Makarchuk, *Russ. J. Inorg. Chem.*, **1982**, *27*, 10.

[22] H. Schafer, R. Gerken and H. Scholz, *Z. Anorg. Allg. Chem.*, **1965**, *335*, 96
S. S. Berdonosov, A. V. Lapitskii and D. G. Berdonosova, *Russ. J. Inorg. Chem.*, **1964**, *9*, 1388
R. E. McCarley and J. C. Boatman, *Inorg. Chem.*, **1963**, *2*, 547.

[23] L. F. Dahl and D. L. Wampler, *Acta Cryst.*, **1962**, *15*, 903
R. Rolsten, *J. Am. Chem. Soc.*, **1958**, *80*, 2952.

[24] S. S. Berdonosov, A. V. Lapitskii and D. G. Berdonosova, *Russ. J. Inorg. Chem.*, **1964**, *9*, 1388; R. E. McCarley and B. A. Torp, *Inorg. Chem.*, **1963**, *2*, 540; H. Schäfer and K.-D. Dohmann, *Z. Anorg. Allg. Chem.*, **1961**, *311*, 134.

[25] L. F. Dahl and D. L. Wampler, *Acta Cryst.*, **1962**, *15*, 903
L. F. Dahl and D. L. Wampler, *J. Am. Chem. Soc.*, **1959**, *81*, 3150.

[26] D. Bauer and H.-G. von Schnering, *Z. Anorg. Allg. Chem.*, **1968**, *361*, 259.

[27] D. Bauer and H. Schäfer, *J. Less-Common Met.*, **1968**, *14*, 476.

[28] B. Bajan and H.-J. Meyer, *Z. Krist.*, **1995**, *210*, 607.

[29] H. M. Artelt and G. Meyer, *Z. Krist.*, **1995**, *206*, 306
D. Bauer, H.-G. von Schnering and H. Schäfer, *J. Less-Common Met.*, **1965**, *8*, 388.

[30] A. Simon, H.-G. von Schnering, H. Wöhrle and H. Schäfer, *Z. Anorg. Allg. Chem.*, **1965**, *339*, 155.

[31] H. Imoto and J. D. Corbett, *Inorg. Chem.*, **1982**, *21*, 308
A. Simon, H.-G. von Schnering and H. Schäfer, *Z. Anorg. Allg. Chem.*, **1967**, *355*, 295.
L. R. Bateman, J. F. Blount and L. F. Dahl, *J. Am. Chem. Soc.*, **1966**, *88*, 1082.

[32] $NbCl_5$(g), and $TaCl_5$(g): A. A. Ischenko, T. G. Strand, A. V. Demidov and V. P. Spiridonov, *J. Mol. Struct.*, **1978**, *43*, 227
$NbBr_5$(g) and $TaBr_5$(g): *Vest. Mosk. Univ. Ser. 2*, **1966**, *21*, 109.

[33] P. Frère, *Ann. Chim.*, **1962**, *7*, 85.

[34] S. S. Berdonosov, A. V. Lapitskii and L. G. Vlasov, *Russ. J. Inorg. Chem.*, **1962**, *7*, 1125.

[35] H. Schäfer and H.-G. von Schnering, *Angew. Chem.*, **1964**, *76*, 833.

[36] H. Schäfer and L. Grau, *Z. Anorg. Allg. Chem.*, **1954**, *275*, 198.

[37] R. C. Young and C. H. Brubaker, *J. Am. Chem. Soc.*, **1952**, *74*, 4967.

[38] J. D. Corbett and P. X. Seabaugh, *J. Inorg. Nucl. Chem.*, **1958**, *6*, 207.

[39] J. G. Converse, J. B. Hamilton and R. E. McCarley, *Inorg. Chem.*, **1970**, *9*, 1366.

[40] N. N. Greenwood and A. Earnshaw, *Chemistry of the Elements*, Pergamon Press, New York, 1984, p. 1155
P. Frère, *Ann. Chim.*, **1962**, *7*, 85.

[41] F. Hulliger, *Structural Chemistry of the Layer-Type Phases*, Reidel, Dordrecht (1976).

[42] G. J. Miller, *J. Alloys Compounds*, **1995**, *217*, 5.

[43] J. Beck, *Angew. Chem. Intl. Ed. Eng.*, **1994**, *33*, 163.

[44] L. Pauling, "*The Nature of the Chemical Bond*", Cornell University Press, Ithaca, NY, 3rd. ed. (1960).

[45] R. D. Shannon and C. T. Prewitt, *Acta Cryst.*, **1969**, *B25*, 925.

[46] G. W. A. Fowles, R. J. Hobson, D. A. Rice and K. J. Shanton, *J. Chem. Soc., Chem. Commun.*, **1976**, 552.

[47] A. O. Baghlaf and A. Thomson, *J. Less-Common Met.*, **1977**, *53*, 291.

[48] D. A. Rice, *Coord. Chem. Rev.*, **1978**, *25*, 199.

[49] S. M. Sinitsyna, V. G. Khlebodarov and N. A. Bukhtereva, *Russ. J. Inorg. Chem.*, **1975**, *20*, 1267.

[50] H. Funk and W. Weiss, *Z. Anorg. Allg Chem.*, **1958**, *295*, 327.

[51] M. G. B. Drew and I. B. Tomkins, *Acta Cryst.*, **1970**, *B26*, 1161.

[52] M. G. B. Drew and I. B. Tomkins, *J. Chem. Soc. A*, **1970**, 22.

[53] N. D. Chikanov, *Russ. J. Inorg. Chem.*, **1968**, *13*, 1483.

[54] L. Guemas, P. Gressier, A. Meerschaut, D. Louer and D. Grandjean, *Rev. Chim. Miner.*, **1981**, *18*, 91.

[55] P. Grenouilleau, A. Meerschaut, L. Guemas and J. Rouxel, J. Solid State Chem., **1987**, *66*, 293.

[56] P. Gressier, L. Geumas and A. Meerschaut, *Acta Cryst.*, **1982**, *B38*, 2877.

[57] P. Gressier, A. Meerschaut, L. Guemas, J. Rouxel and P. Monceau, *J. Solid State Chem.*, **1984**, *51*, 141.

[58] S. Furuseth, W. Hönle, G. J. Miller and H.-G. von Schnering, *9th Int. Conf. on Solid Compounds of Transition Elements, Abstracts*, Royal Society of Chemistry, London, 1988.

[59] G. V. Khvorykh, A. V. Shevelkov, V. A. Dolgikh and B. A. Popovkin, *J. Solid State Chem.*, **1995**, *120*, 311.

[60] This thesis, Chapter Five.

[61] F. A. Cotton and T. E. Haas, *Inorg. Chem.*, **1964**, *3*, 10.
F. A. Cotton, *Ibid.*, **1964**, *3*, 1217.

[62] B. E. Bursten, F. A. Cotton, M. B. Hall and R. C. Najjar, *Inorg. Chem.*, **1982**, *21*, 302.
F. A. Cotton, G. G. Stanley, *Chem. Phys. Lett.*, **1978**, *58*, 540.

B. E. Bursten, F. A. Cotton and G. G. Stanley, *Isr. J. Chem.*, **1980**, *19*, 132.
B. E. Bursten, F. A. Cotton, J. C. Green, E. A. Seddon and G. G. Stanley, *J. Am. Chem. Soc.*, **1980**, *102*, 955.

[63] W. H. McCarroll, L. Katz and R. Ward, *J. Am. Chem. Soc.*, **1957**, *79*, 5410.

[64] D. J. Hintz, G. Meyer, T. Dedecke and W. Urland, *Angew. Chem., Int. Ed. Eng.*, **1995**, *34*, 71.

[65] V. P. Fedin, M. N. Socolov and A. V. Virovets, *Polyhedron*, **1992**, *11*, 2320.

[66] F. A. Cotton, M. Shang and Z. Sun, *J. Am. Chem. Soc.*, **1991**, *113*, 6917.

[67] H.-Jürgen Meyer, *Z. Anorg. Allg. Chem.*, **1994**, *620*, 81.

[68] G. M. Sheldrick, "SHELXS-86", Univ. Göttingen, Germany (1986).

[69] TEXSAN: Single Crystal Structure Analysis Software, Version 5.0; Molecular Structure Corp., The Woodlands, TX (1989).

[70] N. Walker and D. Stuart, *Acta Cryst.*, **1986**, *A39*, 158.

[71] G. J. Miller, *J. Alloys Compounds*, **1995**, *229*, 93.

[72] J. F. Moulder, W. F. Stickle, P. E. Sobol and K. D. Bomben, "*Handbook of X-Ray Photoelectron Spectroscopy*", J. Chastain, ed., Perkin-Elmer Corp., Eden Prairie MN (1992).

[73] U. Müller, "*Inorganic Structural Chemistry*", John Wiley & Sons, Chichester, England (1993).

[74] P. Villars and L. D. Calvert, *Pearson's Handbook of Crystallographic Data for Intermetallic Phases, Volume 3*, American Society for Metals, Metals Park OH (1985) and references therein.

[75] H.-J Meyer and J. D. Corbett, *Inorg. Chem.*, **1991**, *30*, 963.

[76] G. J. Miller and J. Lin, *Angew. Chem. Intl. Ed. Engl.*, **1994**, *33*, 334.

[77] G. M. Sheldrick, "SHELXL93 Program for the Refinement of Crystal Structures", Univ. Göttingen, Germany (1993).

[78] R. Hoffmann and W. N. Lipscomb, *J. Chem. Phys.*, **1962**, *36*, 2179.
J. H. Ammeter, H.-B. Bürgi, J. C. Thibeault and R. Hoffmann, *J. Am. Chem. Soc.*, **1978**, *100*, 3686.

[79] M.-H. Whangbo, R. Hoffmann and R. B. Woodward, *Proc. R. Soc. London, Ser. A*, **1979**, *366*, 23.

[80] E. Clementi and C. Roetti, *At. Data Nucl. Tables*, **1974**, *14*, 177.

[81] S. C. Bevan and D. F. C. Morris, *J. Chem. Soc.*, **1960**, 516.

[82] J. M. Ziman, "*Principles of the Theory of Solids*", Cambridge University Press, London (1964).

[83] S. N. Maganov, P. Zönnchen, H. Rotter, H.-J. Cantow, J. Ren and M.-H. Whangbo, *J. Am. Chem. Soc.*, **1993**, *115*, 2495.

[84] F. W. Brandon, A. Prodan and J. K. Brandon, *J. Phys. Chem.*, **1983**, *16*, 1067.
A. Prodan, V. Marinkovic, F. W. Boswell, J. C. Bennett and M. Remskar, *J. Alloys Compounds*, **1995**, *219*, 69.

[85] M. Conrad and B. Harbrecht, *J. Alloys Compounds*, **1992**, *187*, 181.

[86] X. Yao, G. J. Miller and H. F. Franzen, *J. Alloys Compounds*, **1992**, *183*, 7.

[87] X. Yao and H. F. Franzen, *J. Alloys Compounds*, **1992**, *182*, 299.

[88] X. Yao and H. F. Franzen, *J. Solid State Chem.*, **1990**, *86*, 88.

[89] X. Yao and H. F. Franzen, *Z. Anorg. Allg. Chem.*, **1991**, *598*, 353.

[90] K. S. Nanjundaswamy and T. Hughbanks, *J. Solid State Chem.*, **1992**, *98*, 278.

[91] P. Ettmayer and A. Vendl, *J. Less-Common Met.*, **1980**, *72*, 209.

[92] Y. Wang, L. D. Calvert, E. J. Gabe, J. B. Taylor, *Acta Cryst.*, **1979**, *B35*, 1447.

[93] O. Harneit and H. K. Müller-Buschbaum, *Z. Anorg. Allg. Chem.*, **1992**, *613*, 60.

[94] C.-S. Lee and G. J. Miller, unpublished research.

[95] A. Lachgar, D. S. Dudis and J. D. Corbett, *Inorg. Chem.*, **1990**, *29*, 2242.

[96] A. J. Jacobson, in "*Solid State Chemistry: Compounds*" and references therein. A. K. Cheetham and P. Day, ed., Clarendon Press, Oxford (1992).

[97] J. D. Corbett, in "*Intercalation Chemistry*", M. S. Whittingham and A. J. Jacobson, ed., Academic Press, NewYork (1982).

[98] A. W. Struss and J. D. Corbett, *Inorg. Chem.*, **1977**, *16*, 360.

[99] J. R. Kennedy and A. Simon, *Inorg. Chem.*, **1991**, *30*, 2564.

[100] J. R. Kennedy, P. Adler, R. Dronskowski and A. Simon, *Inorg. Chem.*, **1996**, *35*, 2276.

[101]H.-J. Meyer, *Z. Anorg. Allg. Chem.*, **1994**, *620*, 863.

ACKNOWLEDGEMENTS

I wish to express my sincerest thanks to my research advisor, Professor Gordon J. Miller, for encouragement and direction, of course, but moreso for imparting the lesson to think in a careful and unbiased way about chemistry, and for exposing points of view and ways of thinking that opened up a broader and much more rewarding and fascinating world of science, beyond the mad rush to just "make things".

I also wish to acknowledge the essential help of: Dr. Robert Jacobson for unlimited and unfee'd use of diffractometers, all-around answer man Jim Anderegg for XPS measurements and discussions (and diffractometer salvage), Jerry Ostenson for nearly instant magnetic susceptibility measurements, Alfred Kracher for the microprobe measurements, and Victor Young and Len Thomas for crystallographic training and assistance.

I wish to thank the various members of the Miller group whom it's been my fun privilege to know, and to learn the lab ropes with and from.

Although it will be woefully underexpressed, I wish to thank Dr. Karen Nordell for inexhaustible, true friendship; for sunny energy, laughter, and invigorating chemistry discussions, most even related to our own work.... "Come in, she said, I'll give you / Shelter from the storm".

I also wish to thank my parents, for the surest foundation of support and love a person could know.

"Let there be some more test made of my metal"
W. Shakespeare, Measure for Measure (I,i)

IMAGE EVALUATION
TEST TARGET (QA-3)

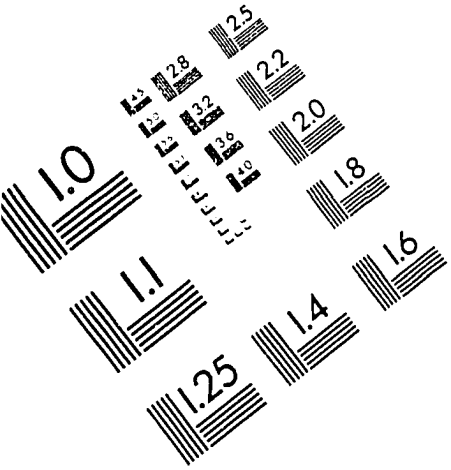

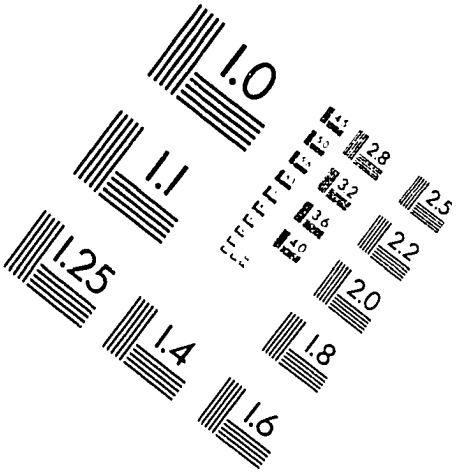

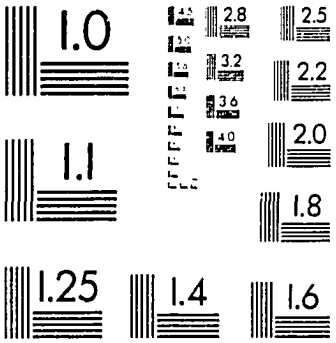

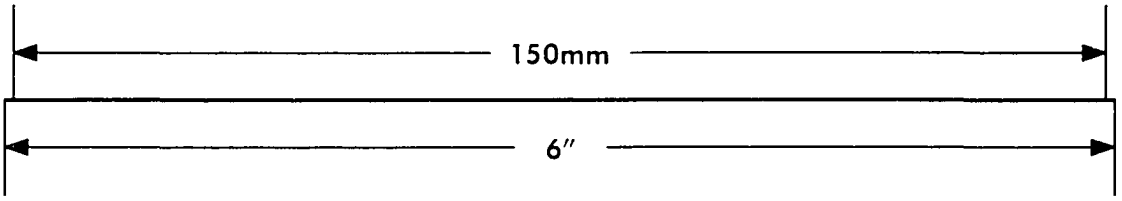

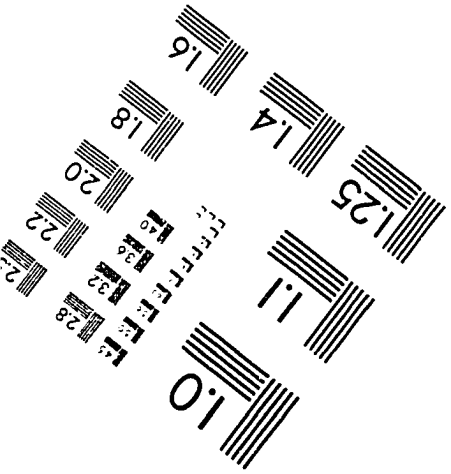

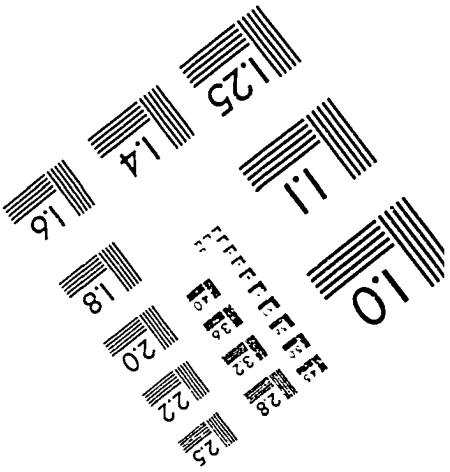

APPLIED IMAGE . Inc
1653 East Main Street
Rochester, NY 14609 USA
Phone: 716/482-0300
Fax: 716/288-5989